AGH AGH University of Science and Technology
Faculty of Physics and Applied Computer Science

Doctoral thesis

Mateusz Marzec

Identification of molecular self-assembled monolayers and their interactions at buried organic material-conductor interfaces in thin film systems

Supervisor: **dr hab. inż. Andrzej Bernasik**

Kraków 2014

This PhD thesis has been completed within the framework of the Human Capital Operational Program POKL.04.01.01-00-434/08-02 co-financed by the European Union.

This PhD thesis was partially supported by the Polish National Science Centre project no. 2013/09/N/ST5/00874.

Oświadczam, świadomy odpowiedzialności karnej za poświadczenie nieprawdy, że niniejszą pracę doktorską wykonałem osobiście i samodzielnie i że nie korzystałem ze źródeł innych niż wymienione w pracy.

data, podpis autora

Oświadczenie promotora rozprawy:

Niniejsza rozprawa jest gotowa do oceny przez recenzentów.

data, podpis promotora rozprawy

Contents

Streszczenie

Oddziaływanie pomiędzy cienką warstwą polimerową a podłożem, na którym została ona utworzona ma istotne znaczenie w wielu zagadnieniach: decyduje o adhezji warstwy polimerowej, wpływa na jej morfologię, a przy wykorzystaniu polimerów przewodzących decyduje o transporcie ładunku elektrycznego pomiędzy tymi dwoma materiałami. Ostatni z wymienionych aspektów jest szczególnie istotny w badaniach nad konstrukcją wysokowydajnych polimerowych układów elektronicznych oraz optoelektronicznych, takich jak tranzystory polimerowe, diody świecące, polimerowe ogniwa słoneczne oraz czujniki chemiczne nie wyłączając biosensorów. Chcąc połączyć wiele aspektów, złącze polimer-podłoże często modyfikowane jest molekularną warstwą samoorganizującą (SAM). Warstwa ta wprowadza zmianę napięcia powierzchniowego podłoża wpływając tym samym na morfologię tworzonej na nim cienkiej warstwy polimerowej, a poprzez moment dipolowy molekuł warstwy SAM, wpływa na wzajemne położenie elektronowych poziomów energetycznych podłoża i polimeru. Powstałe złącze polimer/podłoże może mieć lokalnie niejednorodny charakter, a zaburzenia homogeniczności mogą pojawiać się już w trakcie jego preparatyki. Ze względu na znaczną miniaturyzację układów elektronicznych pojawiające się lokalne mikro- i nano- niejednorodności mogą mieć istotny wpływ na wydajność konstruowanych urządzeń.

Określenie właściwości złącza, a szczególnie jego homogeniczności, jest zagadnieniem trudnym i wymaga stosowania metod o relatywnie dużej głębokości próbkowania oraz wysokiej rozdzielczości powierzchniowej.

Celem pracy było wyznaczenie lokalnych własności elektrycznych złącza pomiędzy warstwą polimerową a organicznym lub nieorganicznym elektrycznie przewodzącym podłożem w modelowych układach cienkowarstwowych. W badaniach wykorzystano niepolarne i polarne polimery konwencjonalne: polistyren, poli(2-winylopirydynę), kwas poliakrylowy oraz polimetakrylan metylu o różnej taktyczności. Drugą grupę stanowiły wybrane polimery sprzężone takie jak poli(3-heksylotiofen), poli(3-oktylotiofen) i ich mieszaniny z fenyloestrową pochodną fullerenu (PCBM) a także polianilina domieszkowana kwasem kamforosulfonowym. W ramach pracy przeprowadzono także syntezę i analizę nanocząstek politiofenu. Cienkie warstwy oraz wielowarstwy o grubości kilkudziesięciu nanometrów zostały wytworzone poprzez rozlewanie roztworów polimerów na wirujące podłoże lub metodą horyzontalnego rozciągania. Jako podłoże zastosowano warstwę złota napyloną na wafel krzemu lub mieszaninę poli(etylendioksytiofen)/polistyren sulfonowany (PEDOT:PSS). Złote podłoża funkcjonalizowane były warstwami samoorganizującymi się z rodziny tioli o różnych grupach funkcyjnych: metylową oraz karboksylową. Funkcjonalizację

przeprowadzono w sposób jednorodny z roztworu lub metodą druku mikro-kontaktowego tworząc w ten sposób kontrolowany wzór o niejednorodnej modyfikacji podłoża. Przewodzące podłoże organiczne PEDOT:PSS modyfikowano jednorodnie alkilosilanami o różnych końcowych grupach funkcyjnych: fluorowej, bromowej, tiolowej oraz aminowej.

Układy na podłożach złota jednorodnie modyfikowanego monowarstwami tiolowymi zostały scharakteryzowane metodami spektroskopii fotoelektronów w zakresie miękkiego promieniowania rentgenowskiego (XPS) oraz ultrafioletu (UPS). Natomiast złącza modyfikowane metodą druku mikro-kontaktowego analizowano kelvinowską mikroskopią sił (KPFM). Metoda ta pozwoliła określić lokalne właściwości elektryczne wewnętrznych złącz z powierzchniową zdolnością rozdzielczą dochodzącą do ok. 60 nm. Zastosowanie spektrometrii mas jonów wtórnych z analizatorem czasu przelotu (ToF-SIMS) umożliwiło wykazanie korelacji pomiędzy niejednorodnościami zobrazowanymi metodą KPFM z powierzchniowym wzorem i składem chemicznym wytworzonego złącza. Otrzymane wyniki zostały poddane dyskusji w oparciu o dyspersyjne, polarne oraz wodorowe oddziaływania pomiędzy polimerem a warstwą SAM. Pokazano również zależność oddziaływania na złączu od struktury konfiguracyjnej i krystaliczności polimeru.

Złącza pomiędzy polimerem a podłożem PEDOT:PSS modyfikowanym jednorodną samoorganizującą się warstwą alkilosilanów badano poprzez profilowanie głębokościowe metodą XPS z użyciem klastrowego działa jonowego. Otrzymane wyniki pozwoliły zlokalizować monowarstwę SAM położoną na złączu oraz wskazać, w przypadku zastosowania samoorganizującej warstwy zawierającej końcową aminową grupę funkcyjną, interakcje zachodzące pomiędzy polimerem przewodzącym a warstwą SAM. Uzyskane wyniki zostały odniesione do wydajności organicznych ogniw fotowoltaicznych w układach o identycznej modyfikacji złącza.

Acknowledgements

First of all I would like to thank my supervisor dr hab. inż. Andrzej Bernasik from the Faculty of Physics and Applied Computer Science, AGH, for his guidance and inspiration during my PhD studies. He introduced me to the field of surface and interface science and created favorable conditions for my work. I would like to take this opportunity to greatly thank dr hab. Jakub Rysz from the Faculty of Physics, Astronomy and Applied Computer Science, Jagiellonian University, for his guidance and ability to explain sophisticated physical concepts in a comprehensible manner. I always admired his talent in research and ability to come up with new ideas and valued him as a good friend.

I would also like to thank prof. dr hab. Andrzej Budkowski from the Faculty of Physics, Astronomy and Applied Computer Science, Jagiellonian University and prof. dr hab inż. Wojciech Łużny from the Faculty of Physics and Applied Computer Science, AGH, for many fruitful discussions on polymer physics.

In addition, I want to thank all members of the Macromolecular Nanofilms group at the Department of Advanced Materials Engineering, Faculty of Physics, Astronomy and Applied Computer Science, Jagiellonian University: Dr Kamil Awsiuk for introducing me the soft-lithography technical concepts and always being the best friend, Dr Joanna Zemła, Monika Josiek and Kasia Fornal who often provided inspiring ideas and helping hands.

Special thanks are due to dr inż. Jakub Haberko who helped me in my early days of my PhD studies and introduced me to physical and technical concepts of AFM and KPFM techniques.

I would like to express my gratitude to prof. dr hab. inż. Marek Przybylski the Director of Academic Center for Materials and Nanotechnology, AGH, for providing me an access to the Laboratory of Photoelectron Spectroscopy, where a part of the measurements involved in this thesis were performed.

Furthermore, the hearty atmosphere during my PhD studies has been carried by all of its members. In particular, many thanks with respect to the wonderful time we spent together go to my fellow colleagues at the Interdisciplinary PhD Studies who graduated along with me.

I would like to thank my whole family, my parents who raised me with a love of science and their encouragement and most importantly, I would like to thank my wife Magdalena, who always kept me on track and supported me during my work.

Dedicated to my son Franciszek

I. Introduction

1. Motivation and Scope

A detailed understanding of the interface dipole formation between metal electrode and thin organic film and at organic/organic heterojunctions plays a key role for the fabrication of organic electronic devices. Energy level alignment across organic interfaces related to e.g. charge carrier injection, is of utmost importance for organic light-emitting diodes (OLEDs), photovoltaics (OPVs), transistors (OFETs) or chemical sensors [1, 2]. The interface energetics determines device performance such as driving voltage and stability of electron and hole injection in OLED [3-5], or open circuit voltages in PV devices [6]. Most of these devices are thin-film based systems, thus interfaces are present within a few nanometers of any active layers and where overall device properties, integrity and stability are determined. Contacts to molecular and polymer films are complex and often difficult to optimize. This is because the energy gaps of most of the organic materials used in organic-based devices are large (exceeding 2.0 eV), making the preparation of satisfactory ohmic contacts for charge injection difficult. The range of work functions of metals or conducting materials that can be used for contact electrodes is also limited. To optimize the contacts the self-assembled monolayers (SAMs) are often placed at the interface [7]. The SAMs not only can control the energy level alignment across the junction, but they also modify morphology of deposited organic layers. Both aspects are intensively studied [8-10]. Deposited SAMs are available with a variety of molecular architectures, or their mixtures allow for a controlled modification of surface tension [11] and for a tunable variation of wettability [12]. This can affect solvent-casting processes and alter morphology of deposited polymer films [13]. In addition, SAM micro-patterns prepared over broad substrate areas can align the domains of spin cast blends of insulating and conjugated polymers, e.g. polystyrene blended with poly(3-alkylthiophene) [14] or polyaniline [15], suggesting a simple method of fabricating polymer-based circuitries.

Analysis of the interfaces formed below thick polymer layers requires techniques with adequately large probing depth. For instance, the buried interface situated up to a few micrometers beneath the surface can be analyzed with optical spectroscopic methods, such as Surface Enhanced Attenuated Total Reflectance Spectroscopy, Surface Enhanced Raman Spectroscopy, or less commonly used Sum Frequency Generation Vibrational Spectroscopy [16]. Recently, spectroscopy of photoelectrons with high kinetic energy has been proposed to examine the interfaces covered with hundred nm thick organic and inorganic multilayers [17, 18]. Electric properties of the interface and their influence on the device performance have been tested by measuring current density versus applied voltage characteristics [19]. The buried interface was also examined with KP method [20] while KPFM was hardly applied. Only very recently the

latter technique was employed to analyze organic multilayers with lateral structure suitable for organic field-effect transistors [21].
Within the framework of this thesis the Kelvin Probe Force Microscopy was proposed as the technique capable of performing nondestructive determination of local inhomogeneities appearing at buried polymer/metal interfaces with sub-micrometer lateral resolution. In order to determine chemical compositions of the interfaces the dynamic secondary ion mass spectrometry (SIMS) measurements were carried out. The studied multilayer organic systems placed on the metallic electrodes can be recognized as model structures for gas sensing devices, sensitive to the work function changes which induce conductance, capacitance and electrochemical potential changes of the modified electrode [22, 23].
In the case of the organic/organic SAM modified interfaces, composed of the materials that form the basis for organic solar cell devices, measurements were carried using novel technique which employs Gas Cluster Ion Beam source for XPS depth profiling. The proposed technique was suitable to determine qualitative and quantitative properties of organic materials while maintaining their initial/bulk chemical structures [24, 25]. The examined thin multilayer structures and applied SAM modifications are correlated with device performance tests of related systems.

2. Outline

The work is divided into four principal parts. Chapter **Theoretical background** gives an introduction into the scientific fields related to interface phenomena and SAM formation mechanisms. It serves mainly as necessary background knowledge and starting point encouraging for further readings. The following Chapter, **Materials and experimental methods** describes all the necessary details of techniques used and lists all materials, additionally defines standard parameters and procedures as well as experimental conditions. The next Chapter, **Results and discussion,** is presented in two parts. In the first part, **Organic/Metal Interfaces**, the experimental data and results of the polymer thin films covering SAM modified gold electrode are discussed. The results therein, represent cases typical for the respective polymer and cover the whole range of observations. The second part, **Organic/Organic Interfaces**, presents the experimental data obtained from XPS depth profiling with Gas Cluster Ion Beam of multilayered organic solar cell-based systems. The work therein deals with feasible detection of buried various SAM layers which were used to modify PEDOT:PSS anode and the influence of such modifications on device performance is discussed. In the last Chapter, **Conclusions**, the results of the whole conducted researches are coherently summarized.

II. Theoretical background

1. Organic/metal and organic/organic interfaces

1.1. Introduction

The relative molecular level energetics across hybrid organic/metal and organic/organic heterointerfaces are of paramount importance for effective optimization of organic electronic devices. The former is a key factor in all important aspects of molecule-based electronics e.g. organic and polymer light-emitting devices (OLEDs and PLEDs) whereas the latter is critical for e.g. efficient charge separation in organic-based photovoltaic cells (OPVs) which significantly affects the open-circuit voltage. These interfaces share some common features but they also exhibit their own characteristic, therefore this chapter will emphasize mutual properties with the differences also noticed. Its aim is to provide the necessary background knowledge and introduce the problems associated with interface interactions appearing between organic/metal and hetero organic/organic thin films. In the following sections the fundamental aspects and equations will be given regarding their relevance for the conducted experiments.

1.2. Electronic structure of solids

One of the most relevant parameters of metals in their application to organic devices is the work function. The valance electrons in a solid are prevented from escaping due to the potential barrier at the surface. The magnitude of this barrier is given by the work function ϕ. Thus it can be stated that the work function is the difference in the potentials inside and outside the solid in such a distance that potential becomes invariant of the exact position of the electron. This potential is commonly referred to as vacuum level E_{vac}. Thus, it can be written that:

$$E_{vac} = \phi + E_F \tag{1}$$

where E_F is the Fermi level. It is of great importance to notice that the experimentally derived vacuum level depends on the orientation and structure of the solid i.e. it cannot be used as a self-contained reference level [3]. It was observed that the work function will varies for the same metal according to surface crystal orientation from which the electrons are traversed [26]. In the jellium model of the interacting electrons in solids, the tailing of the electron density profile at the metal/vacuum interface produces an extra potential which results in a dipole layer formation. Moreover, this dipole layer depends on the degree of tailing which varies from the surface orientation, thus explaining the variations in work function of the same material. Nevertheless, for organic solids the existence of a surface dipole layer, similar to that described for metals, is expected to be insignificant [3].

In the case of the organic semiconductors (e.g. conjugated polymers) or insulators (typical polymers e.g. polystyrene, polymethyl methacrylate) the work function, by definition, is still a value depending on the position of the Fermi level, which therein lies within the band gap or forbidden gap E_G, and its exact position depends sensitively on the charge doping material (in semiconductors). Instead, the ionization potential IP (highest occupied molecular orbital, HOMO) is defined as the difference between E_{vac} and the maximum of the valance band, and the electron affinity EA (lowest unoccupied molecular orbital, LUMO) is introduced as the difference between E_{vac} and the bottom of the conduction band. For an illustration of the terms used in this context refer to Figure 1.

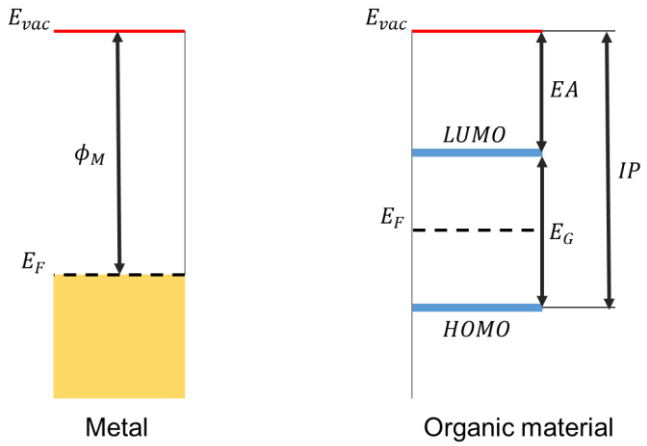

Figure 1. Electronic structure of the metal and organic solid without contact (at infinite distance). Lack of the interactions in this system empowers the assumption that both materials share the same vacuum level E_{vac}. The relevant energy levels for both materials are shown: ϕ_M – work function of a metal, E_F – Fermi level, EA – electron affinity, IP – ionization potential, LUMO – lowest unoccupied molecular orbital, HOMO – highest occupied molecular orbital and E_G – HOMO-LUMO band gap.

Typical values of work functions determined for metals lie in the range of 2 eV (alkali metals) up to 6 eV (platinum).

1.3. Energy level alignment at the organic/metal and organic/organic interfaces

When the organic material, e.g. polymer, is brought into contact with metal or other polymeric material, the adsorption process may result in a wide variety of interactions, depending on the nature of contacting materials. These interactions may be relatively weak in the case of physisorption (van der Waals interactions) and strong when a material becomes linked covalently to the surface (chemisorption). It should be noticed that, in between those two extreme cases, a numerous intermediate situations exist in which different degrees of chemisorption processes may occur. Depending on the type of interactions, contacting materials and obtained experimental results, several basic models were introduced endeavoring to describe qualitatively and/or quantitatively appearing interactions.

The general view on the interface electronic structure between organic and metal is presented in Figure 2.

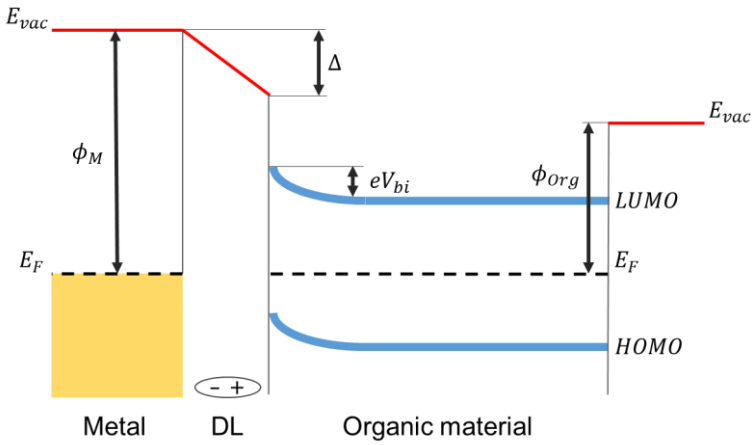

Figure 2. Electronic structure of an organic-on-metal interface showing relevant energy levels on both sides, the metal and organic material work function (ϕ_M and ϕ_{org}, respectively), the interface dipole (DL) shift (Δ), the band bending of LUMO and HOMO levels with built-in potential (eV_{bi}).

In the above situation, the Fermi levels of both materials are aligned which can be stated only if the total number of the available mobile carriers in the organic material is sufficiently large to reach such an equilibrium and thus the junction can follow the Schottky-Mott model. Moreover, the mentioned charge redistribution will take place depending on the relative positions of metal and organic layer work functions (ϕ_M and ϕ_{org}, respectively) as well as HOMO and LUMO level positions. When a redistribution of charges takes place, the emerging potential distribution at the interface can be described by Poisson equation. Resulting diffusion layer will lead to build up built-in potential (eV_{bi}) which will cause HOMO and LUMO band bending at the interface [27]. This situation will take place in the case of the rather thick organic layer deposited on metal substrate [3]. In the case of common non-conducting polymers an alignment of Fermi levels is not supposed to occur.

Apart from the mentioned band bending effect, the dipole layer (DL) which may be formed right at the interface causes the shift (Δ) of vacuum level. Note that the vacuum level at the interface, depicted in Figure 2, is a hypothetical concept to illustrate that the origin of the shift is caused by interface interactions that include e.g. polarization of the electron density of the organic material due to interaction with image charge on the metal surface, charge transfer through covalent bonding between both contacting materials, integer charge transfer through tunneling across the interface, surface rearrangement by diffusion or adsorption induced order or disorder, to name only a few [4]. These possible factors forming the interfacial dipole layer may appear separately, or more probably, intermixed and are schematically depicted in Figure 3. One should notice that these dipoles formation is an additional effect to that already mentioned in Section II.1.2 for free (metal) surfaces.

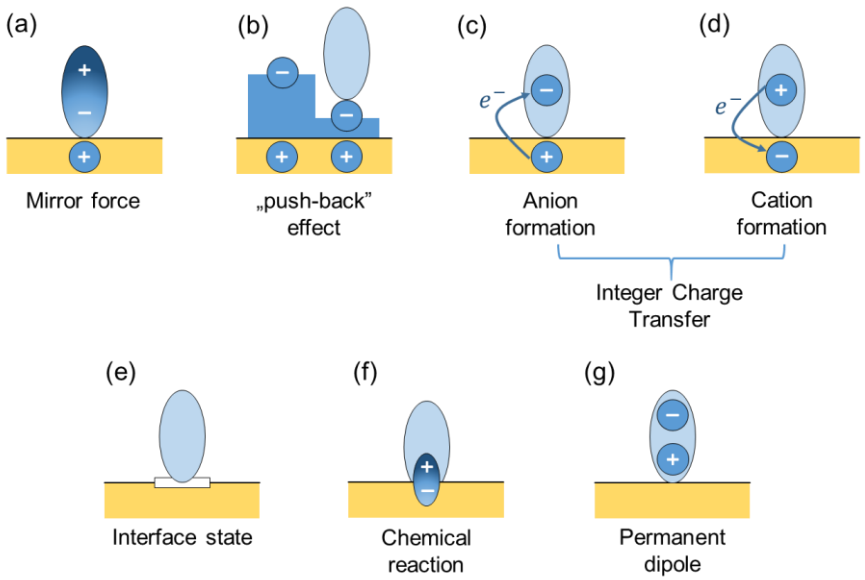

Figure 3. Illustration of factors forming and affecting interfacial interactions due to changes in interface dipole moment: (a) concentration of electrons in the adatom/molecule leading to positive charging of vacuum side (mirror charge), (b) adsorbed species leading to reduction of the electrons density tailing into vacuum ("push-back" effect), (c, d) charge transfer from the surface to adlayer (c) or vice versa (d) leading to adsorbate relaxation comparable to anion or cation formation, respectively (Integer charge transfer), (e) interface states appearance which serve as a buffer of charge carriers (Induced density of interfacial states), (f) strong chemisorption of reactive adsorbents (both directions of dipoles possible) and (g) orientation of polar molecules with functional groups leading to additional dipole formation [3].

In Figure 3 the possible interfacial interactions are presented from the weakest (a, b) to the strongest ones (f, g).

The appearance of mirror force or so-called "push-back" effects (Figure 3a and b) are present in the simple case when non-reactive molecules or atoms are deposited on passivated surfaces as well as on noble metals due to the physisorption process. The interaction is present due to the existence of weak van der Waals forces, and it can be assumed that electronic structure of the substrate and of the adlayer is relatively unperturbed. However, in such a case the work function of that system is neither the work function of the metal nor the ionization potential/work function of the adlayer. Keeping in mind that even for clean free metal surface the dipole moment exists, if now a neutral adsorbate is deposited in close vicinity of the surface the polarization of the molecules takes place and the dipole is aligned to the image charge in the metal (Figure 3a). The physisorbed layer decreases the spill out electron density which consequently lowers intrinsic metal free surface dipole moment, thus decreasing work function of the system (referred as "push-back" effect illustrated in Figure 3b) [4]. This is a well-known effect for gold, where its work function is commonly cited as 5.2±0.1 eV for a clean surface but when it is exposed to ambient air the adsorbed hydrocarbon reduces the metal-surface dipole potential energy up to 0.7 eV [28, 29].

It can be assumed that for the adsorbed molecule/layer an additional interaction mechanism takes place which is schematically presented in Figure 3c and Figure 3d. It

is proposed that the charge transfer from the substrate to the organic layer or vice versa can happen by hopping processes. In this interaction regime it is stated that the wave functions of substrate and molecules/adlayer do not hybridize and their overlap is negligible, but the position of the work function level with respect to the HOMO and LUMO level of adlayer is the priority. If the substrate's work function is lower than the LUMO level in adlayer ($\phi_M < LUMO$) the electrons are transferred from the metal to the available unoccupied states in a molecule. By the acceptance of the integer charge the molecule relaxes into a new state which can be compared to an anion which forms a polaron in the solid (Figure 3c). This state has higher binding energy than the LUMO and is now pinned to E_F of the metal resulting in positive vacuum level shift regarding metal E_{vac}. When the metal work function is in between the LUMO and HOMO levels ($LUMO < \phi_M < HOMO$) then no driving force exists that could promote charge carriers from the metal to the molecular layer or vice versa. In the case when work function of the substrate and HOMO level of the molecule fulfil the condition $HOMO < \phi_M$, then this is an opposite situation to the anion formation i.e. the charge will be transferred from the molecule to the substrate forming the polaron of stabilized hole in the solid (cation formation depicted in Figure 3d). Thereby the new relaxed state with lower binding energy will be pinned to E_F of the metal and the negative vacuum level shift with respect to metal E_{vac} will appear. This Integer Charge Transfer model (ICT) is well applicable for non-reactive molecules on noble metal surfaces or conjugated molecules deposited on passivated surfaces. Additionally, the ICT model can be successfully applied in various cases concerning heterojunctions of organic/organic materials exhibiting semiconducting character – if no significant interfacial chemistry occurs [30, 31].

The next possibility of interfacial interactions depicted in Figure 3e is in the regime of weak chemisorption processes. Therefore, the slight hybridization of the molecular orbitals and the metal states is presumed. In this dynamic regime the molecular states experience reorganization and are filled up to the so-called charge neutrality level. The proposed model to cover such interactions was based on Density Functional Theory (DFT) calculations of density of states and the structural parameters obtained either from experiments or calculations. However, this approach underestimates the complexity of the task due to e.g. lack of considerable van der Waals interactions contribution in DFT calculations or uncovering the influence of "push-back" effect which has strong electron-correlation effect. The Induced Density of States (IDIS) model was proposed as a three step process where molecular orbitals are first calculated using standard DFT method, where solid state screening and polarization effects are incorporated empirically or measured, followed by the calculation of interaction between the molecular orbitals and the metal bands close to the Fermi edge [32]. Nevertheless, this model has achieved limited practical use due to strong dependence of the adsorption sites geometry and molecule-metal distance which change depending

on considered systems. However, it can be successfully applied in the case of aromatic hydrocarbons deposition on slightly reactive metal surfaces [33-35].
When reactive molecules are deposited on metals or organic substrates the complexity of possible interactions is considerably increased. The overlap of the wave functions leads to a strong hybridization between electronic structure of the molecules/adlayer and the electronic bands in the metal. The strong chemisorption process (Figure 3f) implicates variations of the dipole layer on the metal surface depending on the nature of covalent chemical bonds, thus each joint system requires an individual approach. Therefore, the accompanying dipole moment, its magnitude and direction, will differ too, and should be assessed separately for a given molecule structure.
The self-assembled monolayers (SAMs) are one of the most important material class that represents chemisorption to surfaces by formation of strong chemical bonds. Additionally, in the case of polar organic molecules deposited either on metal surfaces or on organic substrates the orientation of the dipole moment attributed to the presence of functional groups in the adlayer leads to a large interfacial dipole formation (Figure 3g). This effect is used in the artificial tailoring of the substrate work function to the desired value, e.g. by self-assembly of polar molecules [36, 37] which are investigated in scope of this work, thus their electronic implications upon deposition on substrates are described in detail in Section II.2.4.

1.4. Methods utilized in buried interface characterization

The understanding and control of organic/metal or organic/organic heterointerfaces becomes difficult due to the decreasing device dimensions, thus necessitating application of nanometer-scale spatial resolution, attomolar sensitive and intermolecular specific techniques.
The dipole layer at the interface has been studied using spectroscopic methods such as Ultraviolet Photoelectron Spectroscopy (UPS) and X-ray Photoelectron Spectroscopy (XPS) [38-41] or Kelvin Probe method [42-44]. The spectroscopic methods allow to determine electric dipole moment quantitatively, whereas its influence on the device performance was tested by measuring current density versus applied voltage (I – V) characteristics [45-47]. The buried interface situated up to a few micrometers beneath the surface can be analyzed by means of optical spectroscopic methods, such as Surface Enhanced Attenuated Total Reflectance Spectroscopy [48], Surface Enhanced Raman Spectroscopy [49], or less commonly used Sum Frequency Generation Vibrational Spectroscopy [16]. All of these methods give information from rather large area of about 1 mm^2 and therefore do not indicate local inhomogeneities in scale of the fabricated devices.
Recently, the vibrational nano-spectroscopic imaging capable of correlating structure with intermolecular coupling and dynamics has been introduced [50]. The technique was able to resolve nanoscale morphology and associated intermolecular interactions,

i.e. directly correlate morphology and spectral signatures assigned to changes in local chemical environment at domain centers in a multicomponent polymeric system.

A very promising method which allows to measure local electrical properties of materials is Kelvin Probe Force Microscopy (KPFM). It can be used as a versatile tool to investigate many electronic properties such as local dopant concentrations [51], surface charging due to photo-induced charge separations [52-55], interface dipole formation between a metal surface and an organic monolayer (SAMs) [56, 57] and an electronic band bending at semiconducting interfaces [58], to name only a few. The greater advantage of the KPFM as compared with UPS/XPS or other methods is the high local spatial resolution approaching even up to about 1 nm. Kelvin Probe Force Microscopy has been widely used for investigation of organic thin film transistors (OTFTs) in UHV [59-61]. Burgi et al. examined the charge injection from the drain and source contacts into the active organic channel layer [62]. The contact resistances can be extracted from the localized voltage drop across the source-polymer or polymer-drain contacts. A large value of these voltage drops indicates a poor contact, because less of the applied bias is used in the channel to drive the drain current. KPFM can be used to optimize the contacts of the drain and source to the organic channels making improvements in the overall device performance. The KPFM technique is also a very useful tool for describing the microscopic mechanisms in the organic photovoltaic solar cells. Maturova et al. have presented a detailed study of both the steady state and time resolved charge distributions in the active layer of polymer-fullerene bulk heterojunction solar cells in the dark and under illumination using both AFM and KPFM methods [63]. They have shown that reduced performance of devices with coarse phase separation is at least partially due to problematic electron transport. De Sio et al. demonstrated that solvent additives can tune the photovoltaic properties of polymer-fullerene solar cells [64]. Structural investigation with KPFM and some other techniques indicated that the solvent additives led to preferential in-plane phase segregation between polymer and fullerene and increased P3HT ordering in the blends. Wang et al. demonstrated that solvent treatment on the organic active layer can effectively change organic/metal interface and improve the electron injection in organic light emitting diodes [65]. Using both KPFM and photovoltaic measurements they revealed the existence of the interface dipole moment, which shifts the vacuum level on the metal side and can reduce the electron injection barrier, thus improving the device performance.

Due to a high lateral resolution of the KPFM method, the electrical properties of individual domains formed in thin organic blends, i.e. at organic/organic heterointerfaces, can be distinguished. It was shown that even very similar topographic features of domains composed of one component may have significantly different CPD signals. These observations were explained that, most likely, the same of these domains were covered with a skin layer of the second component of the blend (filler) [66, 67]. Recently, the KPFM was employed to analyze organic multilayers with lateral structures suitable for fabrication of organic field-effect transistors [21].

2. Self-assembled monolayer (SAM)

2.1. Introduction

The spontaneous formation of complex hierarchical structures from designed molecular blocks is the key process defining the self-assembly. Self-assembled monolayers (SAMs) are ordered molecular layers formed spontaneously by the adsorption of a surfactant, with a specific interaction of its anchoring group, to a substrate. The first important works describing self-assembly phenomena date back to early 80s of XX century i.e. a work by Nuzzo and Allara on alkanethiols [68] and Sagiv's report on silane-based SAMs [69]. Since that time the potential of these systems has become apparent in many fields, which initiated extensive studies on the structural as well as electronic characterization. Nowadays, the SAMs have become basic materials in technical applications e.g. for protective coatings [70, 71], wetting, friction and lubrication control agents [72, 73], adhesion [74, 75], and bio-related applications [76-78]. The large field of SAMs application can be recognized in tuning the electronic properties of functionalized substrates [79-81], which is also in the scope of this work. An excellent and comprehensive reviews dealing with self-assembly phenomena can be found [9, 79, 80, 82-84], so the focus of this chapter is mainly on fundamentals regarding their relevance for the materials used and the conducted experiments.
Within the framework of this thesis two different types of SAMs were used, namely thiole-based and silane-based ones, which share some common features, but e.g. their formation mechanisms and kinetics are different, thus if necessary these types will be discussed individually.

2.2. SAM structure

There are several systems used to form SAMs, and they can be divided regarding e.g. their chemisorbing group to the substrate. The two most-popular classes of SAMs are that of thiols on Au and organosilicon monolayers on hydroxylated surfaces, e.g. silicon oxide. The structure of typical SAM molecule consists of three parts, schematically presented in Figure 4.

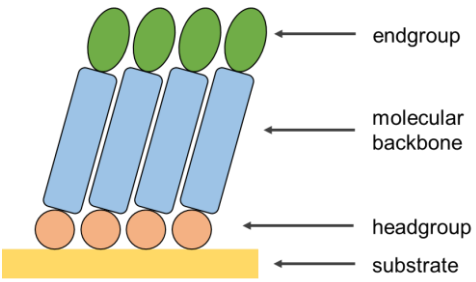

Figure 4. An illustration of SAM structure. The orange circles indicate chemisorbing headgroup and green ovals denote endgroup, which can be chosen from variety of chemical functionalities. The molecular backbone serves as a spacer between both mentioned parts and can be used to tune the resulting monolayer thickness.

In the case of thiol-based SAMs the head group consists of thiolate (-SH) group, whereas for silane-based SAMs it is typically a trialkoxy- or trichlorosilyl- group. The headgroup is responsible for the chemisorption to the substrate which typically for thiols is strong and forms a chemical bond [85]. Molecular backbone plays an important role in the determination of the structure of SAMs. The 2D ordering in these systems is influenced by both intermolecular interactions, such as van der Waals, dipole/dipole, or π – π interactions, and endgroup/endgroup interplay [84]. The intermolecular interactions are related to the spacing between the molecular headgroup and the endgroup [86]. The backbone can be also designed to enable the conductance of the electrons through the film (π – conjugated backbone). The endgroup, sometimes called a terminal functional group, is critical in determination of interfacial properties – the hydrophobic or hydrophilic character and adhesive characteristics. The terminal group reactivity gives the ability to perform further chemical reactions, which is widely utilized in the case of e.g. carboxylic or amine functional groups [87-89].

The two-dimensional arrangement and ordering of SAMs are influenced by nature of the chemical interaction between substrate and adsorbate, as well as previously mentioned types and strengths of intermolecular interactions between the SAM molecules that are necessary to maintain the assembly solidity. Therefore, it needs to be emphasized that there is no unified structure in which SAMs are ordered for different SAMs, moreover same type of SAMs assembled on different substrates exhibit other ordering structures.

Different studies have led to a picture of anchoring positions of alkanethiols compounds on gold, which were formerly under controversial discussion. The packing motif of n-alkanethiols, the most investigated systems among all thiolate-based SAM materials, on a $(23 \times \sqrt{3})$ reconstructed Au (111) surface [90] has been determined to be a $c(4 \times 2)\left(\sqrt{3} \times \sqrt{3}\right)R\ 30°$ overlayer structure [82], where the alkyl chains are tilted by 30° with respect to the surface normal for long chains (e.g. octyl-). There are also reports of similar surface reconstruction process of the gold initiated by monolayer assembly of the adsorbates, but the new model of the chemisorption process is stated [91, 92]. In the case of COOH-terminated thiols, due to steric hindrance and endgroup/endgroup interactions, it was reported that these types of monolayers exhibit high density of gauche defects [93]. However, due to hydrogen interactions between terminal groups in the early stages of self-assembly process, these monolayers demonstrate the formation of well-ordered films [94]. Nevertheless, for mercaptohexadecanoic acid the diffraction peaks corresponding to $\left(\sqrt{3} \times \sqrt{3}\right)R\ 30°$ structure were found [95].

In contrast to well-understood and investigated alkanethiols structure formation on gold, the organosilane monolayers and their mechanism of self-assembly remains a subject of debate [96]. Many groups studied the formation phenomena of organosilanes but the results were often conflicting. It can be somehow explained due to the fact that substrates used in the formation of silane SAMs are typically amorphous

ones and thus the obtained results can be unrepeatable from one experiment to another. However, for the most investigated system of octadecyltrichlorosilane (OTS) on silicon oxide substrate, some general observations can be inferred.
First, due to the steric effects between anchoring groups it was shown that cross-polymerization between headgroups in OTS, considered as a fundamental element in monolayers formation, cannot occur for full surface coverage [97]. These findings were supported as it was calculated that full cross-polymerization would yield an area of 11 $Å^2$ which is not possible and has never been observed. Experimental observations indicate area per chain of around 20 – 25 $Å^2$ similar to that found for hexagonally close packed Langmuir-Blodgett layers of OTS [98-100]. On the other hand, this can be explained as it was shown that only a small fraction of OTS molecules is individually linked to the substrate, thus the picture emerged in which OTS forms an interconnected network of molecules with small minority of covalent bonds attached to the silicon oxide surface [101, 102]. Therefore, the mobility of individual molecules is restricted resulting in a much less ordered structure upon monolayer formation when compared with e.g. fatty acids on AgO or thiols on gold. Concluding, there are no reports of long-range molecular order in organosilanes similar to that found for thiol SAMs on gold.

2.3. Mechanisms and kinetics of SAMs formation

2.3.1. Thiol-based SAMs

The chemisorption process of thiole-based SAMs incorporate a disruption of the intermolecular chemical bonds, in this case a hydrogen-sulfur bond in thiolate group, and formation of sulfur-gold bond, according to the following reaction [83]:

$$R - S - H + Au_n \longrightarrow R - S^- Au^+ + Au_{n-1} + \frac{1}{2} H_2$$

whereas the superscripts on sulfur and gold atoms denote a net charge transfer direction. This reaction may be considered as an oxidative addition of the S-H bond to the gold surface followed by a reductive elimination of hydrogen. The overall process is exothermic and the formed bond strength was found to be about 160 kJ/mol [103]. It can be stated that only one layer of thiolates can be linked to the gold surface. However, additional species may physisorb on the formed monolayer but it can be rinsed off easily in the production process. The self-assembly process from the solution, shown schematically in Figure 5, (as this method was utilized in this work) can be divided into two main parts [82, 104].
The first step occurs within the first few minutes with the majority of the surface sites being occupied by thiolates. The surface coverage was found to reach 80 – 90 % at this time. The strong gold-surface interaction serves as a driving force for nucleation and

diffusion of the molecules to the surface. Within this step the anchored molecules exhibit rather disordered configuration.

The subsequent step in self-assembly takes place within several hours, whilst the disordered molecules are rearranged by the thermally activated motion of molecular backbones (in case of alkyl chains or oligocene). This process is dominated by van der Waals interactions by induced dipoles in adjacent molecules, thereby attractive interactions are maximized which can be related to a stabilization of the binding energy. This is also referred to as surface crystallization due to the increasing local order [83].

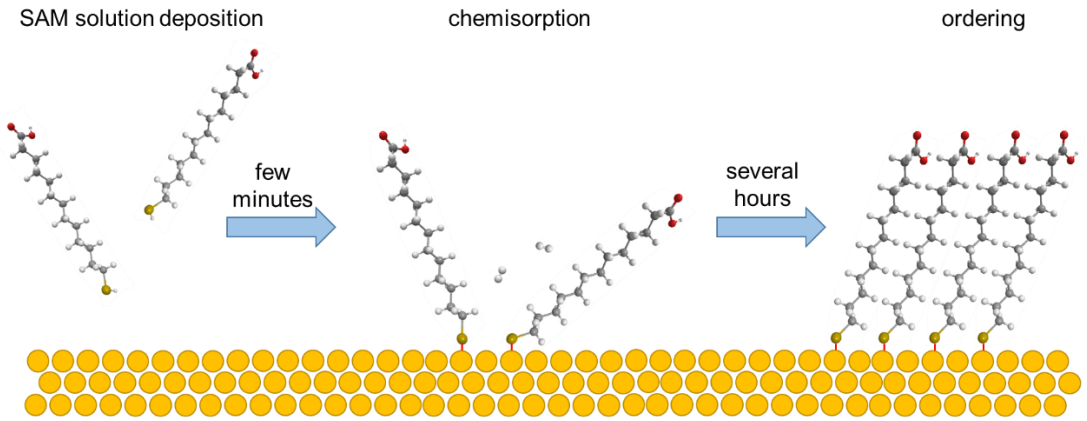

Figure 5. An illustration of mercaptoalkyl acid SAM self-assembly process on atomically clean gold surface. The dilute solution is deposited on gold surface, then within few minutes the chemisorption leads to sulfur-gold bonds formation and hydrogen termination of the thiolate group which is depicted. After several hours of immersion, upon ordering processes, the densely packed monolayer can be formed.

The initial growth process can be successfully described by the Langmuir formalism, which is characterized by the growth rate being proportional to the number of available sites [82]:

$$\frac{d\theta}{dt} = R(1-\theta) \tag{2}$$

where θ is the occupation of binding sites and R is the impingement rate on the surface. The solution of this equation is given by:

$$\theta = 1 - \exp\big(-R(t-t_n)\big) \tag{3}$$

where t_n is an empiric delay time for the onset of nucleation (if considered).

However, the deviations from the Langmuir law need to be addressed, as it is valid only if the adsorbate molecules do not interact with one another, which cannot be certainly stated in case of self-assembly of thiol-based SAMs. As a consequence, an additional term due to surface diffusion can be added, which is included in the Kisliuk model where the occupation of sites θ is diffusion-limited [82]. Therein, the additional sticking

coefficient of already adsorbed molecules k, and the surface diffusion constant D are contained:

$$\theta = \frac{1 - \exp(-D(1+k)t)}{1 + k\exp(-D(1+k)t)} \tag{4}$$

It should be emphasized that all the processes confound in the self-assembly depend on e.g. chain length of alkanethiols ("odd-even" effects), SAM solution concentration, solvent used, temperature of deposition and substrate type, to name only a few [82].

2.3.2. Organosilane SAMs

As it was mentioned earlier the mechanisms of organosilane SAM formation on oxidized substrates, particularly on silicon oxide, remain a subject of debate. A basic question for the growth is whether it proceeds in an island-type mode or homogenous mode, as illustrated in Figure 6.

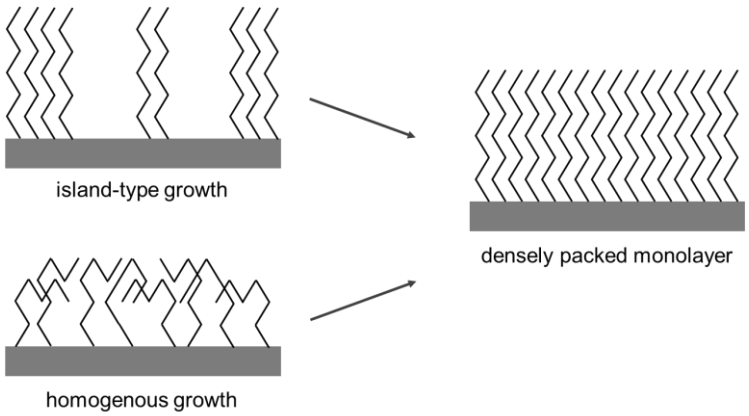

Figure 6. Schematic representation of island-type and homogenous modes of growth of organosilane SAMs.

In homogenous type of growth a layer grows in thickness with the tilt angle decreasing, whereas in island-type mode the thickness of formed SAM islands already corresponds to that of the complete monolayer, where molecules are oriented normal to the surface. The suggested island-type growth mechanism involve collisions between adsorbate molecules moving randomly near the surface and immobile islands. The assumption of permanent attachment to islands led to the creation of fractal shapes [105]. The homogenous growth is similar to that presented for thiol-based SAMs.
It must be noted that growth behavior depend on the conditions under which the experiments are carried. The small differences in water content, which is necessary to hydrolyze the silane group unlocking the anchoring possibility, may result in significant difference in growth mechanism and final monolayer quality [106]. The temperature variations, especially close to room temperature, have a dramatic impact. The critical temperature above which the island-type growth does not occur and below which a

high-quality films may be produced lies in the range of ambient conditions [107, 108]. Additionally, critical temperature depends on melting points of alkane backbones [109]. However, there was proposed a simple two-dimensional model of the growth of alkylsilane monolayers on hydroxylated surfaces [110], which was able to reproduce characteristics such as island growth and first-order Langmuir adsorption kinetics. By studying island formation and growth of organosilane SAMs on mica, Schwartz et al. found that the relation between deposition time and islands number density is proportional to $t^{1/3}$ and island area is proportional to $t^{2/3}$ [111, 112].

2.4. Influence of SAMs deposition on substrate's surface

2.4.1. Surface free energy and wettability

The adsorption of molecules on the surface may significantly change its energetic properties. The surface free energy is one of the most important quantity used to describe monolayers growth. In the equilibrium state the surface free energy γ_s defines the tendency of the surface to bind molecules, and it is equal to the work used to create a surface from the bulk material, by breaking bonds at one site and removing the adjacent molecules or atoms. The surface free energy of solid sample surface can be calculated e.g. in such a way that a droplet of a liquid with known surface tension is placed on the surface forming sessile drop under contact angle θ_C (Figure 7). The relation of the interfacial tensions between air and liquid γ_{al}, liquid and solid γ_{ls}, air and solid γ_{as} and the contact angle are given by Young's equation:

$$\gamma_{al} \cos\theta_C = \gamma_{as} - \gamma_{ls} \tag{5}$$

where it is assumed that solid surface in contact with the liquid is smooth, homogenous, isotropic and non-deformable, thus the validity of this relation might be in some cases unreliable.

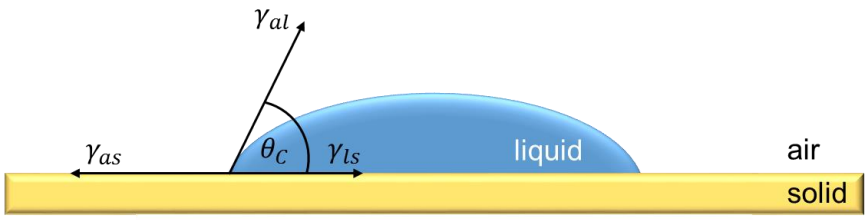

Figure 7. Definitions of the interfacial tensions and the contact angle used in the text.

The quantity contact angle θ_C can be used to determine the wettability of a solid surface by a considered liquid. Due to the fact that wetting properties of a surface are determined by the outermost chemical groups of the solid, it can be used to examine the surface wettability changes driven by the SAM deposition. When the contact angle

is less than 90° it indicates that wetting of the surface is favorable and solid/liquid interactions are strong, whereas in the case of higher contact angles (> 90°) the fluid minimizes contact which means that interactions are weak. In the case of water as liquid medium, the former may be called a hydrophilic surface whereas the latter a hydrophobic one.

2.4.2. Electronic implications on SAM coated electrodes

In the case of chemisorption of SAM molecules on the electrode surface the proceeding changes in energy level alignments lead to the changes in work function of the overall system, thus enabling to tailor the work function of the substrate. In a straightforward approach the interaction of anchoring group with substrate is constrained to the nearest neighborhood of the formed headgroup-substrate bond, while the electronic structure of the molecular states of the remaining parts of the adsorbate remains invariant upon deposition. In the case of hardly polarizable and non-conjugated molecules this assumption is often satisfied [81].
The work function of SAM functionalized surface will change due to at least four major interwoven factors [113, 114].
First, the effects of mirror charge and “push-back” effects, as illustrated in Figure 3a and b, will alter the tailing of the electron cloud out of the surface in turn decreasing the work function.
Next, the magnitude of the molecular dipole moment (Figure 3g) carried by the molecule will further change the energy level alignment. The net dipole moment of the molecule can be seen as the intrinsic dipole moment of the terminal functional group of SAM plus the dipole moment of the backbone and that arising from headgroup-substrate bond (Figure 3f).
Third, the orientation of the above individual molecular dipole moments relatively to the surface normal. This is a crucial parameter as only the component of the molecular dipole moment perpendicular to the surface will induce change of the work function, which will be discussed later.
And last, the depolarization effects, in which the dipole moment of each molecule is reduced compared to that of one isolated molecule, will strongly affect the observed work function changes. This effect arises from the fact that each dipole induces oppositely oriented dipoles in its vicinity. This results in a significant packing-induced charge rearrangement, which is located both on the substituent and backbone, thus a net depolarization in dense SAM monolayer will lead to a lesser extent in work function modification. The magnitude of this effect is correlated to the polarizability of the backbone.
All the above factors must be taken into account in the case of tailoring the work function of the substrate to the desired, specific value. An illustration of the work

function changes, and energy level alignment induced by different thiol-based SAMs used in this work is presented in Figure 8.

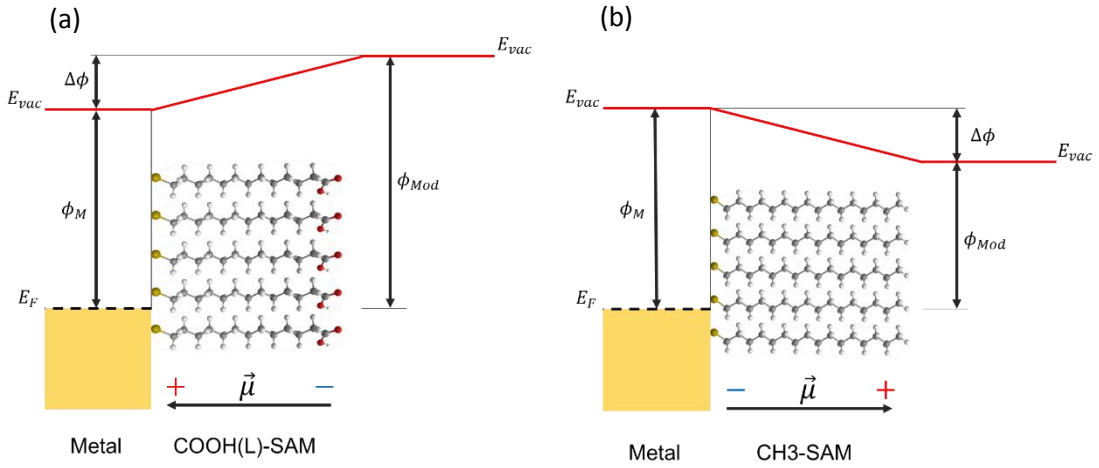

Figure 8. An illustration of the metal work function changes $\Delta\phi$ imposed by self-assembly of (a) mercaptohexadecanoic acid (COOH(L)-SAM) and (b) hexadecanethiol (CH3-SAM) monolayers on the substrates' surface. The former increases the work function of the substrate whereas the latter decreases it (ϕ_{mod}), which is expected due to the directions of both dipole moments ($\vec{\mu}$) carried by SAMs.

The macroscopic quantity of work function change upon SAM deposition $\Delta\phi$ is related to the listed above microscopic parameters through the Helmholtz equation [115]:

$$\Delta\phi = \frac{eN\mu_{\perp}}{\varepsilon_0\varepsilon_{eff}} \tag{6}$$

with N being the density of adsorbed SAM molecules, e the unit charge, ε_0 the vacuum permittivity, ε_{eff} the effective dielectric constant of the SAM and $\mu_{\perp}$ the component of the dipole moment perpendicular to the surface. From the above equation it becomes clear that the orientation of the dipole moment relative to the surface, mentioned above, is crucial for overall work function change of the substrate upon SAM deposition. The contribution of the dipole layer to the resulting work function can be used to tailor this quantity due to the fact that by changing the terminal groups in the molecule the dipole moment will also be changed. Additionally, this equation includes the relation of the surface coverage on the work function change. However, it should be noted that the dependence between ε_{eff} and N exists in a non-trivial way [116].

In the case of the substantial dipole moment carried by the self-assembling molecule it is not sufficient to add the dipole moment of the molecule, but the charge distribution of the mirror image in the substrate needs to be considered and added as mentioned. This effects was found in the electrostatic limit to equal [117]:

$$\Delta E_{vac} = \sum_{i=j} \frac{q_i q_j}{8\pi\varepsilon_0\varepsilon_{eff} r_{ij}} + \sum_{i\neq j} \frac{q_i q_j}{8\pi\varepsilon_0\varepsilon_{eff} r_{ij}} \tag{7}$$

where q_i and q_j denote the charge on the atoms i in the molecule and j in the image, r_{ij} is the distance between species. The first term concern for the self-image interaction whereas the second term describes the cross-image interaction.

3. The basics of polymers

3.1. Introduction

A polymer is a type of macromolecule which consists of a series of chain-like atomic arrangements of repeating units. Due to the fact that all common synthetic polymers have a distribution in molecular weight, the most important parameters describing these materials are molecular weight averages, i.e. the number-average molecular weight M_n,

$$M_n = \frac{\sum_i N_i M_i}{\sum_i N_i} \tag{8}$$

where N_i is the number of molecules of molecular weight M_i, and the weight-avarage molecular weight M_w,

$$M_w = \frac{\sum_i N_i M_i^2}{\sum_i N_i M_i} \tag{9}$$

with the latter always being larger. An additional parameter which is defined on the basis of the above two is called polydispersity index PDI:

$$PDI = \frac{M_w}{M_n} \tag{10}$$

and provides a simple evaluation of the molecular weight distribution. The closer it is to unity the narrower the distribution and generally better (uniform) polymer properties.

Another important property of polymeric materials is their glass-transition temperature T_g. The glass transition is a second-order transition (sometimes called glass-rubber transition) and is a reversible change that occurs in an amorphous polymer or in domains of amorphous polymer in crystalline matrix when it is heated from low temperature into a certain range, highly dependent on the polymer type, characterized by a sudden change from a hard, glassy condition to a flexible, rubber-like, elastomeric condition. The basis of the glass transition is the onset of coordinated molecular motion in the polymer chain. At low temperatures, only vibrational motions are possible, and the polymer is hard and glassy. Within the glass transition range, the polymer softens and the material becomes rubbery. The polymer T_g is defined as the approximate

midpoint of the temperature range over which the glass transition occurs. The glass transition temperature for selected polymer depends on many parameters among which the most important are molecular weight, degree of cross-linking and intermolecular interactions between individual polymer chains. Knowledge of this parameter is very important due to the fact that above and below this temperature the polymer exhibits strongly different properties, including e.g. thermal expansion coefficient, Young's modulus, heat capacity and refractive index.
Polymers may be classified in many groups regarding their e.g. chemical, optical or electrical properties. In this work the polymers are discussed within two groups depending on their electrical properties, namely conventional and conjugated ones.

3.1.1. Conventional polymers

These type of polymers, the conventional ones, are the most typical and technologically the most important ones. They are characterized by chemically saturated main chains where electrons are tightly bound in the σ-bonds between atoms. Since all the available electrons are fixed in the σ-bonds, there are no free electrons to carry an electrical current. Thus, this type of solid materials are electrical insulators. The non-conductive polymers tend to fall into one of two classes. The first class may be defined as non-polar which can be characterized by a relatively constant molar polarization, whilst the second class as polar characterized by high relative permittivities and showing molar polarization that decreases with increasing temperature [118]. This anomalous behavior was first recognized by Debye who attributed it to presence of permanent molecular dipole moments. This is then characteristic (but not limited to and with some exceptions due to geometrical arrangement) for repeating units in polymers which combine atoms of different electronegativity, the heteroatoms, resulting in their partially quasi ionic character and consequently having permanent dipole moment. The most typical heteroatoms are oxygen, nitrogen, fluorine, chlorine and sulfur. Groups containing heteroatoms are often called functional groups. Therefore, polystyrene utilized in this work can be regarded as non-polar polymer whereas other non-conjugated polymers used within the framework of this thesis, namely poly(2-vinylpyridine), poly(acrylic acid) and poly(methyl methacrylate) fall into polar class of polymers.

3.1.2. Conjugated polymers

Conjugated polymers are carbon-based macromolecules through which the valence π-electrons are delocalized. Generally, polyconjugated carbon chains consist of alternating single and double bonds, but nowadays the most important are systems which consist of aromatic units linked together, allowing π orbital conjugation along the length of molecule. Conjugated polymers exhibit electronic properties that are significantly different from those observed in the corresponding inorganic, conducting

and semiconducting, materials. These unusual electronic properties may be attributed mainly to fact that conjugated polymers behave as quasi-one dimensional systems owing to their strong intramolecular electronic interactions and relatively weak intermolecular electronic interactions. Thus, electronic wavefunctions are typically localized on single chains, or to pairs of chains in the case of excited state complexes. This quasi-one dimensionality also means that electron-electron interactions are weakly screened. Therefore, electronic correlations are important in determination of the electronic states character. Another important factor in determining the character of the electronic states is the fact that the electrons and lattice are strongly coupled. As for electron-electron interactions, the effects of electron-lattice coupling are enhanced in low dimensions. As a consequence, the charge carriers in these materials are positive and negative polarons rather than holes and electrons.

The behavior of conjugated polymers is different with respect to conventional polymers, e.g. non-conjugated polymers consist of up to several thousands or millions of monomer units in a chain, are soluble in common organic solvents and melt processible. In turn, polyconjugated systems have a few hundreds of monomers in a chain and due to the alternating single and double bonds their chains are rather stiff when compared with the former. Conjugated polymers exhibit poor solubility, unless side groups are introduced in the main chain or dopant ions to impart processibility [119].

The structure of the conjugated polymer's chain, interchain interactions, disorder and doping level determine the stability of carriers. Undoped (neutral) conjugated polymers are semiconductors, with optical gaps of $\sim 2 - 3$ eV and charge (or band) gaps typically $\sim 0.5 - 1.0$ eV higher in energy, reflecting the large exciton binding energies in these materials [5]. Doped polymers have metallic-like conductivities of typically 10^3 - 10^5 S/cm. However, although the conductivities of conjugated polymers are reasonable, their performance as synthetic metals is strongly affected both by disorder, which means that the conductivity is close to the localization transition, and by the unstable nature when highly doped [120].

The electronic and optical properties of conjugated polymers, coupled with their mechanical properties and intrinsic processing advantages, mean that they are materials particularly attractive for the electronics industry. There are many potential applications, including light emitting devices, nonlinear optical devices, photovoltaic devices, plastic field-effect transistors, and electro-magnetic shielding.

3.2. Chain structure and configuration

3.2.1. Configuration and conformation

One of the most important parameter for polymers is their chain structure described in terms of conformation and configuration, i.e. isomerism which is characterized by identical number of corresponding atoms but with different spatial arrangements. This

can be further differentiated to *constitutional isomers* where molecules have equal composition (equal formula) but atoms are connected to one another in different sequences; or *stereoisomers* with same sequence of atoms but different spatial arrangements. The term conformation refers to the different arrangements of atoms and substituents of the polymer chain brought about by rotations about single bonds. Examples of different polymer conformations include the fully extended planar zigzag, helical, folded chain, and random coils. On the other hand, configuration refers to the organization of the atoms along the chain, and sometimes is referred to as "microstructure" rather than configuration. In the case of polymers the configurational isomerism involves the different arrangements of the atoms and substituents in a chain, which can be interconverted only by the breakage and reformation of chemical bonds.

3.2.2. Stereochemistry of repeating units

One of the most significant examples of configuration dependence on material properties in organic compounds, is the phenomenon that two chemically identical substances rotate plane-polarized light equally but in opposite direction. It was found that the two isomers causing different optical behavior were mirror images of each other. The cause of the optical activity is the asymmetric carbon in the center of molecule (i.e. carbon with four different substituents), known as chiral center. The important point is that the two mirror images are non-superimposable, and the two compounds are really different.

In the case of polymers the situation in which one or more different functional groups are attached to the main chain leads to the structure in which every substituted carbon atom is a chiral center, as presented in Figure 9 for poly(methyl methacrylate) (PMMA). Such carbon atoms are referred to as pseudochiral centers in long-chain polymers because generally polymers do not exhibit optical activity [121]. The reason for this is that at closer examination of the substituents on such pseudochiral center (C^* in Figure 9) the two main chain segments will generally be of unequal length but for the optical activity only the few first atoms of these segments are important. Thus, these near atoms are seen to be the same, and hence the polymer remains optically inactive.

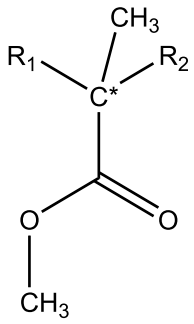

Figure 9. An illustration of pseudochiral carbon atom C^* in the PMMA structure formed due to its substitution with methyl and methoxycarbonyl groups and different length of remaining R_1 and R_2 backbone chains. However, the optical activity is governed only by the first few neighboring atoms thus the PMMA remains optically inactive.

However, the two mirror image configurations remain distinguishable. The different possible spatial arrangements are called the tacticity of the polymer. If the functional groups (R) on pseudochiral carbons all have the same configuration, the polymer is called isotactic. When the pseudochiral centers alternate in configuration from one repeating unit to another, the polymer is called syndiotactic. If the pseudochiral centers do not have any particular order, but in fact are statistical arrangements, the polymer is said to be atactic. In Figure 10, using Natta projection, the actual differences between isotactic, syndiotactic and atactic forms are presented.

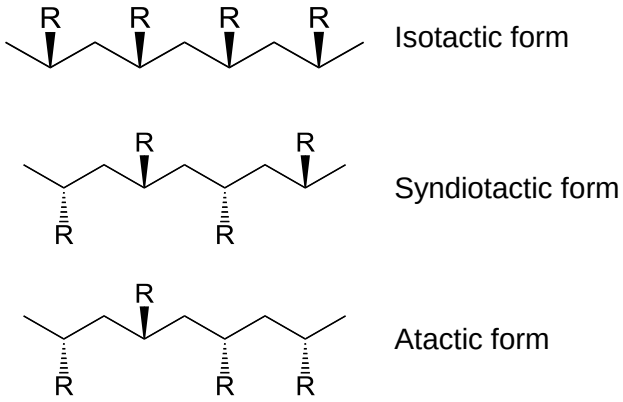

Figure 10. The Natta projection of different types of tacticity in polymers. In this projection the zigzag backbone is in the paper plane with the substituents (R) either sticking out of the paper denoted as triangular bold bond or retreating into the paper as indicated by triangular bond in stripe pattern. From the top: isotactic form in which all substituents lie above or below the plane, syndiotactic form where substituents are alternating above and below the plane and atactic form characterized by statistical arrangement.

The iso- and syndio- tactic polymer structures result in profoundly different physical and mechanical behavior of the material. The isotactic and syndiotactic structures are both crystallizable because of their regularity along the chain. However, their unit cells and melting temperatures are not the same. Atactic polymers are usually completely amorphous unless the side groups are so small or so polar as to permit some crystallinity [121].

When considering polymer chains configurations, in the case of attached pendant groups to main chain, one must take into account head-tail configurations which, however, are not part of tacticity but have strong influence on the material properties, especially in terms of conductivity and processibility in conjugated polymers [122]. In poly(3-alkilothiophenes) (P3ATs) the possible arrangement and resulting polymer structures are presented in Figure 11.

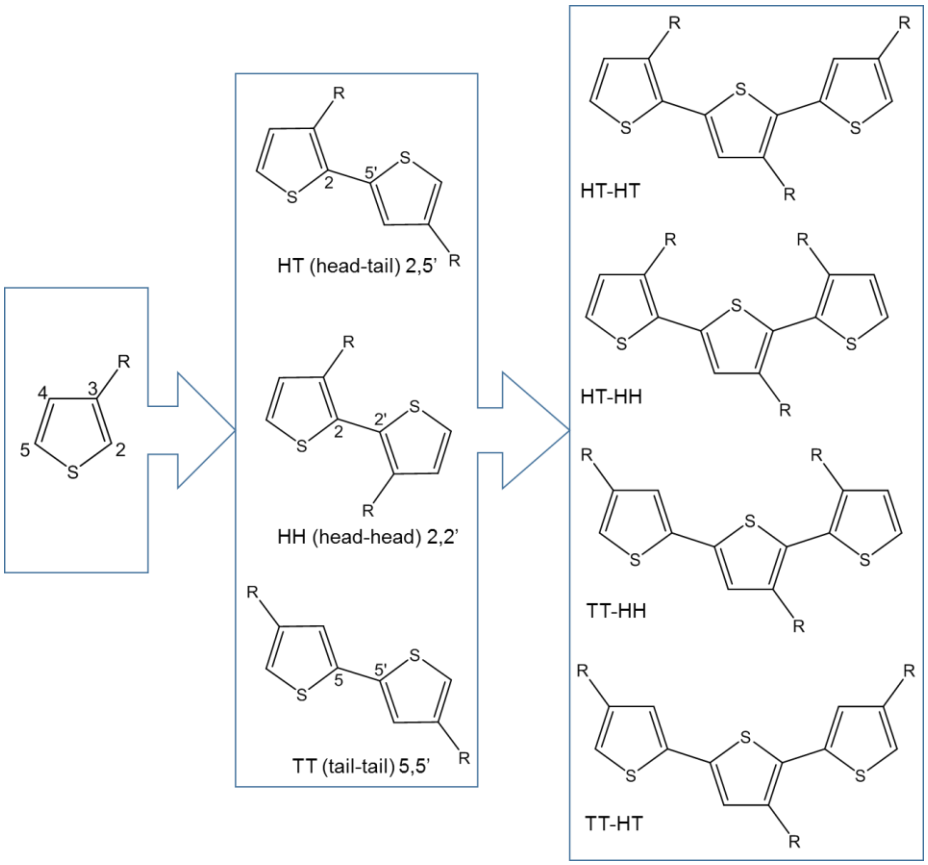

Figure 11. The asymmetric structure of P3AT results in three different arrangements in diads and four in case of triads. The HT-HT coupling is the most favorable one due to outstanding conductivity resulting from low twist between neighboring aromatic rings and is called regioregular form.

Due to the asymmetric structure of 3-substituted thiophene molecule, three orientations are available when two rings become coupled: 2,5' or head-tail (HT) coupling, 2,2' or head-head (HH) coupling and 5,5' or tail-tail (TT) coupling (see Figure 11 for graphic representation). These can be further complicated in the case when three rings are coupled which leads to four possible chemically distinct triad regioisomers as shown on the right in Figure 11. The regioregular P3AT is defined as one with almost only HT couplings. Others are called irregular P3ATs and consist of statistical mixtures of presented triads. However, the regiorandom term is defined for the P3ATs in which the ratio of HH to HT couplings is 1:1.

The loss of regularity, i.e. contamination with HH couplings, leads to sterically twisted structure in the polymer main chain backbone resulting in loss of π-conjugation and as a consequence the high conductivity, characteristic for regioregular P3AT, is strongly diminished [123].

3.3. Solubility Parameters

For many technological and practical aspects the solubility of polymer has a tremendous importance for its effective application. Thus, the polymer dissolution thermodynamics attracted a wide interest, and some models were proposed [124]. Additionally, the

solubility of polymer is directly connected with cohesion energy of the material giving insight on attraction strengths between polymer chains.
The dissolution of polymer in a solvent is governed by the free energy of mixing:

$$\Delta G_M = \Delta H_M - T\Delta S_M \tag{11}$$

where ΔG_M is the change in Gibbs' free energy on mixing, ΔH_M is the enthalpy change on mixing, T is the absolute temperature and ΔS_M is the entropy change on mixing. The negative value of ΔG_M means that the mixing process will occur spontaneously. Otherwise, the dissolution will take place in more phases. Since the dissolution is always connected with increase in entropy $T\Delta S_M$, thus the deciding factor in determining the sign of Gibbs free energy change is the ΔH_M part. For regular solutions it was proposed by Hildebrand and Scott [125] that:

$$\Delta H_M = V_M \left[\left(\frac{\Delta E_1}{V_1} \right)^{1/2} - \left(\frac{\Delta E_2}{V_2} \right)^{1/2} \right]^2 v_1 v_2 \tag{12}$$

where V_M represents the total volume of the mixture, ΔE stands for the energy of vaporization to a gas at zero pressure and V is the molar volume of the components, for both species 1 which by convention is solvent and 2 is the polymer. The quantity v denotes the volume fraction of corresponding components and $\Delta E/V$ represents the energy of vaporization per unit volume and is called the cohesive energy density. The solubility parameter was defined as the square root of the cohesive energy density and it describes the attractive strength between molecules of the material:

$$\delta_i = \left(\frac{\Delta E_i}{V_i} \right)^{1/2} \tag{13}$$

δ_i is called the Hildebrand parameter and its dimension is $MPa^{1/2}$. Therefore, the heat of mixing of two substances 1 and 2 is dependent on $(\delta_1 - \delta_2)^2$. However, this parameter well describes simple systems, i.e. non-polar, non-associating solvents but for strongly interacting systems the free energy change of mixing is dominated by hydrogen bonding forces, van der Waals and dipole-dipole forces. Thus, to accurately describe such mixing, the Hildebrand parameter was extended to polar solvents and polymers by Hansen [126], who decomposed it into three components:

$$\delta^2 = \delta_d^2 + \delta_p^2 + \delta_h^2 \tag{14}$$

where δ_d is the dispersive term describing van der Waals interactions between molecules , δ_p is the polar term considering permanent dipole-dipole interactions and δ_h which describes inter- and intramolecular hydrogen bonding forces. The conclusions

were drawn that the two materials only mix when the corresponding components of polymer and solvent have similar values.

III. Materials and experimental methods

1. Materials

1.1. Polymers

Within the framework of this thesis the polymers used are commercially available, excluding synthesized polythiophene (PT) nanoparticles, and were used as-received, without further purification. The values without references are provided by the material supplier.

1.1.1. Polystyrene (PS)

Polystyrene (PS) is a very common polymeric material with great technical importance for the production of plastic goods. It is a rather stable and rather chemically inert polymer. However, due to the phenyl group presence it can undergo specific interactions of the π-π type when exposed to reagents. Recently, it has been reported that polystyrene also shows great potential for use in future organic electronic devices as dielectric material, due to its advantage of superior quantifiable characteristics in terms of water absorption and dielectric strength [127]. The properties of polystyrene used in this work as well as its chemical structure are presented collectively in Table 1.

Table 1. Characterizations of PS used within the framework of this thesis.

Chemical structure		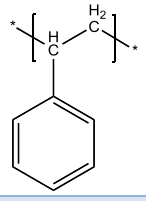
Molecular weight [kDa]		65
Polydispersity index (PDI)		1.04
Tacticity* [%]	syndio	N/A
	hetero	N/A
	iso	N/A
Glass transition temperature (T_g) [°C]		90 ÷ 95
Hansen Solubility Parameters [$MPa^{0.5}$] [128]	dispersion δ_d	19.7
	polar δ_p	3.5
	hydrogen bonding δ_h	1.7
Common solvents		DMF, THF, toluene, chloroform
Supplier		Polymer Standard Service

*If not available (N/A) – the atactic form is stated.

In this work, polystyrene was dissolved in various solvents i.e. chloroform, toluene and THF with concentrations in the range of 10 ÷ 20 mg/ml.

1.1.2. Poly(2-vinylpyridine) (P2VP)

The properties of poly(2-vinylpyridine) (P2VP) used in this work are presented in the Table 2.

Table 2. Chemical structure and principal properties of poly(2-vinyl pyridine) utilized for thin film preparation.

Chemical structure		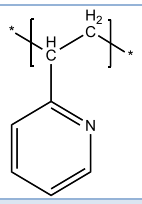
Molecular weight [kDa]		124
Polydispersity index (PDI)		1.06
Tacticity* [%]	syndio	N/A
	hetero	N/A
	iso	N/A
Glass transition temperature (T_g) [°C] [129]		~110
Hansen Solubility Parameters [MPa$^{0.5}$] [128]	dispersion δ_d	19.3
	polar δ_p	8.2
	hydrogen bonding δ_h	0.0
Common solvents		DMF, THF, toluene, methanol, chloroform
Supplier		Polymer Standard Service

*If not available (N/A) – the atactic form is stated.

The P2VP used in this work was dissolved in THF with the concentration of 20 mg/ml.

1.1.3. Poly(acrylic acid) (PAA)

Poly(acrylic acid) (PAA) is commonly used in textile industry as a sizing agent in the manufacture of nylon and other synthetic textiles. It is a hydrophilic and hygroscopic material. The properties and chemical structure of PAA utilized in preparation of thin films discussed within this thesis are presented in Table 3.

Table 3. Properties and chemical structure of poly(acrylic acid) utilized within the framework of this thesis.

Chemical structure		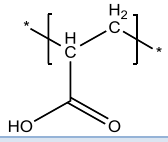
Molecular weight [kDa]		450
Polydispersity index (PDI)		N/A
Tacticity* [%]	syndio	N/A
	hetero	N/A
	iso	N/A
Glass transition temperature (T_g) [°C]		106
Hansen Solubility Parameters [MPa$^{0.5}$] [130]	dispersion δ_d	24.7
	polar δ_p	18.1
	hydrogen bonding δ_h	20.4
Common solvents		water, methanol, ethanol
Supplier		Sigma-Aldrich Co.

*If not available (N/A) – the atactic form is stated.

The PAA utilized in the framework of this thesis was dissolved in ethanol with concentrations in the range of 15 ÷ 25 mg/ml.

1.1.4. Poly(methyl methacrylate)s (PMMAs)

Poly(methyl 2-methylpropenoate) (IUPAC) commonly known as poly(methyl methacrylate) (PMMA) in an amorphous state is a rigid polymer with two outstanding characteristics which are optical clarity (up to 92% light transmission) and unsurpassed resistance to weathering. It is tasteless, odorless and non-toxic. Due to these properties it is a versatile material and has been used in a wide range of applications including transparent glass substitute, medical technologies, plastic car parts manufacturing, etc. Within the framework of this thesis the stereospecific forms of PMMA were used and are presented, namely: atactic (at-PMMA), syndiotactic (syn-PMMA) and isotactic (iso-PMMA) form. The main properties of PMMAs utilized for preparation of thin films and their chemical structures including regularity of the repeating units are presented collectively in Table 4.

Table 4. Properties of stereoregular PMMAs utilized within the framework of this thesis.

		atactic	syndiotactic	isotactic
Chemical structure		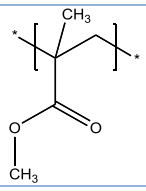	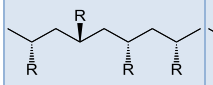	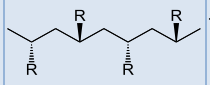
Molecular weight [kDa]		50	35	52.5
Polydispersity index (PDI)		1.09	1.27	1.16
Tacticity [%]	syndio	38	86	0
	hetero	26	14	1
	iso	36	0	99
Glass transition temperature (T_g) [°C]		110	120	52
Hansen Solubility Parameters [MPa$^{0.5}$] [130]	dispersion δ_d	18.6		
	polar δ_p	10.5		
	hydrogen bonding δ_h	7.5		
Common solvents		THF, toluene, dioxane, chloroform		
Supplier		Polymer Source Ltd.		

In this work PMMAs were dissolved in chloroform or toluene to the various concentrations in the range of 10 ÷ 20 mg/ml.

1.1.5. Polythiophene and its derivatives (PT, RP3ATs)

The polythiophene (PT) nanoparticles were synthesized by copper sulfide ($CuSO_4$) catalyzed oxidative polymerization in aqueous medium. The synthesis consists of preparation of the mixture containing deionized water, thiophene, hydrogen peroxide and surfactant which was then stirred for 9 hours at 50°C. After the reaction, the PT nanoparticles were precipitated by addition of sodium chloride followed by

centrifugation. The precipitate was washed with deionized water and dried under vacuum at 60°C for 5 days. The more detailed description can be found here [131]. The nanoparticles were then dispersed in THF and drop-cast onto silicon wafer. Analyzes of obtained material are presented in Section IV.2.5.

Poly(3-alkylthiphene-2,5-diyl)s in regioregular forms (RP3AT)s were used within the carried experiments. The alkyl groups were: hexyl (Poly(3-hexylthiophene-2,5-diyl) (RP3HT)) and octyl (Poly(3-octylthiophene-2,5-diyl) (RP3OT). These conjugated polymers are ones of the mostly utilized in organic electronic devices such as OLEDs, environmental sensors, solar cells (OPV), etc. due to their outstanding properties like solubility, processibility, possibility to organize in well-defined 3D structures and high conductivity after doping. The basic properties as well as the chemical structures of RP3ATs used in the framework of this thesis are presented in Table 5.

Table 5. The main properties of RP3ATs utilized within the framework of this thesis.

	RP3HT	RP3OT
Chemical structure	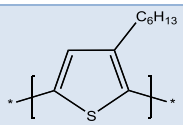	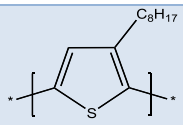
Molecular weight [kDa]	37 – 45	70 – 90
Polydispersity index (PDI)	1.6 – 1.8	N/A
Regioregularity [%]	>94	>94
Glass transition temperature (T_g) [°C] [132]	~125	N/A
Common solvents	chloroform, chlorobenzene, CCl_4, THF, xylene	
Supplier	Rieke Metals, Inc	

In this work the RP3HT and RP3OT were dissolved in chlorobenzene and chloroform, respectively. Both solutions have the concentrations of 12 mg/ml.

1.1.6. Phenyl-C_{61}-butyric acid methyl ester (PCBM)

Phenyl-C61-butyric acid methyl ester (PCBM) is the fullerene derivative which is used in organic solar cell devices. It is an electron acceptor and is often blended with electron donor materials like P3ATs polymers. In this thesis the PCBM was blended in 1:1 (w/w) ratio with RP3HT and used as active material in solar cell fabrication (Section IV.3.3). The basic properties of PCBM used are presented in Table 6.

Table 6. The chemical structure and properties of PCBM utilized in this work.

Chemical structure	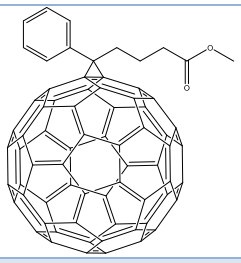
Molar mass [g/mol]	910.88
Purity [%]	>99
Common solvent	chlorobenzen
Supplier	Solenne BV

Within the frame work of this thesis the PCBM solution was prepared by dissolution in chlorobenzene with the final concentration of 10 mg/ml.

1.1.7. Poly(3,4-ethylenedioxythiophene):polystyrene sulfonate (PEDOT:PSS)

Poly(3,4-ethylenedioxythiophene):polystyrene sulfonate (PEDOT:PSS) is a highly stable conducting complex. In its structure the PEDOT segments (usually 1000 – 2500 Da) are tightly, electrostatically attached to PSS chains which have much higher molecular weight. High conductivity of PEDOT:PSS is attributed to stacked fragments of PEDOT chains within a larger structure of water-swollen PSS particles. Such complexes are suitable for film-forming techniques thus they are easily processable into thin coatings leading to the widespread availability of PEDOT:PSS as a commercially useful material. The properties of the PEDOT:PSS dispersion used in this work are presented in Table 7.

Table 7. Characterization of PEDOT:PSS solution utilized within the framework of this thesis.

Chemical structure	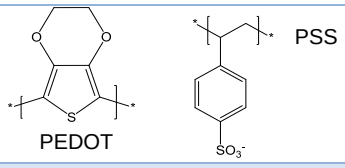
Molecular weight (PEDOT) [kDa]	1.0 – 2.5
Resistivity [ohm*cm]	500 – 5000
Solid content [%]	1.3 – 1.7
Viscosity [mPa*s]	5 – 12
PEDOT to PSS ratio	1 : 6
Supplier	Heraeus Clevios

1.1.8. Polyaniline doped with camphorsulfonic acid (PANI(CSA)) blended with PS

Polyaniline (PANI) is one of the representative of the conjugated polymers. Upon doping this polymer can be tailored for specific applications [133]. Polyaniline becomes electrically conductive in its emeraldine oxidation state when doped with such a salt which protonates the imine nitrogens on the polymer backbone. The structural formula

of polyaniline emeraldine doped state is presented in Figure 12a. Doping process is typically carried out chemically with acids like e.g. camphorsulfonic acid (CSA) (Figure 12b) or dodecylbenzenesulfonic acid (DBSA).

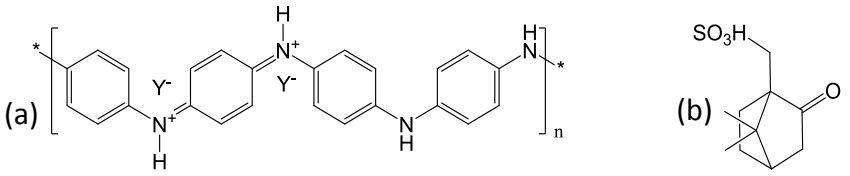

Figure 12. (a) The structural formula of PANI in emeraldine salt state after doping with acid (Y· denotes the acid radical) (b) the structural formula of CSA (IUPAC name: (7,7-dimethyl-2-oxobicyclo[2.2.1]heptan-1-yl)methanesulfonic acid).

The basic properties of PANI and CSA which were utilized in this work are presented in Table 8.

Table 8. The main properties of PANI and CSA used within the framework of this thesis.

	PANI	CSA
Molecular weight [kDa] / Molar mass [g/mol]	5.0	232.30
Purity [%]	N/A	98%
Solubility	N-methyl-2-Pyrrolidinone, DMF	water, alcohols, DMF, DMSO
Supplier	Aldrich	

In this work the polyaniline powder was dissolved in chloroform and doped with camphorsulfonic acid (CSA) with a 1:2 molar ratio of CSA molecules to a phenyl-N groups. The solutions were stirred for 5 days and treated in the ultrasonic bath for short periods of time (10 min). Then, dark green solutions were filtered through Whatman's filters (Puradisc 25 TF 0.2 µm). Concentrations of the filtered solutions were determined by solvent evaporation and were evaluated as equal to 4 mg/ml. Appropriate amount of polystyrene was added to the filtered PANI(CSA) solution in such a way that the final composition was equal to 1:1 by weight. The solutions were injected through the same filter type onto gold-covered silicon wafers rotated at a spin speed of 1000 rpm [134].

1.2. Self-assembled monolayers (SAMs)

All the self-assembled monolayers (SAMs) utilized within the framework of this thesis were used as-received without further purification.

1.2.1. Thiols

The thiol-based SAMs used in the frame work of this thesis were 1-hexadecanethiol containing CH_3- tail group (CH3-SAM), and two SAMs with different backbone length both containing COOH- tail group namely: 16-mercaptohexadecanoid acid (COOH(L)-SAM) and 6-mercaptohexanoic acid (COOH(S)-SAM). The CH3-SAM and COOH(L)-SAM have almost identical molecule length (about 2 nm) whereas COOH(S)-SAM is much shorter (<1 nm). Due to the presence of different tail groups the functionalized surface becomes hydrophobic in the case of CH3-SAM deposition and hydrophilic when COOH(L)-SAM or COOH(S)-SAM are deposited. Deposition of these molecules on gold electrode modify the work function of the underlying material due to the dipole moment carried by the molecules. The absolute dipole moments for free standing molecules for CH3-SAM and COOH(L)-SAM have very similar values but are oppositely directed. The values for free standing molecules were estimated at +2.1 D and −2.5 D for CH_3- and COOH- terminated thiols, respectively, where the positive dipole is defined as directed from the negative pole towards the positive one [36]. Deposition of the SAMs onto gold substrate modifies the work function of the substrates in a different manner depending on the sign of the dipole moment. Positively charged tail groups of the CH3-SAM decrease while negative COOH groups increase the work function of the substrate. Experimentally the CH3-SAM decreases work function of the atomically clean gold substrate by 0.26 eV while the COOH-SAM increases it by 0.24 eV [36, 56]. According to theoretical studies these values should be equal to 1.0 eV for CH3-SAM and 1.2 eV for COOH-SAM deposited on gold [135]. However, the theoretical studies refer to perfectly ordered monolayers deposited on the substrate with well-defined crystallographic structure. The experimental values depend on the quality of the organic films and the substrate determined by macroscopic and microscopic defects. These may induce the difference but the observed trends of the work function changes are maintained. The calculated dipole moment of the COOH(S)-SAM molecule was not reported but theoretical studies have shown that this type of SAM decrease the work function of gold, i.e. like CH3-SAM molecules [135]. This is caused by a much shorter backbone of this molecule when compared with COOH(L)-SAM which results in strong interactions between dipole moments attributed to head and tail groups. In the case of long COOH- terminated molecules the tail-group dipole moment dominates the work function change but in the case of shorter molecules (e.g. COOH(S)-SAM) the less polarizable oppositely directed head-group dipole moment dominates. The SAMs chemical structures are presented in Figure 13 and basic properties of these thiol-based materials, utilized within the framework of this thesis, are listed in Table 9.

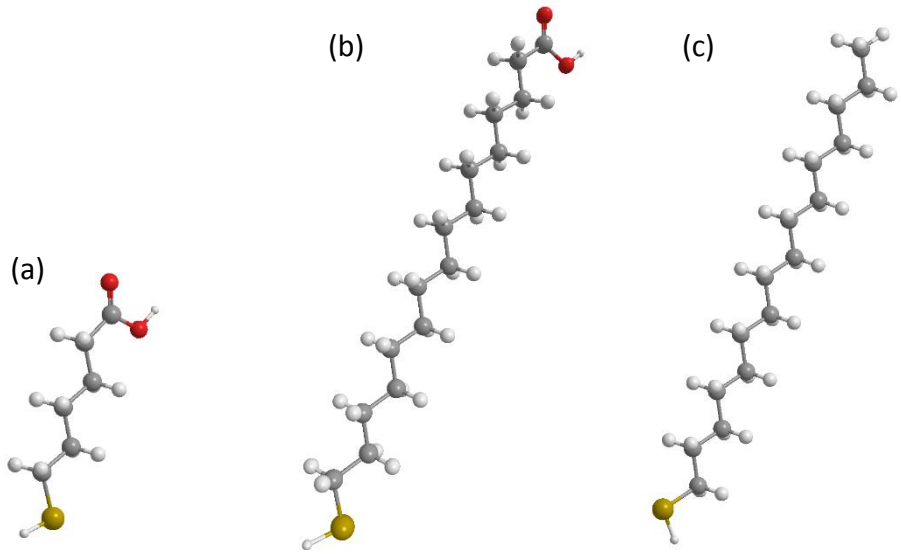

Figure 13. The molecular structures of (a) COOH(S)-SAM, (b) COOH(L)-SAM and (c) CH3-SAM used in this work. The grey balls reflects carbon, red balls stands for oxygen, yellows are sulfur and whites are attributed to hydrogen.

Table 9. Characterizations of the thiol-based SAMs used in this work.

Thiols	**COOH(S)-SAM**	**COOH(L)-SAM**	**CH3-SAM**
Formula	$C_6H_{12}O_2S$	$C_{16}H_{32}O_2S$	$C_{16}H_{34}S$
Molar mass [g/mol]	148.22	288.49	258.51
Density [g/mL]	1.07	N/A	0.84
Purity [%]	90	99	99
Dipole moment [D]	N/A	2.1	2.5
Molecule length [nm]	N/A	2.1	2.2
Common solvents	methanol, ethanol		
Supplier	Sigma-Aldrich Co.		

In this work the preparation of thiol-based SAM molecules solutions were performed under inert Ar atmosphere in a glove box. As a solvent the anhydrous ethanol purchased from POCH (purity >99,6%) was used. SAMs were dissolved to a concentration of 10mM.

1.2.2. Silanes

The organosilane SAMs used in this work were: trimethoxy(3,3,3-trifluoropropyl)silane (F3Si-SAM), (3-bromopropyl)trimethoxysilane (BrSi-SAM), (3-aminopropyl)triethoxy-silane (APTES) and (3-mercaptopropyl)trimethoxysilane (MPTES). The 3D chemical molecular structures for these SAMs are presented in Figure 14. In Table 10 the main properties of silanes used are listed.

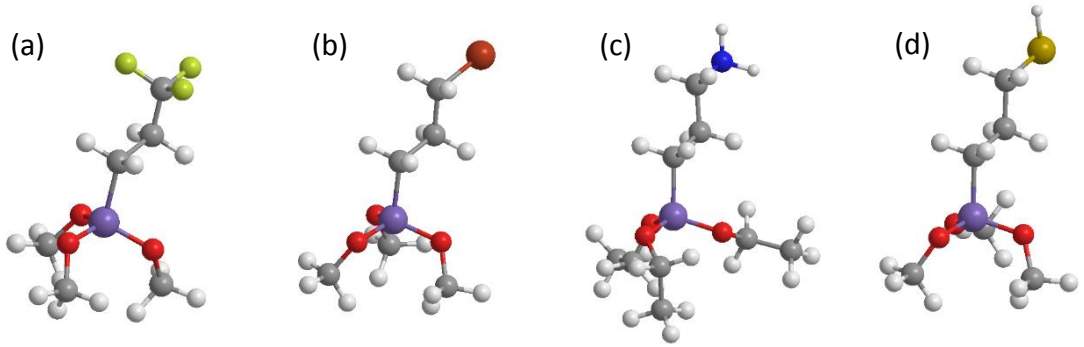

Figure 14. The molecular structures of silane-based self-assembled monolayers used in this work: (a) F3Si-SAM, (b) BrSi-SAM, (c) APTES and (d) MPTES. The grey balls reflects carbon, red balls stands for oxygen, green is fluorine, blue is nitrogen, violet silicon, orange is bromine, dim yellow is sulfur and whites are attributed to hydrogen.

Table 10. Properties of silane-based SAMs used within the framework of this thesis.

Silane	**F3Si-SAM**	**BrSi-SAM**	**APTES**	**MPTES**
Formula	$C_6H_{13}F_3O_3Si$	$C_6H_{15}BrO_3Si$	$C_9H_{23}NO_3Si$	$C_6H_{16}O_3SSi$
Molar mass [g/mol]	218.25	243.17	221.37	196.34
Density [g/mL]	1.14	1.30	0.95	1.06
Purity [%]	97	97	99	95
Common solvents	ethanol, methanol, toluene			
Supplier	Sigma-Aldrich Co.			

All the silane-based SAMs solutions were prepared under inert Ar atmosphere in a glove box. Tolene was used as the solvent and the SAM solutions concentrations were 10 mM.

2. Sample preparation techniques

2.1. Substrate preparation

2.1.1. Si wafer conditioning

The silicon wafers were conditioned using wet chemical methods to avoid organic and inorganic contamination which may disturb later steps in substrate preparation. The removal of particles and chemical impurities was done without damaging or deleteriously altering the substrate surface. After silicon wafer was cut into desired pieces (usually 15 mm x 10 mm for spin-coating and 10 mm x 75 mm for horizontal-dipping) four steps were applied for the cleaning process. First, the so called piranha solution was used which is 3:1 volume ratio of 98 wt% H_2SO_4 (sulfuric acid) and 30 wt% H_2O_2 (hydrogen peroxide). The wafers were cleaned at a temperature of 100°C for 15 minutes followed by rinsing in distillated water (H_2O). In this step the organics were destroyed and eliminated by chemical oxidation [136]. Next, the ammonia/peroxide solution was used for 15 minutes at 75°C. The solution consists of a mixture of NH_4OH (ammonium hydroxide), H_2O_2 and H_2O with composition of 1:1:5 parts by volume, respectively. The third step is the immersion of silicon wafer into the

hydrochloric/peroxide solution for 15 minutes at 75°C. The specified composition of this solution consists of a mixture of HCl (hydrochloric acid), H_2O_2 and H_2O with composition of 1:1:5 parts by volume, respectively. This process was followed by a quench and overflow rinse in running distillated H_2O. In the last step, wafers were dried under a flow of Ar for complete removal of water. After the treatment processes the substrates were kept under clean Ar atmosphere in the MBraun glove box which assured stable oxygen free and humidity free (below 0.1 ppm) atmosphere during storage.

2.1.2. Metallic layer deposition

The physical vapor deposition (PVD) method was used for deposition of thin (from 80 to 150 nm) metal layer. Vaporizing of the base material was done by thermal evaporation in vacuum. In this method the deposited metal i.e. gold is placed in resistive element (basket) and due to a high current flow through the element the temperature rises causing the metal to melt and evaporate. This involves two parallel processes evaporation of source metal and condensation on the substrate. The cleaned silicon wafers were used as substrates for uniform metal layer deposition. One of the problems in the deposition of thin gold film is its weak adhesion to inert substrate (such as glass, silica substrates etc.). The common method to overcome this problem, applied in this work, is the use of a very thin (up to 10 Å) intermediate layer of chromium which can enhance gold adhesion [137, 138]. Quartz crystal monitors were utilized to monitor and control film thickness during deposition.

2.2. Soft lithography

2.2.1. Introduction

Soft lithography is the name for a collection of non-photolithographic methods that can fabricate micro- and nano- patterned structures [139-141]. This technique uses soft organic materials to generate structures without use of light or other high-energy electron or ion beams and it is based on self-assembly and replica molding of organic or polymeric molecules. There are several different methods that are regarded as soft lithography methods among which the most important and commonly used are microcontact printing (μCP), replica molding (REM), micromolding in capillaries (MIMIC) and microtransfer molding (μTM) [142]. The main advantage of these methods is the possibility of rapid and inexpensive way of forming and transferring patterns onto or even into other materials. In the framework of this study the μCP and MIMIC techniques have been used and described in details.

2.2.2. Elastomer stamp fabrication

The fabrication of stamp is the first stage in soft lithography since it is used to generate the pattern. The stamp is usually made of poly(dimethylsiloxane) (PDMS) also known commercially as Sylgard 184. There are several properties making PDMS a convenient material for formation of high-quality patterns and structures in soft lithography [139]. First, it is a polymer with viscoelasticity (elastomer) that conforms to the surface over a large area even though the surface can be non-planar on the micrometer scale [143]. PDMS provides a surface that is chemically inert due to low interfacial free energy [144] and additionally, it is isotropic, homogenous and optically transparent down to 300 nm [145]. Finally, PDMS is a durable elastomer which makes it resistant to pattern degradation upon usage. There are also some drawbacks of this material among which the most significant is low Young module that leads to a situation in which too large microstructures may fall under their own weight or collapse. Moreover, PDMS shrinks by a factor of about 1% upon curing and can be swelled by many solvents such as toluene or hexane which change the dimension and shape of protrusions [144]. Thus, the use of PDMS stamp is limited to inks soluble in ethanol which has a minimal swelling effect [146].

To make a stamp a template (master) having relief structure on its surface is needed. In this work, the master used to cast the PDMS stamp was fabricated using electron beam lithography. The patterns were plotted on the silicon wafers. PDMS is a two component heat-curing system and it consists of a base and a curing agent. Once both were mixed and degassed the solution was dispensed over the whole area of master and then cured typically at 120°C for 20 minutes. In the final step the stamp was peeled off from the template and became ready to use. In Figure 15 the (a) schematic view, (b) AFM topography map and (c) cross-section of the brick-wall structured stamp used in this work are presented.

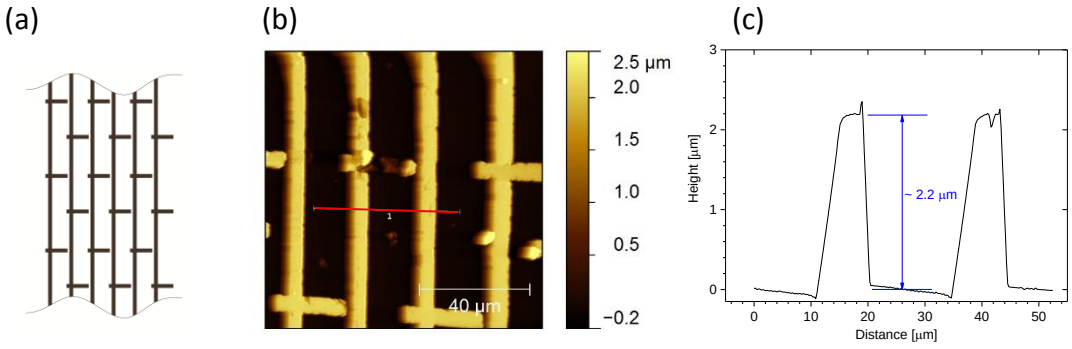

Figure 15. (a) Illustration of the brick-wall structure on the PDMS stamp: vertical and horizontal periods are 50 µm and 25 µm, respectively. (b) AFM topography map of PDMS stamp structure used in the experiments, estimated structure height is about 2.2 µm as shown on the (c) profile taken from the red line area region depicted in topography map.

2.2.3. Micro-contact printing of SAMs

Microcontact printing is one of the most versatile and cost-effective soft lithography method for the fabrication of patterned SAMs [142]. In this technique the elastomeric stamp with a relief pattern on the surface is inked with SAM solution and then the SAMs patterns are made by physical contact of the stamp with the substrate surface. The use of µCP for SAMs of alkanethiols on gold was demonstrated for the first time over 20 years ago [147]. Since that time many different groups have extended this technique to a number of other systems including different SAMs and substrates [13, 142, 143, 148-151]. The formation of SAMs during µCP may occur within a few seconds – the contact time varies for different molecules and solution concentrations: over 0,3 seconds is sufficient for the formation of dodecanethiol on gold (100 mM ethanol solution) [152] and up to 20 seconds for 2mM of hexadecanethiol in ethanol to form highly ordered SAMs [153]. The schematic view of the procedure of µCP used in this work is presented in Figure 16.

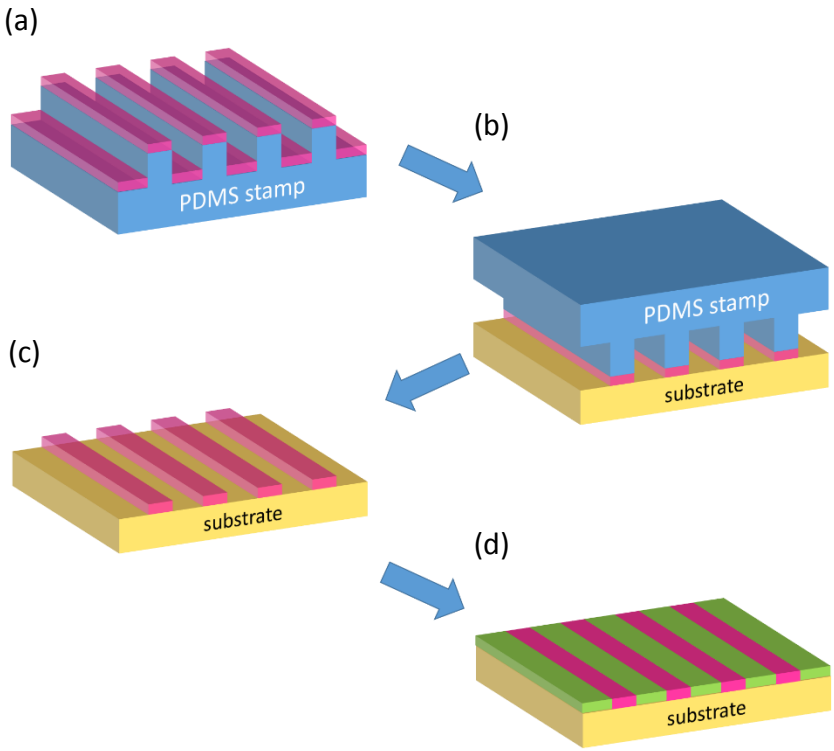

Figure 16. Schematic illustration of the µCP procedure for patterning substrate with different molecules of SAMs: (a) PDMS stamp structure is inked with one type of SAM which is then (b) transferred to a substrate resulting in (c) localized self-assembly. In the next step (d) unprinted regions are functionalized with second type of SAM by immersion in its solution.

The PDMS mold inked with 10 mM solution of COOH(L)-SAM or CH3-SAM in ethanol (a) is gently pressed on the gold substrate (b) to localize SAM pattern (c). To enhance the differences between unprinted and printed regions some of the patterned substrates

containing empty areas not initially printed are further on functionalized by immersion in 10 mM CH3-SAM ethanol solution (for COOH(L)-SAM pattern) or 10 mM COOH(L)-SAM ethanol solution (for CH3-SAM pattern) for 30 minutes. Then the substrate is rinsed with ethanol and dried under a flow of Ar for 5 s. This procedure provides self-assemble array containing two regions of monolayers terminated with different chemical functionalities with micrometer scale spatial arrangement (Figure 16d).
Although µCP is a well-understood technique it requires experience from the user otherwise several fabrication defects in final pattern may occur. During the cross-linking process some uncured and low molecular weight fragment may remain and contaminate the substrate during contact [154]. This results in the decrease of the monolayer quality and presence of undesired impurities at the surface. This effect is also enhanced when the PDMS stamp is pressed too hard to the substrate and when the ink molecules contain polar groups [155].

2.2.4. Micromolding in capillaries

Micromolding in capillaries (MIMIC) is soft lithography method capable of fabricating complex microstructures on planar and even curved surfaces [156]. In this technique the PDMS stamp is placed on the surface with relief structures facing toward the substrate forming a network of empty channels. Then the liquid polymer solution is placed at the one open end of the channels and due to the capillary action phenomenon the liquid fills the narrow canals. In the beginning MIMIC was developed for UV, heat or chemically curable materials like polyurethane or epoxy but it has been extended to solvent contained systems [139]. The solvents are evaporated after the solution fills the channels. The main requirement is that the solvent does not swell the PDMS stamp. Within the framework of this thesis the MIMIC was used to prepare an array of various micrometer scale width lines of poly(3-hexylthiophene) and poly(styrene) on flat gold substrates. Figure 17 shows AFM topography maps of fabricated structures.

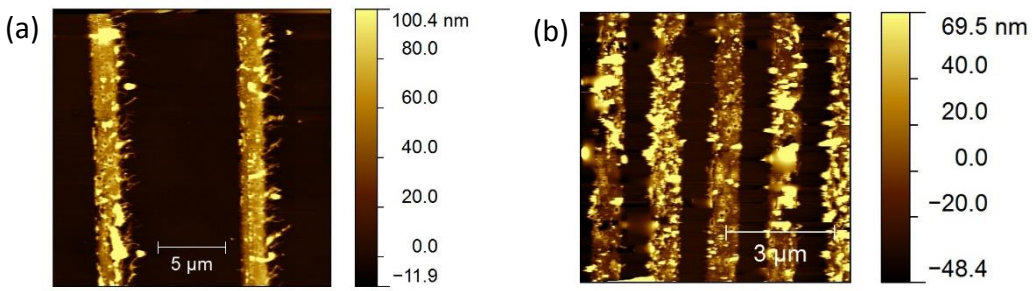

Figure 17. AFM topography images of (a) polystyrene and (b) poly(3-hexylthiophene) microstructures fabricated by MIMIC. The polystyrene line structures are 2 µm wide and poly(3-hexylthiophene) are 800 nm wide.

2.3. Polymer thin film preparation

2.3.1. Spin-coating

Spin coating is a simple, one-step method for application of thin, uniform polymer films to flat substrates over a large area with highly controllable and reproducible thickness [157]. Spin coating is used in various applications among which the most significant are microelectronic applications [158-160], sensors [161, 162], protective [163], optical [164] or paint [165] coatings. A typical process is schematically presented in Figure 18. The first stage is the deposition of the coating fluid onto the substrate (1). The second stage (2) is the substrate angular acceleration up to its final desired speed. In this stage, due to the centrifugal forces, aggressive fluid expulsion from the wafer/substrate surface by the rotational motion occurs. In the next stage (3), the substrate spins at a constant rate and fluid viscous forces dominate coating thinning behavior. Fluid thinning is generally quite uniform, though with solutions containing volatile solvents, it is often possible to see interference colors "spinning off", and doing so progressively more slowly as the coating thickness is reduced. The fourth stage (4) is when the substrate spins at a constant rate and solvent evaporation dominates the coating thinning behavior. At this point, the evaporation of any volatile solvent species becomes the dominant process occurring in the coating. In fact, at this point the coating gels effectively because as these solvents are removed the viscosity of the remaining solution is likely to rise –freezing the coating in place effectively. Stages 3 and 4 describe two processes that must occur simultaneously throughout all times – viscous flow and evaporation.

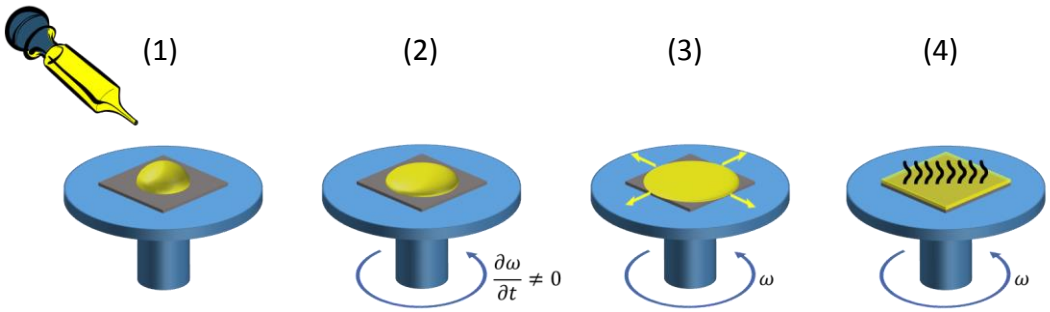

Figure 18. Schematic diagram of the major steps in spin-coating process: (1) solution deposition onto substrate, (2) substrate acceleration, (3) solution spread out and thinning, (4) solvent evaporation and final thinning.

Spin-coating is a complex process due to many mechanisms and factors involved but several theoretical models of the process were described [166-169]. Extensive work has been done on deducing empirical correlations between experimental parameters and final film thickness [169-173]. Conclusions drawn from this investigations are that angular velocity, solution viscosity and solution concentration affect the film thickness

significantly, whereas the amount of solution initially deposited on the substrate and total spin time have limited or no effects [157, 174]. For polymer solutions the viscosity is related to concentration thus the angular velocity and concentration have been correlated to the film thickness as presented in Figure 19.

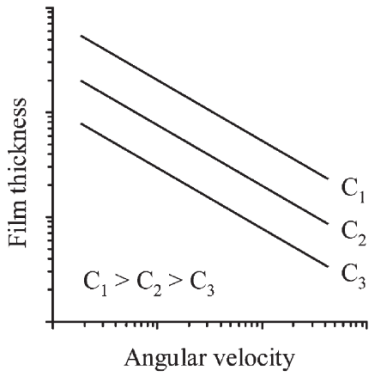

Figure 19. Illustrative view of relation between film thickness, angular velocity and concentrations in spin-casting process.

Generally, the empirically derived dependence of film thickness has the following mathematical form [157]:

$$h = k \cdot C_0 \cdot \omega^{-\alpha} \tag{15}$$

where h is the film thickness, C_0 is the polymer concentration in the solution, ω is the angular velocity and k and α are empirically determined constants. The α exponent has been set at about 0.5, which stands in good agreement for various polymer/solvent systems [170, 171]. The k constant is dependent on many parameters including solution viscosity, solvent evaporation rate, volatility and solute diffusivity, to name only a few. Most of the polymer films presented in this thesis were prepared using KW-4A (Chemat Technology Inc.) two-stage precision spin-coater with an adjustable speed in a range of 1000 – 8000 rpm and speed stability under 1%. The spin-coater was placed in the MBraun glove box which assured stable oxygen free and humidity free atmosphere under film preparation. The spin–coated polymers were: polystyrene, poly(2-vinyl pyridine), poly(acrylic acid), poly(methyl methacrylate)s, poly(3-alkylthiophenes), polyaniline, poly(3,4-ethylenedioxy-thiophene): polystyrene sulfonate and blends of [6,6]-phenyl-C_{61}-butyric acid methyl ester and poly(3-hexylthiophene). Depending on the polymer solubility various solvents were used including chloroform (PS, PMMA, P2VP, RP3OT, RP3HT), toluene (PS, PMMA), ethanol (PAA), chlorobenzene (PCBM, RP3HT) and water (PEDOT:PSS). The concentrations of the polymer solutions were in the range of 10 ÷ 30 mg/ml resulting in the film thickness in the range of 75 ÷ 130 nm. Example of film thicknesses obtained for PS and PMMA films is shown in Figure 20.

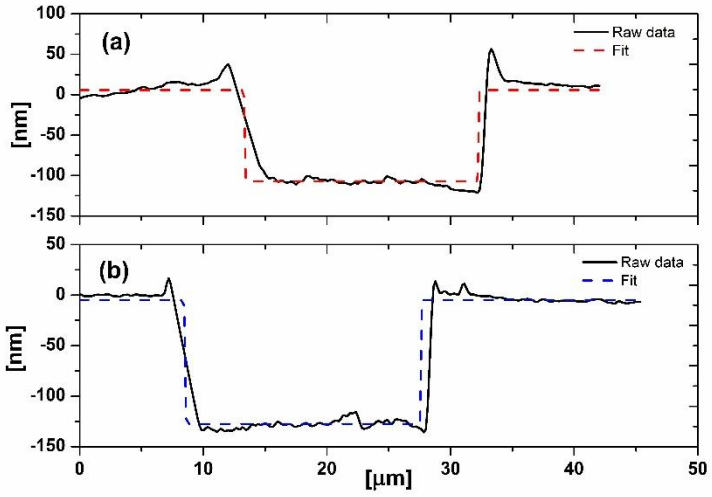

Figure 20. Cross sectional analysis of the furrow region scratched in (a) PMMA and (b) PS films. Raw data (solid line) fitted with a negative step function (dashed line) indicates film thickness equal to 113±6 nm and 123±3 nm for PMMA and PS, respectively [175].

2.3.2. Horizontal-dipping

The horizontal-dipping method (H-dipping) was applied by means of a home-built apparatus which is shown schematically in Figure 21.

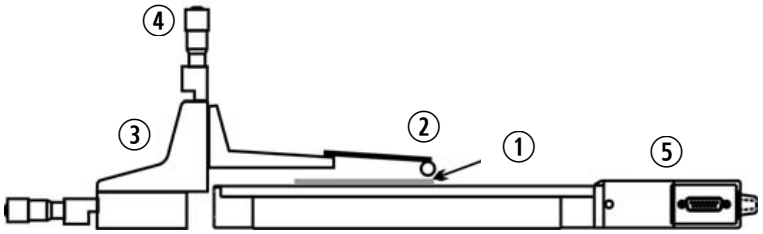

Figure 21. Schematic diagram of the home build apparatus for H-dipping: ① substrate; ② glass bar glued to microscopic glass slide; ③ 3-axis linear stage; ④ micrometer positioner; ⑤ linear stage [176].

In this coating process, a coating glass bar (5 mm diameter) glued to a microscopic glass slide, which is mounted on a 3-axis linear stage (Newport 460A-XYZ), hangs continuously at an adjustable (by micrometer positioner) height (*d* in Figure 22) above a specially cut silicon substrate that is attached to a carrying stage that transports the substrate horizontally [176-178]. Then a small amount of polymer solution is introduced into the empty space between the barrier and the substrate by capillary action, which results in a uniform downstream meniscus of the solution on the substrate with attraction to the glass bar. In the next step, the substrate is transported horizontally using a computer-controlled linear stage (Newport UTS100) with a velocity up to $v = 40\ mm/s$ and the maximum acceleration $a = 2\ mm/s^2$ (Figure 22).

Figure 22. Schematic presentation of the coating process, the wet film thickness depends on the coating bar diameter Φ, the distance between the bar and the substrate d, and the velocity v [176].

In order to prepare gradient samples a polymer solution was drawn with constant acceleration a = *0.5 mm/s²* over initially resting substrate. Estimation of solution drawing velocity was done by measuring the distance from the starting position and the relation between displacement s, velocity v, and acceleration a in a uniformly accelerated motion:

$$v = \sqrt{2 \cdot s \cdot a} \tag{16}$$

Formation of the wet film behind the downstream meniscus can be described in the framework of the model proposed by Landau and Levich [179]. For small capillary numbers, ($C_a = (\mu v/\sigma) \ll 1$, where μ and σ represent viscosity and surface tension, respectively, and v is the drawing speed), the thickness of the dry film is given by the following equation [178]:

$$h = 1.34 \left(\frac{\mu v}{\sigma}\right)^{\frac{2}{3}} R_d \kappa \tag{17}$$

where R_d is the radius of the downstream meniscus which depends on the diameter of the bar Φ and it is constant for the constant height d. The constant κ is the ratio between dry and wet film thickness. The Landau–Levich model shows that the thickness of wet films depends on the coating speed. Variation of PQT-12:dPBrS film thickness, as a function of the local withdrawing speed, in the film prepared by H-dipping with constant acceleration, is presented in Figure 23.

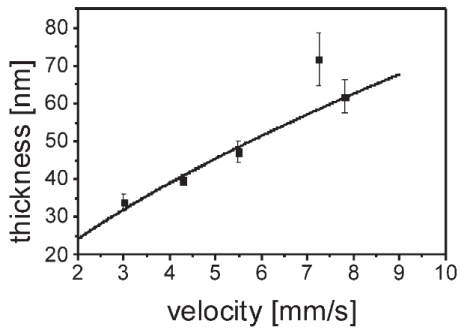

Figure 23. Thickness as a function of local deposition velocity in films of PQT-12:dPBrS blend prepared by withdrawing polymer solution (c_p=20 mg/mL) with constant acceleration a=0.5 mm/s². Solid line marks the thickness variation predicted by equation 17.

For the experimental conditions: acceleration $a = 0.5\ mm/s^2$, $v_0 = 50\ mm/s$, concentration c_p=20 mg/mL, monotonic growth of film thickness (see solid line in Figure 23) can be assumed. At lower coating speeds, the thickness can pass through a minimum and increase again with decreasing speed [180].
H-dipping combines simplicity of dip-coating with the advantages of blade-casting. Similarly to the dip-coating method, a wet layer of dissolved material is formed by withdrawing the substrate under a meniscus of the coating solution. The meniscus is formed between a cylindrical bar kept at a constant height and a solid substrate that is drawn horizontally, as in blade-casting. The relative speed of the cylinder and the substrate is so small that the shape of the meniscus is retained. However, in contrast to dip-coating only a small amount of the solvent is necessary to cover a large area of substrates [176].
In this work the samples of at-PMMA dissolved in chloroform were prepared using H-dipping method resulting in a film thickness in the range of 30 ÷ 140 nm.

2.3.3. Drop casting

Drop-casting is a method in which a small amount (drop) of polymer solution is placed on top of the substrate and allowed to dry (solvent evaporate) [181]. The film thickness is rather non-uniform but this technique is very simple and can be used for solutions for which other casting methods cannot be applied due to e.g. dewetting. In this work the synthesized polythiophene nanoparticles were drop-cast from the tetrahydrofuran (THF) solution (1mg/ml) onto silicon wafer.

3. Experimental methods

3.1. Scanning probe spectroscopy

3.1.1. Atomic Force Microscopy

The invention of the scanning tunneling microscope (STM) in 1982 made a revolution in the field of surface science due to the possibility of real space atomic imaging [182]. Four years later the invention of atomic force microscopy (AFM) extended the imaging capabilities to non-conductive materials [183]. Since then the rapid development has led to the novel dynamic mode of AFM [184].
AFM is based on the van der Waals forces between sharp tip, which is mounted to a cantilever and the sample surface. The tip interacts with the surface causing the cantilever to bend. The cantilever movement is measured by a laser beam which is reflected from its backside and detected by a position sensitive photodiode. An illustration of AFM setup is shown in Figure 24.

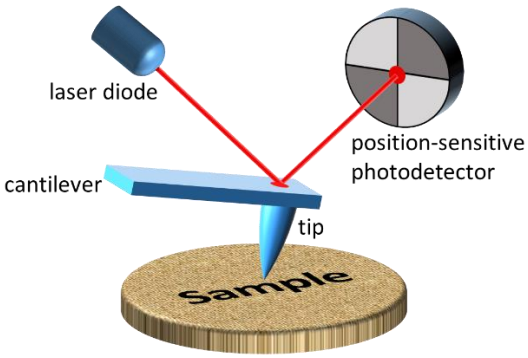

Figure 24. The basics of AFM setup. The movement of the cantilever, caused by the tip-sample interactions, is tracked by changes of the position (position-sensitive photodetector) of focused, reflected laser beam.

When the tip approaches the sample the force interactions change and can be described by the Lennard-Jones interaction potential (Figure 25). At the long range part of the curve the tip and sample are separated by a large distance. As they get closer, the tip and sample atoms first attract weakly each other due to London dispersion forces. In this regime the AFM operates in so called non-contact mode or dynamical mode [184]. As the tip approaches the surface, the repulsive van der Waals force predominates. When the total force becomes positive (repulsive), the tip and surface are in the "contact" regime (contact mode or static mode) [185, 186]. These two regimes are separated by so called "intermittent-contact" region which consist of varying attractive and repulsive forces (tapping mode). The additional forces including strong capillary and adhesive forces that attract the tip to the surface must be addressed due to their considerable contribution to overall interactions.

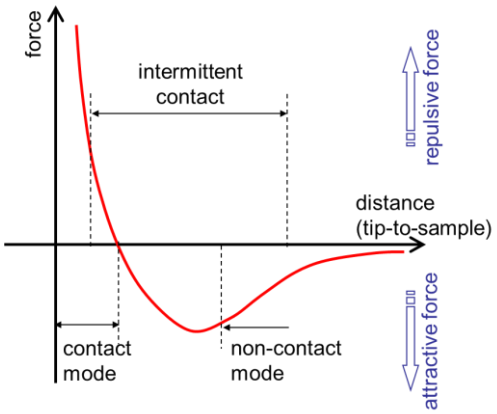

Figure 25. Lennard-Jones interaction potential which describes typical interaction of an AFM tip and the sample surface in close proximity.

The tapping mode is referred to intermittent contact mode due to the alternating contact of the tip with the sample surface. In this mode, cantilever is vibrated in

sinusoidal motion at, or near, one of its resonance frequencies. The tip-sample interactions cause changes in the amplitude, phase and resonance frequency and thus different signals containing useful information can be collected simultaneously. The tip oscillation amplitude (amplitude modulation mode - AM) or frequency (frequency modulation mode - FM) is measured by a reflected laser beam at the photosensitive detector and processed through lock-in amplifier. A feedback system is employed to maintain the amplitude (AM) or frequency (FM) at the desired value. The obtained topography image is the voltage (multiplied by constant (nm/V)) applied to the Z axis piezoelectric element required to keep the oscillation amplitude or frequency constant. Within the framework of this study tapping-mode was used (unless otherwise stated) since contact mode is unsuited to soft organic materials due to the possibility of scratching the film and/or contamination of the tip [187, 188]. The non-contact mode, in turn, was unavailable in our AFM instrument. In the intermittent contact mode, when the tip approaches the sample surface it moves through an interaction potential that includes long range and short term repulsive forces. The force between the oscillating tip and the surface is almost perpendicular to the surface, resulting in very little lateral force. As a consequence the tip or specimen degradation is minimized making it possible to get images of soft organic materials [189].
In this study the Agilent 5500 apparatus running in tapping mode was used to obtain topography maps.

3.1.2. Kelvin Probe Force Microscopy

Kelvin Probe Force Microscopy (KPFM) was first developed by Nonnenmacher et al. [190] and it allows to map the surface potential or more precisely, the local contact potential difference (CPD) between the tip and the surface. The basic idea of this technique originates from macroscopic method Kelvin Probe (KP) developed by Lord Kelvin in 1898 which uses parallel metal plates forming capacitor, where the voltage applied to one vibrating plate is controlled in a way that no current flow is induced by vibration of plates. This applied voltage corresponds to the CPD between these two plates thus, knowing the metal forming one plate the second one can be described. The main difference between KP and KPFM is that the latter uses electrostatic force rather than current control since in the microscopic scale the plates are too small to generate sufficient current and in turn, desired sensitivity [186]. Similarly to the topography measurement, the CPD measurement also can be determined in amplitude modulation mode (AM-KPFM) or frequency modulation mode (FM-KPFM) which differs in the possible resolutions and application capabilities [191, 192]. Regarding the way of topography mapping during KPFM measurements the two additional approaches can be identified: the “single-pass” with simultaneous use of probe resonance frequency for topography maps and lower frequencies for CPD mapping or “two-pass lift mode”

where the first pass is used to track the sample surface and then the tip is positioned 10-20 nm above the sample and, following the previously obtained topography, maps the CPD signal [189]. In this study the single-pass AM-KPFM has been used and is described.

The energy of the capacitor U_C can be written as:

$$U_C = \frac{1}{2} C V^2 \tag{18}$$

where C is the capacitance and V is the voltage between the plates. The electrostatic force in KPFM between the tip and the sample, considering the tip and the sample as a parallel capacitor, can be expressed as follows:

$$F_{el} = -\nabla U_C = -\frac{1}{2}\frac{\partial C}{\partial z} V^2 \tag{19}$$

where z is the distance between the tip and the sample, V is the voltage applied to the tip and $\partial C/\partial z$ is the capacitance gradient of the tip-sample system [191]. The magnetic forces which should be considered are only present if the tip and/or sample material are magnetic. If it is not the case then these forces and their contribution to the overall interaction can be neglected [186]. When the AC voltage with frequency ω_e and amplitude V_{AC}, superimposed on a DC voltage V_{DC}, is applied to the tip, the expression of the electrostatic force can be rewritten as:

$$F_{el} = -\frac{1}{2}\frac{\partial C}{\partial z}[V_{DC} - V_{CPD} + V_{AC}\sin(\omega_e t)]^2 \tag{20}$$

where V_{CPD} is the potential induced by work function (Φ) difference of the tip and the sample:

$$V_{CPD} = \frac{\Phi_{tip} - \Phi_{sample}}{e} \tag{21}$$

and e is the elementary charge. The above equation can be decomposed into three different spectral components:

$$F_{DC} = -\frac{\partial C}{\partial z}\left[\frac{1}{2}(V_{DC} - V_{CPD})^2 + \frac{V_{AC}^2}{4}\right] \tag{22}$$

$$F_{\omega} = -\frac{\partial C}{\partial z}(V_{DC} - V_{CPD})V_{AC}\sin(\omega_e t) \tag{23}$$

$$F_{2\omega} = \frac{\partial C}{\partial z}\frac{V_{AC}^2}{4}\cos(2\omega_e t) \tag{24}$$

The first one is the static part which produces the deflection of the cantilever but it is very low and difficult to detect [193, 194]. In AM-KPFM the electrostatic force at ω_e frequency (F_ω) is measured by detection of the cantilever deflection by means of lock-in amplifier referred to ω_e. The CPD is directly determined by a feedback loop which nullifies the detected amplitude by applying the V_{DC} voltage which is equal to V_{CPD}. Interpretation of the last component ($F_{2\omega}$) related to $\partial C/\partial z$ is not very often considered in KPFM measurements. Nevertheless it gives additional information regarding local capacitance or permittivity of material between the tip and the conducting part of the sample [195]. The CPD is commonly related to electronic properties of the outermost surface layer, while the $\partial C/\partial z$ signal is considered to provide information from deeper regions of the surface layer [196].

There are many features involved in measured CPD signal depending on the sample type. In the case when the metal tip approaches a metal surface, the AM-KPFM method measures work function difference of these two materials ($\Delta\Phi_{MT}$) (Figure 26a). The DC voltage aligns vacuum levels (VL) of the tip and the sample, the electrostatic force is minimized and CPD indicates directly $\Delta\phi_{MT}$. If the metal surface is covered with a dipole layer the vacuum level of the sample surface is shifted (Figure 26b). The VL alignment determines the sum of the work function difference and energy of the dipole ($\Delta\phi_{MT} + \Delta$). An additional organic layer, which covers the dipole layer introduces further shift of the vacuum level due to band bending (eV_b) (Figure 26c). This can be observed for the metal substrate which stays in electronic equilibrium with the organic layer. In this case the metal and polymer Fermi levels are aligned. The equilibrium can be achieved e.g. for conducting or semiconducting polymers. In the case of non-conducting polymers such as polystyrene, one can expect that the polymer layer does not stay in equilibrium with substrate and misalignment of Fermi levels can occur [134].

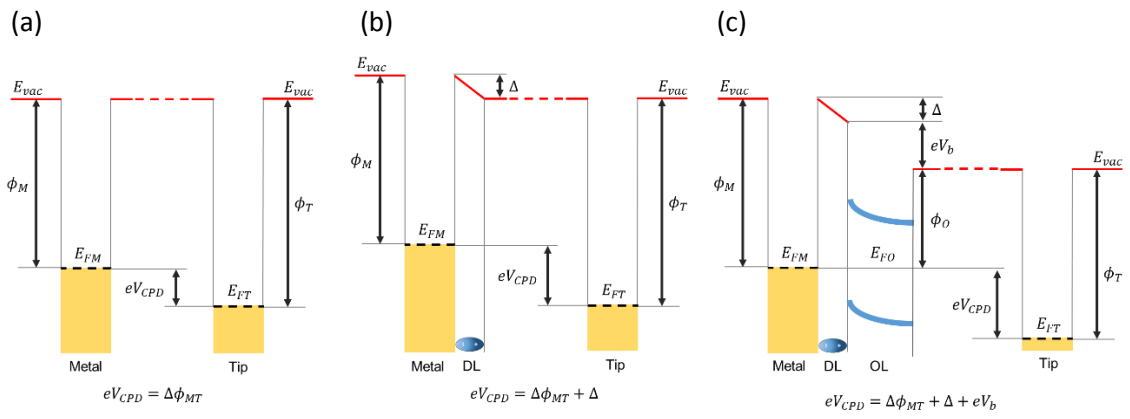

Figure 26. Electron energy diagram of a metal (Met.) (a) covered with an organic dipole layer (DL) (b) and then with organic overlayer (OL) being at electronic equilibrium with metal substrate (c), examined with a tip (E_F — Fermi level, $\Phi_{M,T}$ — work function, $\Delta\Phi_{MT}$ — tip-metal work function difference, eV_b — band bending energy shift, Δ — dipole energy step, eV_{CPD} — energy induced by contact potential difference when vacuum levels (E_{vac}) of the tip and surface are aligned; M, O and T subscripts denotes metal, organic overlayer and tip, respectively).

The topography (a) and CPD (b) map obtained with KPFM of 5 µm wide RP3HT stripes deposited by MIMIC procedure on gold substrate are shown in Figure 27. It directly gives information about regions of higher values of work function (dark areas) compared with areas of lower work function values (bright regions). A combination of the CPD map with topography map gives qualitative results about specimen, in this example gold has higher work function than the polythiophene, as expected. However, the CPD image scale bar is insufficient in order to exactly determine CPD differences between distinguishable regions. In such a case, further analysis can be taken to obtain quantitative results from the analyzed map. In this study, the CPD image histograms were used to analyze CPD differences between dark and bright areas.

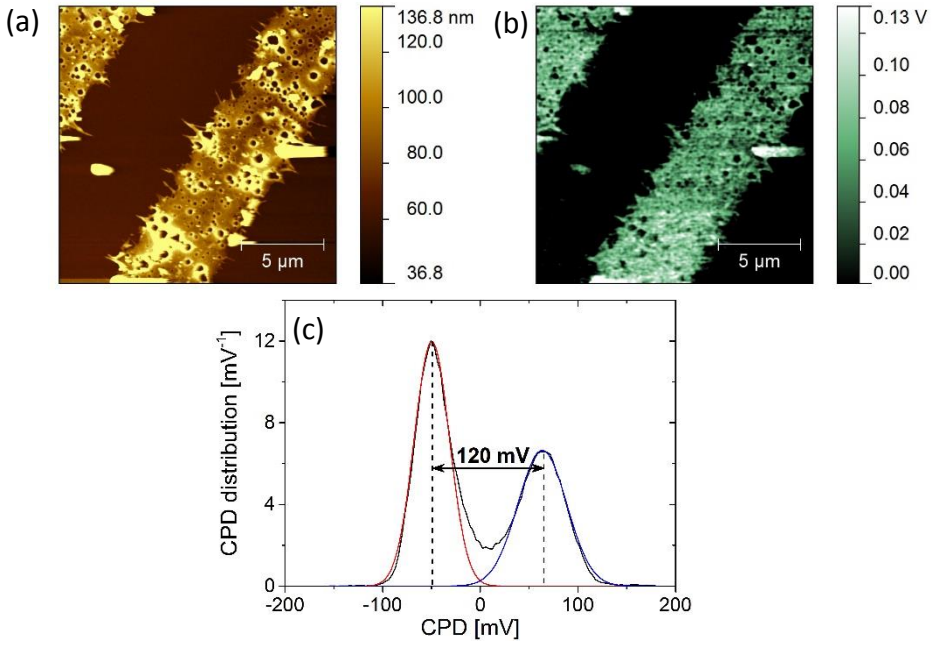

Figure 27. (a) KPFM topography and (b) CPD maps of RP3HT stripes on gold fabricated by MIMIC technique. (c) Histogram of the CPD map showing the density distribution of the data (black line). Red and blue lines correspond to the fitted Gaussian functions. The CPD difference was estimated at 120±31 mV.

The histogram (Figure 27c) plots the distribution density of the data and can be used to estimate the probability density function of the underlying CPD values. The most probable CPD values and their uncertainty were determined by fitting Gaussian functions:

$$y_i = \frac{A_i}{\sigma_i\sqrt{\pi/2}} exp\left(-\frac{\left(x - x_{c_i}\right)^2}{2\sigma_i^2}\right) \tag{25}$$

where x_{c_i} are the expected values of the measured voltages (maxima), σ_i are their standard deviations indicating uncertainties and A_i are constants. The CPD difference between distinct regions is calculated as the difference between the calculated

expected values with uncertainty being the quadratic mean of the original standard deviations.

In the histogram presented in Figure 27c the CPD the difference between dark and bright areas is equal to 120 mV. In this case uncertainty given by equation:

$$\sigma = \sqrt{(\sigma_1)^2 + (\sigma_2)^2} \tag{26}$$

is equal to 31 mV. Concluding above remarks, CPD difference can be written as 120±31 mV.

KPFM can also be used as a quality control tool for correctness of SAM pattern fabrication. In Figure 28 the KPFM CPD map of at-PMMA thin film spin-coated on COOH(L)-SAM pattern complemented with CH3-SAM showing defects in µCP procedure is presented. In this case the stamp inked with polar COOH(L)-SAM was pressed too hard to substrate which resulted in a deposition of stamp material (black) in the middle of polar SAM areas (bright green). Contrary to the expectations, the material which should have been deposited by PDMS mold in the middle was localized on both sides of patterning structure.

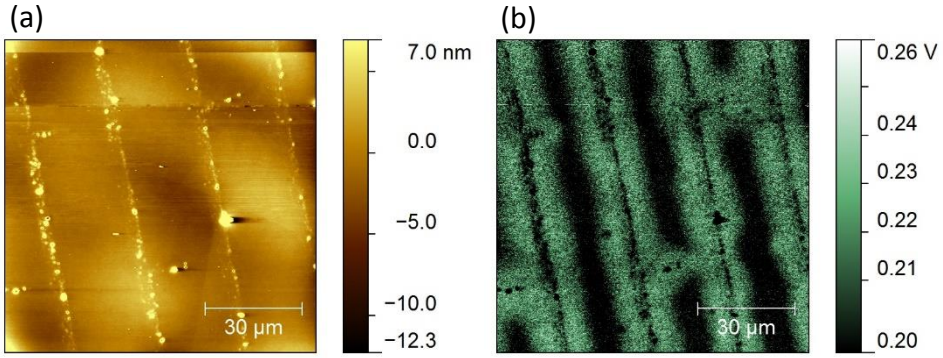

Figure 28. (a) Topography and (b) CPD map of at-PMMA spin-coated on COOH(L)-SAM pattern complemented with CH3-SAM. The CPD shows fabrication defects during micro-contact printing procedure. The stamp was pressed too hard to the substrate which resulted in deposition of stamp material and this effect is depicted also on the topography image.

In this study, measurements with KPFM working in amplitude modulation and intermittent-contact mode, were performed with the Agilent 5500 apparatus recording surface topography simultaneously with the maps of CPD and $\partial C/\partial z$ signals. All measurements were performed under ambient conditions. Some of them were repeated in dry (argon) atmosphere. The cantilevers used were: Au covered monolithic silicon cantilevers (BudgetSensors) with a spring constant of 3 N/m, quality factor of about 100 and resonance frequency of 65 kHz, Pt/Ir covered monolithic silicon cantilevers (Olympus) with a spring constant of 2 N/m, quality factor between 100 and 200 and resonance frequency of 75 kHz and Au covered monolithic silicon cantilevers (NanoSensors) with a spring constant of 2.5 N/m, quality factor of about 100 and resonance frequency of 70 kHz. Maximum scan size range was 100×100 µm^2. DC voltage

and AC voltage with frequency of 10 kHz were applied to the cantilever in all measurements.

3.2. Time-of-Flight Secondary Ion Mass Spectrometry

Secondary ion mass spectrometry (SIMS) is one of mass spectrometry methods in which ionized particles are emitted due to surface bombardment by energetic primary particles. SIMS examines the mass of ions which escaped from the surface bringing information on surface chemistry. The term "secondary ion" distinguishes the particles emitted from the surface from those which strike ions from the surface (primary ions). The observation of release of positive ions and neutrals from solid surface under ion bombardment was first described by British physicist J. J. Thompson in 1910 [197].
There are two parallel processes involved in the production of secondary ions: sputtering and ionization which can occur simultaneously or consecutively. Sputtering is the process in which secondary particles are emitted from the surface as a result of high energy primary particle impact. A number of mechanisms are involved in sputtering process which are presented schematically in Figure 29.

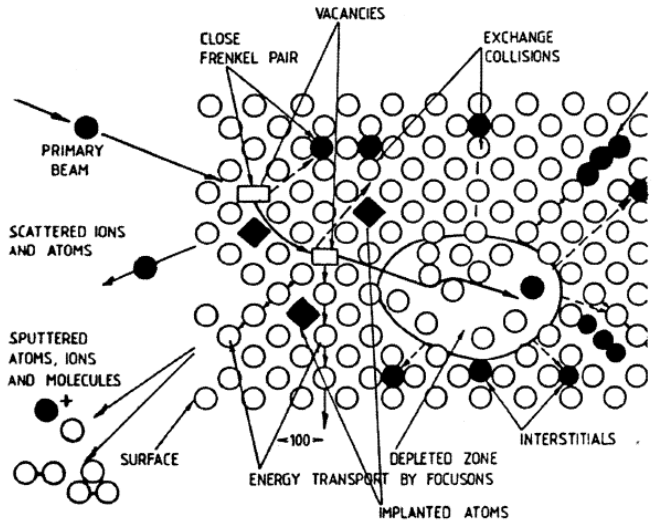

Figure 29. Schematic diagram of the processes which take place after ion impact onto a surface. SIMS is concerned with analysis of the sputtered ions. The impact of one primary ion can cause many target atom displacements which affect the surface seen by subsequent ion impacts. Adapted from [198].

The types of the processes occurring during sputtering depend on the primary particle energy, flux, mass and ion type. For primary particle energies in the few keV range used in SIMS, most of the energy is transferred to the sample by nuclear collisions. The primary ion energy is transferred to target atoms via atomic collisions and a so-called collision cascade is generated. Part of the energy is transported back to the surface allowing surface atoms and molecular compounds to overcome the surface binding

energy. The interaction of the collision cascade with surface molecules is soft enough to allow even large and non-volatile molecules with masses up to 10,000 u to escape without or with little fragmentation. Ionized atoms, clusters and molecules provide signal for SIMS.

The basic SIMS equation can be written as follows:

$$I_A = I_P \cdot T_{SPEC} \cdot Y_{tot} \cdot \alpha_A^{\pm} \cdot c_A \tag{27}$$

where I_A is the measured intensity of secondary ion current of species A, I_P is the primary ion beam intensity, T_{SPEC} is the transmission of the analysis system, Y_{tot} is the sputter yield, $\alpha_A^{\pm}$ is the ionization probability to positive or negative ions and c_A is the fractional concentration of species A in the surface layer. Due to the surface bombardment, the neutral particles and positively and negatively charged particles are emitted. The parameter which describes the number of sputtered particles (neutral and ionic) per primary particle is called sputter yield ($Y_{tot} = N_S/N_p$ where N_S is the number of secondary atoms emitted and N_P is the number of impacted primary ions). This needs to be distinguished from the secondary ion yield which is described by: $Y_A^{\pm} = Y_{tot} \cdot \alpha_A^{\pm}$ and gives the information on secondary ions of species A emitted per primary ion impact. Positive and negative sputter yields depend on the type of the projectile employed in sputtering. For example, the cesium reflects high secondary ion yields for negative ions while oxygen enhances yield for positive ions. The ionization probability $\alpha_A^{\pm}$ is strongly influenced by electron exchange process between the departing species and the surface. The secondary ion sputter yields of elemental species can vary by several orders of magnitude across the Periodic Table and are very dependent on the chemical state of the surface. This phenomenon is known as the matrix effect and in addition to the previously mentioned factors, it results in significant complications when absolute quantitative data are required. In spite of this SIMS is very sensitive and concentrations in the range of few ppb can be evaluated.

Initially, the primary ions used in SIMS were Ga^+, Ar^+ and Cs^+ but the latest technique developments have led to the use of cluster ions like Au_n^+ (n=1-5), Bi_n^+ (n=1-7), C_{60}^+, Ar_n^+ (n=1000-5000) and others [199]. These cluster ions generate higher secondary ion yields from molecular fragments thus increasing sensitivity of the technique. The increase in secondary ion yield in the case of cluster primary ion usage is due to the fact that when the cluster hits the surface the projectile energy is portioned among all the atoms and as a result they generate much less chemical damage [200]. Moreover, the sputter rate is so high that most of the damage material is removed by following impacts resulting in greatly reduced damage cross-section [201].

One of the two basic operating modes is called static SIMS (sSIMS) and allows to acquire spectra for the first monolayer with very low probability (due to low ion dose) of multiple sputtering events from the same site. A typically used ion dose in sSIMS is in the range of 10^{11} – 10^{12} ions/cm^2 (to compare: monolayer contains 10^{15}

atoms/molecules per cm^2). This technique dates back to 1969 and prof. Benninghoven at the University of Münster, whose group applied it to study surfaces in UHV using low primary ion currents at large areas [202]. Since that time sSIMS has become a widely used tool for surface analysis with great advantages over other techniques which are e.g. detection of all chemical elements within periodic table, detection of elements in concentrations as low as 1 ppb and very high surface sensitivity limited to one or two atomic layers.

The second mode is called dynamic SIMS (dSIMS), in which the sample surface is eroded by sputtering with a mono-energetic beam of primary ions in the energy range typically 0.25 keV to 50 keV. This mode gives the ability of depth profiling with SIMS. The sputter rate U of the removed material can be described as follows:

$$U = \frac{j_P \cdot Y_{tot}}{e \cdot \rho} \tag{28}$$

where j_P is the density of primary ion current, e is the elemental charge and ρ is the elemental atomic density. The sputter yield of the target depends either on the ion energy and species as well as the target atomic number or on the surface crystallinity and topography. However, theoretical sputter yields calculated for smooth amorphous targets are generally in good agreement with values found from experimental depth profiles of single element targets. Therefore, theoretical sputter yields can be profitably used to calculate erosion rates in dynamic SIMS measurements. This in turn allows the SIMS depth profile which is given in terms of the sputter time to be converted in terms of sputtered depth.

Depth resolution is a measure of the ability to localize a concentration measurement at a depth and to distinguish between features at different depths. When a solid is bombarded by a beam of ions, the accompanying sputtering, beam induced mixing and probe atom incorporation give rise to an altered layer in the surface of the material (Figure 30). The altered layer is then a disordered mixture of the original matrix elements and probe atoms. Except for favorable combinations of primary beam and target material, the surface of the sample becomes textured on the nano- to micro-scale, and this imposes a significant, and usually depth-dependent limitation on the achievable depth resolution and quantitative accuracy.

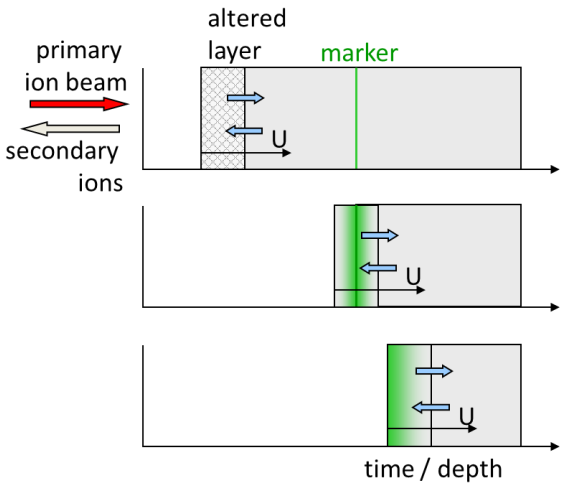

Figure 30. Schematic view of the influence of altered layered on depth resolution during ion beam sputtering process.

The key to instrumental developments in the mass spectrometry was the introduction of time-of-flight mass spectrometer (ToF-SIMS) which increased the sensitivity, mass resolution and mass range in orders of magnitude (as compared to quadrupole mass analyzer instruments). Spectrometers of this kind extract the secondary ions which then travel the drift tube along known flight path until hitting the detector. Velocity of a given ion is proportional to the square root of its mass, thus measured flight time will vary according to the mass/charge ratio (*m/z*). The spectrometer works in a pulsing mode and allows for simultaneous detection of all secondary ions of given polarity.

High spatial resolution imaging can be realized if the primary ion beam is capable of well focusing and rastering over a selected area of the sample. Secondary ions intensities are monitored as a function of the position of the primary ion beam on the surface resulting in a quasi-3-dimensional analysis (x- and y- position on the surface and in each point full mass spectra). Liquid metal ion beam sources (Bi_n^+) can be operated with beam diameters down to 50 nm reaching the feasible spatial resolution of about 100 nm [203].

Dynamic ToF-SIMS can be used as a high precision depth profiling and quasi-4-dimensional (x, y, z and in each voxel full mass spectra) characterization technique if combined with imaging capabilities. In a dual beam instrumentation mode of this method (Figure 31) one gun is responsible for sputtering (high ion dose density for high sputter yield, low energy resulting in low penetration depth, relatively large spot size) while the other is used for analysis (low ion dose density, high energy, small spot size).

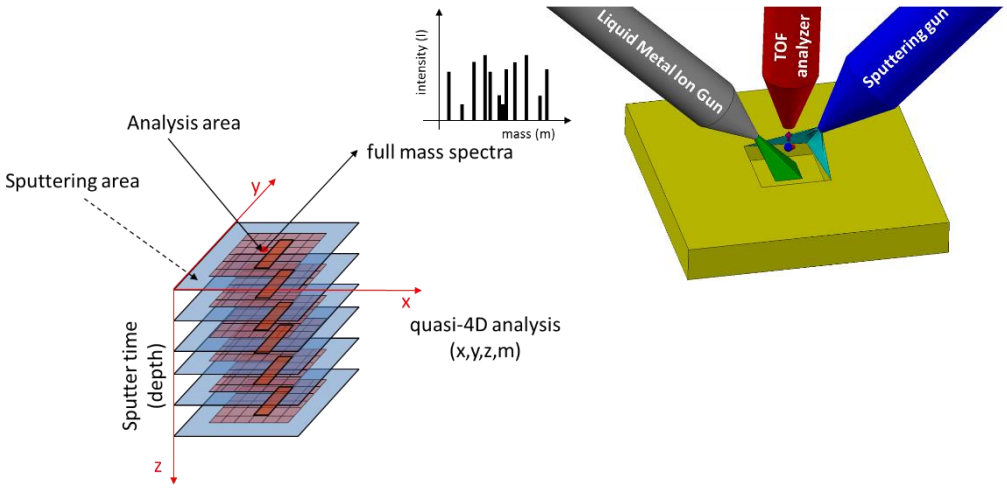

Figure 31. Illustration of the basics of ToF-SIMS dual beam depth profiling. First ion gun (LMIG) is responsible for analysis and the second one (sputtering gun) is used for material removal. Combining high-lateral resolution of the analyzing gun and specificity of ToF mass spectrometer the 4D-analysis can be carried out.

Sputtering beams commonly used are oxygen, cesium, gallium, fullerenes, argon or xenon. dSIMS is a versatile and sophisticated technique but there are many parameters involved in the sputtering process which need to be well understood to set up the experiment properly if high depth and lateral resolution, sensitivity and dynamic range have to be obtained. These parameters are e.g. ion implantation, diffusion, segregation, preferential sputtering of certain species, charge up built in non-conducting materials, changes of sputtering rate and ionization coefficient, matrix effects and surface induced roughening, to name only a few [199, 204-209]. Correctly set instrument can diminish the influence of the above mentioned effects and push the capabilities of organic depth profiling with dSIMS to the limits.

In dSIMS depth profiling of 3D objects the original Z-axis is inverted due to the projection of 3D data onto 2D image plane. Initial height variations of polymer film are transferred as interface undulations due to the fact that when collecting data in SIMS the starting surface is assumed to be ideally flat. This results in an inverted image matrix. Assuming the constant sputter rate of polymer film (which is generally true) and flat polymer/metal interface (evaporated gold on Si wafer is a good illustration of flat surface), the secondary ion signal topography variations at the interface can be considered as surface waviness and/or polymer film disruptions.

Within the framework of this study imaging mode sSIMS measurements of self-assembled monolayers deposited by µCP on gold were performed using the TOF.SIMS 5 (ION-TOF GmbH, Muenster, Germany) instrument, equipped with 30 keV cluster bismuth liquid metal ion gun and ToF mass spectrometer. The Bi_3^+ clusters were used as the primary ions, with the ion dose density lower than 1.1×10^{12} ions/cm^2, rastered randomly over a region of 150 µm x 150 µm.

Dual-beam depth profiling in negative polarity (negatively charged ions measured) of all studied multilayer polymer films was performed with a 1 keV Cs^+ ion beam operating

at 40 nA, which sputtered the area of 450 × 450 µm^2. After each sputtering cycle a sample composition at a given depth was determined using 30 keV Bi_3^+ clusters, in which case the beam current was 0.1 pA and the area of analysis was 100 × 100 µm^2. The Bi_3^+ beam was operating in the mapping mode that is at each depth a 256 × 256 map of chosen secondary ion intensities was collected, showing the lateral distribution of sample components. For given parameters the sputter rates were estimated at 0.7 nm/s for PMMA and 0.05 nm/s for PS.

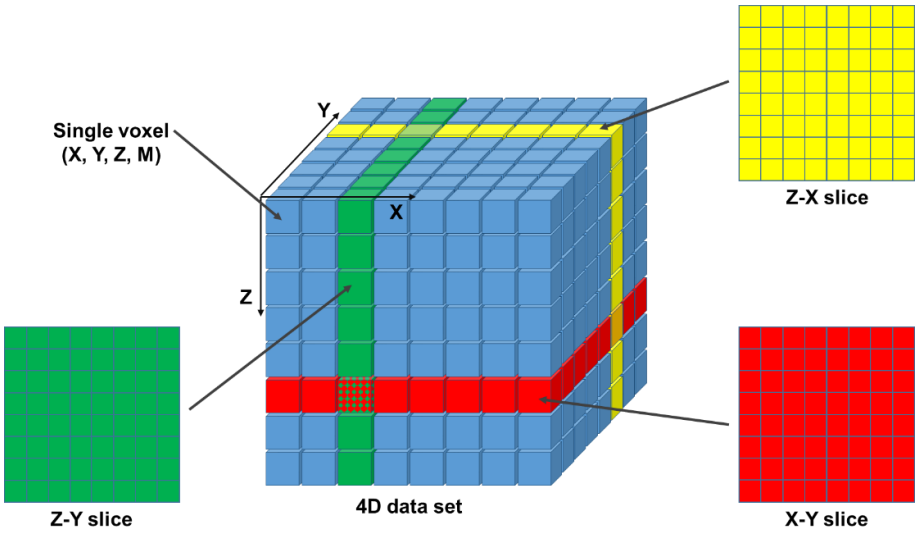

Figure 32. Different possibilities of analyzing data obtained from ToF-SIMS depth profiling measurements. Each slice projected on the proper plane can be extracted and analyzed. Slices can be chosen as simple one pixel flat maps or a stack (sum) of all slices which are obtained as a sum of all intensities projected onto each plane.

An example of possible ways to extract desired information from ToF-SIMS quasi 4-dimensional data set obtained during dual beam depth profiling is shown in Figure 32. One can select a demanded plane and corresponding slice (cross-sectional view) and gain information about secondary ion mass intensities in this region. As each voxel includes a full mas spectra, it gives very powerful and exhaustive ways to obtain desired results. As an example of utilization presented possibilities of data interpretation, the ToF-SIMS depth profiling of multilayer system i.e. PS spin-coated on inhomogeneously modified with thiols gold surface evaporated on silicon wafer, is shown in Figure 33. Each layer can be readily observed using SIMS depth profiling as indicated also by vertical cross-sectional views and 3D sample reconstruction data for chosen species.

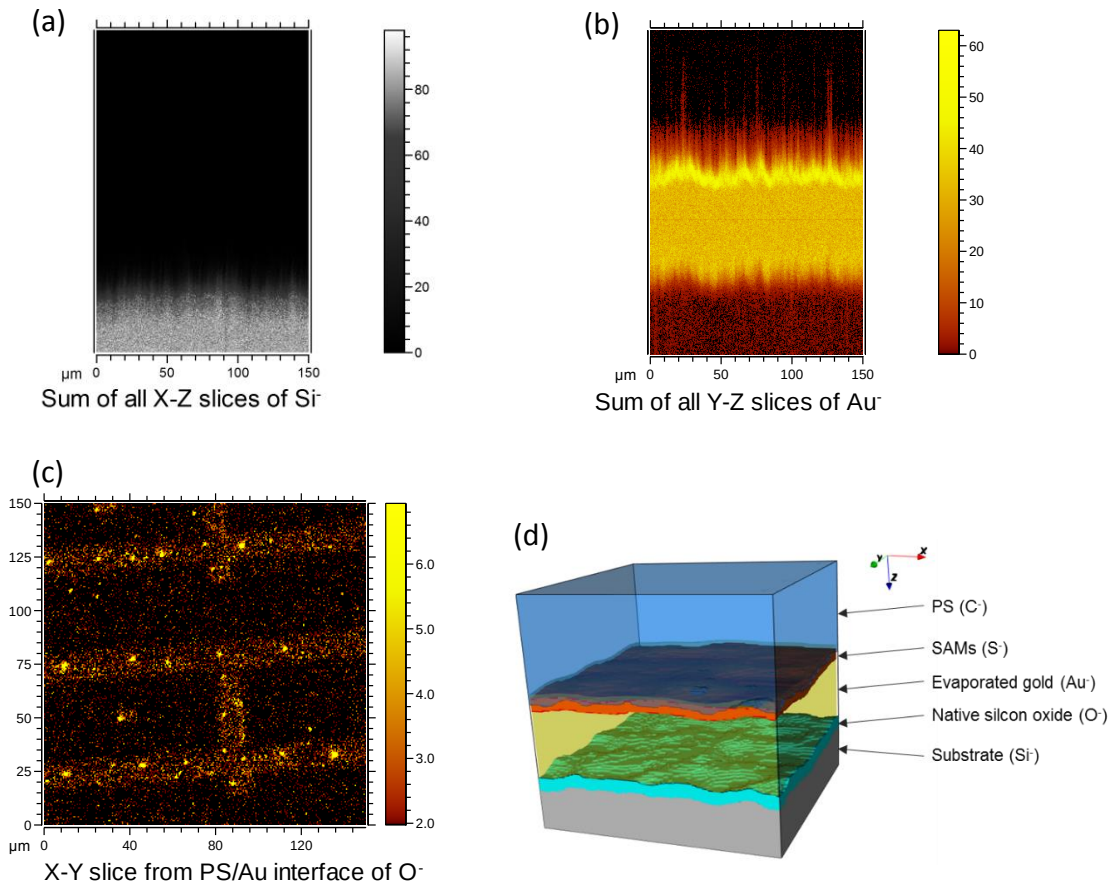

Figure 33. An example of possible ways to examine and present results obtained from ToF-SIMS depth profiling: (a) cross sectional-view on Si^- ion intensity obtained by summation of all slices in X-Z plane, (b) sum of all slices from Y-Z plane for Au^- ion intensities, (c) X-Y slice (map) of O^- ion intensities from interface region which shows COOH(L)-SAM pattern from µCP, (d) 3D view which depicts origin of chosen, characteristic for each layer, secondary ions, enabling to quasi-reconstruct the multilayer composition of examined sample. The term "quasi-reconstruction" is used due to the fact that the z-axis is in time units (sputtering time) and does not reflect corresponding layers thicknesses because of different sputtering yield for each layer.

3.3. Photoelectron Spectroscopy

3.3.1. X-ray Photoelectron Spectroscopy

X-ray Photoelectron Spectroscopy (XPS) also known as ESCA (Electron Spectroscopy for Chemical Analysis) is a technique which analyses the energy of electrons emitted from the sample surface, exhibiting the photoelectric effect, as a consequence of soft X-ray irradiation. Albert Einstein, using Planck's quantization of energy concept, explained the photoelectric effect and was awarded Noble Prize for this discovery in 1921. As an analytical tool XPS was first applied in 1951 by Steinhardt and Serfass [210]. In the 50s and 60s of the 20th century Kai Siegbahn developed the high resolution instrumentation and expanded the theory of ESCA (he was first to coin this term) known unto this day [211]. For his work in the field of photoelectron spectroscopy Siegbahn was awarded

Nobel Prize in Physics in 1981. Since that time XPS has experienced a period of rapid growth and spread across a wide range of scientific and technological areas [212].
The core-level photoemission process that is the basis of XPS is the total transfer of the photon energy to the electron. The electrons emitted from core levels due to the soft X-ray irradiations are called photoelectrons. The basic physics of this process can be described by the following equation:

$$E_B = h\nu - E_{kin} - \Phi_{SP} \tag{29}$$

where E_B is the binding energy of the electron in the atomic core level, $h\nu$ is the energy of the irradiating X-rays, E_{kin} is the kinetic energy of the emitted electron – value measured within the XPS spectrometer and Φ_{SP} is the work function of the spectrometer. The quantity E_B for non-scatter or elastic scatter electrons provides valuable information about photoemitting atom and can be obtained due to known value of $h\nu$, measured E_{kin} (in the electron energy analyzer) and calibration procedure which gives the value of Φ_{SP} (typically between 4 – 5 eV). The binding energy varies with the type of atom (i.e. change in nuclear charge changes electron bound to the atom) and its local environment and chemical state (covalent or ionic bounds alter the electron distribution). Binding energy lines in the spectrum are labelled according to the energy level from which they originate – first the periodic table element label, then the principal quantum numbers (1, 2, 3, 4…), next the angular momentum denoted as s, p, d, f (0, 1, 2, 3) and in the end, the total angular momentum which is given by the absolute value of the sum of angular (L-S coupling) and spin momentum (j-j coupling). As an example the fourteen electrons in the gold 4f subshell are split into $Au4f_{5/2}$ (six electrons) and $Au4f_{7/2}$ (eight electrons). The variations in the binding energy of specific atom are called binding energy shifts or chemical shifts and they provide the chemical information (chemical bonding) about surface composition. The XPS can then be seen as a qualitative method making it possible to evaluate chemical states present on the surface.
The depth analysis in XPS varies with kinetic energy of the detected photoelectrons. For electrons in the energy range 10 ÷ 2000 eV the distance that may be travelled before undergoing inelastic collision (inelastic mean free path) is typically in the order of 2 ÷ 5 nm [213]. A number of terms for describing inelastic scattering effects have been proposed: the inelastic mean free path, the attenuation length and the escape depth. If one considers that photoelectrons are created at a depth z below the surface with a certain angular distribution, and only inelastic scattering leads to electron attenuation, the decrease in the number of photoemitted electrons may be described by Beer-Lambert law [214]:

$$I_E = I_0 e^{\left(-\frac{z}{\lambda \sin\theta}\right)} \tag{30}$$

where I_E is the intensity emitted from the atoms at depth z, I_0 is the intensity from the surface atoms and θ is the electron take-off angle to the surface. In such a case λ is the inelastic mean free path of the measured electrons. For a sample where bulk material B is covered with a thin layer of material A and thickness d, the above equation leads to the expressions:

$$I_A = I_A^0 \left[1 - e^{\left(-\frac{d}{\lambda_A \sin\theta}\right)}\right] \tag{31}$$

$$I_B = I_B^0 \left[e^{\left(-\frac{d}{\lambda_B \sin\theta}\right)}\right] \tag{32}$$

where I_A and I_B are the measured intensities, I_A^0 and I_B^0 are the intensities form bulk A and B, λ_A and λ_B are inelastic mean free paths (generally these will differ because λ is a function of the kinetic energy) of the measured core electrons of A and B, respectively travelling through material A. However, the elastic scattering events lead to longer trajectories compared with the straight line trajectory, thus experimental and theoretical determinations lead to λ values less than the inelastic mean free path by 30% or even more [214]. The experimentally derived results of the λ should be then referred to "attenuation length" (λ_{AL}) (Figure 34).

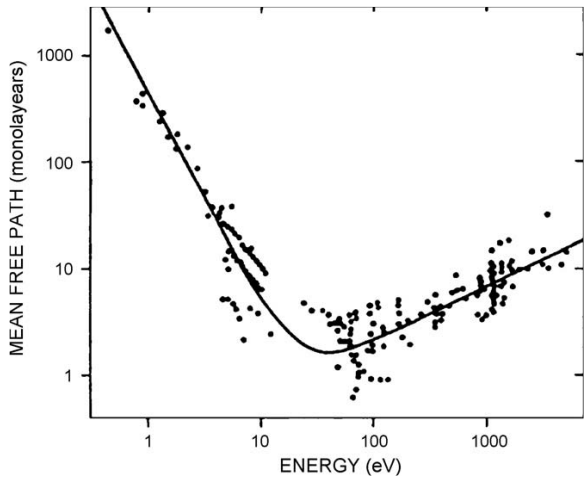

Figure 34. Experimentally derived attenuation length of various materials (dots). The solid line is the theoretically expected inelastic mean free path (adapted from [215]).

Considering the electrons that emerge for a take-off angle θ to the sample surface some 95% of the signal in electron spectroscopy emanates from the depth of $3\lambda_{AL}\sin\theta$ and it is taken as a sampling depth of this method (<10 nm for θ=90°). The variation of this parameter with take-off angle is the basis of angle-resolved XPS (AR-XPS) to obtain compositional depth profiles which will be discussed in more detail later.

The intensities of the photoelectron lines are important for quantification and depend upon the various factors [216]:

$$I_A(k) = I_X \cdot p \cdot S \cdot \sigma_A \cdot L \cdot T \cdot D \cdot \int_0^\infty N_A(z) \cdot e^{\frac{-z}{\lambda_A \cdot \sin\theta}} \cdot dz \tag{33}$$

where: I_A is the area of peak k from element A, I_X is the X-ray flux, p is a surface roughness factor (shadowing effects), S is the analysis area, σ_A is the photoionization cross-section of peak k from element A, L is the angular asymmetry factor for orbital k of element A, T is the spectrometer transmission efficiency, D is is the detector efficiency and $N_A(z)$ is the distribution of atoms A with depth z. If it can be assumed that X-ray flux is constant and that the analyzed volume is of uniform composition and under fixed experimental conditions, then the above equation can be simplified to:

$$I_A(k) = const \cdot \sigma_A \cdot N_A \cdot \lambda_A \sin\theta \tag{34}$$

From the above equation it is clear that detected intensity is linearly related to the atom concentration. Since the constant term contains a roughness term it would be very difficult to derive N_a knowing $I_A^\infty(k)$ – intensity from pure element A. Due to this fact all XPS data are quoted in terms of atom fractions from all atoms detected (hydrogen is excluded). This is achieved using relative sensitivity factors (RSF), with F1s peak taken as the standard to which other peaks are referred. From the equation 34 defining $I_F(1s) = 1.00$ and cancelling identical terms give:

$$\frac{I_A(k)}{I_F(1s)} = \frac{const \cdot \sigma_A \cdot N_A \cdot \lambda_A \sin\theta}{const \cdot \sigma_F \cdot N_F \cdot \lambda_F \sin\theta} \rightarrow I_A(k) = \frac{\sigma_A \cdot \lambda_A}{\sigma_F \cdot N_F \cdot \lambda_F} \cdot N_A = S_A \cdot N_A \tag{35}$$

where S_A is the RSF of element A (at level k). Elemental sensitivity factors are determined for each instrument. With known RSF for elements (S_n) the relative atomic concentration of any chosen element X is then simply obtained from:

$$c_X = \frac{I_X \cdot S_X}{\sum_n (I_n / S_n)} \tag{36}$$

where c_X is expressed as atomic % of all elements measured excluding hydrogen.
Although XPS is a method of surface analysis, it is possible to use it to provide compositional information as a function of depth. This can be achieved by non-destructive or destructive methods. Non-destructive in-depth resolution can be achieved, according to described earlier attenuation of the photoemitted electrons, by variations of the excitation energy (energy-resolved XPS) [17] or by variations of the photoelectron take-off angle – AR-XPS [217]. The destructive methods are typically ion

sputtering, chemical etching or removing material mechanically with angle lapping and ball cratering [218].

Within the framework of this study AR-XPS technique or gas cluster ion beam sputtering were used for depth profiling and these two methods are briefly described.

It is clear from the equations 30 and 33 that the depth analysis is dependent on the electron take-off angle (θ). If the spectra are recorded, with good angular resolution, at a low value of θ (10° ÷ 20°) an extremely surface sensitive analysis will be carried out. At normal to the surface (θ=90°) the analysis depth will be equal to maximum sampling depth of the method mentioned above. The schematic view of the basics of AR-XPS method is shown in Figure 35.

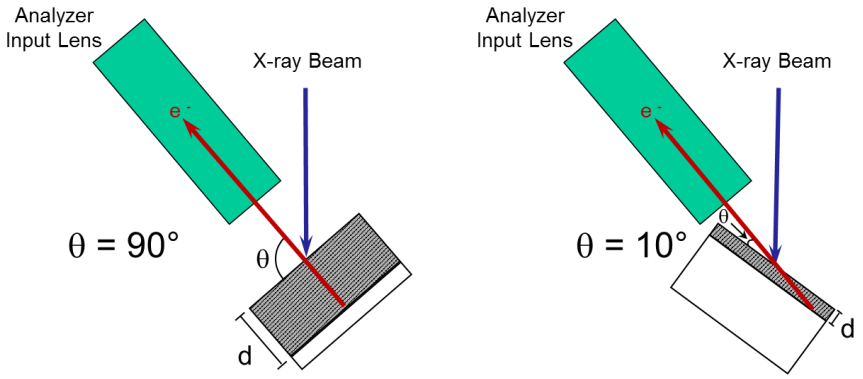

Figure 35. The basic concept of ARXPS depth profiling. When the sample surface is perpendicular to the electron analyzer (Θ = 90°) the sampling depth reaches its maximum value. If the sample surface is tilted and almost parallel to analyzer (e.g. Θ = 10°) an extremely surface sensitive analysis can be carried out.

The surface region, analyzed by XPS, could be composed of up to 30 atomic layers. Each of these layers may have a different composition, thus the recorded spectrum is a convolution of the information from all layers. For homogenously distributed atoms in the analyzed sample, the ratio of total intensity of the photoemitting atoms does not vary with take-off angle. However, if we consider a sample with an overlayer of one type of atoms on a substrate consisting of the second type of atoms, the ratio of the intensities during sample tilt changes relatively to the take-off angle. This situation is presented in Figure 36.

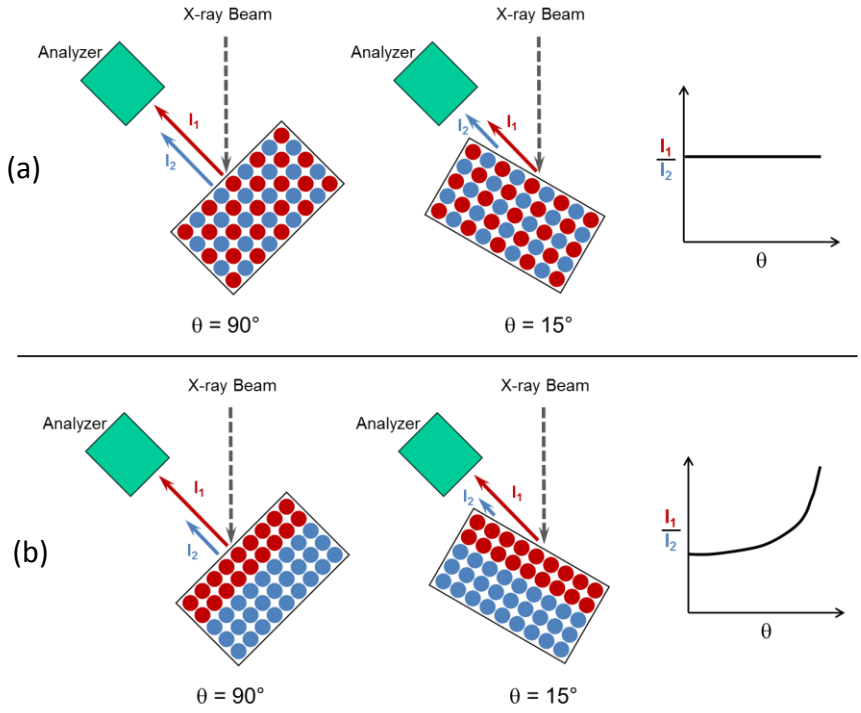

Figure 36. Influence of specimen morphology on angular dependence of XPS signal intensities. (a) In the case of homogenous atoms distribution within a sample, the ratio of the intensities of both species is constant at any angle. (b) When considering the layered structure, in which the red atoms form an overlayer on blue atoms being substrate, the intensity ratio between those two species will increase in an exponential fashion with sample tilt [219].

AR-XPS is used to deconvolute from the obtained spectra, at different take-off angles, the composition as a function of depth. A number of algorithms for performing deconvolution of "angle vs composition" to "depth vs composition" have been published [220-224], however, no unique transformation from angle-dependent intensities to depth-dependent concentration exists. The specific algorithms must be used depending on the measured material and other instrumental geometrical factors. XPS combined with argon ion sputtering allows to investigate chemical composition of the materials from the surface to hundreds of nanometers or more into the bulk. However, in some cases, depth profiling with ion sputtering of organic and certain inorganic materials can be problematic due to a chemical structure damage caused by the ion beam sputtering, especially when using high primary ion energies (see also SIMS section). Thus, many types of polymeric and biological materials, and inorganic oxides can be disrupted, usually reduced to lower oxidation states, by monoatomic ion bombardment, resulting in XPS spectra that do not reflect real bulk chemical composition [24, 225].

The gas cluster ion beam (GCIB) was introduced as a versatile tool for in-depth molecular characterization of organic and some inorganic systems [25, 226]. When a cluster ion hits a surface, the cluster breaks apart and each atom in the cluster retains only a fraction of the initial energy of the ion, thus resulting in a significant reduction in penetration depth of the ions, which causes surface localized damage and finally, it

preserves the chemical structure in the subsurface region. For a given cluster energy, the damages in, for example, polymeric materials decrease with increasing the cluster size owing to the reduction of energy per atoms [24]. In addition, argon gas cluster ion beam (Ar-GCIB) does not deposit surface carbon contamination compared with organic-one [227]. As a result argon gas cluster ion beam sputtering combined with XPS measurements allows to perform depth profiles maintaining chemical information from deeper region of the analyzed materials [228, 229].

Within the framework of this thesis XPS studies of surface composition and XPS angle-resolved and sputtering depth profiling were carried out on a PHI 5000 VersaProbeII (ULVAC-PHI, Chigasaki, Japan) system using microfocused (typically 100 µm, 25 W) Al K_α X-ray beam (1486,6 eV, ΔE = 0.3 eV). The surface composition studies were carried out at a photoelectron take-off angle of 45°. The photoelectron kinetic energies were analyzed in hemispherical capacitor analyzer operating in Fixed Analyzer Transmission (FAT) mode. A dual-beam charge neutralizer was used to compensate the charge-up effect. Survey spectra and high resolution spectra were collected with analyzer pass energy of 117.4 and 46.95 eV, respectively. All the XPS peaks were referred to the neutral (C-C) carbon C1s peak at binding energy of 284.8 eV. Spectral backgrounds were subtracted using the Shirley method [230].

AR-XPS spectra were acquired at photoelectron take-off angles of 15°, 30°, 45° and 75°. Eucentric tilt was employed to accurately align the analysis position at all angles. This is required if the analysis position is at some distance from the tilt axis. Ulvac-PHI MultiPak v9.5.1 software was used for structure analysis to estimate the present layers thicknesses using the algorithm described by Seah [231].

XPS sputter depth profiling was carried out with Ar-GCIB mounted on the spectrometer analytical chamber. Neutral argon clusters were generated by adiabatic expansion of compressed Ar gas through a narrow nozzle. Following ionization by electron bombardment, the cluster ion beam was focused, mass separated, accelerated to the desired energy (10, 15 or 20 kV) and scanned (in a range of 1 x 1 mm^2 to 4 x 4 mm^2) to irradiate polymer surface uniformly. The mean cluster size was adjusted in a range of 1000 ÷ 4000 atoms per cluster (typically 1000, 2500 or 4500). Ion beam current was attuned in a range of 1 ÷ 10 nA depending on the preferred sputter rate. In comparison with Ar_n^+ clusters ion beam, mono-atomic 2.5 kV gas Ar_1^+ gun was also used for depth profiling. In Figure 37 sputtering effects of Ar-GCIB on polystyrene and poly(methyl methacrylate) thin films compared with monoatomic ion gun are presented. Additionally, the 3D reconstruction of high resolution spectra of O1s region for Ar-GCIB and monoatomic Ar irradiation effects is shown in Figure 38.

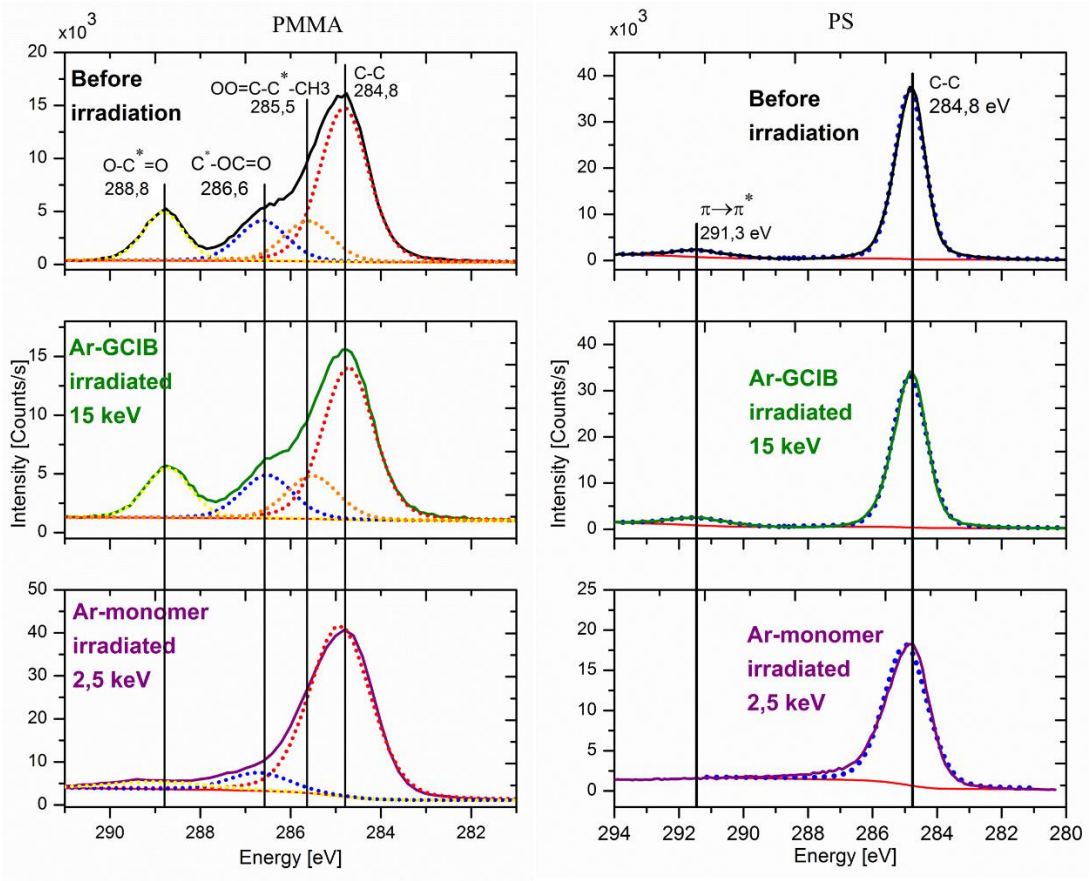

Figure 37. (left) High resolution C1s spectra of the as received and modified PMMA sample surfaces irradiated by Ar^+ monomer and Ar_{2500}^+ cluster ion beams. (right) High resolution C1s spectra of the untreated and modified PS sample surfaces irradiated by Ar^+ monomer and Ar_{2500}^+ cluster ion beams. Solid lines indicate experimental data and dotted lines are fits corresponding to the polymer structure.

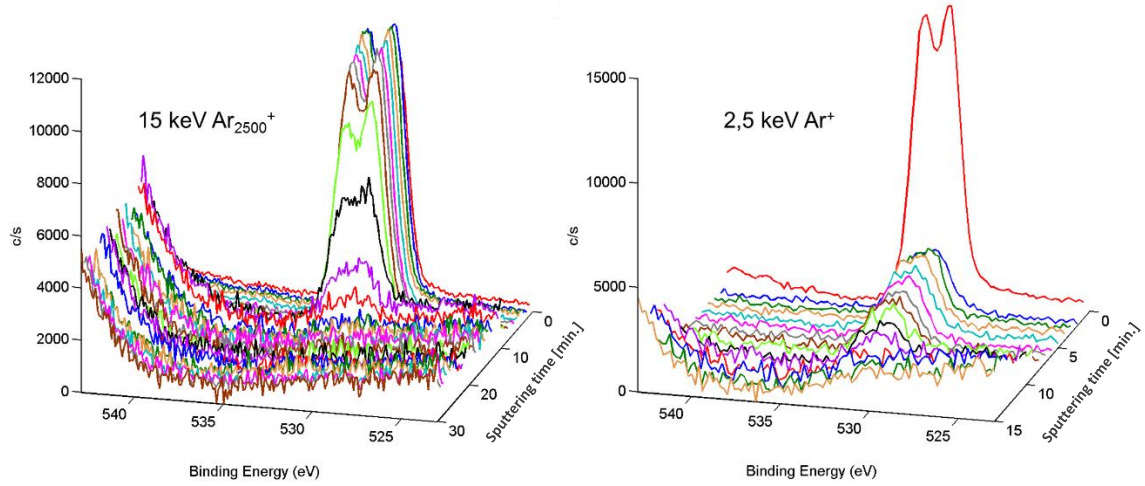

Figure 38. 3D data reconstructions of O1s spectra obtained during sputtering with (left) Ar-GCIB or (right) Ar-monomer ion beams the PMMA film. Presented spectra indicate that only with Ar-GCIB one can accurately identify chemical composition of the sputtered material within thin film.

3.3.2. Ultraviolet Photoelectron Spectroscopy

Ultraviolet photoelectron spectroscopy (UPS) is a technique which is based on the same phenomena as XPS but the important difference is that it uses ultraviolet photon source instead of soft X-rays to eject electrons. Because of much lower energy of the irradiation beam, this technique makes it possible to explore the electronic structure in the conduction and valance band region of a wide variety of materials [232]. The most commonly used resonance lines are He 1α at 21.2 eV [233] and He 2α at 40.1 eV [234]. Since the bandwidth of the conduction and valance bands is in the range 4 ÷ 10 eV of most solids, these photon energies are sufficient to probe the entire band structure region. The typical spectrum of pristine silver surface observed in UPS is shown in Figure 39.

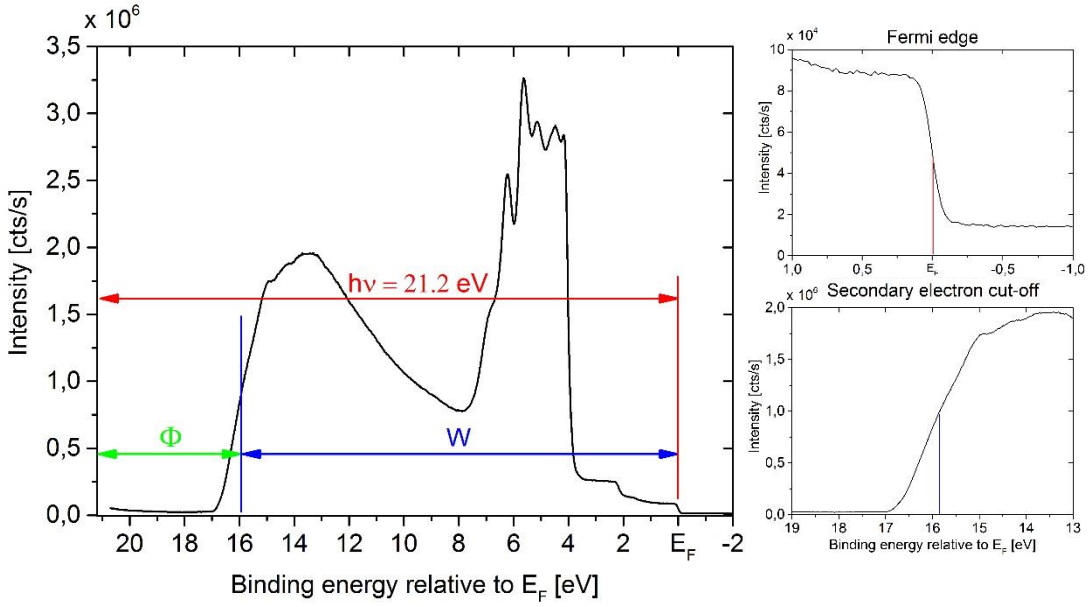

Figure 39. UPS He 1α spectra of ion etched silver foil. The insets show Fermi edge (E_F) and cut-off regions. Calculated work function is 5.2 eV.

The photo-emitted electrons have energies typically less than 17-18 eV using He 1α and consist of two groups [235].

The first group are photoelectrons excited within the first few atomic layers and which escaped into the vacuum suffering no inelastic collision. Generally, the energy and the direction of emission of such electrons may be related to their binding energy within solid and to wave vector associated with their original state. The measured binding energy of this group of electrons is simply related to the observed kinetic energy via the previously introduced equation 29 for XPS in section III.3.3.1 and can be associated with valance states and/or core levels.

Inelastically scattered electrons form the second group of electrons observed on the UPS spectrum. They have enough energy to escape into the vacuum and are detected as secondary electrons which form the background.

From the UPS experiments the information about distribution of electrons in the outermost valance or conduction band region can be obtained. These regions are responsible for the chemical, magnetic and optical properties of materials [236]. In simple terms UPS can be used to determine the work function of the metal (see Figure 39). By measuring the width W of the emitted electrons from the onset of the secondary electrons (cut-off edge) up to the Fermi edge and subtracting W from the energy of the incident UV photon energy hv, the work function Φ_m is then given by:

$$\Phi_m = hv - W \tag{37}$$

For UPS measurements we used helium ionization source with photon energy of 21.2 eV (He 1α) produced by cold cathode capillary discharge. The UV source was mounted on the same analytical chamber as previously described XPS system (section III.3.3.1) sharing the same photoelectron energy analyzer. The UPS spectra were taken at a photoelectron take-off angle of 90°. High resolution spectra were collected with analyzer pass energy of 2.95 eV. The instrument resolution was determined on the Fermi edge of gold at ambient temperature and was equal to 150 meV.

IV. Results and discussion

1. Substrate characterization

1.1. Metal electrode

The very first studies were carried out to determine properties of gold substrate as a support for almost all further experiments. As mentioned previously in the Section III.2.1.2, the thin layer of gold was deposited in vacuum onto silicon wafer by thermal evaporation of Au with the Cr sublayer for better adhesion.
In the first step the surface properties were examined by KPFM with the results shown in Figure 40. Although small features, characteristic for the method of layer fabrication, can be seen on topography map (a), the CPD map (b) in turn is homogenous and, with reference to the histogram (c), the avarage CPD is estimated at 53±11 mV. The CPD between gold-coated AFM tip and gold surface is expected to become zero, due to identical work function of materials (see Section III.3.1.2), but this is usually disturbed when measurements are taken under ambient atmosphere, not in the vacuum, as it was in this case. The humidity and the presence of a very thin layer of contamination either on the tip or on the sample may result in a change of measured CPD signal, which is pointed out in this case as 53±11 mV shift.

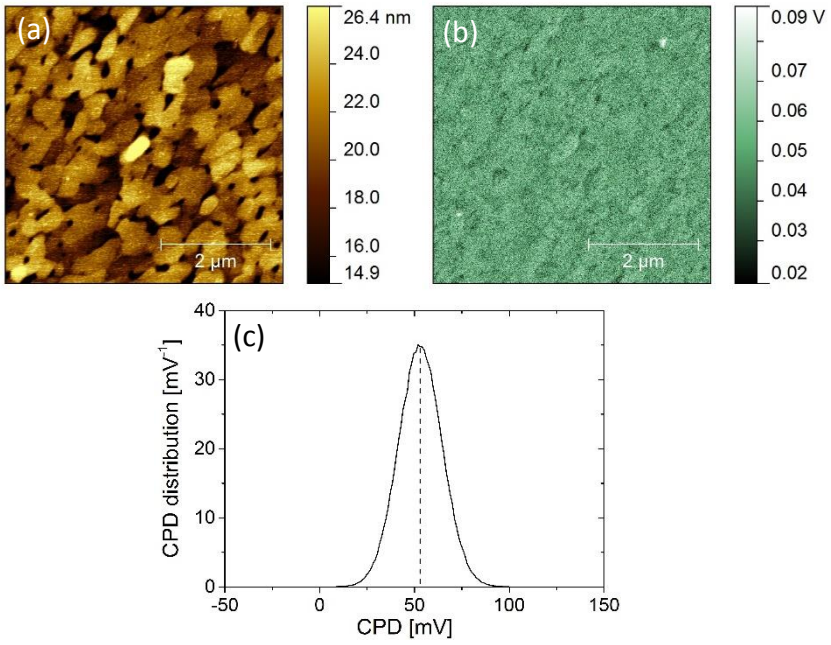

Figure 40. Thermally evaporated thin gold film (thickness of about 100 nm): (a) topography image, (b) CPD map and (c) CPD map histogram. According to histogram the CPD between gold-coated AFM tip and gold surface can be estimated at 53±11 mV.

Additional information is extracted from XPS data. In Figure 41 the survey spectrum of the gold substrate is depicted. As only gold lines are found on the spectra one can conclude that substrate surface is clean, which is largely due to the fact that after evaporation the samples were transported to glove box and then conveyed to XPS analysis chamber in a specially designed transport vessel. The transport vessel ensures stable oxygen and humidity free atmosphere and is designed to introduce samples to the high vacuum XPS system without opening to ambient conditions.

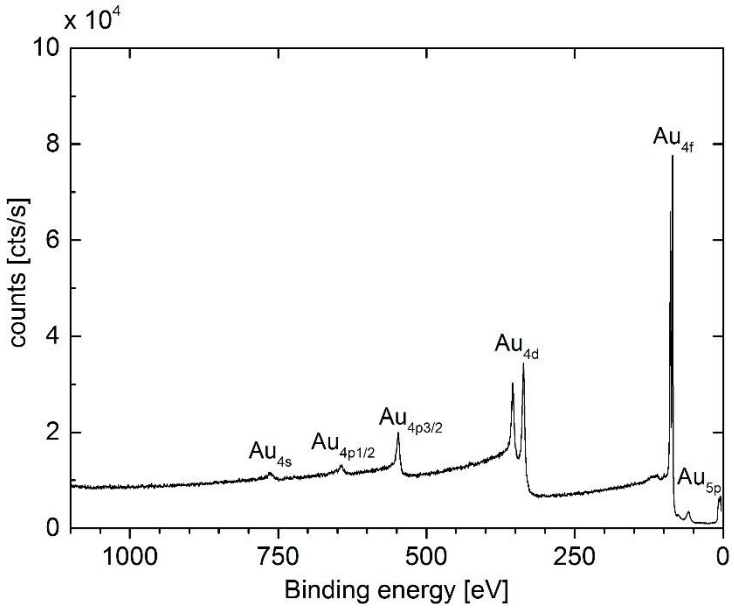

Figure 41. The survey spectrum of the gold substrate provides evidence for a pristine sample as only gold lines are found.

To fully determine the properties of obtained gold surface the electronic structure was determined by UPS measurements. From the UPS spectra shown in Figure 42 we defined, using previously mentioned method (Section III.3.3.2), the gold-coated substrate work function at 5.1±0.15 eV (where 0.15 eV is the resolution of the instrument). This value is in reasonably good agreement with literature value 5.2 eV [28] and is used later in this work as a reference in discussion of SAM influence on metal work function changes. The good agreement with the literature value also indicated that neither the inclusion of Cr nor the silicon substrate had a measureable effect on the work function of gold surface.

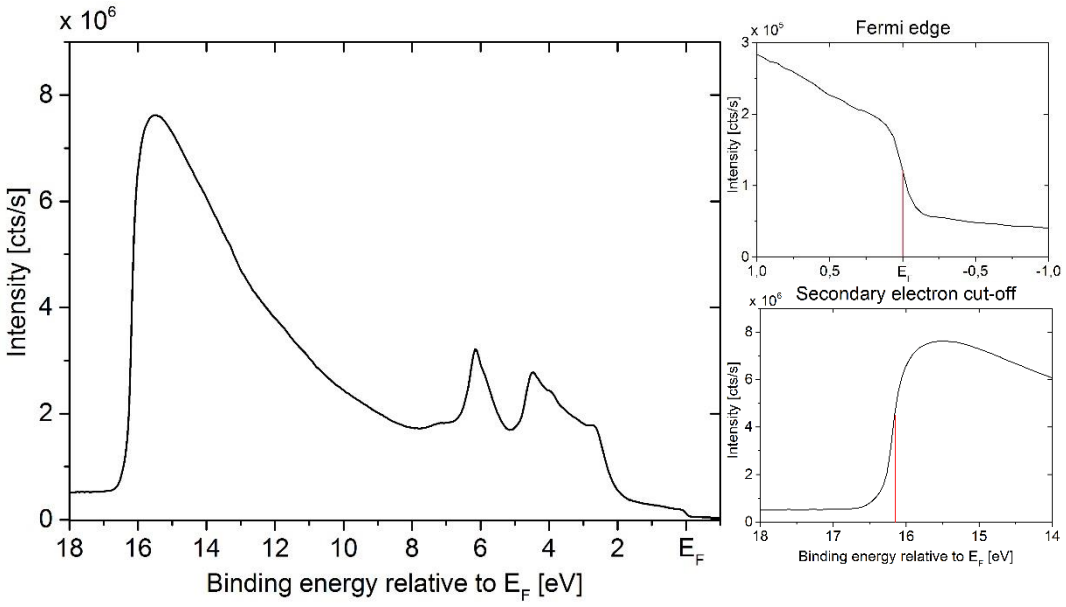

Figure 42. The UPS spectra of gold substrate with Fermi edge and secondary electrons cut-off regions close-ups. The calculated work function is estimated at 5.1±0.15 eV.

1.2. Self-assembled monolayers

1.2.1. Verification of SAM formation

To investigate formation of self-assembled monolayers on gold substrates, the homogenous samples of each type of SAM were prepared and analyzed using XPS, ARXPS and UPS methods.

The XPS high resolution scan in the C1s region of CH3-SAM modified gold surface shows characteristic component of aliphatic chain -C-C- at 284.8 eV. The presence of formed SAM is evidenced by high resolution spectrum of S2p region where only one sulfur component can be found which is coordinated in the S-Au bond. The respective binding energy of the $S2p_{3/2}$ is found at 162.0 eV. Elemental sulfur can be expected at 160.0 eV, thiolate H-terminated sulfur and oxidized sulfur at 163.0 eV and 167.0 eV, respectively [237, 238]. Since none of these species were found, the SAM formation at 162.0 eV can be confirmed as previously stated [239].

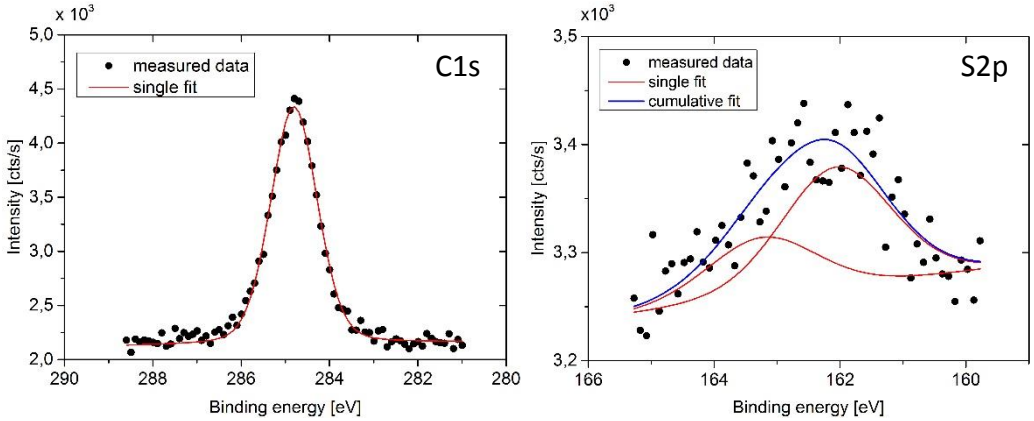

Figure 43. High resolution XPS spectra of C1s and S2p regions of CH3-SAM deposited on gold surface.

A very comparable situation is found for the COOH(L)-SAM monolayer deposited on gold. However, due to the fact that this type of SAM contains a carboxyl group –C(O)OH the C1s spectrum reflects additional peak (Figure 44 left side). The fitted lines indicate the presence of aliphatic chain -C-C- at 284.8 eV and carboxyl group at 288.7 eV [240]. The binding energy of $S2p_{3/2}$ at 162.0 eV is exactly the same as for previously described CH3-SAM monolayer and confirms S-Au bond formation. Rather broad and symmetric O1s signal can be decomposed into two contributions centered at binding energy of 532.5 eV and 533.7 eV for carbonyl C=O and hydroxyl –COH groups, respectively [241]. The area ratio of fitted peaks was about 1:1 of the hydroxyl group and the carbonyl group as expected. For the COOH(S)-SAM functionalized substrate the situation is different and presented on the right side of Figure 44 . The C1s spectra are similar to that obtained for COOH(L)-SAM, however, the second peak at higher binding energy is shifted towards lower value at 288.2 eV which can be due to the fact of existence of carboxylate COO^- group[242]. This is also evidenced at O1s spectrum which is asymmetric and reveals –C=O- rich composition of the studied monolayer. The above results can lead to the statement that the carboxyl group is partially deprotonated to the carboxylate state [242]. In the case of COOH(L)-SAM monolayer, the O1s spectrum can be fitted with two peaks with area the ratio of 1:1 and additionally, C1s spectrum reflects the presence of carboxyl group, thus the absence of deprotonation within monolayer can be stated. Due to the above results and COOH(S)-SAM monolayer instability, this type of SAM was not used in further research.

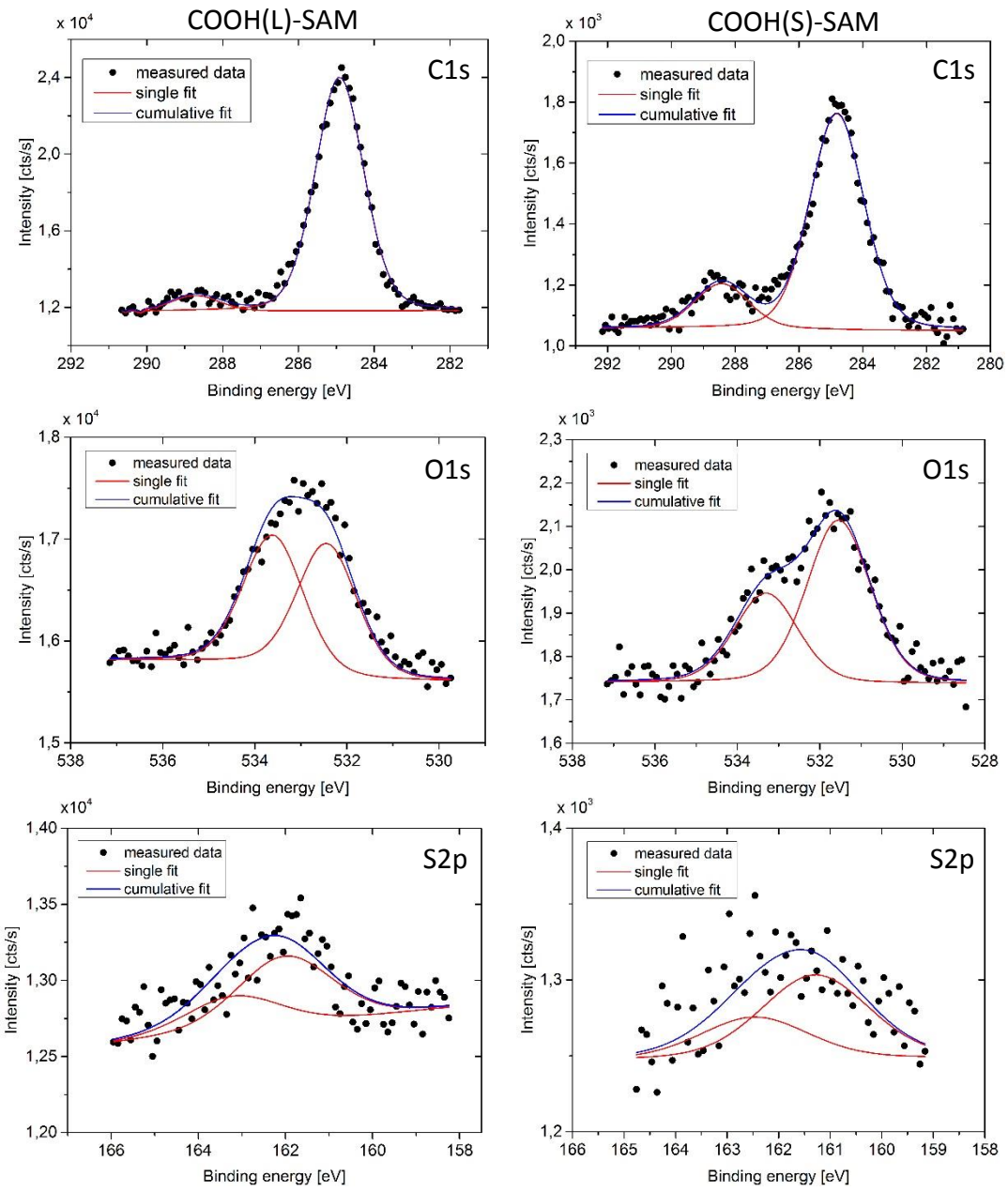

Figure 44. High resolution XPS spectra of (from the top) C1s, O1s and S2p regions of (left) COOH(L)-SAM and (right) COOH(S)-SAM deposited on gold surface.

The stoichiometry was calculated for both monolayers and is listed in Table 11. The results presented there indicate the formation of CH3-SAM and COOH(L)-SAM monolayers without chemical changes when taking into consideration that quantification method may have a margin of error of up to 10% for the weakest signal obtained for the sulfur region. For the COOH(S)-SAM monolayer the previously described instability led to the considerable difference between expected and measured compositions.

Table 11. Stoichiometry of CH3-SAM and COOH(L)-SAM monolayers on gold, calculated from the intensities in the high resolution XPS spectra. The experimentally determined sample composition stays in good agreement with molecular formula.

	Carbon	Sulfur	Oxygen
CH3-SAM (formula)	94.1 %	5.9 %	-
CH3-SAM (measured)	93.8 %	6.2 %	-
COOH(S)-SAM (formula)	66.7 %	11.1 %	22.2 %
COOH(S)-SAM (measured)	72.9 %	6.8 %	20.3 %
COOH(L)-SAM (formula)	84.2 %	5.3 %	10.5 %
COOH(L)-SAM (measured)	85.5 %	4.6 %	9.9 %

As stated in Section III.3.3.1, the ARXPS measurements can estimate the overlayer thickness due to the concentration changes along with the photoemission angle change. In this study, we applied this technique to determine the composition changes which allowed to calculate layer thickness of the CH3-SAM, COOH(L)-SAM and COOH(S)-SAM monolayers deposited on gold substrates. In Table 12 the surface elemental composition as a function of photoemission angle for above mentioned monolayers is presented. Additionally there is a reference sample which is represented by gold surface without functionalization (obtained at the same time as SAM functionalized samples) whose overlayer was constituted only by the airborne contamination layer.

Table 12. Comparison of the surface elemental composition at four different acquisition angles (15°, 30°, 45° and 75°) for each SAM-functionalized gold sample. The reference stands for non-functionalized gold surface.

Element	Reference	CH3-SAM	COOH(L)-SAM	COOH(S)-SAM	Acquisition angle
C1s	97.1	62.1	66.9	55.6	15°
O1s	-	-	11.1	13.1	
S2p	-	1.9	3.1	1.4	
Au4f	2.9	36.0	18.9	29.9	
C1s	48.1	69.8	73.6	61.3	30°
O1s	-	-	11.7	18.1	
S2p	-	1.9	3.1	1.4	
Au4f	51.9	28.3	11.6	19.2	
C1s	33.3	66.4	71.9	60.3	45°
O1s	-	-	9.8	15.1	
S2p	-	2.1	3.1	3.0	
Au4f	65.7	31.5	15.3	21.6	
C1s	22.7	53.3	65.0	52.4	75°
O1s	-	-	14.5	15.6	
S2p	-	7.9	3.7	5.2	
Au4f	77.3	38.8	16.8	26.8	

The layers thicknesses were determined with *MultiPak's Ultrathin Film Analysis* software (v9.5.0.8) using the algorithm described in Section III.3.3.1. The measured signals presented in Table 12 for studied SAMs allow to define different layers regarding head group (sulfur), backbone (aliphatic chain) and, in acid-terminated alkanethiols, endgroup (carboxyl group). The calculated layers' thicknesses are schematically

presented in Figure 45. These values are approximated and cannot be taken as real reflection of overlayer thickness due to the fact that the algorithm used assumes ideally flat layers which is not satisfied in the case of our samples as presented in AFM topography image of gold surface (Figure 40a). This leads to overestimation of these values, however, the tendency is maintained – the longer the SAM molecule the higher the thickness. Moreover, it was possible to distinguish the origin of oxygen and sulfur signals, which gives valuable information about self-organized SAM structure. The sulfur signal was detected mainly near gold surface in contrast with oxygen (in the case of acid-terminated SAMs) whose signal originates from the topmost layer.

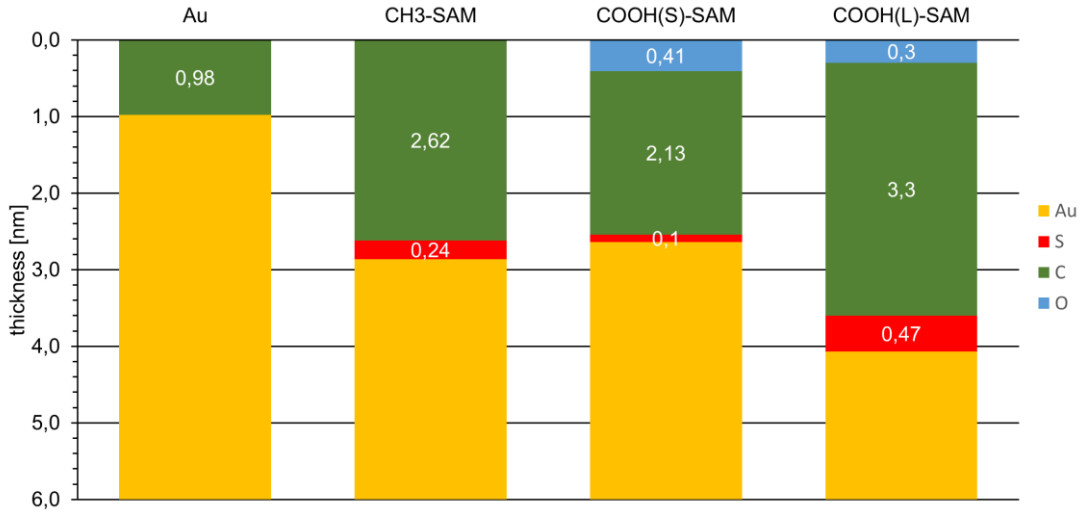

Figure 45. Schematic diagram of calculated layers thicknesses from ARXPS studies for reference gold sample (Au) and CH3-SAM, COOH(S)-SAM and COOH(L)-SAM monolayers deposited on gold surface. The calculated layer thicknesses are given on each layer in nm. The yellow color denotes gold substrate, red reflects sulfur, green and blue is attributed to aliphatic carbon chain and oxygen from carboxyl group, respectively. The overall thickness is equal to 2.86, 2.64 and 4.07 nm for CH3-SAM, COOH(S)-SAM and COOH(L)-SAM monolayers, respectively.

The UPS technique was also applied for homogeneously deposited monolayers. These measurements allow to investigate the work function changes due to the SAM deposition for both CH_3- and COOH- terminated molecules. The CH3-SAM and COOH(L)-SAM molecules carry a dipole moment of about -2.1 D and +2.5 D, respectively [36]. Thus, the covered metal surfaces should show opposite effects on the work function change. Indeed, from Figure 46 it is clear that both molecules alter the gold work function in a different way. The work functions of functionalized gold substrates were estimated at 5.4 eV and 4.9 eV for COOH(L)-SAM and CH3-SAM monolayers, respectively. This stands in good agreement with literature values found by applying Kelvin Probe method [36]. Comparing this values with the previously obtained work function of clean gold surface (5.1 eV) gives the shift of about +300 and -200 mV for COOH- and CH3- terminated molecules, respectively.

The above results indicate the formation of S-Au anchored, pristine monolayers of studied SAMs.

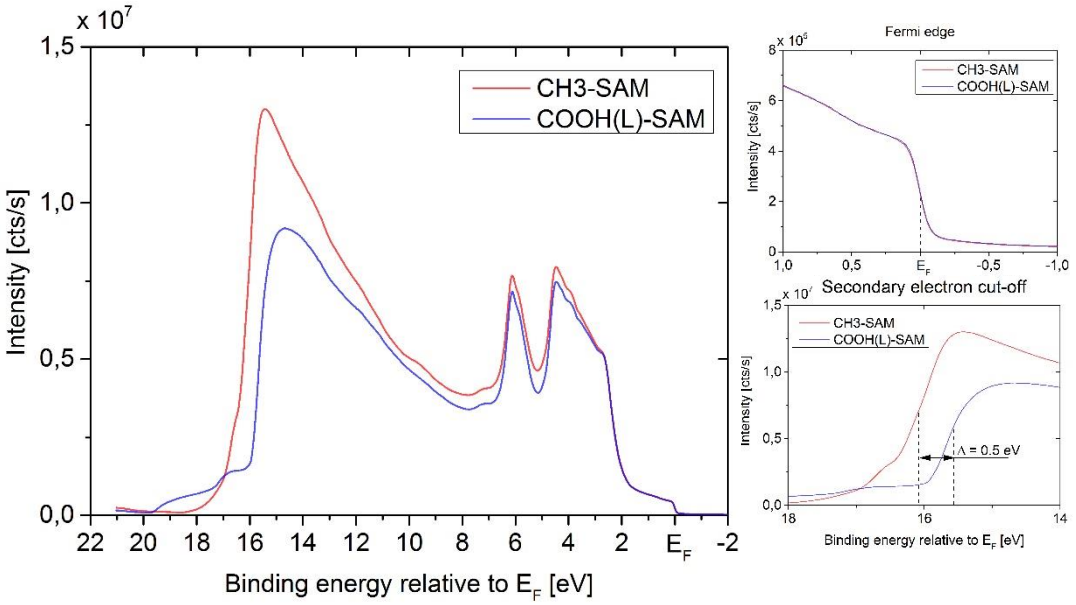

Figure 46. The UPS spectra of CH3-SAM (red line) and COOH(L)-SAM (blue line) monolayers deposited on gold surface. Fermi edge and secondary electrons cut-off regions are also presented on the right side. The total shift in work functions between deposited molecules is estimated at 0.5 eV.

1.2.2. Patterning SAMs using µCP – local surface potential changes

As revealed in the previous section, the deposited SAMs induce work function changes of the underlying substrate and can be used to tune this value. Here, changes in electronic properties of the gold substrate by application of µCP technique to locally deposit SAMs are described. As the dimensions of the structures lie in the micrometer scale it was not feasible to use spectroscopic methods either XPS or UPS due to the lateral resolution constrains of both methods. The proposed technique to detect micrometer or even nanometer inhomogeneities of the surface potentials was KPFM. Additionally, to reveal accompanying chemical differences between functionalized areas and to prove the origin of the measured CPD signals, sSIMS working in imaging mode was applied.

In the first step, the patterns consisting of one type of SAM were deposited on the gold substrates using the PDMS stamp with the “brick wall” structure. There were two different sample types prepared: one with COOH(L)-SAM and second with CH3-SAM both deposited on gold surface. These two molecules were chosen as they exhibit significant and opposite influence on the electronic properties on the functionalized surface. Indeed, from KPFM maps presented in Figure 47 it is clear that both molecules induce differently directed CPD in relation to unprinted surface.

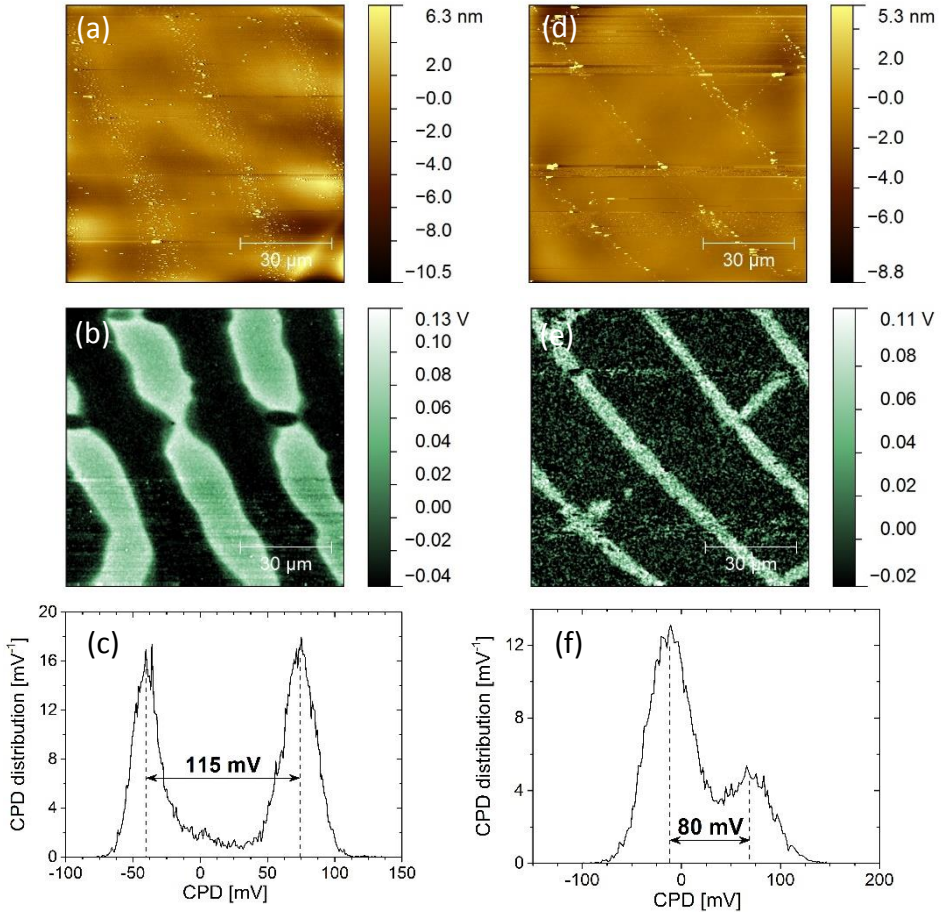

Figure 47. KPFM measurements of (left) COOH(L)-SAM and (right) CH3-SAM deposited on gold: (a,d) topography and (b,e) CPD maps. From the corresponding histograms (c,f) the influence of SAMs was determined in quantitative way and estimated at 115±16 mV and 80±33 mV for COOH(L)-SAM and CH3-SAM, respectively.

The COOH(L)-SAM deposited on gold surface induced lower CPD signals which was expected due to the dipole moment direction. The SAM functionalized regions can be recognized due to the asymmetrical stamp pattern, where at some locus there are crossbars which can be seen in Figure 47b as broader dark areas. Additionally, on the topography image (Figure 47a) the existence of small spots, possibly originating from PDMS mold material deposition, confirms the areas where the stamp adhered to the surface. The overall wider areas of COOH(L)-SAM compared to the stamp pattern might be due to the excess of remaining SAM solution on the stamp during patterning or for the reason that the stamp was pressed too hard to the surface. For the CH3-SAM monolayer deposited on gold substrate (Figure 47d, e) the situation looks similar to the previously presented acid-terminated SAM. However, due to the fact that this type of molecule carries opposite dipole moment to COOH(L)-SAM, the areas of CH3-SAM deposition show higher CPD signals than unprinted regions. The visible pattern has about same size as the PDMS mold structures, thus a well-made µCP functionalization can be stated.

The CPD difference between deposited and unprinted regions is estimated from histograms (Figure 47c, f) at 115±16 mV and 80±33 mV for COOH(L)-SAM and CH3-SAM

molecules, respectively. These values are underrated when compared with one obtained from UPS measurements (300 mV for COOH- terminated and 200 mV for CH_3-terminated molecules). That effect can be assigned to not perfectly ordered monolayer arising from the usage of µCP method and/or contamination of unprinted gold areas. Nevertheless, the direction of the work function changes induced by both monolayers is consistent with expectations and proves localized self-assembly of SAMs used.

In the second step, the proposed surface pattern can be seen as the evolution of the previously described method. In this stage, after localized deposition of COOH(L)-SAM molecules by µCP, the patterned substrate was immersed in the solution of CH3-SAM in ethanol whereas previously unprinted regions had been functionalized.

The sSIMS measurements in imaging mode were used to localize the COOH(L)-SAM regions deposited on the gold surface by collecting the O^- signals. This signal can be attributed to carboxylic terminal groups. Figure 48a illustrates SIMS O^- map measured for the patterned substrate showing the COOH-SAM inked relief structure of the PDMS stamp. Additionally, complementary image (Figure 48b) to that obtained for the COOH-SAM recognized presence of CH3-SAM molecules by mapping the $Au_2[M-H]^-$ secondary ions signal [243], where M denotes the complete hexadecanethiol molecule. The results indicate the localized formation of both monolayers with supposed spatial arrangement.

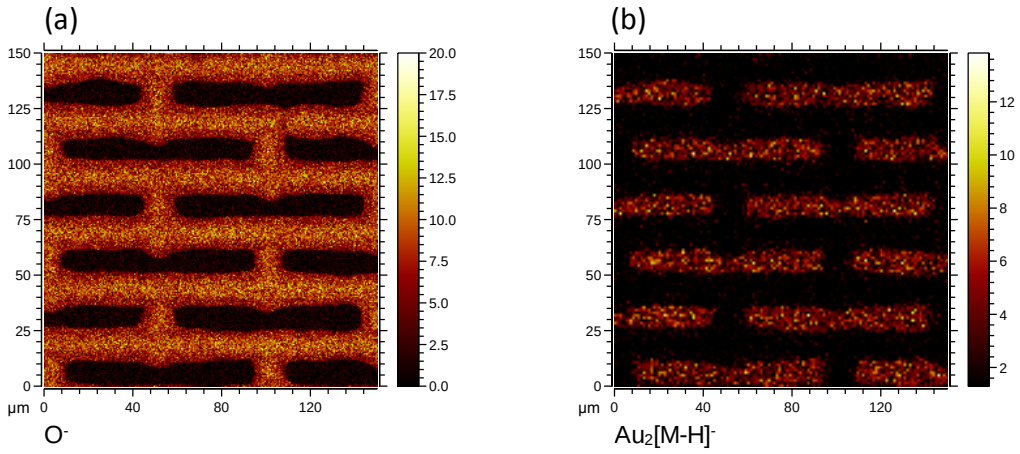

Figure 48. sSIMS intensity maps of negatively charged (a) oxygen ions O^- revealed the localization of COOH(L)-SAM on the surface, and (b) $Au_2[M-H]^-$ secondary cluster ions intensity map indicates regions of CH3-SAM deposition (where M denotes the molecular weight of the intact CH3-SAM molecule).

A similar image with the characteristic relief was also acquired by KPFM measurements (Figure 49b). The lower CPD signal corresponds to the higher O^- signal and can be attributed to the COOH(L)-SAM regions. The lower CPD signal indicates higher work function of the substrate, which is expected for the COOH(L)-SAM due to the direction of the net dipole moment of the layer. Regions with high CPD correspond to the CH3-SAM, which decreases the substrate work function. The difference in CPD between

these two regions, according to the histogram presented in Figure 49c, was estimated at 270±29 mV. In Figure 49a the topography map shows no visible stamp pattern (except spots from stamp material) which also proves deposition of both self-assembled monolayers.

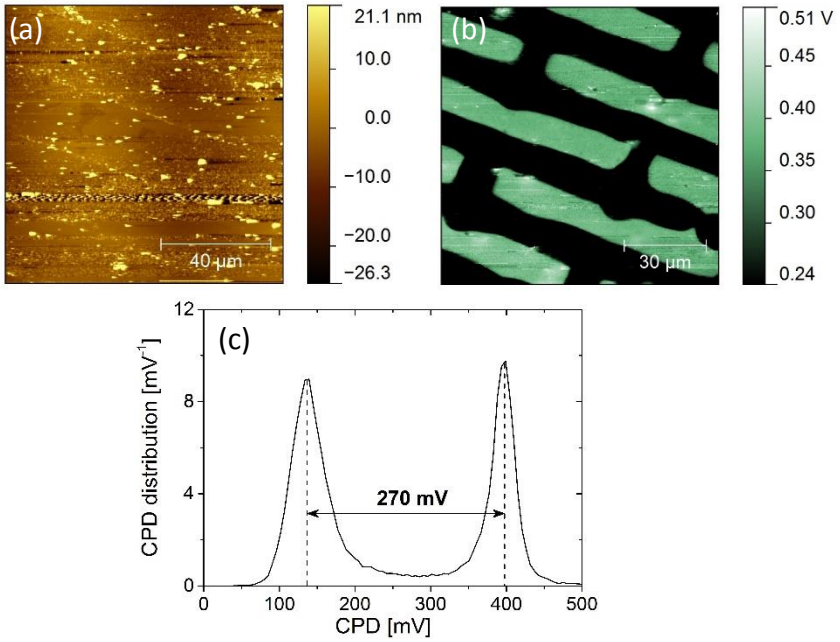

Figure 49. The gold surface micro-contact printed with COOH(L)-SAM and then CH3-SAM self-assembled from solution: (a) topographic image of the SAMs covered surface, (b) CPD map obtained using KPFM: dark regions correspond to the areas of COOH-SAM while bright regions localize the CH3-SAM presence – voltage difference of 270±29 mV as determined from (c) histogram.

2. Organic/metal model systems

2.1. PS

At the beginning of organic/metal interface studies the main focus was on thin polystyrene film which can be treated as a nonpolar model system due to its chemical structure and polarity described in details in Section III.3.1.1. As mentioned there, the polystyrene also shows great potential for use in future organic electronic devices as a dielectric material, due to its advantage of superior quantifiable characteristics in terms of water absorption and dielectric strength [127].

Within the framework of this thesis, polystyrene was treated as a non-interacting well-described and easily processable polymer. The first characteristics were carried out by studying CPD differences of 4 µm wide polystyrene stripes on gold fabricated by the MIMIC procedure (see Section III.2.2.4). Figure 50 presents the KPFM measurements of simultaneously acquired topography and CPD maps on the small section of a single PS stripe. The dark areas on the CPD image correspond to the polystyrene presence, thus contact potential difference can be estimated at about 60 mV. The gold work function

is about 5.1 eV and work function of polystyrene is equal to 5.38 eV [244]. The obtained results show lower difference (60 mV) than expected (280 mV) which may be due to the contamination of unprinted gold areas originating from PDMS stamp. The presence of unforeseen layer can result in an increase of gold work function but the direction of the CPD between PS and Au is maintained. This experiment illustrates that KPFM can be used to monitor contact potential differences of various materials including conducting (gold) and non-conducting ones (PS). Simultaneously obtained topography map helps to clearly determine the origin of CPD variations.

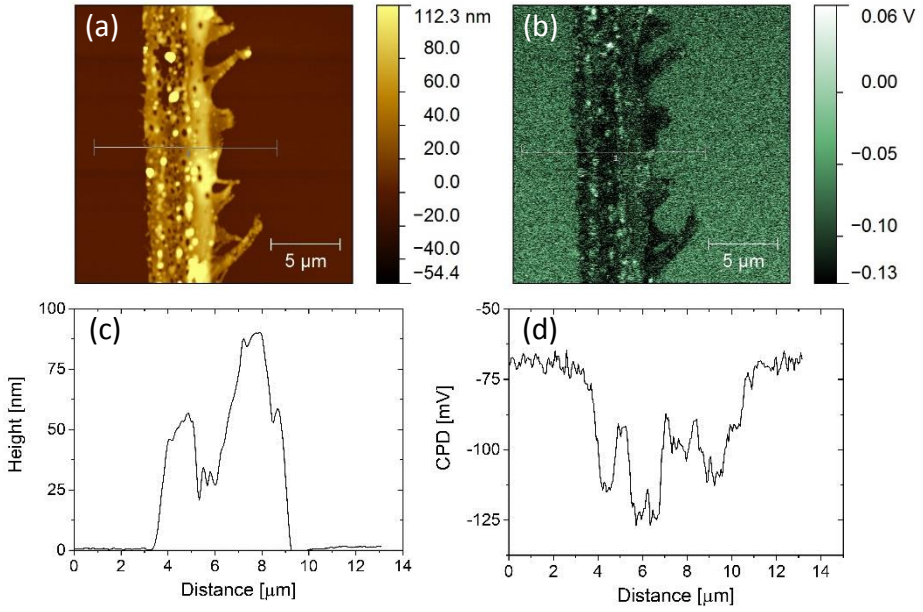

Figure 50. (a) Topography and (b) CPD maps of polystyrene stripe on gold fabricated by MIMIC. (c) The cross-section of topography signal shows the height of the stripe which can be estimated at 60 nm. (d) The cross-section of CPD map at the PS stripe shows a potential difference of about 60 mV.

To explore further polystyrene as an ideal non-polar model, a sample consisting of µCP COOH(L)-SAM pattern on gold with spin-cast polystyrene layer was examined (Figure 51). While the COOH(L)-SAM/Au substrate pattern is only roughly reproduced on the topography map (Figure 51a), it is clearly represented on the CPD image (Figure 51b). Higher CPD signal (80 mV as determined from the CPD histogram in Figure 51c) is observed in these image areas whose shape resembles concave regions of the PDMS stamp and therefore must correspond to the Au substrate left bare after µCP. In turn, dark areas of the CPD image (with the lower signal of −10 mV) reflect the COOH(L)-SAM monolayer at the interface between polymer and metal (cf. Figure 51b and a). Additionally, from topography maps, the height difference between printed and unprinted regions is about 1.5 nm which stays in a good agreement with expected 2 nm from COOH(L)-SAM molecule length. Performed experiments show that even after covering a patterned substrate with thin PS film the CPD signal can be attributed to the dipole moment of the SAM monolayer placed at the buried PS/gold interface. Dipole

induced by COOH(L)-SAM monolayer increases effectively the work function of gold and then lower CPD signal is measured. The difference in CPD signals from SAM printed and unprinted areas can be estimated from histogram (Figure 51c) at 90±20 mV. The measured signal for the uncovered COOH(L)-SAM pattern deposited on gold substrate was equal to 115±16 mV what stays in good agreement, within the error, with above results. This indicates that PS film has negligible impact on the measured signal which means there is no interaction between polymer and patterned substrate.

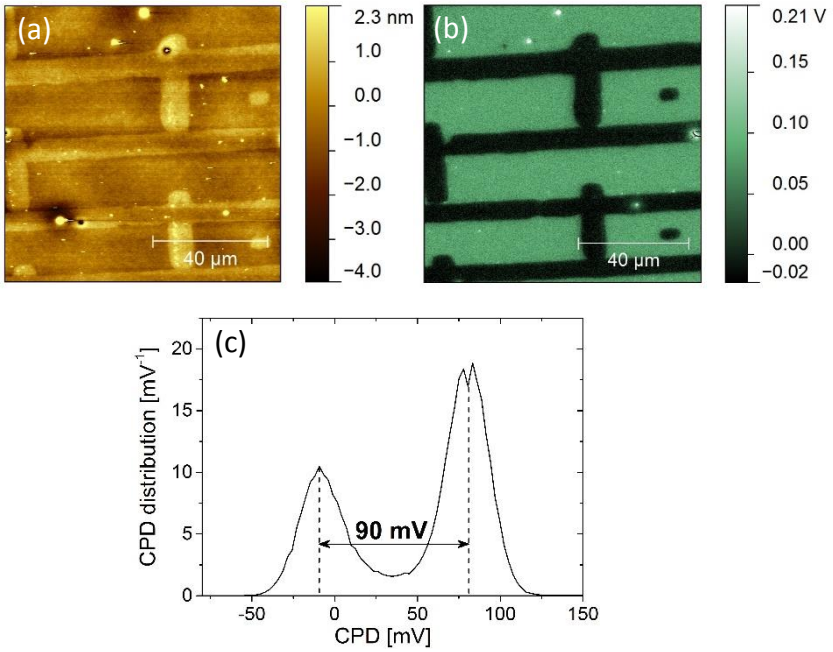

Figure 51. Thin polystyrene PS film (thickness 82 nm) spin-coated on a COOH-SAM/Au substrate pattern (COOH-SAM regions micro-contact printed onto Au): (a) topography image, (b) CPD image where lower signal/dark areas correspond to COOH-SAM regions (c) profile showing differences of 90±20 mV.

In the next step, the previous approach to µCP gold surfaces with self-assembled monolayers is extended. In this case, the initially unprinted areas are immersed in the opposite SAM solution. Schematic view of the COOH(L)-SAM patterned gold substrate immersed in CH3-SAM solution is presented in Figure 52.

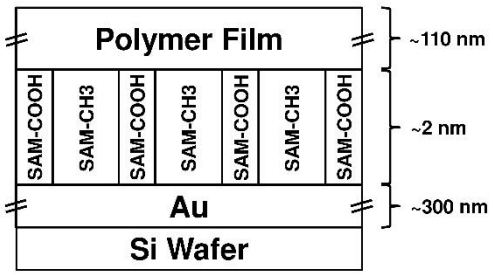

Figure 52. Schematic view of the sample structure.

First, the samples were examined by SIMS mapping performed simultaneously with depth profiling. For the thin film of PS, spin-cast on the gold substrate with COOH(L)-SAM stamp pattern complemented with CH3-SAM, maps collected at the interface show regions with higher intensities of O^- signal (Figure 53). These regions are attributed to the presence of COOH(L)-SAM monolayer placed at the interface. Additionally, a uniform map of S^- signal at the interface indicates the deposition of both self-assembled monolayers. The illustrated waviness of S^- signal which needs to be noticed originates from undulated polymer surface (this effect was described in Section III.3.2).

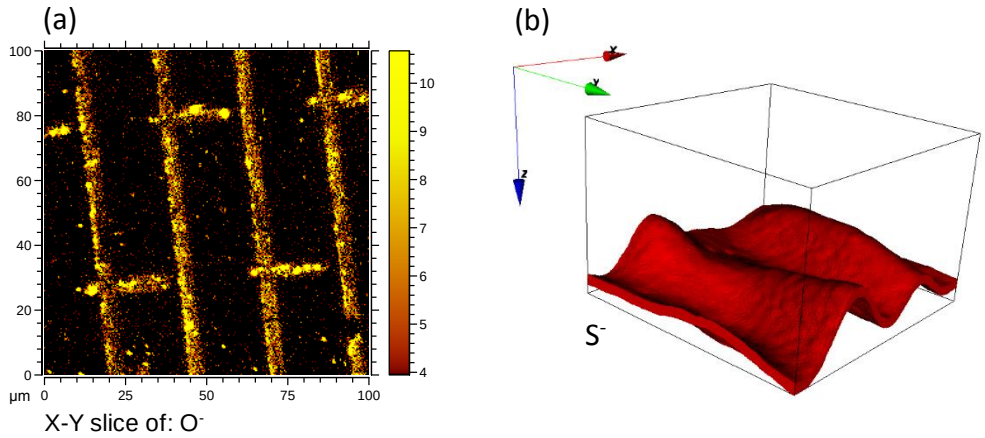

Figure 53. SIMS maps and depth profile of PS covered COOH stamp immersed in CH3 solution on gold. (a) The O- signal indicates the location of COOH pattern at the interface. (b) S^- signal intensity presented in 3D view indicates homogenous sulfur presence at the interface and also PS surface waviness.

Analogous SIMS depth profiling and mapping for a thin film of PS spin-coated on the CH3-SAM patterned gold substrate complemented with COOH(L)-SAM is presented in Figure 54. Maps collected at the interface show regions with visibly higher intensities of O^- signal (Figure 54a) which originates from COOH(L)-SAM presence. The image signal is not so clear, sharp and distinguishable as in the case of COOH(L)-SAM pattern which may be due to the different way of patterning resulting in different monolayer density and coverage. Nevertheless, the areas of decreased O^- signal are observable and arranged in a characteristic brick-like structure. Signal of S^- is expectedly uniform at the interface confirming both SAM layers deposition (Figure 54b). Similarly to the previously mentioned waviness effect, in this case the sample surface is also slightly undulated which is shown in the 3D view as variations of S^- signal map.

The above illustrated results indicate that SIMS measurements can provide information on lateral chemical composition within multilayer polymer/SAM/metal structures with high depth and lateral resolutions.

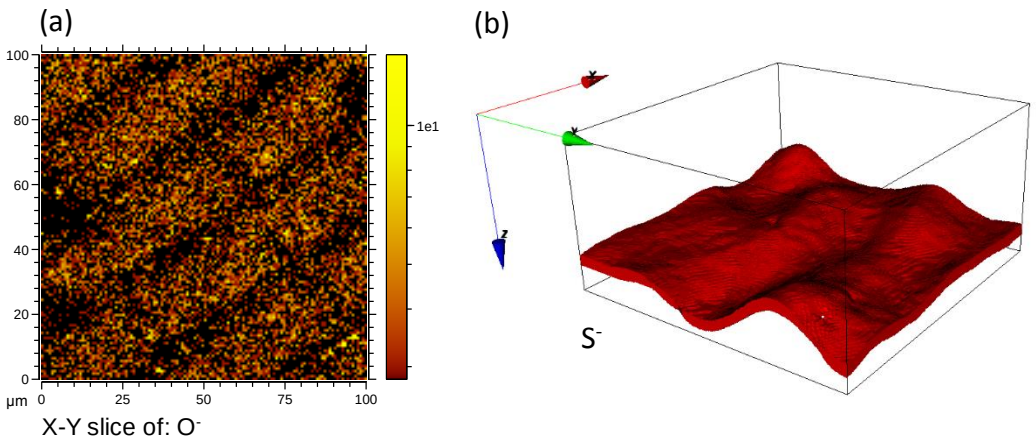

Figure 54. SIMS maps and 3D view of thin PS film covering localized CH_3-terminated SAM structures completed with COOH(L)-SAM molecules deposited on gold. (a) The O- signal indicates the location of COOH(L)-SAM pattern at the interface. (b) The 3D view of S^- signal indicates homogenous sulfur presence at the interface and additionally PS surface waviness.

Nearly flat surfaces, although locally defected and weakly undulated (with corresponding roughness of about 0.3 nm), are revealed by the topography images in Figure 55a and Figure 56a. They correspond to the PS films deposited on the COOH(L)-SAM/CH3-SAM and CH3-SAM/COOH(L)-SAM substrate patterns, respectively. Both patterns, resulting from the µCP of COOH(L)-SAM followed by CH3-SAM formation or from the same procedural sequence applied first to CH_3- and then COOH-terminated molecules, should result in flat substrates as both SAM monolayers have the same length. Therefore, the flat surfaces observed for spin-cast polystyrene films suggest their uniform thickness with no visible impact of the hydrophilic or hydrophobic SAMs on polymer film formation during the spin-coating. Such an SAM effect on the surface topography has been reported recently for PS blend films cast from the same solvent as used here [13].

Although none of the substrate patterns, COOH(L)-SAM/CH3-SAM or CH3-SAM/COOH(L)-SAM, are detected on topography images, CPD micrographs show them very clearly with high accuracy (see Figure 55b and Figure 56b, respectively). In addition, the CPD images show reversed contrast, with lower CPD intensities always detected for the regions where COOH(L)-SAM was locally placed at the polymer/metal interface. These regions are smaller (as the thiol-printed areas) and with average signal of −50 mV for the COOH(L)-SAM/CH3-SAM substrate as depicted by the histogram in Figure 55c. In turn, they are larger (as the areas filled by subsequent SAM formation) and with average signal of 30 mV (Figure 56c) for the CH3-SAM/COOH(L)-SAM substrate. The CPD signal difference was estimated from histograms at 200±35 mV and 125±25 mV, for the COOH(L)-SAM/CH3-SAM and the CH3-SAM/COOH(L)-SAM substrate patterns, respectively (Figure 55c and Figure 56c). In addition, comparison of the CPD images recorded for COOH(L)-SAM/Au (Figure 51b and c) and COOH(L)-SAM/CH3-SAM (Figure

55b and c) indicates contrast enhanced for the latter with signal difference increased from 90±20 mV to 200±35 mV.

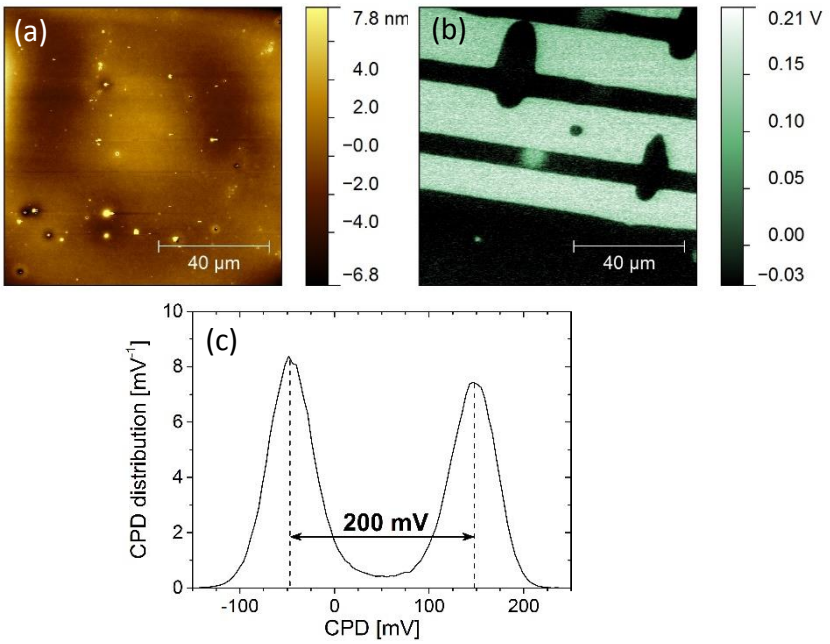

Figure 55. Thin polystyrene PS film (thickness 87 nm) spin-coated on the COOH(L)-SAM/CH3-SAM pattern on Au substrate (resulting from micro-contact printing of COOH(L)-SAM followed by CH3-SAM formation): (a) surface topography, (b) CPD image where lower signal/dark areas correspond to COOH-SAM regions, and (c) CPD histogram showing the differences between dark and bright areas of 200±35 mV. Note enhanced contrast in (b) as compared to Figure 51b

.

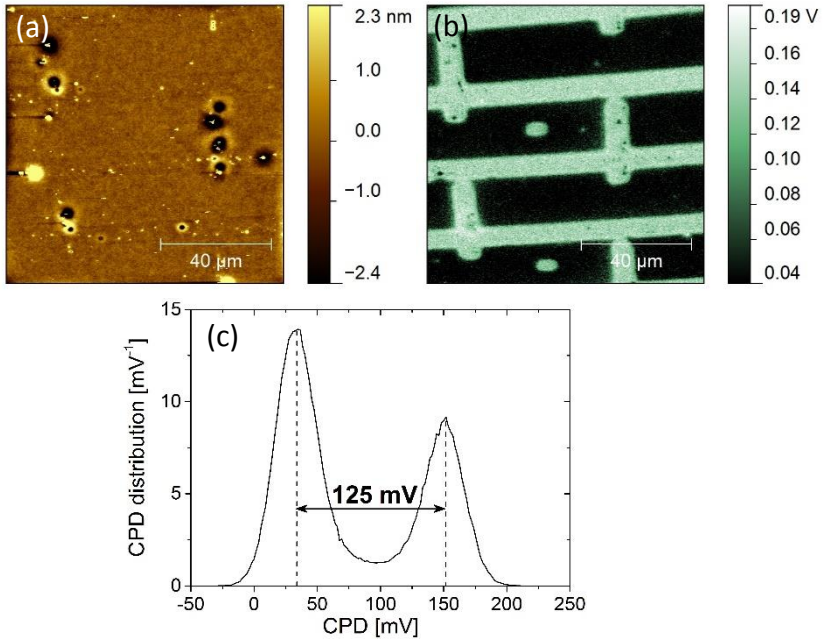

Figure 56. Thin polystyrene PS film (thickness 92 nm) spin-coated on a CH3-SAM/COOH(L)-SAM pattern on Au substrate (resulting from micro-contact printing of CH3-SAM followed by COOH(L)-SAM formation): (a) surface topography, (b) CPD image where lower signal/dark area values correspond to COOH(L)-SAM regions, and (c) CPD histogram showing the differences between dark and bright areas of 125±25 mV. Note reversed contrast in (b) as compared to Figure 55b.

The results presented here indicate that the measured CPD signal does not depend on polymer surface topography and can be attributed to the dipole moment of the SAM monolayer placed at the buried polymer/metal interface. Dipole induced by CH3-SAM decreases effectively the work function of the gold substrate and then higher CPD signal should be measured (cf. Figure 55b and Figure 56b). For the COOH(L)-SAM monolayer, opposite dipole orientation induces higher effective work function of the substrate and lower CPD signal. Indeed, the CPD signal on COOH-SAM regions is ca. 80 mV lower than that on Au areas (Figure 51b and c). In turn for the substrate patterns consisting of COOH(L)-SAM and CH3-SAM, it is observed that the CPD signal difference between the CH3-SAM and COOH(L)-SAM regions depends on the mechanisms (due to fast μCP or slower adsorption from solution) and the sequence of SAM depositions, altering it from 200±35 mV (for COOH(L)-SAM/CH3-SAM) to 125±25 mV (for CH3-SAM/COOH(L)-SAM). Specifically, different SAM formation mechanisms might lead to monolayers with different surface densities and varied overall order of molecular arrangement. Surface density and numbers of defects would change the average dipole moment of the SAM monolayer. For higher density lower net dipole moment is expected [36, 135].

Absolute values of CPD signal averaged for the studied substrates should be treated with care and cannot be used for precise determination of their work function. There are two reasons for this. First, the work function of the tip as a reference electrode may vary in wide range. In the case of gold, work function may change from 5.4 to 4.5 eV for clean and contaminated surface, respectively [28]. Second, non-conducting polystyrene film does not stay in electronic equilibrium with the substrate and a shift of energy levels can be induced by charging. However, within the time-scale of one map acquisition, the shifts of CPD signal due to the charging effects are negligible, as concluded on the inspection of the KPFM maps presented above. Also changing the atmosphere from humid (ambient air) to dry (argon) did not have any significant influence on the measured signal. In contrast, the CPD maps recorded in separate measurements for the same sample area show visible signal shifts.

Another point of investigation was considering the influence of the solvent used and the shape of the applied stamp structure on the measured CPD signal. To study this effect, polystyrene films were cast from varying solvents onto COOH(L)-SAM patterned gold substrate (with different stamp structures) complemented with CH3-SAM monolayer. The results are presented collectively in Figure 57.

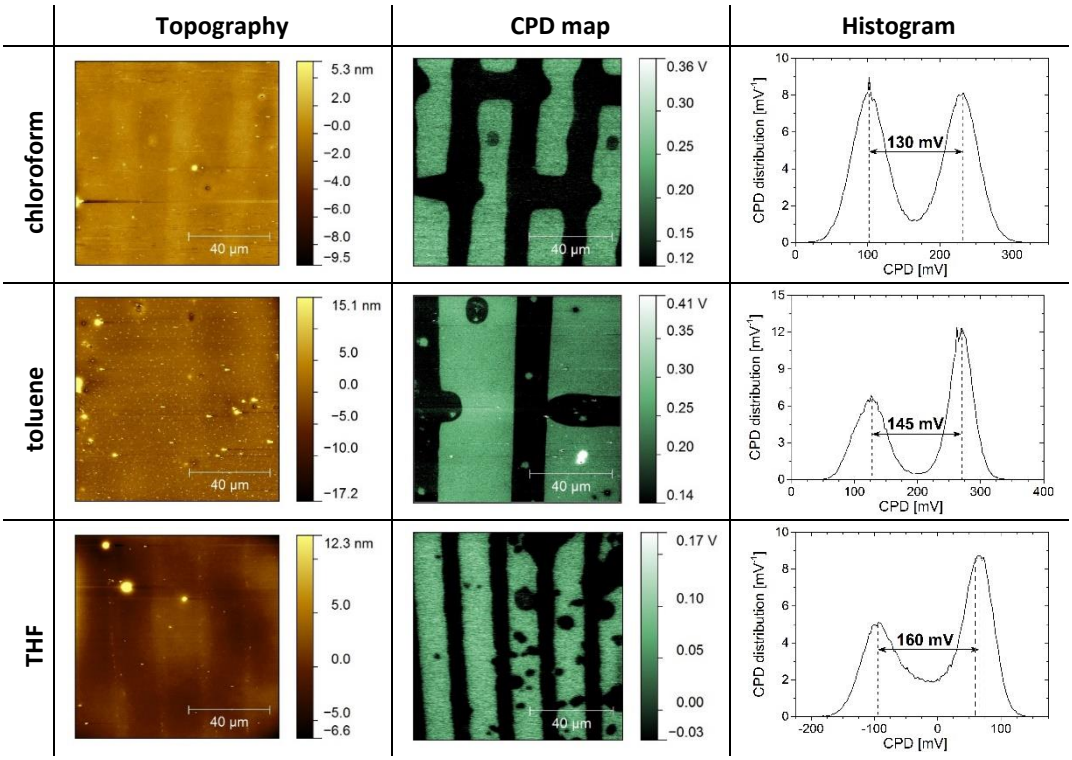

Figure 57. Influence of solvent used and stamp structure applied on the measured CPD signal in KPFM. (top line) Topography map, CPD map and histogram of polystyrene film cast from chloroform solution onto brick-wall patterned COOH(L)-SAM structures (with 25 µm period) complemented with CH3-SAM. (middle line) Topography map, CPD map and histogram of polystyrene casted from toluene solution onto similarly to the previously described brick-wall patterned substrate but with 50 µm period. (bottom line) Topography map, CPD map and histogram of polystyrene film cast from tetrahydrofuran (THF) solution onto 6 µm x 12 µm aperiodic stripes (whereas 6 µm wide stripes localize COOH(L)-SAM). The CPD signal differences between COOH(L)-SAM and CH3-SAM areas are estimated from histograms at 130±35, 145±32 and 160±34 mV for chloroform, toluene and THF polystyrene's solvents, respectively.

For all the investigated films, CPD maps clearly distinguish COOH(L)-SAM and CH3-SAM areas while topography images are almost flat with weakly visible stamp patterns. In all CPD maps the COOH(L)-SAM regions have lower values of CPD while higher values correspond to CH3-SAM which indicates that neither the solvents used nor the stamp structure sizes influence the expected directions of the SAMs induced dipole moments. The CPD signal differences between COOH(L)-SAM and CH3-SAM areas are estimated from histograms at 130±35, 145±32 and 160±34 mV for chloroform, toluene and THF solvent, respectively. These values are close to the previously determined CPD differences for polystyrene cast onto both COOH(L)-SAM (200±35 mV) and CH3-SAM (125±25 mV) patterned substrates complemented with corresponding SAMs. The differences between the measured signals may be mainly due to the mechanisms and the sequence of SAM depositions which were previously described. It might be then concluded that polymer solvents have none or negligible influence on measured CPD signals.

2.2. P2VP

The poly(2-vinylpyridine) polymer was chosen as an evolution of polystyrene one due to the possibly more interacting character as indicated by Hansen Solubility Parameters which are 19.3, 8.2 and 0.0 $MPa^{0.5}$ for dispersion, polar and hydrogen bonding contributions, respectively. To study the interactions the thin film of P2VP was spin-cast on the COOH(L)-SAM brick wall-like patterned substrate complemented with CH3-SAM monolayer in unprinted regions.

SIMS depth profiling in imaging mode confirms the presence of stamp-localized COOH(L)-SAM regions by mapping O^- signal at the interface as depicted in Figure 58a. The mapped S^- secondary ion signal indicate both monolayers deposition due to its homogenous distribution at the interface (Figure 58b).

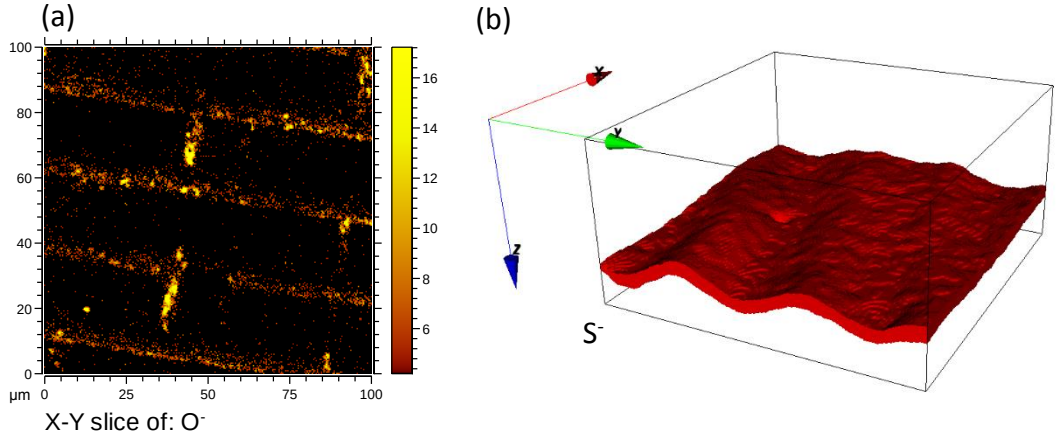

Figure 58. SIMS map and 3D view of P2VP spin-cast on the COOH(L)-SAM stamp localized monolayer followed by immersion in CH3-SAM solution. (a) The O^- signal indicates the location of COOH(L)-SAM pattern at the interface. (b) S^- signal presented in 3D view indicates homogenous sulfur presence at the interface which confirms both SAMs deposition.

The KPFM measurement results are presented in Figure 59. First, it should be noted that the resulting film surface, as inspected on the raw topography map in Figure 59a, has significant waviness reaching at same points almost 60 nm height. The CPD map (Figure 59b) shows broad dark areas of characteristic stamp structures (as concluded from the presence of the crossbars) and small but clearly distinguishable two different bright regions, showing higher CPD values, whereas darker one will be named here as a "dim" one. However, the area of characteristic brick wall structure of O^- signal is not as narrow as indicated by the SIMS measurements presented in Figure 58a, but this could be explained by the different analysis positions of KPFM and SIMS measurements and local character of the fabricated structure. The effect of the much wider COOH(L)-SAM deposition areas, when compered with CH3-SAM regions, can be explained by the excess of the locally remaining SAM solution on the PDMS stamp and/or by the too large force applied during µCP. The CPD differences between the dark areas and two different bright regions were extracted using histogram in Figure 59c. The estimated

CPD differences between these areas were equal to 30±20 mV for the dim areas related to dark regions and 91±24 mV for the brightest regions referred to dark zones.

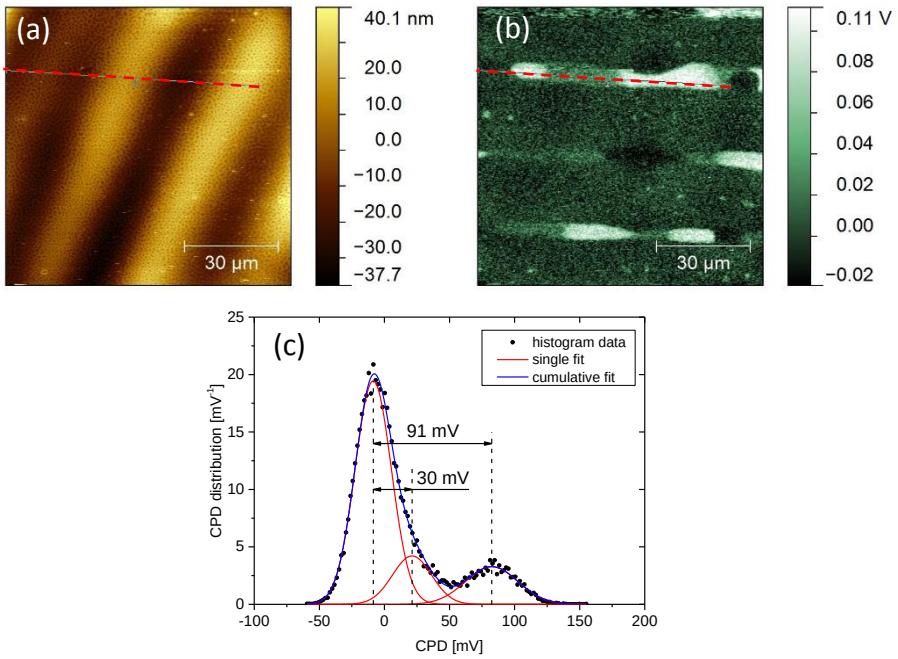

Figure 59. Thin P2VP film spin-coated on a COOH(L)-SAM/CH3-SAM pattern on Au substrate: (a) surface topography, (b) CPD image where lower signal/dark area values correspond to COOH(L)-SAM regions, and (c) CPD histogram with fitted Gauss functions for the estimation of CPD differences between three different areas: dim and dark areas with CPD difference of 30±20 mV and bright and dark areas with difference of 91±24 mV.

The appearance of two distinct bright areas distinguishes this system from PS one, but it should be noted that the direction of the CPD changes, driven by the deposition of SAMs at the interface, are in accordance with that found for uncovered SAM-printed gold surface and PS covered system with identically modified with SAMs gold interface. However, for the P2VP system a few additionally observed effects need to be addressed. The cross-sections from the corresponding areas on topography and CPD map were taken (see red line in Figure 59a, b) and are presented in Figure 60. First it can be concluded that the effect of two different bright areas could not be described as surface waviness driven as both profiles do not exhibit the interdependencies. Moreover, after filtering out the topography image from waviness (as shown on topography image placed above presented profiles in Figure 60) it turns out that the film morphology consist of two different spatial structures which are marked with red rectangles (Figure 60a and b). The first type (a) forms a hole-like structures with dimensions of about 0.5 µm and 10 nm deep whereas the second type (b) is characterized by bicontinuous morphology with length reaching 2 µm, width of about 0.5 µm and depth of 10 nm. The ratios of high topography areas to lower ones were determined using Minkowski measures [245] and were equal to 1.4 and 1.0 for hole-like and bicontinuous structures, respectively. However, from the inspection of the topography map together with corresponding CPD map (shown above topography map

in Figure 60), taking into account the locations of different P2VP surface morphologies, it can be noted that variations of CPD signals for bright areas are not connected with the differences of surface structures. According to carried experiments, within the framework of this thesis, the effect of two distinct bright regions on CPD map cannot be straightly explained and thus, additional studies should be undertaken.

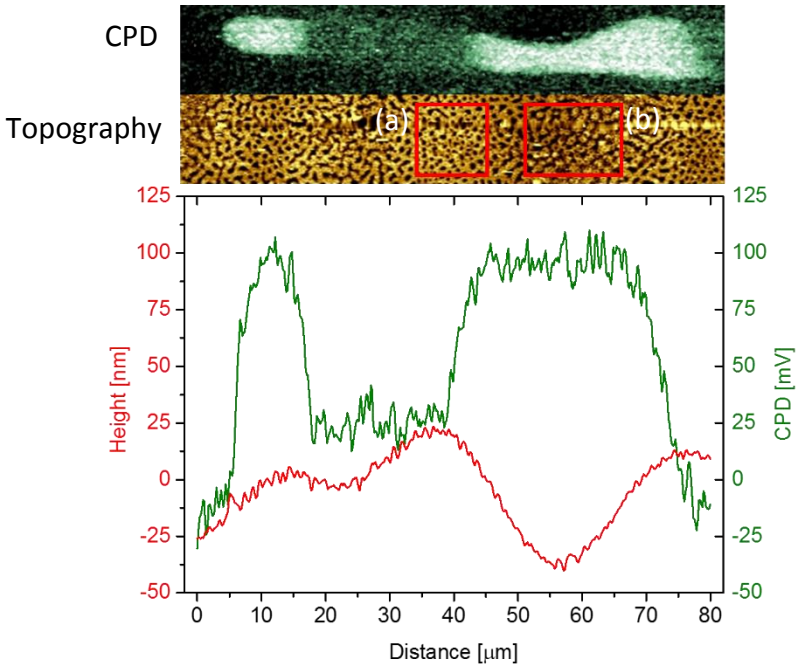

Figure 60. The cross sections from (red line) topography and (green line) CPD maps presented in Figure 59a and b. The insets show extracted topography images (after filtering out surface waviness) form the corresponding CPD areas where (a) refer to dim regions and (b) to bright regions of CPD. Field of view of the insets is 9 x 9 μm².

2.3. PAA

The system studied next was a thin film of PAA spin-cast onto COOH(L)-SAM stamp patterned substrate followed by the immersion in CH3-SAM solution. This polymer was proposed due to its high values of Hansen solubility parameters, especially in terms of polar and hydrogen bonding contributions (18.0 $MPa^{0.5}$ and 20.35 $MPa^{0.5}$, respectively), which might suggest the possibility of interaction with the polar SAM groups.

First, the system was studied by SIMS depth profiling measurements running in imaging mode to reveal the spatial and chemical composition at the interface. In Figure 61a the O^- secondary ion signal collected at the interface revealed the location of COOH(L)-SAM. The signal is weak which can be explained by the oxygen ions interference originating from PAA film (high yield) and COOH- terminated SAM. Additionally, the O^- signal at the interface is also disturbed by the initial surface undulation which is transformed as small islands of high signal at the interface. However, a homogenously distributed S^- signal, as presented in Figure 61b, provides evidence of both SAMs deposition.

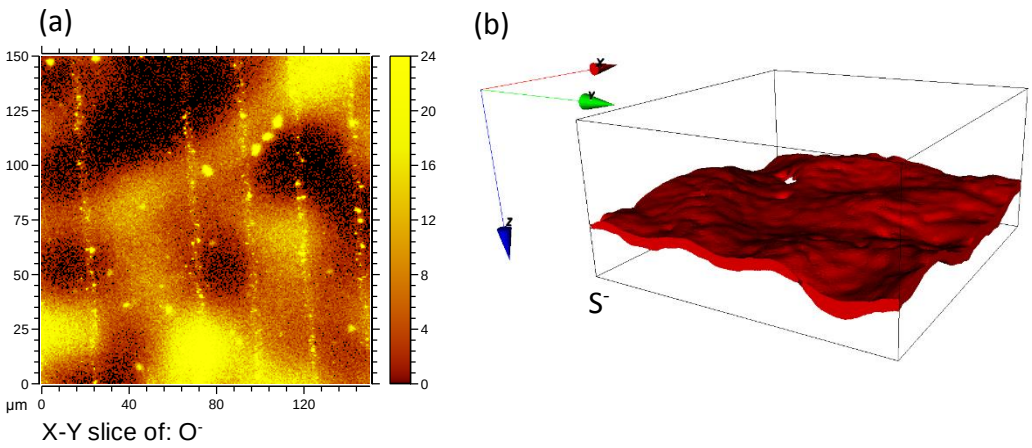

Figure 61. dSIMS results of PAA spin-cast on the COOH(L)-SAM patterned substrate followed by immersion in CH3-SAM solution. (a) The O^- signal indicates the location of COOH(L)-SAM pattern at the interface and indicate initial undulated film surface. (b) 3D view of S^- signal indicates homogenous sulfur presence at the interface which provide evidence of both monolayers deposition.

The KPFM results presented in Figure 62 reveals different behavior of PAA film in contact with SAM patterned substrate, when compared with the previously studied polymers. On the topography map in Figure 62a one can notice weak but visible stamp structure shapes due to the remaining contamination, probably from the PDMS mold, but these structures or even any other shapes expected from the different SAM presence at interface are absent on the CPD map (Figure 62b). The CPD map is almost uniform, with a small, high-CPD spot possibly originating from the charging effect, and with average narrowly distributed CPD value estimated at -105±8 mV, using the histogram depicted in Figure 62c.

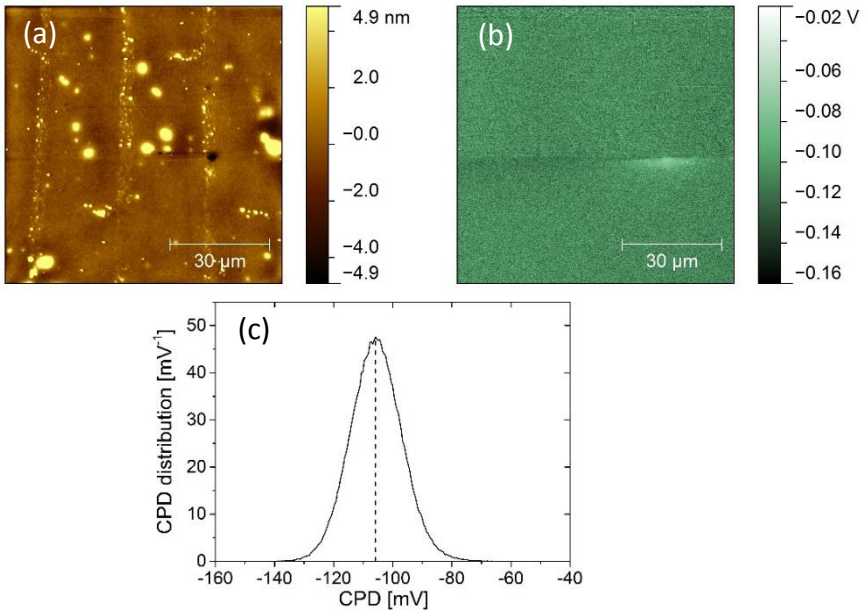

Figure 62. Thin film of PAA prepared by spin-casting on a COOH(L)-SAM/CH3-SAM pattern on Au substrate: (a) surface topography, (b) CPD image showing homogenous signal and (c) the corresponding histogram with CPD estimated at -105±8 mV.

Since the PAA can be discussed as a non-conductive polymer, the observed effect can be explained by considering hydrogen bonding formation which may occur between carboxyl group of the COOH(L)-SAM molecule and carboxyl group from PAA monomers, schematically shown in Figure 63. This approach is also supported by the high values of polar and hydrogen bonding contributions of Hansen Solubility Parameters for PAA which may suggest formation of this type of interaction. The hydrogen bond may be formed between positively charged hydrogen atom and a lone pair on the negatively charged oxygen atom.

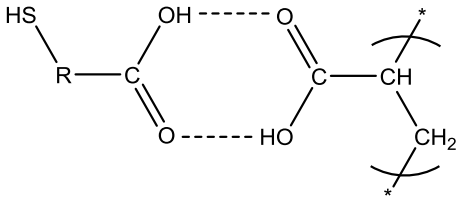

Figure 63. The formation of hydrogen bonding interactions (dashed lines) between carboxylic groups of (left) COOH(L)-SAM and (right) PAA monomers.

The presented interaction is well-known for carboxylic acids which results e.g. in their higher boiling points when compared with the alkanes of similar sizes. According to the literature, the type of centro-symmetrical bonding formation presented in Figure 63, is the most energetically preferable [246]. The polar groups of PAA film during spin-casting from solution may have the ability to adopt various chain conformation at the interface with the substrate, regarding its functional character (polar or non-polar) as it was found for other polar group containing polymers [247, 248]. As the solvent evaporates the polymer configuration and orientation is frozen into this structure [249]. On the other hand, the net dipole moment of the SAMs deposited on the gold surface can be divided into two main components as presented schematically in Figure 64.

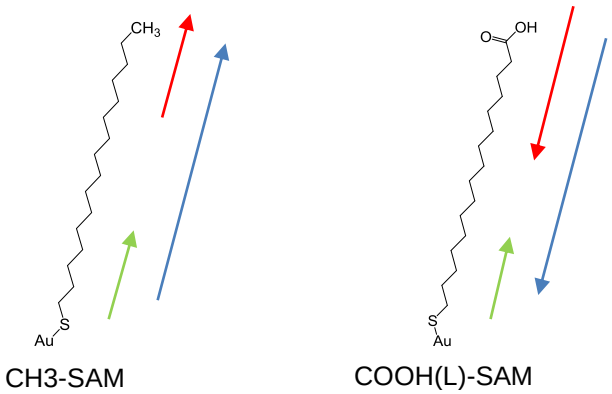

Figure 64. Schematic illustration showing the dipole moment orientations (arrows) of the SAMs originating from backbone (green) and tail (red) groups as well as the resultant net dipole moments (blue) of both molecules.

The first one is attributed to the backbone, which is the same for both molecular layers and is directed away from the gold surface. The second dipole is related to the tail group and it is oriented in the same or in the opposite direction for the CH_3- or the COOH-group, respectively. The molecule net dipole moment is then a resultant dipole moment of both contributions. Due to the symmetrical geometry of both interacting carboxyl groups (Figure 63) the resultant dipole moment may be diminished. Thus, it can be stated that the tail group dipole moment of COOH(L)-SAM molecule which interacts with PAA carboxyl group is reduced. In this case net dipole moments of both CH3-SAM and COOH(L)-SAM molecules will become almost equal and accordingly directed which explains homogenous CPD map of the studied system. A similar depolarization effect cannot be expected for CH_3- terminated molecules due to a non-polar character of the tail group.

The KPFM studies of PAA system also reveal another important feature which influences CPD signal. In the topography map shown in Figure 65a, a small crystalline domains of PAA can be observed. These are also well resolved on the CPD map presented in Figure 65b, with CPD difference estimated at 25±14 mV (Figure 65c) in relation to amorphous state. This effect can be expected due to the fact that e.g. the ITO work function changes caused by the changes in crystalline to amorphous phase ratio were observed [250]. On the topography map, the stripes derived from PDMS mold deposition can be noticed, which indicates substrate functionalization, but they are not resolved on CPD map – instead, the CPD map shows differences of crystalline and amorphous phases.

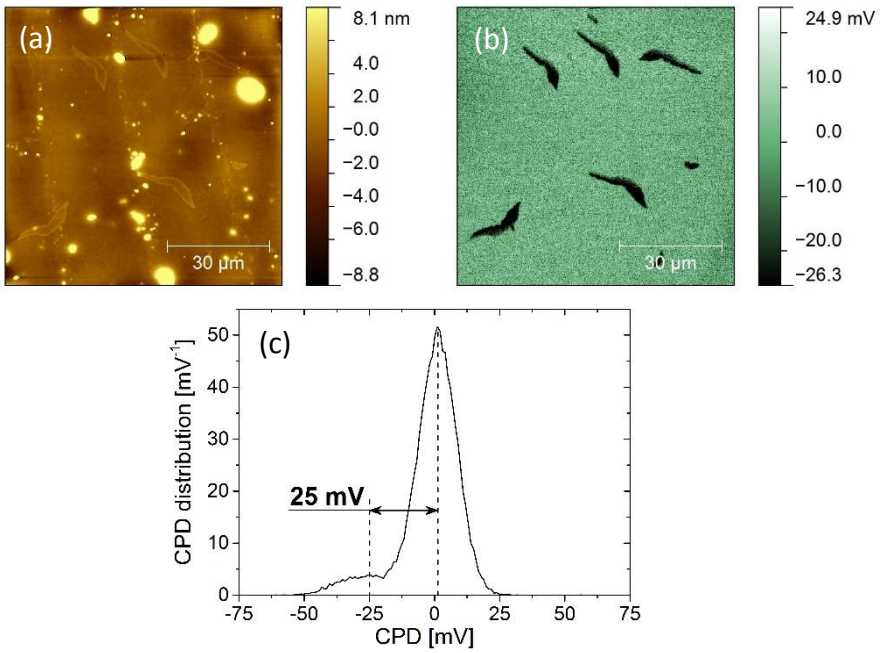

Figure 65. Thin film of PAA prepared by spin-casting on a COOH(L)-SAM/CH3-SAM pattern on Au substrate: (a) surface topography with noticeable crystalline-like domains and stripes of PDMS mold contamination deposition, (b) CPD image showing homogenous signal with clearly distinguishable lower signal originating from crystalline domains (c) the corresponding histogram with CPD difference estimated at 25±14 mV.

To summarize, the PAA thin film deposited on the locally polar and nonpolar functionalized substrate indicates no changes in CPD signal which can be explained due to the hydrogen bonding interactions between carboxyl groups of both polymer and SAM, which leads to the depolarization effect. The other studies of PAA shown that polymer crystallinity has influence on measured CPD signal, thus care must be taken when interpreting KPFM data from mixed amorphous and crystalline phases, which might differ in their electronic properties.

2.4. PMMA

The PMMA, as the main representative of methacrylates type polymers, was chosen as the development of previously studied systems. It is characterized by high values of Hansen solubility parameters in terms of hydrogen bonding and polar contributions, however, these values are significantly lower than that for PAA. In this part of the thesis, the influence of polymer layer thickness on CPD signal in KPFM is studied. Additionally, the aspect of stereoregularity of polymer chains and their contribution to substrate/polymer interaction is introduced. Thus, this paragraph is divided in three parts according to polymer tacticity, starting from atactic PMMA through syndiotactic form and ending with isotactic one.

2.4.1. Atactic PMMA

The at-PMMA films were prepared using horizontal dipping method described in detail in section III.2.3.2. Here, as a remainder, it is only noticed that this technique is capable of one-step fabrication of polymer films with gradient thickness. As a substrate a gold-coated slice of silicon wafer was used. The gold surface was further on patterned with “brick wall“ structure PDMS mold inked with COOH(L)-SAM molecules solution. As the substrate for H-dipping method is quite long, the patterns were made one after another along the full length assuring that the spaces were not wider than half of the overall stamp size. After this step the unprinted regions were functionalized with CH3-SAM monolayer and at-PMMA gradient film was formed.
First, the at-PMMA covered SAM pattern was investigated by SIMS depth profiling performed in the imaging mode. The measurements were localized close to the middle between the starting and the ending point of the prepared gradient film. In Figure 66a, the O^- secondary ions map, acquired at the interface, is presented. The characteristic “brick wall” structure can be recognized which confirmed COOH(L)-SAM pattern formation, as the collected O^- ions originate from carboxyl group of the SAM molecules. Additionally, homogenously distributed S^- ions, in 3D view representation presented at

Figure 66b, indicate substrate functionalization of both COOH- and CH_3- terminated SAMs.

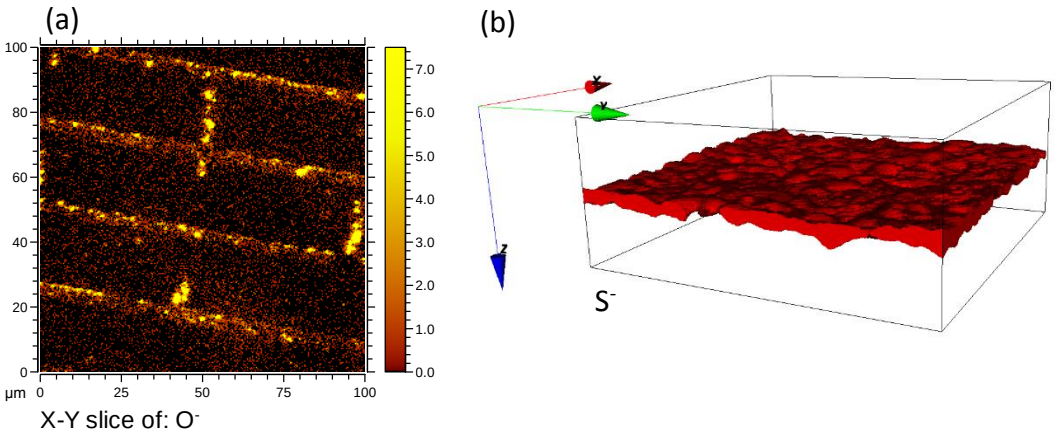

Figure 66. SIMS results presenting intensities for chosen ions collected at the interface of at-PMMA H-dipped on the COOH(L)-SAM multi-patterned substrate followed by immersion in CH3-SAM solution. (a) The O^- signal indicates the location of COOH(L)-SAM pattern at the interface (b) S^- secondary ions signal, presented in 3D view, indicates homogenous sulfur presence at the interface which acknowledges both monolayers deposition.

The polymer film thickness, nearby each KPFM analysis point, was determined with topographic AFM measurement performed on a previously scratched region of the film. Furrow was formed on the films by scratching the surface with gently pressed stainless steel needle. The KPFM results for different at-PMMA thicknesses are presented collectively in Figure 67.

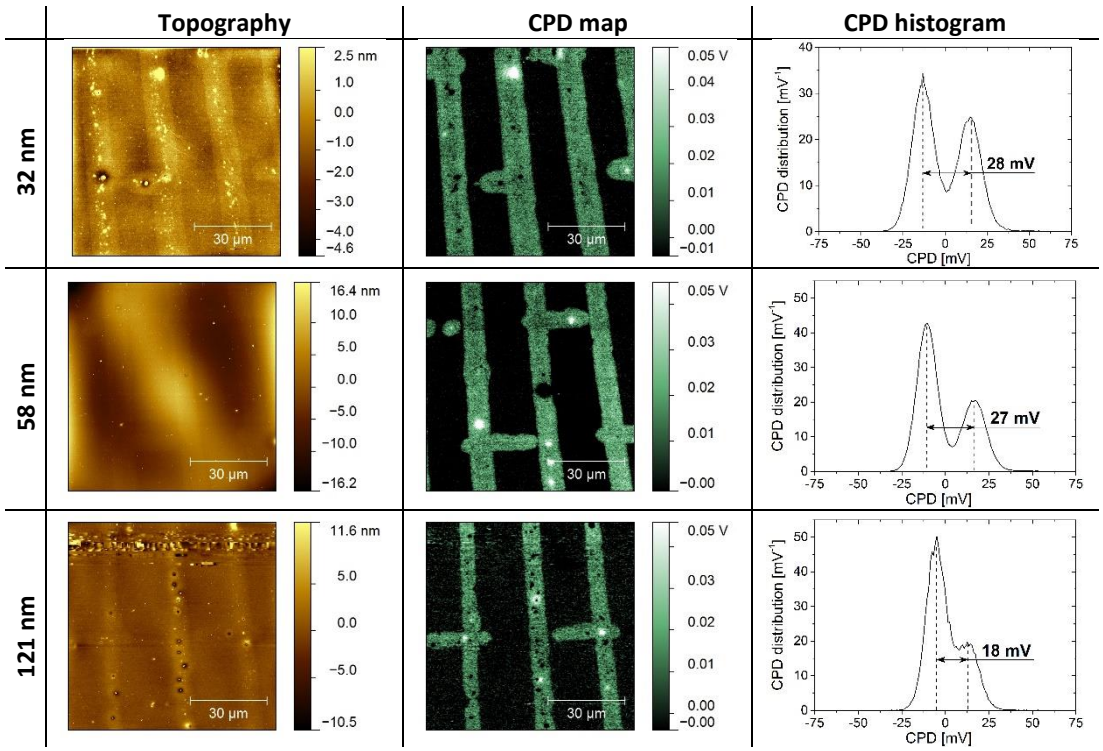

Figure 67. Influence of the at-PMMA film thickness on the measured CPD signal in KPFM. The film thickness is in the range of 32 to 121 nm with corresponding topography and CPD maps presented in each line. The CPD signal differences between COOH(L)-SAM and CH3-SAM areas are estimated from histograms at 28±10 mV, 27±9 mV and 18±8 mV for increasing film thickness, respectively.

From the inspection of the presented CPD maps and histograms collected for different film thicknesses it can be concluded that polymer film thickness has negligible or no influence on measured CPD due to the fact that estimated differences, even with very low uncertainty, overlap.

An interesting issue arising from these results is the inversion of the CPD signal when compared with that obtained for uncovered and PS- or P2VP- covered substrates. Although the same SAM pattern is present at the interface (as confirmed by SIMS measurements in Figure 66a), the CPD signal is inverted. In comparison, the CPD maps and related histograms for PS- and at-PMMA covered COOH(L)-SAM "brick wall" patterned gold substrates completed in unprinted areas with CH3-SAM are presented in Figure 68.

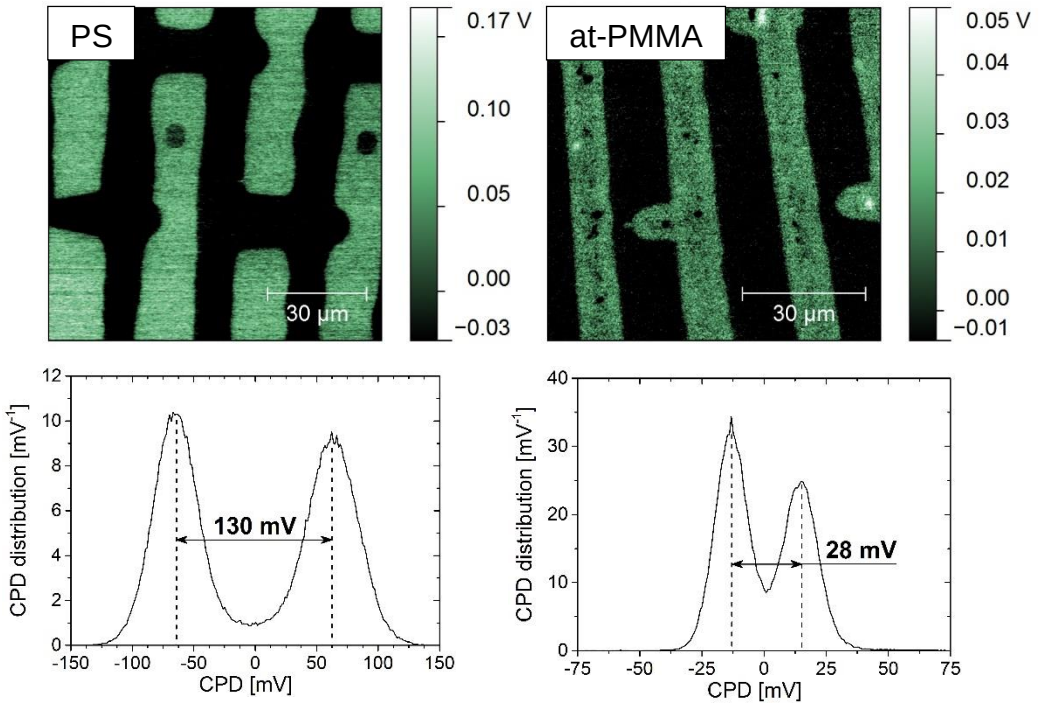

Figure 68. The comparison of CPD maps of PS (left) and at-PMMA (right) thin films deposited on the same way patterned substrate (COOH(L)-SAM "brick wall" stamp functionalization followed by immersion in CH3-SAM solution) and corresponding histograms. The CPD differences were estimated at 130±29 mV and 28±10 mV for PS and at-PMMA samples, respectively.

The inversion of the CPD signals can be explained by inter-association and depolarization effects [251, 252] between the at-PMMA and COOH(L)-SAM monolayer caused by hydrogen bonding interactions, similarly as in the case of previously presented PAA system. However, for the at-PMMA and COOH(L)-SAM molecules the interacting groups are not identical, thus different effect can be considered. Two types of hydrogen bond interactions are expected, as presented in Figure 69. The first one may appear between the carbonyl group of PMMA and the hydroxyl group of COOH(L)-SAM, whereas the second type is expected between the methoxy group of at-PMMA and the carbonyl group of COOH(L)-SAM. The assumed driving force for conformational

changes at the interface, which enables such interactions, is the possible hydrolysis of the PMMA ester group which might lead to the appearance of strong ionic bonds additionally reinforced by the acid-base interactions involving PMMA carbonyl groups and COOH(L)-SAM hydroxyl groups [253, 254].

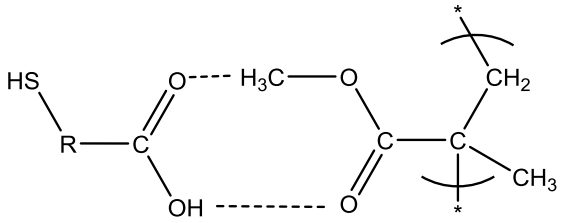

Figure 69. Schematic illustration of hydrogen bonding interactions appearing between at-PMMA carbonyl and methoxy groups and carbonyl and hydroxyl groups of COOH(L)-SAM.

In turn, appearing interactions change the direction and the net dipole moment of the COOH(L)-SAM layer, which becomes slightly smaller but now points in the same direction as in CH_3-tailed monolayers, which is schematically presented in Figure 70. This explains the much smaller difference (28±10 mV) between the bright and the dark regions on the CPD map for the at-PMMA film as compared with the PS one (130±29 mV).

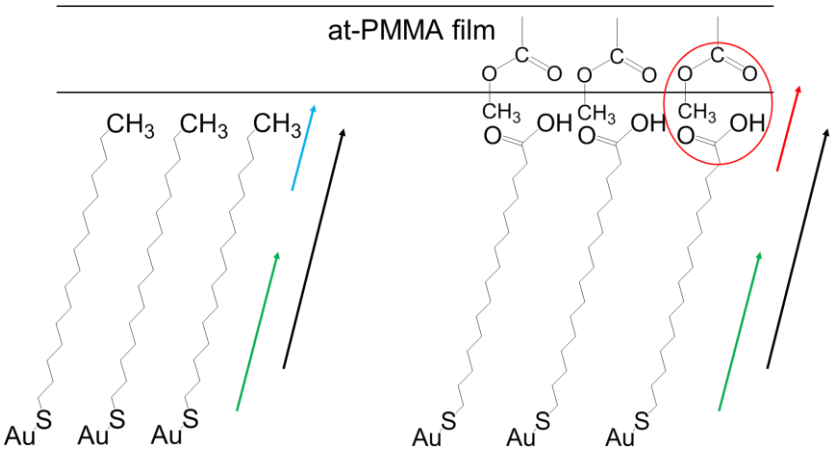

Figure 70. Schematic illustrations showing the dipole moment orientations of the SAMs' tail and head groups as well as the resultant dipole moments at the substrate covered by at-PMMA film.

In order to become convinced that the observed effect is repeatable, the sample of inversed pattern at the interface was prepared. In Figure 71, the KPFM results for at-PMMA film covering μ-contact printed CH3-SAM "brick wall" pattern with empty areas functionalized with COOH(L)-SAM is presented.

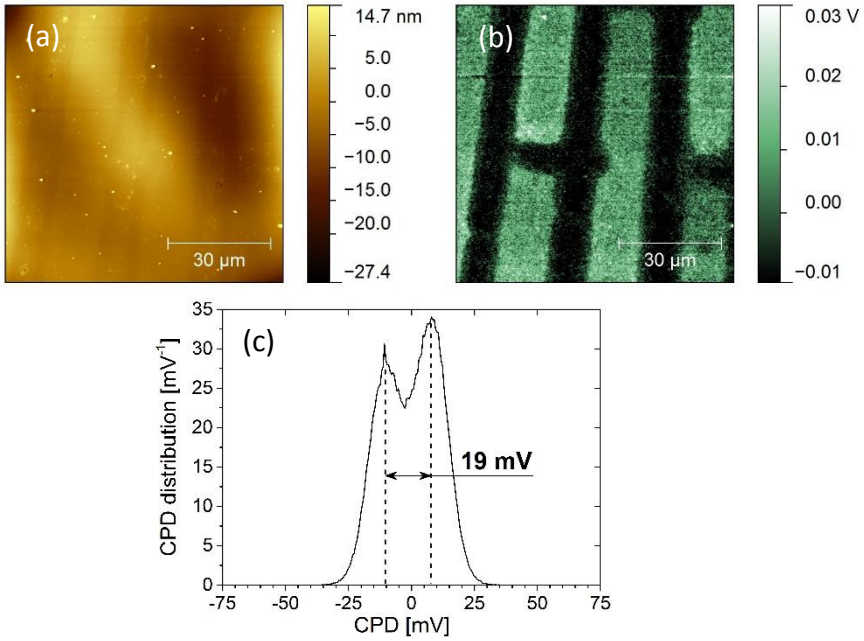

Figure 71. Thin film of at-PMMA prepared by spin-casting on a CH3-SAM/COOH(L)-SAM pattern on Au substrate: (a) surface topography with noticeable undulation, (b) CPD image showing clearly lower signal values from "brick wall" areas where CH3-SAM was adsorbed and (c) the corresponding histogram with CPD difference estimated at 19±9 mV.

The topography map (Figure 71a) reveals wavy polymer surface with a weakly visible stamp structure. However, on the CPD map (Figure 71b) the contrast derived from substrate functionalization is evident. Nevertheless, the lower CPD signal here is measured in the areas where CH3-SAM was locally placed at the interface, whereas a higher CPD is recognized in COOH(L)-SAM regions. Here, the stamp pattern placed on gold substrate was inverted but the previously described interactions remained unchanged. The CPD difference between the dark and bright areas was estimated at 19±9 mV, according to the histogram presented in Figure 71c. These results are consistent within previously described at-PMMA system, where CPD difference was estimated at 28±10 mV, and both are contrary to that found for PS and P2VP.

To understand better the CPD inversion effect the at-PMMA was dissolved in another solvent. The main purpose of this procedure was to exclude the solvent dependency on the observed effect. The results are presented in Figure 72 showing the at-PMMA spin-cast from chloroform onto COOH(L)-SAM patterned substrate complemented in unprinted regions with CH3-SAM.

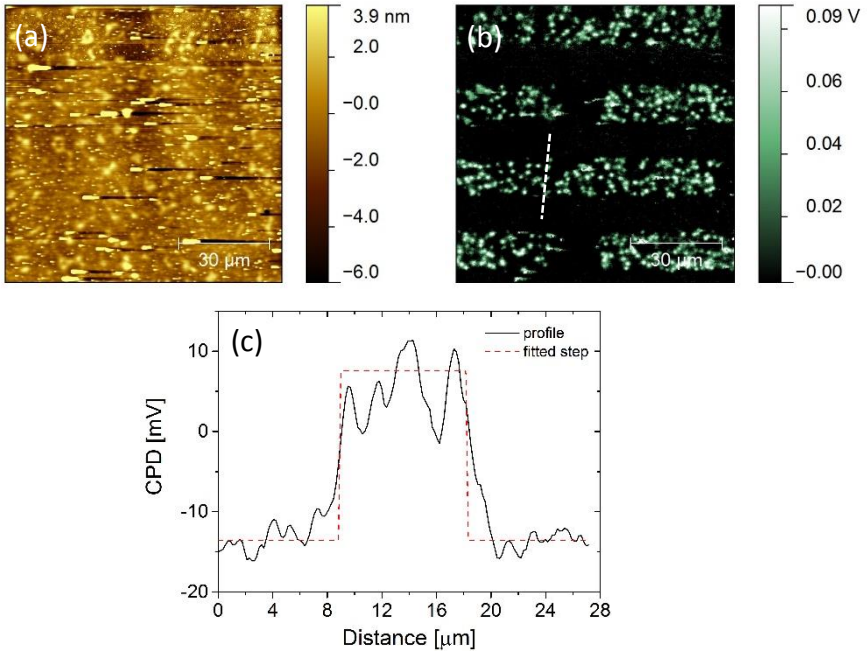

Figure 72. Thin film of at-PMMA cast from chloroform on a CH3-SAM/COOH(L)-SAM pattern on Au substrate: (a) surface topography showing rough polymer surface with flocks, (b) CPD image showing lower signal values from "brick wall" areas where CH3-SAM was printed, whereas bright signal originating from COOH(L)-SAM is non-uniform and (c) the cross-section from the CPD map (dashed line in (b)) with fitted step function from which the CPD difference was estimated at 21±3 mV.

From the topography map presented in Figure 72a one can observed that polymer surface is rough, possibly indicating the presence of flocks from undissolved polymer in the spin-cast solution. On the CPD map (Figure 72b) the dark regions correspond to the "brick wall" pattern indicating that this signal is measured for areas where CH3-SAM was locally placed at the interface. However, the bright areas on the CPD map are not uniform and consist of multiple small spots with dimensions of ca. 2 µm.

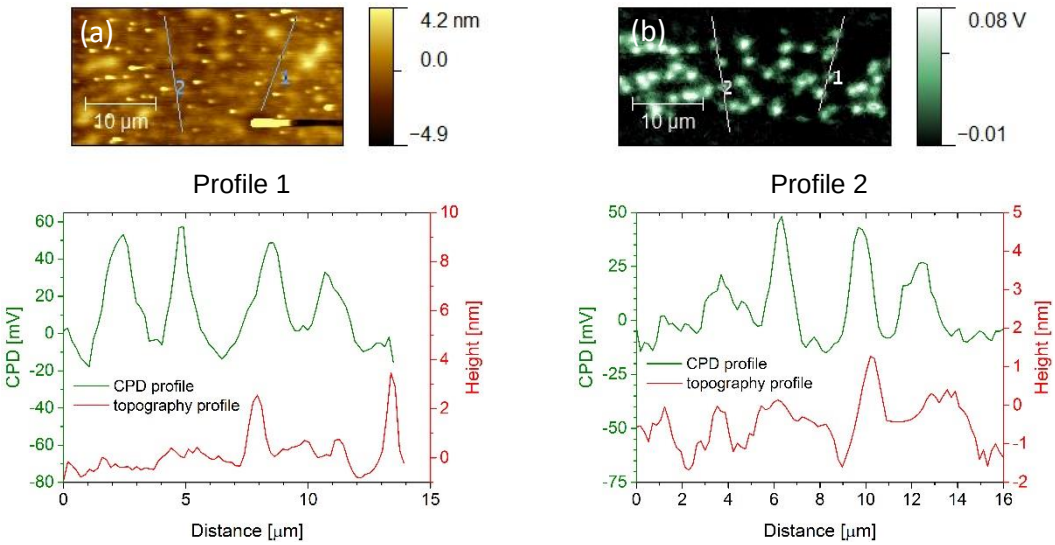

Figure 73. Zooming of the (a) topography and (b) CPD maps with marked two independent cross-sections taken form the same sites at both maps and their comparison on cross-sections. From this comparison it can be stated that small spots on the CPD maps do not origin from the polymer structure.

The average CPD difference set from the cross-section analysis, taken from the CPD map where a white dashed line is drawn, was estimated, by fitting positive step function to the profile (Figure 72c), at 21±3 mV what is in good agreement with the previously found values.

Nevertheless, the non-uniformity of CPD signal from bright areas was taken into consideration and in the first approach the influence of polymer film morphology on the measured CPD was examined. Two different cross-sections were taken from the same areas of topography and CPD maps and were compared, as presented in Figure 73.

Both profiles indicate that the measured CPD signal is not connected with morphology of polymer film, as the topography height profile maxim or minima do not match CPD signal variations accordingly. Thus, the morphology effect of the at-PMMA film cast from chloroform on appearance of small spots on CPD map may be neglected. It can be concluded that these characteristic CPD small dots might appear due to the real variations of COOH(L)-SAM adsorption sites at the gold substrate which arise from disturbance in self-assembly process. There might be two reasons for that. First, the functionalization of CH3-SAM using PDMS stamp might lead to the situation where this monolayer was placed not only in areas that derive from stamp structure but also in between – occupying the free sites where COOH(L)-SAM could be adsorbed. Second, this effect might be due to the too short duration of self-assembly of COOH-termianted molecules. As inspected in the CPD maps in Figure 72b and Figure 73b, there are only two different areas of intensity indicating that the first reason is the most probable one. If the observed effect arises from the presence of free unoccupied sites on the substrate, it would suggest that a third CPD signal should appear, originating from non-functionalized gold substrate.

2.4.2. Syndiotactic PMMA

The polymer studied next was syndiotactic rich PMMA, prepared in the same way as for previous experiments with at-PMMA. The multilayer samples consist of gold substrate “brick wall” patterned with COOH(L)-SAM complemented with CH3-SAM molecules and finally covered by spin-casting with thin film of syn-PMMA. The dSIMS measurements running in imaging mode revealed spatial chemical composition of constituents at the interface, and are presented in Figure 74. The results obtained for O^- secondary ions map acquired at the interface indicate the presence of stamp structure as expected (Figure 74a) and confirm the COOH(L)-SAM deposition. Additional 3D view localizing S^- secondary ions, depicted in Figure 74b, shows a homogenous distribution of sulfur at the interface, thus both COOH- and CH_3- terminated monolayers self-assembly is evidenced.

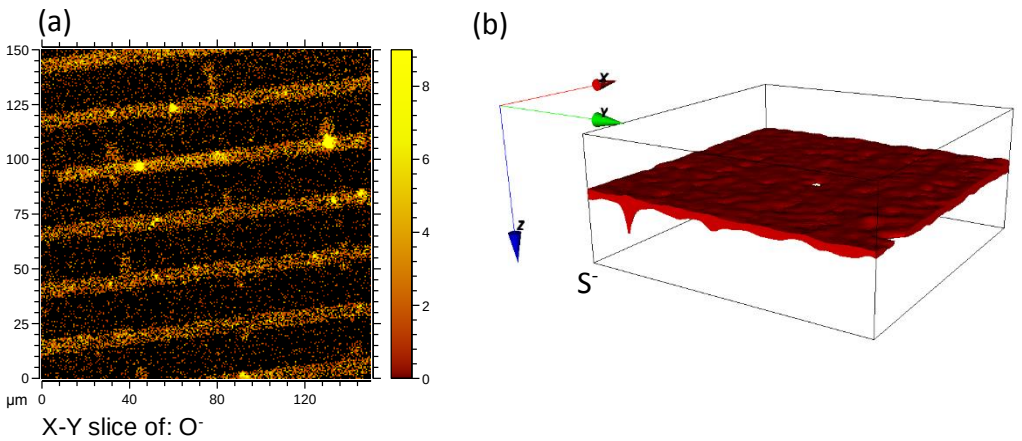

Figure 74. dSIMS secondary ion intensities collected at the interface of syn-PMMA spin-coated on the COOH(L)-SAM patterned substrate followed by immersion in CH3-SAM solution. (a) The O^- signal indicates the location of COOH(L)-SAM pattern at the interface (b) S^- secondary ions signal 3D view indicates homogenous sulfur presence at the interface which confirms both monolayers deposition.

In the next step, the syn-PMMA model systems were analyzed with KPFM. The results for syn-PMMA dissolved in chloroform are presented in Figure 75. The topography map (Figure 75a) shows a flat but coarse polymer surface with lots of spikes possibly originating from contamination. However, these effects are not reflected in CPD map, presented in Figure 75b, where a stamp structure can be easily recognized.

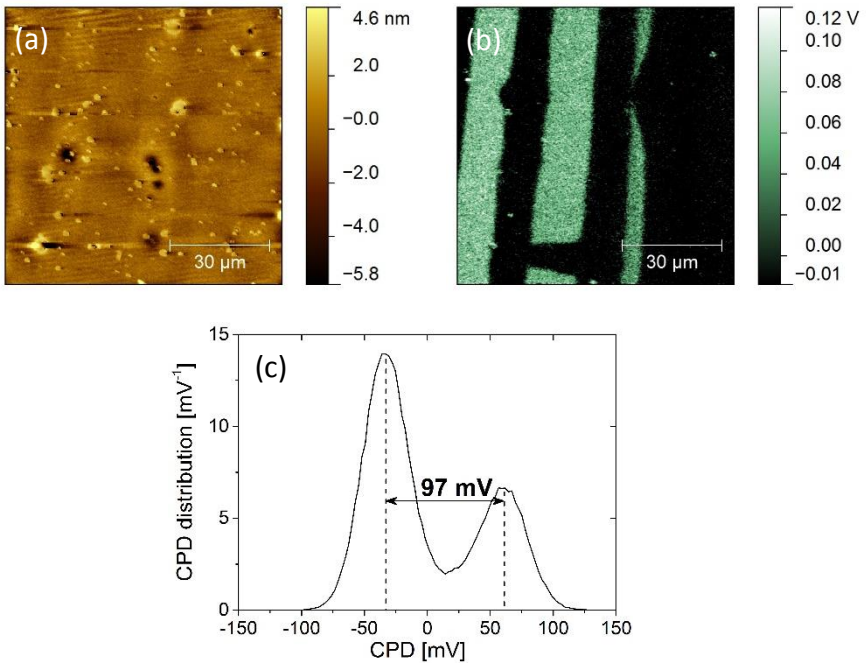

Figure 75. Thin film of syn-PMMA(chloroform) spin-coated on the COOH(L)-SAM/CH3-SAM pattern on Au substrate (resulting from micro-contact printing of COOH(L)-SAM followed by CH3-SAM formation in empty areas): (a) surface topography, (b) CPD image where lower signal/dark area values correspond to COOH(L)-SAM regions, and (c) CPD histogram showing the differences between dark and bright areas of 97±28 mV.

The broad dark part on the right side of the map derives from the physical end of the pattern structure at the mold surface. This part of the stamp is flat and of the height

corresponding to that which localizes brick wall structure, thus in this region, due to the conceivable solution existence, the COOH(L)-SAM monolayer is also deposited. Despite this effect, the location of COOH(L)-SAM is revealed due to the asymmetrical PDMS mold pattern where crossbar indicates stamp localized material. All these lead to the conclusion that in the case of syn-PMMA film the inversion of the CPD signal does not exist. The CPD difference between dark and bright areas, estimated from the histogram presented in Figure 75c, is equal to 97±28 mV. This stays in good agreement with the CPD difference obtained for PS, and indicates very weak and insignificant interactions of syn-PMMA with the patterned substrate.

To associate the possible solvent influence on the obtained results, the same model multilayer system as the previously described one was prepared with syn-PMMA spin-coated from toluene solution. The substrate was first patterned with COOH(L)-SAM followed by CH3-SAM functionalization in the remaining empty regions. KPFM results of this system are presented in Figure 76.

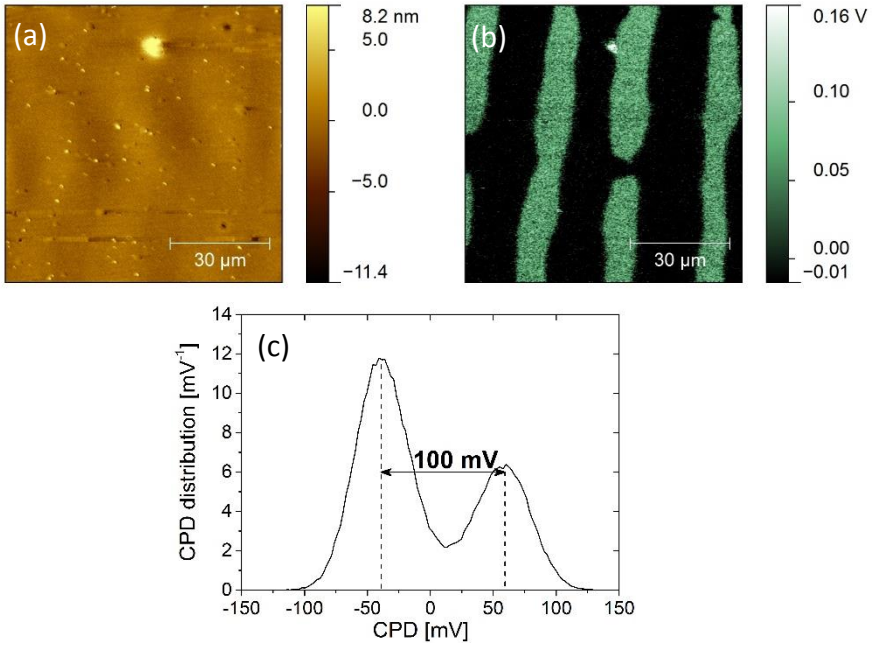

Figure 76. KPFM results of thin film of syn-PMMA(toluene) spin-coated on the COOH(L)-SAM/CH3-SAM pattern on Au substrate: (a) surface topography map indicating flat and uniform polymer surface, (b) CPD image where lower signal/dark area values correspond to COOH(L)-SAM regions, and (c) CPD histogram showing the differences between dark and bright areas of 100±33 mV.

The topography map (Figure 76a) indicates satisfactory flat, uniform polymer surface with a small amount of contamination driven spikes. The CPD map presented in Figure 76b clearly differentiates two regions of appropriate signals derived from SAM localized functionalization. Similarly to the previous case of syn-PMMA dissolved in chloroform, the asymmetrical stamp structure reveals that dark areas correspond to the COOH(L)-SAM deposition sites, whereas bright regions disclose CH3-SAM functionalized areas. Additionally, from the histogram shown in Figure 76c, the CPD difference is estimated

at 100±33 mV which gives conforming result, like for chloroform dissolved syn-PMMA. These results resemble the former case of syn-PMMA, and indicate that both presented here toluene or chloroform solvents have insignificant impact on measured CPD signal and besides, confirm the non-inverted CPD behavior.

2.4.3. Isotactic PMMA

The last studied stereoisomer of poly(methyl methacrylate) was the isotactic one. Likewise the former researches the iso-PMMA was spin-cast from the chloroform solution onto micro-contact printed COOH(L)-SAM pattern on gold complemented with CH3-SAM in theunprinted areas.

Imaging mode SIMS depth profiling was utilized to reveal the spatial arrangement of constituents at the interface. By tracking the origin of O^- secondary ions signal the stamp structure was acquired and is presented in Figure 77a. Although the examined polymer film was rich in oxygen, due to the chemical composition of PMMA, the enhanced signal derived from COOH(L)-SAM presence at the interface can be detected. There are also weakly observable crossbars from the stamp structure which confirms COOH-terminated molecules localization. Additionally, 3D view of the obtained S^- secondary ions signal (Figure 77b) carries information about the homogenous distribution of sulfur at the interface and provides evidence of both monolayers deposition.

Thin films of isotactic PMMA form were also studied using the KPFM method with the results presented in Figure 78. The topography map (Figure 78a) bear evidence of a uniform, slightly undulated polymer film surface with small amount of spikes. In the upper right part of the map there is a characteristic domain structure which might suggest a partially crystalline state of iso-PMMA. On the CPD map shown in Figure 78b the stamp pattern is clearly outlined. Similarly to previous discussions, the asymmetrical stamp structure, due to the presence of crossbars, together with dSIMS maps taken at the interface confirm that dark areas/lower CPD signal correspond to COOH(L)-SAM functionalized regions whereas bright areas/higher CPD signals originate from CH3-SAM deposition sites.

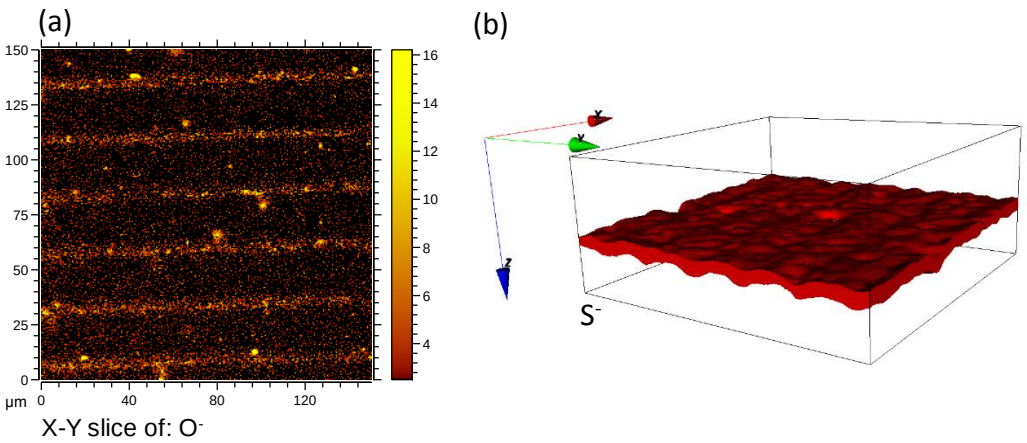

Figure 77. dSIMS results from the interface of iso-PMMA spin-coated on the COOH(L)-SAM patterned substrate followed by immersion in CH3-SAM solution. (a) The O^- signal indicates the location of COOH(L)-SAM pattern at the interface and (b) 3D view of S^- secondary ions signal indicates homogenous sulfur distribution at the interface which provides evidence of both monolayers deposition.

According to the histogram of CPD map (Figure 78c), the CPD difference between both regions can be estimated at 95±34 mV, which stays in good agreement with the values found for similar systems covered with syn-PMMA (100±33 mV) and PS (e.g. 130±35 mV). According to these results, there is every indication that iso-PMMA film remains inert within studied systems likewise it was found for syn-PMMA and PS, and the direction of SAM's dipole induced CPD variations is consistent with that determined for polymer non-covered COOH(L)-SAM/CH3-SAM functionalized gold substrate.

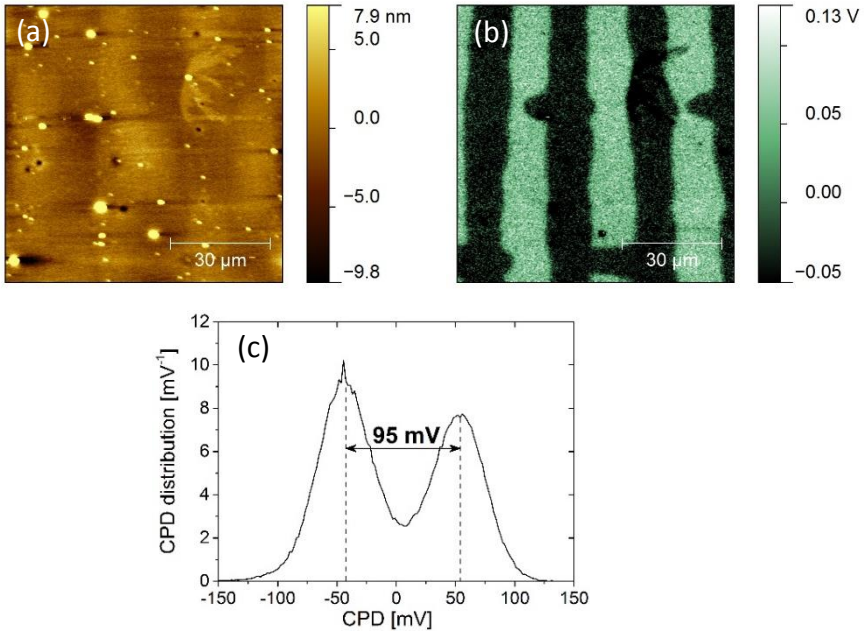

Figure 78. KPFM results of thin film of iso-PMMA(chloroform) spin-coated on the COOH(L)-SAM/CH3-SAM pattern on Au substrate: (a) surface topography map indicating flat and uniform polymer surface with small crystalline-like domain, (b) CPD image where lower signal/dark area values correspond to COOH(L)-SAM regions, and (c) CPD histogram showing the differences between dark and bright areas of 95±34 mV.

In the close-ups of the topography and CPD map in the region of crystalline domain presence which was mentioned before, it could be observed that except two main regions of different CPD signal two more can be recognized, as presented in Figure 79. These additional areas of other CPD values arise from different properties of amorphous and crystalline phases like it was found for PAA crystalline domains. However, here this effect is additionally interlaced with local substrate functionalization driven CPD changes. Due to the fact that the crystalline domain lies partially on COOH(L)-SAM and CH3-SAM functionalized regions, it causes shift in both signals which are expected to have the same value and direction. Indeed, from the inspection of histogram (Figure 79c) taken from the red rectangular area denoted in Figure 79b, four different regions can be recognized and were fitted with Gaussian functions. The CPD differences between functionalized areas under crystalline domain or amorphous phase are in good agreement and were estimated at 105±25 mV and 103±22 mV, respectively. The CPD shift between crystalline and amorphous phases can be also calculated from the presented histogram and is estimated at 45±23 mV. These results revealed that both crystalline and amorphous phases stay inert in contact with mixed polar/non-polar functionalized substrate but their different response for CPD was maintained.

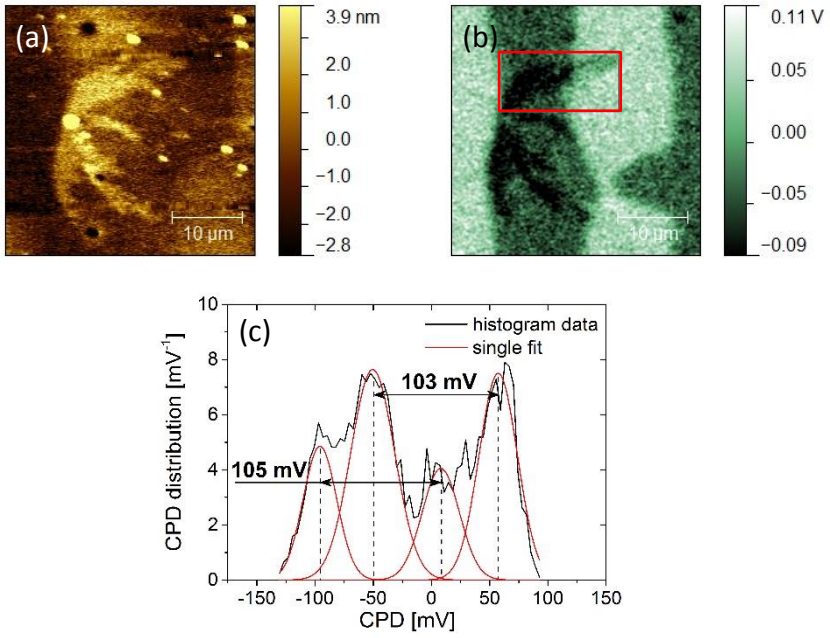

Figure 79. Zooming of the (a) topography map and (b) CPD map in region of crystalline domain presence. Four different regions of CPD signal can be distinguished and are fitted in the (c) CPD map histogram. The CPD differences originating from areas of crystalline domain and amorphous phase placed on variously functionalized substrate were estimated at 105±25 mV and 103±22 mV, respectively. The shift in CPD between amorphous and domain phases is estimated at 45±23 mV.

2.4.4. Conclusions appearing from the stereoregular poly(methyl methacrylates) studies

The studies of PMMA interactions with SAM functionalized gold substrate in function of its stereoregularity gave surprising results. It was shown that for iso- and syndiotactic PMMAs none or very weak interaction with the polar SAM functional groups is observed and these types of polymers behave similarly to PS one. However, the situation became different for the atactic form of PMMA. For this type of PMMA the CPD signal was inverted when compared with PS covered and uncovered SAM functionalized substrate, regardless of the solvent used and film thickness (in the studied range). These results are rather startling since no differences in the nature of the interfacial interactions are expected for the chemically identical PMMA isomers. The inversion of the CPD signal was discussed in terms of hydrogen bonding and dipole-dipole intermolecular interactions between polar groups of COOH(L)-SAM and PMMA. However, a diminished contribution of these interactions for stereospecific forms of PMMA both iso- and syndio- tactic needs to be addressed. First, it should be noticed that interactions between chains in bulk polymer samples can be related to its glass transition temperature (T_g). Generally, T_g will depend on many parameters, e.g. its chain length and mobility, polydispersity index and tacticity [255]. However, as these effects are well understood for the bulk samples, in the case of supported polymer thin films they need to be reconsidered. In ultrathin and thin films the mobility and the dynamics of polymer chains near surface and interface might play significant role in the overall interactions between polymer segments due to their favourable contribution in overall polymer volume. Thus, depending on the surface chemistry, or generally speaking on its polar or non-polar character, polymers at interfaces might exhibit entropic effects (e.g. chain end segregation, disentanglement or confinement effects) [256, 257] and/or enthalpic forces [258] which will lead to the substantial decrease or increase of T_g, respectively. Considering one type of the polymer, like in this case PMMA, with similar values of molecular weight but different tacticity, the variations of T_g will reflect the intramolecular interactions between polymer chains also indicating their possibilities to engage in interactions with chemically modified surfaces. The appearing strong ionic bonds enhanced by acid-base interactions at the interface of PMMA/polar functionalized substrate will lead to the local conformational changes which influence the change in arrangement and packing density of the chains at the interface [259-261]. As it was shown for various thicknesses of stereoregular and atactic PMMA thin films spin-coated on aluminum and silicon substrates pretreated in different manner to modify surface properties (hydrogen or hydroxyl passivation) and thus polymer/substrate interactions [262], the atactic form exhibits the highest value of T_g among all studied PMMAs. This was discussed in terms of its higher density of interfacial interactions at the interface due to the chain end segregation and disentanglement. The iso- and syndio- tactic forms of PMMAs due to the tactic structure of polymer chain might resist to this effect and the density of interactions may be diminished. These

results can serve as an explanation of inversion of CPD signal in the case of at-PMMA presented in this thesis. It should be noticed that COOH(L)-SAM localized functionalization of the gold substrate can be seen as more reactive and thus more attractive surface than silicon and alumina substrates studied in the cited work. Presumably, this may enlarge the effects of interfacial interactions density. Here, the effect of saturation of the COOH(L)-SAM carboxyl groups with appropriate at-PMMA groups placed on the COOH(L)-SAM, due to the high interfacial interactions density, is proposed. In such a case, the dipole moment of the COOH(L)-SAM monolayer is substantially affected leading to the overall change in the resultant dipole moment direction as it was meticulously described in Section IV.2.4.1. Such an effect is not present for tactic forms of PMMA due to the diminished possibility of dense interfacial interactions formation. These stereoregular polymers might be seen as more confined systems due to their tactic nature.

2.5. Polythiophene and its derivatives

The next group of polymers studied within the framework of this thesis were conjugated, conductive polymers. The first one presented here is the poly(alkyl thiophene)s group, namely poly(3-hexylothiophene) and poly(3-octylothiophene), both in the regioregular forms. These polymers are one of the most important materials used in organic electronic devices due to the e.g. high drift mobility and are utilized as hole transporting materials. Thus, especially interfacial level alignment between these organic semiconductors and electrodes, in multilayered structures of plastic electronics, plays a key role for the overall device performance.

First, the 4 µm wide RP3HT stripes, deposited on the gold substrate using MIMIC technique, were examined with KPFM, with the results presented in Figure 80. From the inspection of the topography map (Figure 80a) it can be observed that the formed RP3HT stripe is non uniform laterally and with varying height. This might be the effect of fabrication technique in which during the evaporation process of the solvent the appearing concentration gradients may cause local variations in stripe thickness and continuity. The deposited stripe influenced the local CPD (Figure 80b) values as expected due to the different work function values of gold and RP3HT. The CPD difference between RP3HT stripe and gold using histogram shown in Figure 80c is estimated at 290±45 mV, whereas RP3HT is found to exhibit lower work function than gold (higher CPD value). Thus, taking the previously determined gold work function of 5.10±0.15 eV and subtracting measured CPD value gives work function (or more precisely level of highest occupied molecular orbital) of RP3HT of about 4.81±0.16 eV, whereas literature reported values are in the range of 4.5 – 4.8 eV [263, 264] which confirms validity of the determined result.

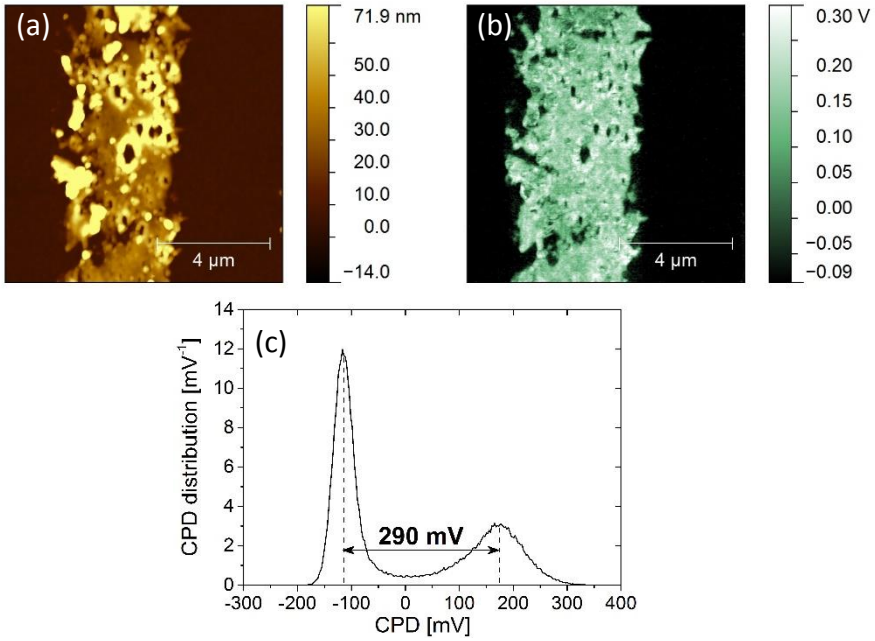

Figure 80. The KPFM (a) topography and (b) CPD maps of 4µm wide RP3HT stripe on gold fabricated by MIMIC technique. (c) The CPD map histogram shows a difference in CPD of about 290±45 mV.

To study the possible interactions that may appear at the interface of thin layer of semiconducting RP3OT and functionalized gold substrate (electrode), samples consisting of RP3OT spin-coated on the COOH(L)-SAM stamp functionalized gold substrate complemented in empty areas with CH3-SAM, were prepared. First, the depth profiling measurements were conducted in the imaging mode to resolve spatial chemical composition in the thin film and at the polymer/gold interface.

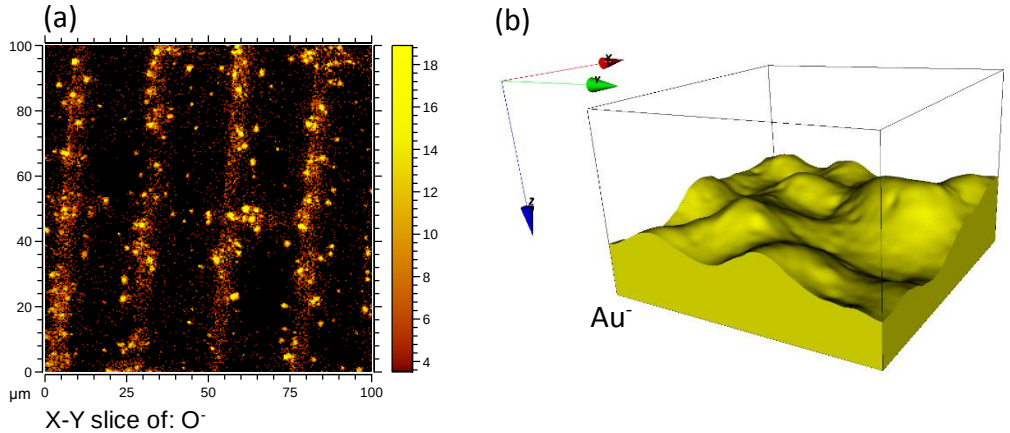

Figure 81. dSIMS maps and 3D view representation of secondary ions intensities collected at the interface of RP3OT spin-coated on the COOH(L)-SAM patterned substrate followed by immersion in CH3-SAM solution. (a) The O^- signal indicates the location of COOH(L)-SAM pattern at the interface and (b) 3D view of Au^- secondary ions signal shows waviness of polymer surface.

In Figure 81a the map of O^- secondary ions signal collected at the interface is presented and indicate COOH(L)-SAM formation due to characteristic “brick wall” shapes of

acquired O^- intensities. In Figure 81b, the 3D view of Au^- signal indicates the undulated polymer surface. The S^- signal cannot be used to confirm both monolayers deposition, as it was used in the previous cases, due to the fact that polymer itself contains sulfur, thus its homogenous distribution at the interface is expected without necessity of SAMs deposition. Unfortunately, none of the other signals can be used to monitor deposition of CH3-SAM, due to the chemical nature of these molecules which, except sulfur, contain aliphatic chain indistinguishable from that present in RP3OT structure.

Thin film of RP3OT on variously SAM functionalized substrate was analyzed with KPFM technique which needs a few words of explanation, due to the semiconducting nature of the polymer. As far as polymer film is non-conductive, it should be clear that the measured CPD signal for variously functionalized metal substrate, in a properly set measuring system, gives information about interface phenomena. However, for semiconducting material, the measured CPD may be disrupted or the interfacial effects may be screened due to the appearing short-circuit, thus KPFM may map potentials present on the surface of conjugated polymer possibly interlaced with effects derived from interface functionalization. These are expected in a greater amount as the more conductive the examined layer becomes. The results of KPFM measurements on the samples previously studied by dSIMS are presented in Figure 82.

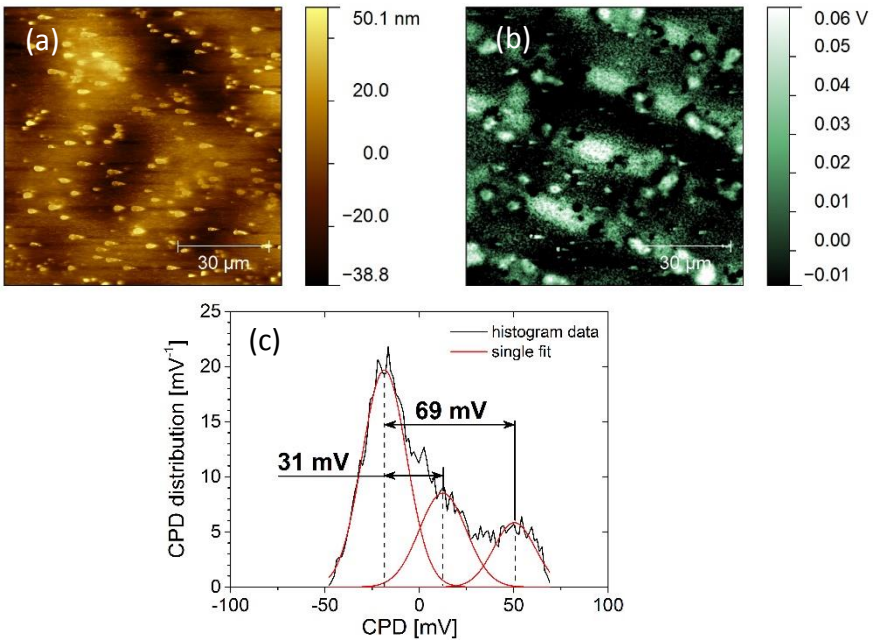

Figure 82. The KPFM results of spin-coated RP3OT on COOH(L)-SAM stamp functionalized substrate complemented with CH3-SAM in unprinted areas. (a) topography map which gives evidence of polymer surface waviness, (b) CPD map showing disrupted swinging signal with some visible order of high intensity signals originating from stamp deposited SAM structures, (c) CPD map histogram where three different areas of CPD signals gain differences in CPD of 69±16 mV and 31±17 mV.

The topography map (Figure 82a) confirms undulated polymer surface what was also found with SIMS. On the CPD map, presented in Figure 82b, the high CPD areas show some order which can be associated with the stamp presence. However, the CPD areas

of different signals are not as sharp and apparent as for previously examined systems. Presumably, due to the weakly visible, but present “brick wall” stamp driven cross-bar areas of lower CPD, it can be concluded that the RP3OT film does not interact strongly with substrate and the direction of CPD signals remains the same as for PS coated substrate. It should be noticed that there are at least three different areas of CPDs that can be distinguished on the CPD map. Indeed, from the inspection of the histogram presented in Figure 82c, the CPD differences between dark areas and two regions of higher CPD signal intensities can be estimated at 69±16 mV and 31±17 mV. Both measured differences of CPD are lower than those found for uncovered and PS covered substrate, what can be explained due to previously mentioned screening effects, but the practicability to measure interfaces is maintained and can be used to evaluate possibly appearing interactions and disorders.

Thin films are the most popular form in the design of organic electronic devices, however, unsubstituted polythiophene (PT), due to its fastness to common organic solvents, is very limited in application. The insolubility issue is overcome by introduction of different kinds of substituents to the PT backbone, like aliphatic ones with examples presented previously (RP3HT, RP3OT), making the polymer material soluble in organic solvents. The main drawback of that is the complexity of synthesis procedure and others e.g. need of toxic solvents incorporation. Additionally, side chains attached to the main PT backbone are passive in terms of light harvesting and charge transport and may unfavorably change mechanical properties of the material. The alternative might be the synthesis of PT nanoparticles which can be dispersed in common organic or inorganic (including water) solvents with advantages of substantial surface development which is very desirable in, e.g. gas sensor applications.

Within the framework of this thesis, the PT nanoparticles were synthesized by copper sulfide ($CuSO_4$) catalyzed oxidative polymerization in aqueous medium as described in detail in this work [131]. The obtained PT nanoparticles were dispersed in THF and drop-cast onto the silicon wafer with a thin native oxide. The results of KPFM measurements of such prepared layer are presented in Figure 83. From the inspection of topography map (Figure 83a), it is clear that the resultant PT layer is discontinuous due to the dewetting process and casting method. Inside the observed quasi-circular hollows small spots can be observed. The origin of these spots is explained by the examination of the corresponding CPD map presented in Figure 83b. The PT occupied regions are found with lower CPD values, whereas hollows exhibit higher CPD signal – except small spots which give similar signal to PT layer and thus indicate their presence but in a lesser extent. The CPD difference between bright and dark areas of CPD map were estimated, using the histogram shown in Figure 83c, at 40±20 mV. The reported work function values of silicon (with native oxide) are in the range of 4.0 ÷ 4.1 eV [41], whereas the work function of polythiophene nanoparticles was not reported. From KPFM measurements presented here it appears that synthesized PT nanoparticles exhibit

higher work function than silicon which can be seen as a reasonable statement if compared to alkyl substituted PT equivalents (Φ = 4.3 ÷ 5.0 eV [265-267]).

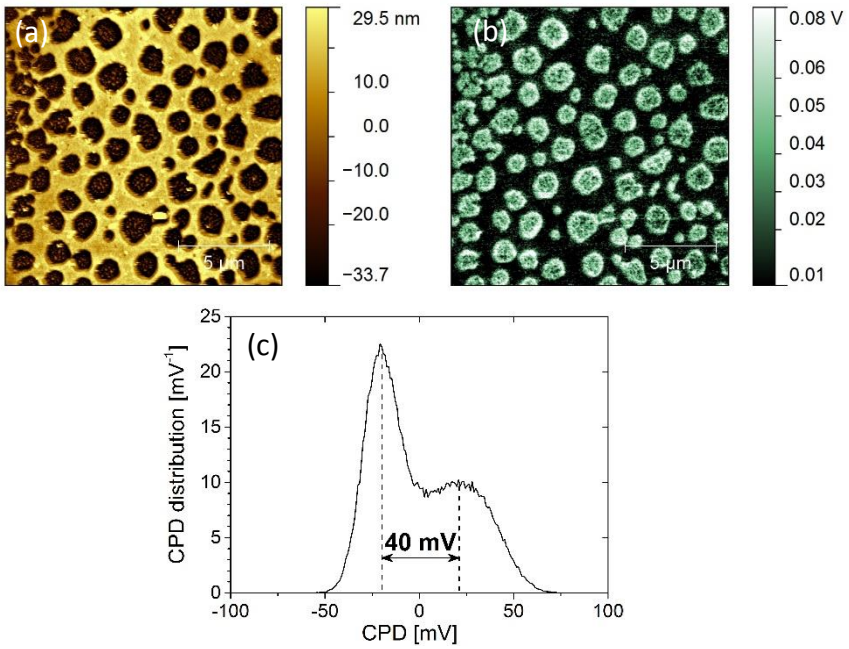

Figure 83. The KPFM results of THF dispersed PT nanoparticles drop-cast on silicon: (a) topography map indicating non-uniform discontinuous layer, (b) corresponding CPD map which indicate different areas for PT covered and uncovered silicon, (c) CPD map histogram where difference between CPD from PT and silicon can be estimated at 40±20 mV.

However, form the previously studied maps it was not possible to observe and confirm the preparation of PT nanoparticles, thus detailed measurements were taken in a very small area of 1.5 µm x 1.5 µm and are presented in Figure 84. The previous statement of existence the small spots of PT nanoparticles inside the hollows is now evident, as they are well resolved on the topography map depicted in Figure 84a. Furthermore, it is clear that the layer of PT nanoparticles is in form of coagulum, and small spots are also formed as groups of particles. Additionally, from the topography map, the average dimensions of nanoparticles are estimated at 39±5 nm. The simultaneously acquired CPD map, shown in Figure 84b, clearly distinguishes areas occupied by PT nanoparticles from those of uncovered silicon. The CPD map can be also used to determine the lateral resolution of KPFM method, by normalizing measured signal intensity taken at the edge of different CPD regions (as marked by line on the CPD image) and calculating the distance between 16% and 84% intensity points (IUPAC recommended method). The calculation is shown in Figure 84c, where the resolution was estimated at 62 nm. It should be noted that the KPFM lateral resolution found is a rough value and it is expected to be improved when a precisely determined edge is chosen.

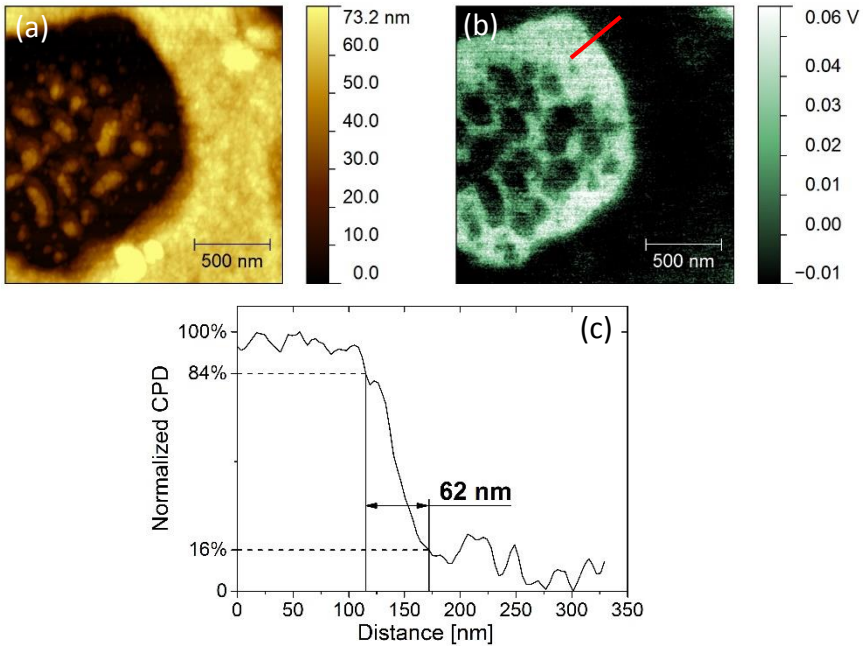

Figure 84. High resolution images of PT nanoparticles drop-cast onto silicon wafer: (a) topography map of a region where hollow formed due the dewetting is found. From the map inspection it is clear that inside the hollow PT nanoparticles are deposited and that the matrix PT layer consists of nanoparticle coagulum. (b) corresponding CPD map with well resolved PT features and (c) cross-section, taken from the marked line in CPD map, which was used to estimate the spatial resolution of KPFM method – the calculation gives 62 nm.

To summarize the presented results of the P3AT measurements, it can be stated that KPFM enable to characterize the conjugated polymers in a semiconducting state. Furthermore, it was successfully applied to study buried interface of SAM functionalized gold and polymer thin layer, however, a few issues due to screening effects were addressed. The synthesized nanoparticles were dispersed and thin layer, resulting from drop-casting over silicon, was characterized in terms of nanoparticles dimensions and work function. Additionally, the KPFM spatial resolution was determined on high resolution maps of PT nanoparticles.

2.6. PANI(CSA)-PS blend

The interpretation of KPFM observations made previously for the PS and PMMA model systems, consisting of SAM-patterned metal interfaces covered with uniform films of insulating polymers, is employed here to discuss the KPFM results for thin film blends of PS and conducting polyaniline doped with camphorsulfonic acid (Figure 85).

Topographic image (Figure 85a) indicates elevated larger domains surrounded by an almost flat polymer matrix with smaller holes. Topography reflects surface phase domain arrangement, tentatively suggested by previous reports [15, 268-270]. As indicated therein, the elevated larger domains are formed by PANI(CSA), while the matrix is composed of flat PS-rich host with pores rich in PANI(CSA). It is of interest to compare the PANI(CSA)/PS blend film topography (Figure 85a) with the CPD image (Figure 85b). Both images show very similar morphological features specifying separate

larger (protrusions) and smaller (holes) domains rich in PANI(CSA), all embedded in the PS-rich host. However, contrary to the topography map, where the signal contrast is comparable for all domains of the same type, here the CPD signal is constant within each individual domain but it varies from one domain to another (Figure 85b). For instance, in comparison to the PS-rich host the CPD signal is higher of about 430±105 mV for one domain and lower by about 290±120 mV for the other (see maxima in histogram, taken from the marked region in CPD map, shown in Figure 85c).

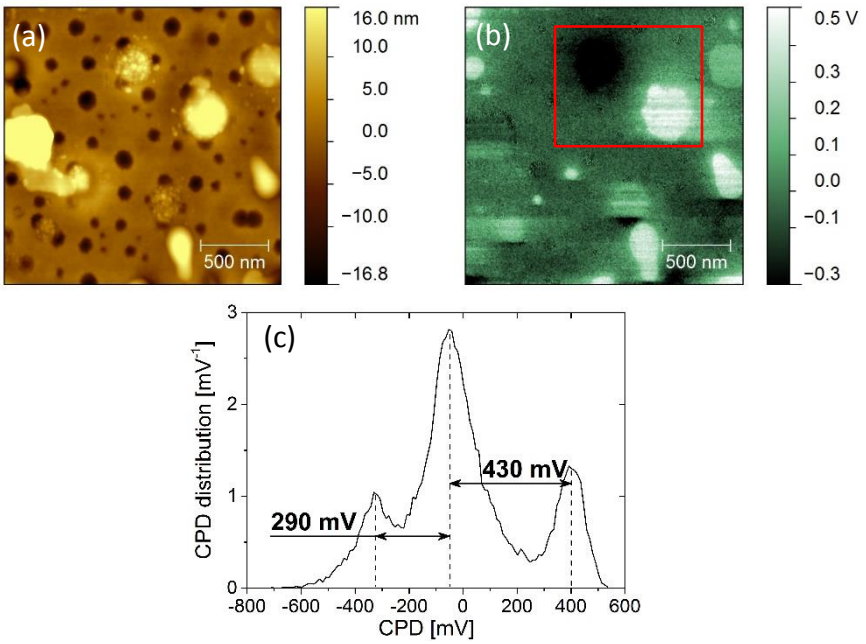

Figure 85. Thin film (thickness ~100 nm) of polyaniline doped with camphorsulfonic acid PANI(CSA)/polystyrene blend spin-coated on Au substrate: (a) surface topography, (b) CPD image and (c) corresponding histogram taken at rectangle marked area at CPD map. Note reversed contrast between different regions in (b) expressed by three different maxima in (c).

The interpretation of CPD data for the model systems (PS/SAM or PMMA/SAM - patterned Au substrates) presented previously may lead to the conclusion that the variations in the CPD signal can be induced here by a different interaction between individual PANI(CSA)-rich domains and the Au substrate. It was indicated for PS or PMMA thin films that the variations in the CPD signal visible in Figure 85b can be induced by opposite polarization of the interface between the PANI(CSA) domains and the Au substrate. The observed large variation of the CPD signals (Figure 85c) suggests that net dipole moments formed at the interfaces are much larger than in the case of CH3-SAM or COOH(L)-SAM. The observed polarization may be explained by water vapor interaction with the PANI(CSA) domains during spin-coating. Evaporation of the solvent (chloroform) lowers the temperature of the solution and induces condensation of the sub-micron water droplets. Since polyaniline is hydrophilic, the condensation should occur at the PANI(CSA) domains. The water molecules may interact with PANI(CSA) and replace the dopant (CSA), which segregates from the substrate [269]. This might cause polarization of the interface. At moderate vapor pressure of ambient atmosphere the

droplets may interact with the domains randomly. Therefore, different domains reveal different polarization at the interface. The presented results indicate that the variations in the CPD signal between individual domains of conjugated polymer are due to the modified interactions of these domains with the buried substrate. Alternative explanation has been proposed recently for conjugated polymer–fullerene blends applied in the fabrication of organic solar cells [66]. The suggested mechanism involved formation of a skin layer covering the protruding domains.

3. Organic/organic model systems

The molecular interactions appearing at the interfaces between many classes of soft matter control the macroscopic properties and performance of organic electronics devices from which they are composed. In this chapter the model systems of multilayer organic solar cells consisting of the following materials (from the top): polymer layer/SAM-functionalization/PEDOT:PSS/ITO were studied by deposition of different silane-based SAMs at the surface of thin film of PEDOT:PSS. However, the self-assembly process of the SAMs at organic materials is complex, largely unexplored and requires special pretreatment of the surface [271]. Here, the inhomogeneous self-assembly on the PEDOT:PSS is evidenced by the KPFM and sSIMS studies. After this step the XPS depth profiling with GCIB is employed to study the chemical composition through multilayer samples with homogenously deposited various silane-based SAMs at the interface between PEDOT:PSS and, first PS and then RP3HT:PCBM blend. The obtained results were related to the acquired I-V characteristics of the analogically prepared organic solar cells.

3.1. Micro-contact printed APTES pattern on PEDOT:PSS surface – evidence of SAM formation

In the first step, the evidence of SAM self-assembly on PEDOT:PSS was studied by µCP APTES molecules with “brick wall” stamp on the thin film of PEDOT:PSS surface (ITO was used as the substrate). sSIMS technique working in the imaging mode was used to localize the deposition of SAM at the surface by tracking the Si^- secondary ion signal with results shown in Figure 86a. The stamp structure is clearly observable and indicates localized deposition of APTES molecules on the PEDOT:PSS surface. This is also confirmed by mapping the S^- secondary ion signal (Figure 86b) which originates from the PEDOT:PSS and due to the coverage, the lower signal is detected at the areas of SAM deposition.

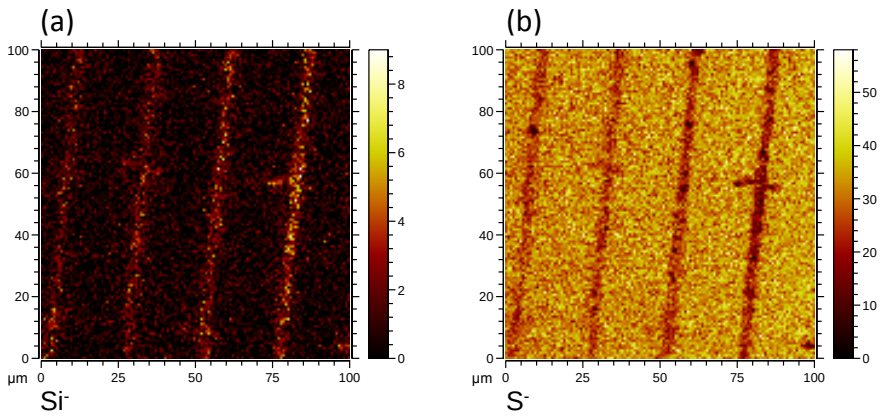

Figure 86. sSIMS maps of µCP SAM on the PEDOT:PSS surface: (a) Si^- signal indicates the location of APTES pattern on the surface which is also confirmed by (b) S^- secondary ions signal map whereas lower signal form substrate is detected in SAM deposition areas.

In the next step, the samples were analyzed with KPFM. From the inspection of a topography map, depicted in Figure 87a, the presence of SAM may be demonstrated by elevated surfaces with the characteristic stamp shapes. This is also acknowledged on the CPD map (Figure 87b), whereas well resolved higher CPD signal areas are arranged in the stamp structure indicating SAM localized decrease of PEDOT:PSS work function.

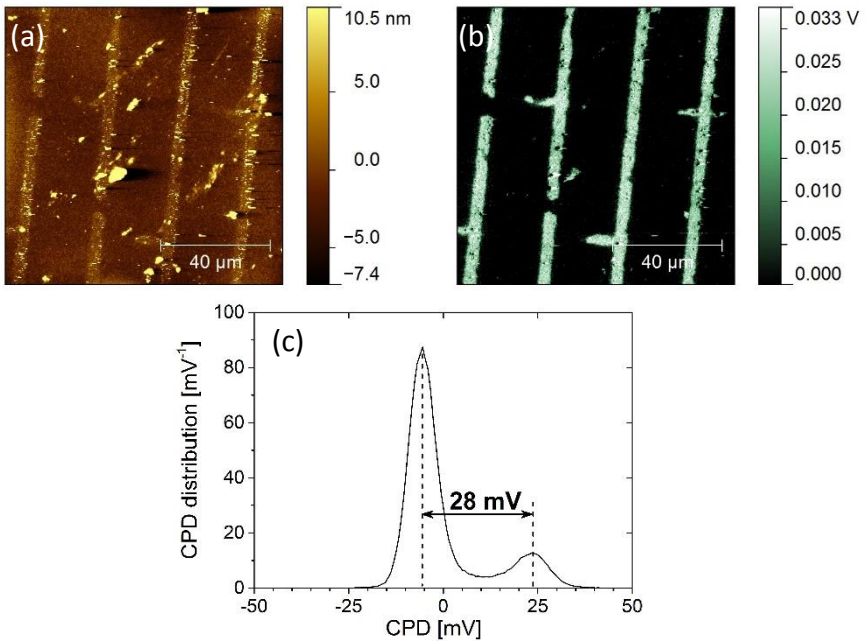

Figure 87. The KPFM results of APTES localized stamp functionalization on the PEDOT:PSS surface. (a) surface topography map with clearly visible areas of stamp deposited SAM (b) simultaneously acquired CPD map reveals decrease of PEDOT:PPS work function due to the APTES localized functionalization which can be estimated from (c) histogram at 28±6 mV.

Quantitatively, the decrease of the substrate work function can be estimated from the histogram presented in Figure 87c, which gives the value of 28±6 mV. Generally, silane-based monolayers assembled on silicon/silicon oxide substrates exhibit much lower

order than corresponding thiols [82] and this disorder might be extended on polymer substrates like PEDOT:PSS due to the fact that ordering and packing is determined by the underlying surface structure, which in the case of most polymers is amorphous. From the theoretical modelling of free molecule dipole moment of APTES it appears that its direction is almost perpendicular to the backbone, thus resultant influence on the CPD will vary with the tilt of the adsorbed molecule with respect to surface the normal [83]. Presented KPFM results have shown that this inconvenience, in the case of designing appropriate properties of the junction, can be assigned and detected at an early stage of device fabrication.

The main purpose of employing KPFM to these systems was to demonstrate its utility to examine the inhomogeneities appearing at the surface and interface of organic conducting materials. Additionally, this technique made it possible to confirm SAMs deposition and reveal self-assembly driven influence on the contact potential difference.

3.2. PS covered PEDOT:PSS SAM functionalized electrode

To study the chemical composition and specificity of the organic/organic interfaces, the XPS depth profiling with GCIB was proposed. First, this technique was applied for a model multilayer organic system which consists of polystyrene thin film covering F3Si-SAM homogenously functionalized PEDOT:PSS thin layer spin-cast on silicon (with native oxide). The sample structure is schematically shown in Figure 88.

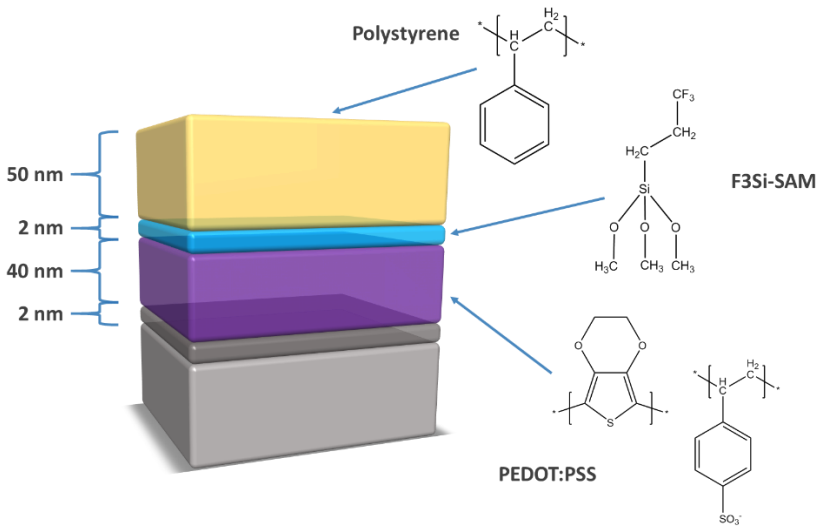

Figure 88. Illustration of multilayer sample architecture with the chemical structures of corresponding materials. The overall thickness of this stack (including silicon native oxide) is about 100 nm. The silicon wafer with its native oxide forming 2 nm thick overlayer (dark grey) was used as a substrate.

The bonding states obtained for C1s, F1s, O1s and Si2p core levels at each cycle of sputtering are shown in Figure 89. In the polystyrene layer, the C1s region (Figure 89a) consists of the main symmetric peak at 284.8 eV assigned to sp^3 carbon-carbon bonding

and the second peak at 291.5 eV which describes shake-up satellite due to the aromatic benzene ring excitation. The bold blue spectra line, terminated with dots, reflects the carbon states at the interface and additionally, to that found for polystyrene, it includes the peak at 287.4 eV and the tiny peak 292.5 eV for carbon-oxygen and carbon-fluorine bondings, respectively. Further on, the small peaks at higher binding energies disappear and the remaining spectrum for PEDOT:PSS layer consist of carbon-carbon, carbon-sulfur (lying very close to C-C line) and carbon-oxygen lines. At the analogous stack of spectra acquired for F1s region shown in Figure 89b, the only visible signal comes from the interface and is indicated by strong symmetric peak at 688.5 eV attributed to fluorine-carbon. This signal describes well the presence of F3Si-SAM at the interface and indicates undisturbed structure of the monolayer end group. The corresponding spectra of O1s regions (Figure 89c) show visible signal starting from the interface which is the convolution of at least two peaks at 531.8 eV and 532.8 eV which are assigned to oxygen-carbon and oxygen-silicon. The first peak originates from the PEDOT:PSS presence whereas the second one is expected due to the F3Si-SAM functionalization at the interface and disappears shortly after the ongoing sputtering process, thus indicating e.g. no SAM diffusion into PEDOT:PSS. After the interface, the O1s signal is stable, characteristic for PEDOT:PSS until reaching silicon native oxide on the silicon wafer where the oxygen-silicon line at 532.8 eV becomes the leading one and disappearing due to the sputtering and silicon borrow appearance. The adequate spectra were taken for Si2p core-level areas and are presented collectively in Figure 89d. The silicon signal first becomes visible at the interface at the binding energy of 103.7 eV and is assigned to silicon-oxygen bondings appearance due to the F3Si-SAM presence, additionally providing and ensuring monolayer formation. Through the PEDOT:PSS layer the silicon signal disappears and becomes significant reaching first silicon native oxide (103.7 eV) and then silicon wafer where a major peak at 100.1 eV attributed to silicon-silicon bondings is the most visible.

The deconvoluted spectra, in terms of chemical bonding identification for all measured constituents, can be used to plot the atomic concentration depth profile regarding material from which they derived from. The resultant depth profile is shown in Figure 90. It should be noted that four different layers can be easily recognized and assigned. First, PS layer, is composed only of carbon which is evident at the profile where carbon reaches and stabilizes at about 100%. Noteworthy, at the interface (see inset), due to the F3Si-SAM presence and its chemical structure, the expected value of fluorine to silicon (F/Si) ratio is 3.0, whereas experimentally determined ratio was found at 2.7 which gives a very good agreement and additionally assures pristine monolayer presence. The exact composition of the monolayer cannot be determined at this stage due to the interleaving of signals originating both from PS layer residue and incoming

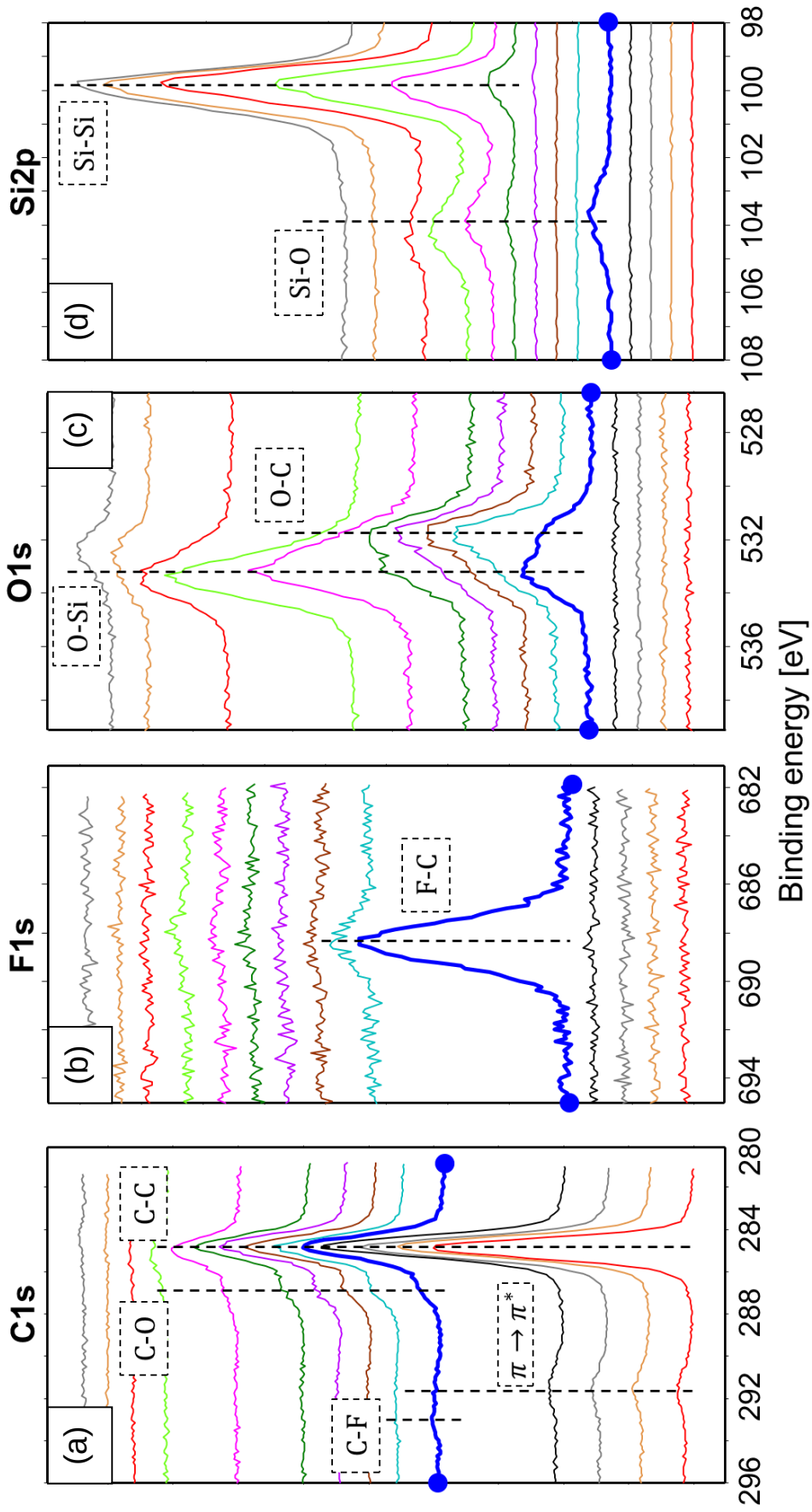

Figure 89. XPS depth profiles of (a) C1s, (b) F1s, (c) O1s and (d) Si2p core levels obtained with Ar GCIB sputtering process of the PS/3FSi-SAM/PEDOT:PSS/SiO/Si structure. The corresponding lines indicate chemical composition and structure of the constituents in each depth. The bold blue spectra terminated with dots reflect the interface structure and composition between PS and PEDOT:PSS including SAM. Note that during the sputtering process with GCIB the specific chemical structure of each layer is maintained. The lowest spectra reflect the surface whereas the highest one corresponds to silicon substrate.

PEDOT:PSS layer. The next layer of PEDOT:PSS is characterized by three signals: C1s, O1s and S2p which are stable and with average experimentally derived concentrations of 68.8%, 20.3% and 7.4%, respectively. The expected composition for PEDOT:PSS is 66.7%, 23.8% and 9.5% atomic percent of carbon, oxygen and sulfur, respectively. Thus, the experimental values are in reasonably good agreement with the expected ones and provide evidence of GCIB usefulness for chemically stable depth profiling. Additionally, the effect of significant difference between sputter ion yields of polymer/organic materials and inorganic ones during GCIB sputtering is highlighted as silicon oxide layer, which has a similar thickness as the F3Si-SAM monolayer, but appears very broad and blunt.

The presented results of XPS depth profiling with GCIB on model multilayer system demonstrate that this method can be successfully employed for characterization and detection of chemical compositions within organic thin film stacks, including very thin SAMs formed between organic layers, moreover, providing accurate quantitative and qualitative information through the analyzed material.

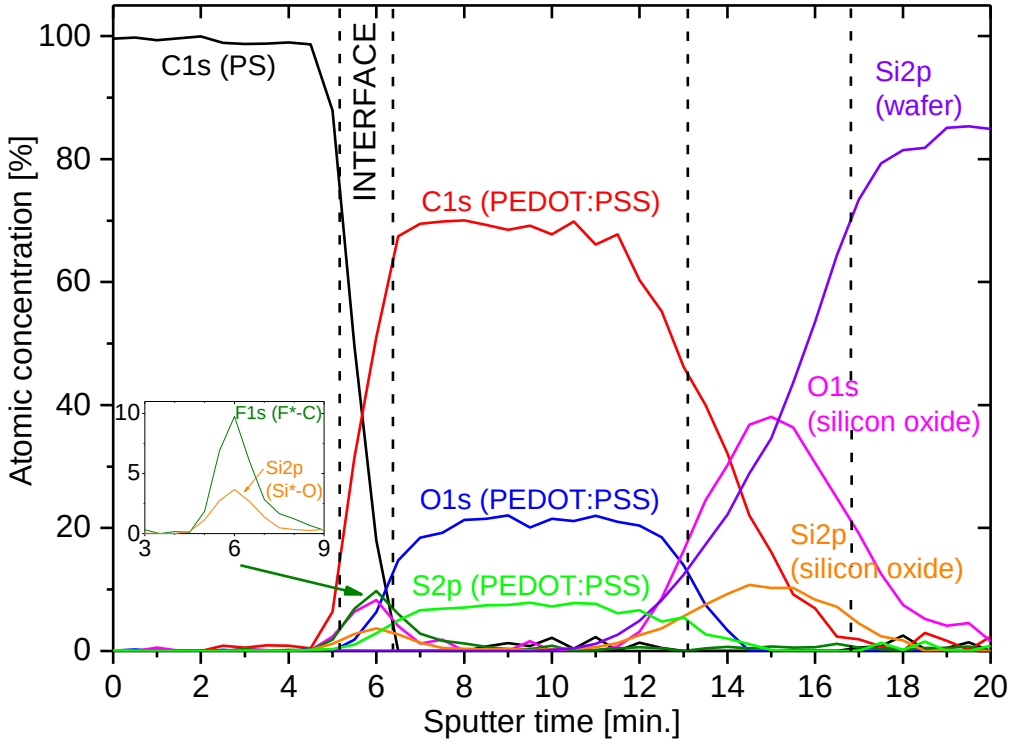

Figure 90. Atomic concentration XPS depth profile obtained with GCIB sputtering of PS/F3Si-SAM/PEDOT:PSS/SiO/Si multilayer model system. The presence of F3Si-SAM at the interface is revealed by F1s and Si2p signals with experimentally derived F/Si ratio of 2.7, whereas expected, theoretical value is 3.0. The signals of C1s, O1s and S2p for PEDOT:PSS are stable and indicate no sputtering driven chemical composition changes of examined polymer film.

3.3. RP3HT:PCBM/SAM/PEDOT:PSS/SiO_2/Si

In the previous section, on the basis of the obtained results from XPS depth profiling with GCIB, it was shown that this method, applied to a model multilayer organic system, gives satisfactory quantitative and qualitative analysis of surface and bulk chemical

composition changes. Here, this method is applied for multilayer thin film stacks used in designing the heterojunction-based organic solar cells. As the active material, the RP3HT:PCBM blend was spin-cast on the PEDOT:PSS anode modified by various self-assembling silane-based molecules. The XPS sputter depth profiling with Ar cluster ion beam has been used to control structure and adsorption of SAM molecules on the PEDOT:PSS surface and to demonstrate interactions that might arise between both materials. Finally, the obtained results are discussed in terms of experimentally derived device performance changes due to the SAM deposition.

In Figure 91 the 3D representation of examined organic layers locations within the multilayer structure obtained with dSIMS is presented. The C_8^- secondary ion mass signal at the top is attributed to the RP3HT:PCBM blend layer presence whereas the layer visualized as second, obtained by tracking SiO^- signal, determines silane-SAM deposited onto PEDOT:PSS (CHO_2^-) thin film. The Si^- signal situates the substrate. It should be noted that the z-scale does not correspond to the real thicknesses variations of the involved layers due to the different sputter yields of these materials, but it reflects the sputtering time.

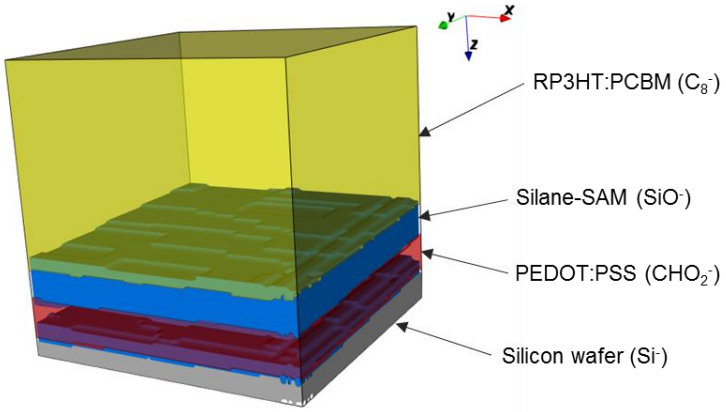

Figure 91. 3D graphic representation of multilayer structure (PS/Silane-SAM/PEDOT:PSS/Si) obtained by tracking chosen masses of secondary ions acquired with ToF-SIMS depth profiling, characteristic for each layer.

Two sample series were prepared at the same time using the same procedure – one batch with silicon wafer as the substrate and second one employing the ITO. The first one was used for XPS depth profiling whereas the second, with thermally evaporated aluminum electrode on top, for performance studies.

3.3.1. F3Si-SAM

First, the multilayer structure similar to that presented for a model system, where PEDOT:PSS anode was modified with F3Si-SAM was studied, but here the polystyrene layer is exchanged for thin film of RP3HT:PCBM blend. Atomic concentration XPS depth profiles for involved constituents are presented in Figure 92. Four different layers can be recognized with a fifth layer forming the substrate. The RP3HT:PCBM blend is

evidenced by tracking spectra of C1s, S2p and O1s regions. The first two specified regions, C1s and S2p, are stable through the layer with average atomic concentrations of 94.3 % and 4.4 %, respectively. The third one, O1s, is weakly visible due to very low atomic concentration of the oxygen in the overall film composition (it originates from PCBM's ester group). However, the calculated average atomic concentration from this region is about 1% and falls to zero when the RP3HT:PCBM layer is sputtered out, thus, confirms its origin from the polymer blend. With the end of the first layer, the interface appears where the F3Si-SAM was deposited on PEDOT:PSS. Indeed, the SAM layer is evidenced from the inspection of the Si2p and F1s regions where the appearing lines and their positions can be attributed to Si-O and F-C bonds, similarly as for the previously presented model system.

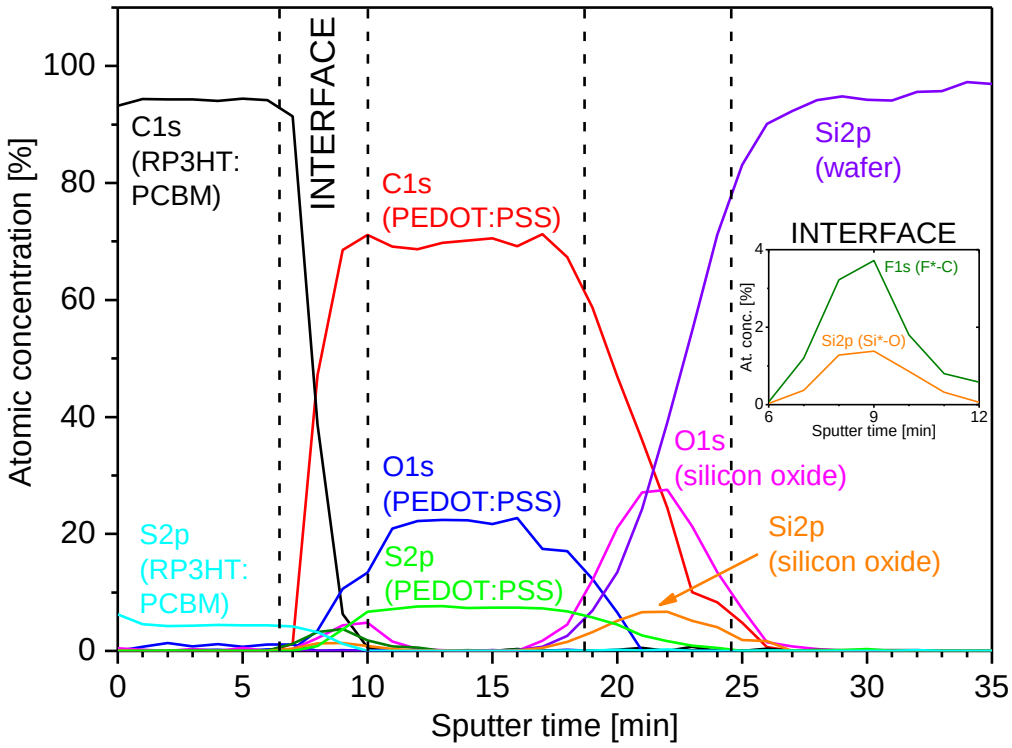

Figure 92. XPS atomic concentrations depth profiles of RP3HT:PCBM/F3Si-SAM/PEDOT:PSS/SiO/Si structure showing four different regions attributed to four layers with fifth layer forming substrate. The elemental composition of each layer is determined by tracing the areas of appropriate lines attributed to adequate chemical states of involved elements. The inset shows interface composition determined by F1s and Si2p core-level regions revealing the F3Si-SAM presence additionally confirmed by estimated F/Si atomic concentration ratio at 2.7 whereas theoretical predictions give value of 3.0.

The inset presented in Figure 92 shows interface atomic composition depth profile of both components which additionally proves the presence of F3Si-SAM monolayer. The experimentally derived F/Si ratio is about 2.7 whereas the expected value is 3.0. The PEDOT:PSS film is well described by tracking the C1s, O1s and S2p core-level regions. All three lines in this area are stable with average atomic composition estimated at 69.6%, 22.3% and 7.9% for C, O and S, respectively. These values are in very good agreement with the expected ones for PEDOT:PSS composition mentioned previously for PS model

system in chapter I.3.2. After sputtering out the PEDOT:PSS layer, the existence of thin native oxide of silicon is evidenced by O1s and Si2p lines. Due to the large difference in sputtering yields between organic materials and inorganic ones, this thin native oxide appears very broad presented in function of sputtering time.

3.3.2. BrSi-SAM

The system studied next was the multilayer stack where PEDOT:PSS anode was modified with bromine terminated silane-based SAM. The XPS atomic concentration depth profiles for this system are presented in Figure 93.

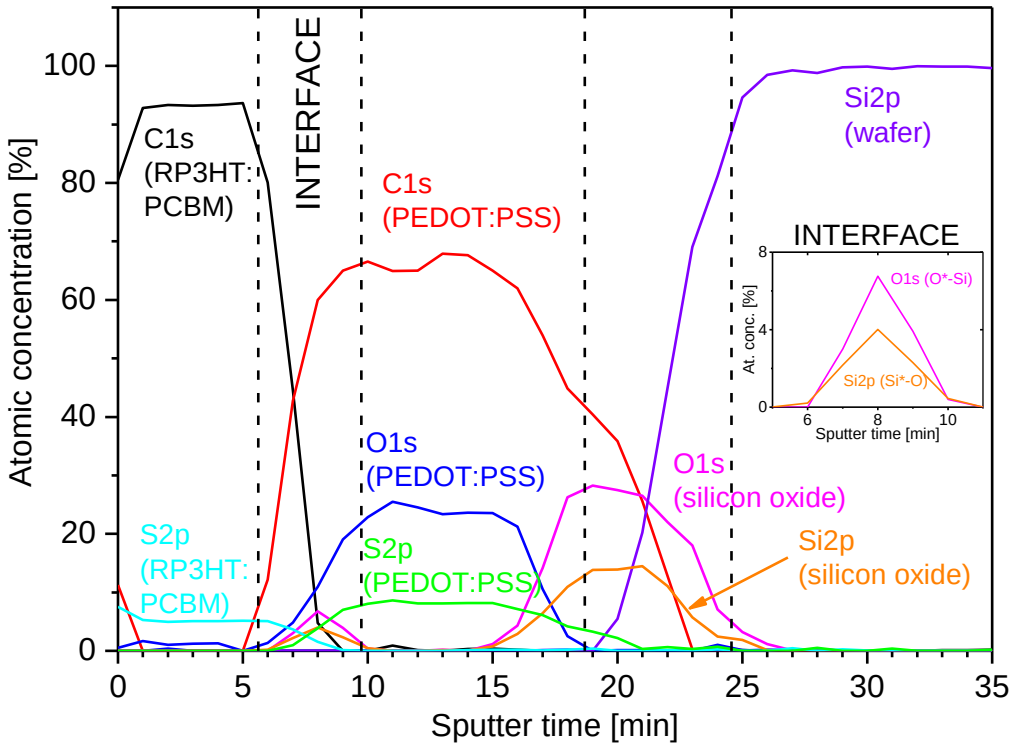

Figure 93. Atomic concentration depth profiles of RP3HT:PCBM/BrSi-SAM/PEDOT:PSS/SiO/Si structure derived from areas of specific line positions in the core-level regions of C1s, S2p, O1s and Si2p. The inset shows the interface atomic composition of elements which are attributed to self-assembled BrSi-SAM monolayer.

The active layer consisting of RP3HT:PCBM blend is stable and with average atomic concentration of involved elements similar as for the previously described system. It is worth noting that due to the radiation induced by exciting X-ray beam, the degradation of organic materials might appear especially for materials containing heteroatoms like chlorine, bromine and iodine, which manifest in strong decrease of relative concentrations of these elements [214]. Thus, in this case the Br3d core-level region of bromine cannot be used to mark the BrSi-SAM presence at the interface. However, there is still a possibility to use appropriate lines at Si2p and O1s regions attributed to silicon-oxide and oxide-silicon bonds, respectively. Indeed, by the examination of these regions at the interface, what is shown as inset in Figure 93, the Si2p and O1s core-level

spectra reflect the existence of the BrSi-SAM monolayer. The expected O/Si atomic concentration ratio at the interface originating from the anchoring groups of perfectly ordered BrSi-SAM molecules at PEDOT:PSS is 2.0, whereas experimentally derived amounts to 1.8 which is a satisfactory result considering presumably non-perfectly homogeneous BrSi-SAM monolayer. The next layer of PEDOT:PSS is described by stable atomic concentrations of carbon, oxygen and sulfur with average values similar to the previously reported F3Si-SAM multilayer system and in good agreement with theoretical predictions. The native silicon oxide covering silicon substrate is also evidenced from the inspection of Si2p and O1s spectra, similarly to the previously described systems.

3.3.3. APTES

For the multilayer system where APTES was used to modify PEDOT:PSS anode, the obtained XPS atomic composition depth profiles, presented in Figure 94, reveal different behavior when compared with previously described cases.

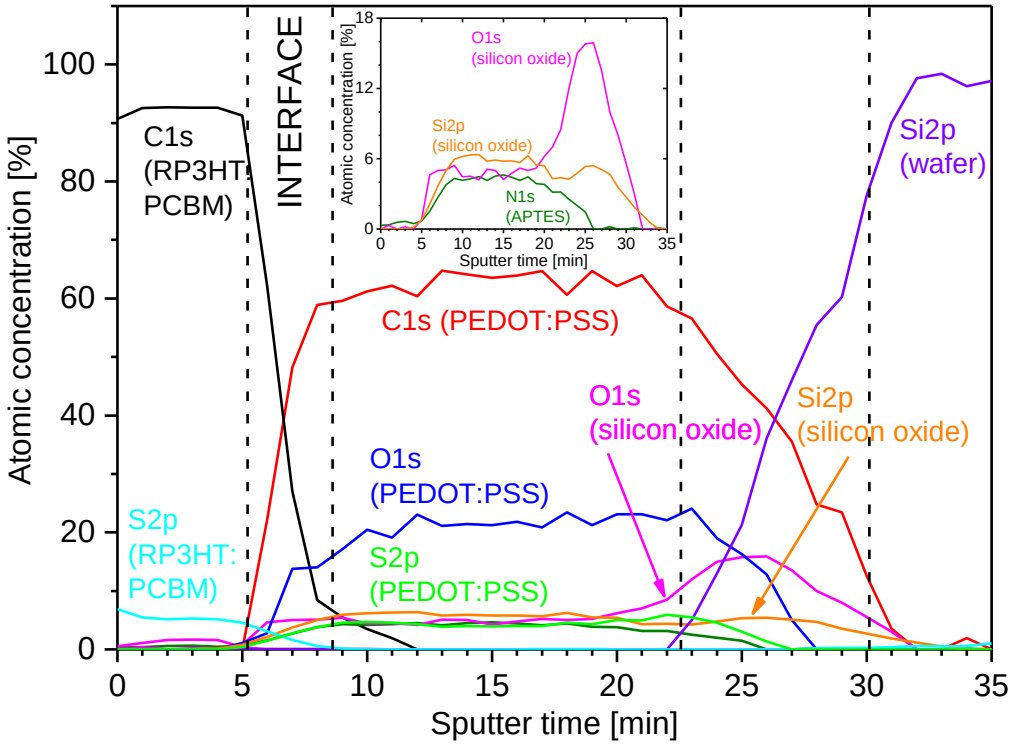

Figure 94. XPS atomic composition depth profiles of RP3HT:PCBM/APTES/PEDOT:PSS/SiO/Si structure obtained by tracking areas of specific line positions, attributed to each material, of C1s, S2p, O1s, N1s and Si2p core-level regions. The APTES originating concentrations of nitrogen, oxygen and silicon are depicted as an inset and are detected throughout the PEDOT:PSS layer, indicating its intermix with anode material..

The beginning of the composition profile, in the region where RP3HT:PCBM blend was spin-cast, is similar to that found for other systems where stable compositions of carbon, sulfur and oxygen were determined. However, at the interface between polymer blend and PEDOT:PSS anode the core-level regions of Si2p and N1s reveal

APTES treatment of PEDOT:PSS but corresponding atomic concentrations stabilize and are continuously detected within PEDOT:PSS layer up to its ends. Moreover, when compared with the previously presented results, where the procedure was the same for PEDOT:PSS layer preparation, this layer here is much broader indicating APTES treatment driven changes. The atomic concentrations ratio obtained from examination of the areas of specific lines positions at C1s, O1s and S2p core-levels for PEDOT:PSS is similar to that found previously. Nevertheless, due to the almost identical atomic concentrations, derived from the core-level regions of S2p (from PEDOT:PSS), N1s (APTES), Si2p (APTES) and O1s (APTES), their profiles interlace each other, thus to visualize better the ongoing concentration variations the inset in Figure 94 depicts only elements originating from APTES. The N1s and Si2p derived concentrations attributed to SAM layer are stable throughout the PEDOT:PSS layer and the N/Si atomic concentration ratio is close to 1.0 which is an expected value due to the APTES structure. However, the theoretically predicted O/N or O/Si ratio should be equal to 3.0 for free standing molecules and 2.0 for ideally ordered SAM on substrate but experimentally derived ratio amounts to 1.0. This indicates that the anchoring groups of APTES undergo unusual interactions, including oxygen-silicon bonds breaking, with PEDOT:PSS forming bonds that are not present in the case of simple self-assembly process. That was only to be expected because the APTES monolayer was not formed on the surface of anode but, as indicated by XPS depth profiles, it was intermixed with PEDOT:PSS. With the end of PEDOT:PSS layer the nitrogen concentration falls down, and a small decrease in concentration of silicon is also evidenced but then it rises again due to the appearance of native silicon oxide. The same is true for oxygen concentration attributed to O-Si bonds which increase strongly when the native oxide is reached.
The obtained results indicated that the procedure used for anode modification with APTES is not suitable, due to the intermixing with substrate material which changes layer thickness and introduces unpredictable chemical reactions of head SAM head group leading to unspecified oxygen loss.

3.3.4. MPTES

The last multilayer structure studied was composed of MPTES modified PEDOT:PSS anode. The XPS atomic concentration depth profiles of involved constituents are presented in Figure 95. The first layer of RP3HT:PCBM shows similar atomic composition of carbon, sulfur and oxygen and roughly the same thickness as in the case of the previously described systems. The interface between polymer blend and PEDOT:PSS layer is clearly outlined and the oxygen and silicon concentrations attributed to MPTES structure appear as presented on the inset in Figure 95. It should be noted that due to the sulfur presence, both in SAM and PEDOT:PSS structure, the atomic concentration of this element cannot be used to distinguish SAM from anode material because both materials consist of sulfur-carbon bonds and their binding energy shift is indistinguishable. Similarly to BrSi-SAM modified PEDOT:PSS, this necessitated

employment of silicon and oxygen atomic concentration profiles derived from areas of lines ascribed to silicon-oxygen bonds originating from MPTES head group. As for the previous cases the O/Si atomic concentration ratio for a perfectly ordered monolayer should be equal to 2.0, whereas experimentally derived value is about 2.4, which is in reasonably good agreement for surely not well-ordered and non-fully homogenous MPTES monolayer. Further on, the atomic concentrations attributed to MPTES molecules decrease to zero at the stage where stable atomic concentrations of carbon, oxygen and sulfur indicate undisturbed PEDOT:PSS layer presence. The average atomic concentrations for that layer are similar to that found for the previously discussed systems and the layer thickness, related to sputtering time, seems to be comparable. Here, the concentration profiles of silicon and oxygen reveal native silicon oxide presence at the silicon substrate.

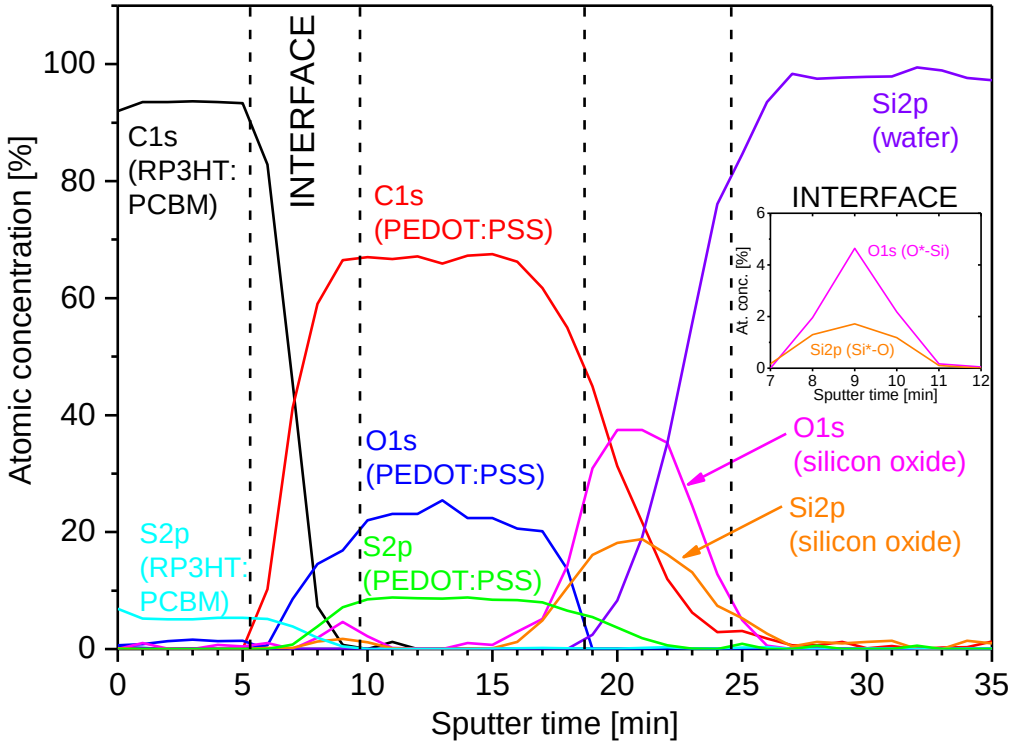

Figure 95. Atomic concentration depth profiles of RP3HT:PCBM/MPTES/PEDOT:PSS/SiO/Si structure obtained for specified binding energy chemical shifts related to each of the material, for core-level regions of C1s, S2p, O1s and Si2p. The inset shows the atomic concentrations of elements attributed to MPTES presence.

3.3.5. Influence of the PEDOT:PSS modification on the performance of organic solar cells

The XPS depth profiling of organic multilayer systems with GCIB gives opportunity to study unaltered chemical composition throughout the examined materials with satisfactory and feasible qualitative and quantitative results. The obtained results from depth profiling of organic solar cell multilayer structures, with different SAMs employed

to modify the PEDOT:PSS anode, show that the studied silane-based self-assembling molecules can be successfully deposited on the anode's surface with the only exception of APTES SAM which intermixed and reacted with the PEDOT:PSS. The aim of these SAM modifications was to examine its influence on the overall solar cell performance (power conversion efficiency) compared with unaltered PEDOT:PSS anode. These stages of device testing and performance studies do not constitute the part of this thesis but are presented here to demonstrate differences appearing within the same multilayer organic structure driven by the changes in self-assembling molecule end group. The device performance results are presented in Table 13.

Table 13. Influence of the PEDOT:PSS anode modification with various SAMs on organic solar cell performance (PCE – power conversion efficiency). The value in brackets for APTES modification was obtained using other technique of deposition (see text for details) [272].

	F3Si-SAM	BrSi-SAM	APTES	MPTES
PCE [%]	0.90	0.22	<0.01 (0.57)	<0.01

It is clear that SAM modification strongly influences the performance of organic solar cells made out of RP3HT:PCBM blend as the active material. The best result was obtained for F3Si-SAM functionalized PEDOT:PSS anode with the power conversion efficiency (PCE) of about 0.90 %. The device performance with anode modified by APTES and MPTES with the procedure presented in this thesis gives PCE values beneath 0.01%, but when the procedure for APTES was changed to vapour-driven functionalization the device performance reached 0.57 %.

V. Conclusions

Within the framework of this thesis a large variety of interfaces between both organic-metal and organic-organic thin films were studied.

In the first part of the presented results, the interactions between polymer films and the metal substrate, originating from either desired SAM deposition or film/blend fabrication variations, are discussed.

The evaporated gold layer used as a substrate was meticulously described in terms of surface topography and electronic properties as studied using KPFM, XPS and UPS methods. It was found that the pristine, flat gold layer with electronically repeatable properties can be prepared.

With the well-defined substrate, the influence of CH3-SAM, COOH(L)-SAM and COOH(S)-SAM deposition with varying dipole moments was addressed, including ascertaining XPS measurements of their deposition. These reveal partial deprotonation to the carboxylate state of COOH(S)-SAM, excluding this self-assembling material from further investigations. The additionally conducted ARXPS measurements prove layer deposition and give valuable information on self-organized SAM structure. From the UPS measurements of homogenously functionalized gold substrates it was shown that deposition of COOH(L)SAM or CH3-SAM induce work function changes of the underlying substrate and that they can be used to tune this value, according to the direction and net dipole moment value of the molecules forming monolayer. Due to the chemically different end groups, the deposition of COOH(L)-SAM monolayer on the substrate makes surface hydrophilic, whereas CH3-SAM functionalization results is their hydrophobic behavior. All described results for homogenously deposited SAMs indicate formation of S-Au anchored, pristine monolayers.

To model the inhomogeneous interfaces, the µCP method was applied to locally deposit one type of SAM on the substrate and where unprinted areas were filled with the second type of SAM. The resulting structures were characterized with sSIMS running in imaging mode which confirmed local deposition of both SAMs. To study the effects of work function changes, driven by the submicron inhomogeneous SAM pattern presence at the surface, the KPFM technique was used. It was shown that in the areas of COOH(L)-SAM deposition the work function increases, whereas CH3-SAM decreases this property and that the difference of both shifts is in a good agreement with results found from UPS measurements on homogenously functionalized substrates.

In the next step, the SAM's patterned substrates where covered with thin layers of polymers which differ strikingly in terms of inter- and intra- molecular interactions as indicated by their hydrogen and polar contributions of Hansen Solubility Parameters. It was assumed that due to mixed hydrophobic and hydrophilic substrate surface properties, some interactions might appear between polar groups of hydrophilicity-causing COOH(L)-SAM and functional, polar groups in polymers. To study the interactions at buried interfaces, in the submicron range, the KPFM method was used,

whereas chemical compositions at the interfaces where revealed using dSIMS depth profiling in imaging mode.

First, the polystyrene, treated as a non-interacting and well-described polymer was chosen. The performed experiments show that even after covering a patterned substrate with a thin PS film, the KPFM CPD signal can be attributed to the dipole moment of the SAM monolayer placed at the buried PS/gold interface. On the other hand, dSIMS measurements provide information on lateral chemical composition within multilayer PS/SAM-pattern/metal structures with high depth and lateral resolutions and, by tracking O^- secondary ion signal at the interface, give possibility to attribute CPD variations found with KPFM to specific SAM molecules. It was found that even after covering with PS film, the CPD variations remain almost identical to those obtained for uncovered substrate. It was also pointed out that the measured CPD signal does not depend on polymer surface topography and, according to experiments repeated on PS dissolved in different solvents, it was concluded that solvents used have none or negligible influence on the measured CPD signals.

The P2VP polymer was chosen as an evolution of polystyrene one due to the possibly more polar and thus more interacting character as indicated by Hansen Solubility Parameters. For this system a few additional effects were addressed due to the presence of two distinct areas on the same SAM functionalized region as indicated on KPFM CPD map. It was concluded that the effect of two different bright areas could not be described as surface waviness driven. Moreover, after filtering out the topography image from waviness it turns out that the film morphology consist of two different spatial structures: hole-like and bicontinuous. It was concluded that, according to carried experiments, the effect of two distinct bright regions on CPD map cannot be straightly explained and thus additional studies should be undertaken.

The system studied next was a thin film of PAA spin-cast onto SAM patterned substrate. This polymer was proposed due to the expected possibility to involve in hydrogen bondings and polar interactions, as indicated by its high contributions values of corresponding Hansen Solubility Parameters. First, it was noticed that net dipole moment of the SAMs deposited on the gold surface can be divided into two main components attributed to backbone and end group which, for studied SAMs, causes dipole moment direction difference for both molecules. It was found that PAA thin film deposited on the locally polar and nonpolar functionalized substrate, as revealed with dSIMS depth profiling, results in flat, uniform KPFM CPD map with narrowly distributed CPD on the histrogram, contrary to that found for PS and P2VP. This effect was explained due to the hydrogen bonding interactions between end groups of COOH(L)-SAM and PAA polar groups, which led to depolarization effects and, according to the “dipole divided” model, caused net dipole moments of both SAM molecules to become almost equal and identically directed, therefore explaining obtained homogenous CPD map. The additional studies of PAA shown that polymer crystallinity has influence on

measured CPD signal, thus care must be taken when interpreting KPFM data from mixed amorphous and crystalline phases which might differ in their electronic properties.

The PMMA, as the main representative of methacrylates type polymers, was chosen as a development of the previously studied systems. It is characterized by high values of Hansen Solubility Parameters in terms of hydrogen bonding and polar contributions, however these values are significantly lower than those for PAA. In this part, the influence of polymer layer thickness on CPD signal in KPFM was studied. Additionally, the aspect of stereoregularity of polymer chains and their contribution to substrate/polymer interaction was introduced.

From the KPFM measurements of atactic PMMA gradient film thickness samples, it was concluded that polymer film thickness has negligible or no influence on the measured CPD in the range of 30 ÷ 140 nm due to the fact that estimated CPD differences, even with very low uncertainty, overlap each other. The interesting issue was that for the at-PMMA it was found that CPD signal was inverted when compared with that obtained for uncovered and PS- or P2VP- covered substrates, despite the presence of identical SAM pattern at the interface, as confirmed by dSIMS measurements. The inversion of the CPD signals was explained by inter-association and depolarization effects, similarly to PAA case, however, for the at-PMMA and COOH(L)-SAM molecules the interacting groups are not identical, thus different effect can be considered. Two types of hydrogen bond interactions were proposed. The first one may appear between the carbonyl group of PMMA and the hydroxyl group of COOH(L)-SAM, whereas the second type is expected between the methoxy group of at-PMMA and the carbonyl group of COOH(L)-SAM. It was stated that the assumed driving force for conformational changes at the interface, which enables such interactions, was the possible hydrolysis of the PMMA ester group which might lead to the appearance of strong ionic bonds additionally reinforced by the acid-base interactions involving PMMA carbonyl groups and COOH(L)-SAM hydroxyl groups. In turn, appearing interactions changed the direction and the net dipole moment of the COOH(L)-SAM layer, which became slightly smaller but now points in the same direction as in CH_3-tailed monolayers. Additionally, the KPFM measurements carried on inversely patterned substrate, confirmed the inversion of CPD signals and due to the fact that prepared polymer film exhibits non-uniform morphology it leads to the conclusion that the measured CPD signal is not connected with polymer film morphology.

The system studied next was syndiotactic rich PMMA containing multilayer system, prepared in the same way as for previous experiments with at-PMMA. In the case of syn-PMMA film the inversion of the CPD signal was not observed. The CPD difference, driven by buried SAM induced dipole moments at the interface, is in good agreement with that obtained for PS, and indicates none or non-measureable interactions of syn-PMMA with the patterned substrate. To study the possible solvent influence on KPFM signal, the samples with syn-PMMA dissolved in different solvents were prepared. The KPFM results for these systems resemble the former case of syn-PMMA, and indicated

that both solvents used, toluene or chloroform, had insignificant impact on the measured CPD signal and besides, confirmed the non-inverted CPD behavior.

The last studied stereoisomer of poly(methyl methacrylate) was the isotactic one. According to KPFM results obtained for iso-PMMA there is every indication that iso-PMMA film remains inert within studied systems, likewise it was found for syn-PMMA and PS, and the direction of SAM's dipole induced CPD variations was consistent with that determined for not-covered COOH(L)-SAM/CH3-SAM patterned gold substrate, as confirmed by dSIMS depth profiles. Additionally, it was found that both crystalline and amorphous phases stay inert in contact with mixed polar/non-polar functionalized substrate but their different response for CPD was maintained, confirming results obtained for PAA system.

The next group of polymers studied within the framework of this thesis were conjugated polymers following polythiophene and its derivatives and polyaniline/PS blends.

The PT nanoparticles were synthesized by catalyzed oxidative polymerization in aqueous medium and the average dimension of obtained particles was estimated at 39±5 nm. From presented KPFM measurements of this material it appeared that PT nanoparticles exhibit higher work function than silicon which can be seen as a reasonable statement when compared with alkyl substituted PT equivalents. Additionally, the KPFM spatial resolution obtained on high resolution CPD map of drop-cast PT nanoparticles, was roughly estimated at 62 nm.

When summarizing the KPFM measurements of P3AT systems, it can be stated that KPFM made possible to characterize the conjugated polymers in a semiconducting state. Furthermore, it was successfully applied to study buried interface of SAM functionalized gold and polymer thin layer, however, a few issues due to screening effects were addressed.

The interpretation of KPFM observations made previously for the PS and PMMA model systems, consisting of SAM-patterned metal interfaces covered with a uniform films of insulating polymers, were employed to discuss the KPFM results for thin film blends of PS and conducting polyaniline doped with camphorsulfonic acid. It was found that on the topography map, the signal contrast was comparable for all domains of the same type, and the CPD signal was constant within each individual domain but it varied from one domain to the other. The interpretation of CPD data for the model systems (PS/SAM or PMMA/SAM -patterned Au substrates) presented previously leads to the conclusion that the variations in the CPD signal can be induced by different interaction between individual PANI(CSA)-rich domains and the Au substrate. The observed polarization was explained by water vapor interaction with the PANI(CSA) domains during spin-coating and due to the fact that polyaniline is hydrophilic, the condensation should occur at the PANI(CSA) domains. It was proposed that the water molecules may interact with PANI(CSA) replacing the dopant (CSA), which segregated from the

substrate. This might cause polarization of the interface and explains CPD signal alteration for the same PANI(CSA) domains.

The second part of this thesis deals with organic-organic thin film interfaces that play a key role in fabrication of organic solar cells. The main driving force for these investigations was to reveal interactions appearing at the interfaces between PEDOT:PSS anode modified with various silane-based SAMs and RP3HT:PCBM blend and their relation to the device performance. The XPS depth profiling with GCIB was utilized and gave opportunity to study unaltered chemical composition throughout the examined materials with satisfactory and feasible qualitative and quantitative results. The obtained results from depth profiling of organic solar cell multilayer structures, with different SAMs employed to modify the PEDOT:PSS anode, show that the studied silane-based self-assembling molecules can be successfully deposited on the surface of anode with the one exception of APTES SAM, which intermixed and reacted with the PEDOT:PSS. It was mentioned, according to device performance studied not covered by this thesis, that SAM modification strongly influences the performance of organic solar cells made of RP3HT:PCBM blend as the active material. The device performance with anode modified by APTES and MPTES with the procedure presented in this thesis gave the lowest values but when the procedure for APTES was changed to vapour-driven functionalization the device performance increased five times.

References

[1] M. Gobbi, L. Pietrobon, A. Atxabal, A. Bedoya-Pinto, X. Sun, F. Golmar, R. Llopis, F. Casanova, L.E. Hueso, Determination of energy level alignment at metal/molecule interfaces by in-device electrical spectroscopy, Nat Commun, 5 (2014).

[2] M. Oehzelt, N. Koch, G. Heimel, Organic semiconductor density of states controls the energy level alignment at electrode interfaces, Nature Communications, 5 (2014).

[3] H. Ishii, K. Sugiyama, E. Ito, K. Seki, Energy level alignment and interfacial electronic structures at organic/metal and organic/organic interfaces, Advanced Materials, 11 (1999) 605-625.

[4] S. Braun, W.R. Salaneck, M. Fahlman, Energy-level alignment at organic/metal and organic/organic interfaces, Advanced Materials, 21 (2009) 1450-1472.

[5] J. Hwang, A. Wan, A. Kahn, Energetics of metal-organic interfaces: New experiments and assessment of the field, Materials Science & Engineering R-Reports, 64 (2009) 1-31.

[6] C. Goh, S. Scully, M. McGehee, Effects of molecular interface modification in hybrid organic-inorganic photovoltaic cells, Journal of Applied Physics, 101 (2007).

[7] S.A. DiBenedetto, A. Facchetti, M.A. Ratner, T.J. Marks, Molecular self-assembled monolayers and multilayers for organic and unconventional inorganic thin-film transistor applications, Advanced Materials, 21 (2009) 1407-1433.

[8] Q. Guo, F. Li, Self-assembled alkanethiol monolayers on gold surfaces: resolving the complex structure at the interface by STM, Physical Chemistry Chemical Physics, 16 (2014) 19074-19090.

[9] R. Otero, J. Gallego, A. de Parga, N. Martin, R. Miranda, Molecular Self-Assembly at Solid Surfaces, Advanced Materials, 23 (2011) 5148-5176.

[10] F. von Wrochem, D. Gao, F. Scholz, H.-G. Nothofer, G. Nelles, J.M. Wessels, Efficient electronic coupling and improved stability with dithiocarbamate-based molecular junctions, Nat Nano, 5 (2010) 618-624.

[11] D. Janssen, R. De Palma, S. Verlaak, P. Heremans, W. Dehaen, Static solvent contact angle measurements, surface free energy and wettability determination of various self-assembled monolayers on silicon dioxide, Thin Solid Films, 515 (2006) 1433-1438.

[12] J. Genzer, R.R. Bhat, Surface-bound soft matter gradients, Langmuir, 24 (2008) 2294-2317.

[13] B. Bergues, J. Lekki, A. Budkowski, P. Cyganik, M. Lekka, A. Bernasik, J. Rysz, Z. Postawa, Phase decomposition in polymer blend films cast on homogeneous substrates modified by self-assembled monolayers, Vacuum, 63 (2001) 297-305.

[14] J. Jaczewska, A. Budkowski, A. Bernasik, I. Raptis, E. Moons, D. Goustouridis, J. Haberko, J. Rysz, Ordering domains of spin cast blends of conjugated and dielectric polymers on surfaces patterned by soft- and photo-lithography, Soft Matter, 5 (2009) 234-241.

[15] J. Haberko, J. Raczkowska, A. Bernasik, J. Rysz, A. Budkowski, W. Łuzny, Pattern replication in polyaniline-polystyrene thin films, Synthetic Metals, 157 (2007) 935-939.

[16] Z. Chen, Investigating buried polymer interfaces using sum frequency generation vibrational spectroscopy, Progress in Polymer Science (Oxford), 35 (2010) 1376-1402.

[17] M. Gorgoi, S. Svensson, F. Schäfers, G. Öhrwall, M. Mertin, P. Bressler, O. Karis, H. Siegbahn, A. Sandell, H. Rensmo, W. Doherty, C. Jung, W. Braun, W. Eberhardt, The high kinetic energy photoelectron spectroscopy facility at BESSY progress and first results, Nuclear Instruments and Methods in Physics Research, Section A: Accelerators, Spectrometers, Detectors and Associated Equipment, 601 (2009) 48-53.

[18] E.M.J. Johansson, R. Schölin, H. Siegbahn, A. Hagfeldt, H. Rensmo, Energy level alignment in TiO 2/dipole-molecule/P3HT interfaces, Chemical Physics Letters, 515 (2011) 146-150.

[19] H. Yip, S. Hau, N. Baek, H. Ma, A. Jen, Polymer solar cells that use self-assembled-monolayer-modified ZnO/Metals as cathodes, Advanced Materials, 20 (2008) 2376-+.
[20] I. Lange, J.C. Blakesley, J. Frisch, A. Vollmer, N. Koch, D. Neher, Band Bending in Conjugated Polymer Layers, Physical Review Letters, 106 (2011) 216402.
[21] A. Liscio, E. Orgiu, J. Mativetsky, V. Palermo, P. Samori, Bottom-Up Fabricated Asymmetric Electrodes for Organic Electronics, Advanced Materials, 22 (2010) 5018-+.
[22] A. Oprea, N. Barsan, U. Weimar, Ammonia detection mechanism with polyacrylic acid sensitive layers: Field effect transduction, Sensors and Actuators, B: Chemical, 111-112 (2005) 577-581.
[23] M. Hoerter, A. Oprea, N. Bârsan, U. Weimar, Kelvin Probe measurements of polymer coated gold substrates: Mechanism studies, Sensors and Actuators, B: Chemical, 134 (2008) 266-272.
[24] D. Yun, C. Jung, H. Lee, K. Kim, Y. Kyoung, A. Benayad, J. Chung, Damage-Free Photoemission Study of Conducting Carbon Composite Electrode Using Ar Gas Cluster Ion Beam Sputtering Process, Journal of the Electrochemical Society, 159 (2012) H626-H632.
[25] D. Yun, J. Chung, C. Jung, Y. Chung, S. Kim, S. Lee, K. Kim, H. Han, G. Park, S. Park, A novel approach for the characterization of a bilayer of phenyl-c71-butyric-acid-methyl ester and pentacene using ultraviolet photoemission spectroscopy and argon gas cluster ion beam sputtering process, Journal of Applied Physics, 114 (2013).
[26] R. Strayer, W. Mackie, L. Swanson, Work Function Measurements By Field-Emission Retarding Potential Method, Surface Science, 34 (1973) 225-248.
[27] Y. Gao, Surface analytical studies of interfaces in organic semiconductor devices, Materials Science & Engineering R-Reports, 68 (2010) 39-87.
[28] W. Osikowicz, M.P. De Jong, S. Braun, C. Tengstedt, M. Fahlman, W.R. Salaneck, Energetics at Au top and bottom contacts on conjugated polymers, Applied Physics Letters, 88 (2006).
[29] M. Fahlman, A. Crispin, X. Crispin, S. Henze, M. de Jong, W. Osikowicz, C. Tengstedt, W. Salaneck, Electronic structure of hybrid interfaces for polymer-based electronics, Journal of Physics-Condensed Matter, 19 (2007).
[30] R. Murdey, W. Salaneck, Charge injection barrier heights across multilayer organic thin films, Japanese Journal of Applied Physics Part 1-Regular Papers Brief Communications & Review Papers, 44 (2005) 3751-3756.
[31] W. Osikowicz, M. de Jong, W. Salaneck, Formation of the interfacial dipole at organic-organic interfaces: C-60/polymer interfaces, Advanced Materials, 19 (2007) 4213-+.
[32] H. Vazquez, F. Flores, A. Kahn, Induced Density of States model for weakly-interacting organic semiconductor interfaces, Organic Electronics, 8 (2007) 241-248.
[33] H. Vazquez, F. Flores, R. Oszwaldowski, J. Ortega, R. Perez, A. Kahn, Barrier formation at metal-organic interfaces: dipole formation and the charge neutrality level, Applied Surface Science, 234 (2004) 107-112.
[34] H. Vazquez, R. Oszwaldowski, P. Pou, J. Ortega, R. Perez, F. Flores, A. Kahn, Dipole formation at metal/PTCDA interfaces: role of the charge neutrality level, Europhysics Letters, 65 (2004) 802-808.
[35] W. Lin, S. Lee, M. Karakachian, B. Yu, Y. Chen, Y. Lin, C. Kuo, J. Shyue, Tuning the surface potential of gold substrates arbitrarily with self-assembled monolayers with mixed functional groups, Physical Chemistry Chemical Physics, 11 (2009) 6199-6204.
[36] N. Gozlan, U. Tisch, H. Haick, Tailoring the work function of gold surface by controlling coverage and disorder of polar molecular monolayers, Journal of Physical Chemistry C, 112 (2008) 12988-12992.
[37] N. Peor, R. Sfez, S. Yitzchaik, Variable density effect of self-assembled polarizable monolayers on the electronic properties of silicon, Journal of the American Chemical Society, 130 (2008) 4158-4165.

[38] S. Kera, Y. Yabuuchi, H. Yamane, H. Setoyama, K.K. Okudaira, A. Kahn, N. Ueno, Impact of an interface dipole layer on molecular level alignment at an organic-conductor interface studied by ultraviolet photoemission spectroscopy, Physical Review B - Condensed Matter and Materials Physics, 70 (2004) 085304-085301-085304-085306.
[39] D. Cahen, A. Kahn, Electron energetics at surfaces and interfaces: Concepts and experiments, Advanced Materials, 15 (2003) 271-277.
[40] C. Tengstedt, W. Osikowicz, W. Salaneck, I. Parker, C. Hsu, M. Fahlman, Fermi-level pinning at conjugated polymer interfaces, Applied Physics Letters, 88 (2006).
[41] S. Braun, W. Osikowicz, Y. Wang, W. Salaneck, Energy level alignment regimes at hybrid organic-organic and inorganic-organic interfaces, Organic Electronics, 8 (2007) 14-20.
[42] A. Oprea, N. Bârsan, U. Weimar, Work function changes in gas sensitive materials: Fundamentals and applications, Sensors and Actuators, B: Chemical, 142 (2009) 470-493.
[43] H. Ishii, N. Hayashi, E. Ito, Y. Washizu, K. Sugi, Y. Kimura, M. Niwano, Y. Ouchi, K. Seki, Kelvin probe study of band bending at organic semiconductor/metal interfaces: Examination of fermi level alignment, Physica Status Solidi (A) Applied Research, 201 (2004) 1075-1094.
[44] M. Pfeiffer, K. Leo, N. Karl, Fermi level determination in organic thin films by the Kelvin probe method, Journal of Applied Physics, 80 (1996) 6880-6883.
[45] C. Shen, A. Kahn, J. Schwartz, Chemical and electrical properties of interfaces between magnesium and aluminum and tris-(8-hydroxy quinoline) aluminum, Journal of Applied Physics, 89 (2001) 449-459.
[46] C. Shen, A. Kahn, J. Schwartz, Role of metal-molecule chemistry and interdiffusion on the electrical properties of an organic interface: The Al-F16CuPc case, Journal of Applied Physics, 90 (2001) 6236-6242.
[47] A. Wan, J. Hwang, F. Amy, A. Kahn, Impact of electrode contamination on the alpha-NPD/Au hole injection barrier, Organic Electronics, 6 (2005) 47-54.
[48] I. Ortiz-Hernandez, C.T. Williams, In Situ Investigation of Solid−Liquid Catalytic Interfaces by Attenuated Total Reflection Infrared Spectroscopy, Langmuir, 19 (2003) 2956-2962.
[49] D. Adil, S. Guha, Surface-enhanced Raman spectroscopic studies of the Au-pentacene interface: A combined experimental and theoretical investigation, Journal of Chemical Physics, 139 (2013).
[50] B. Pollard, E. Muller, K. Hinrichs, M. Raschke, Vibrational nano-spectroscopic imaging correlating structure with intermolecular coupling and dynamics, Nature Communications, 5 (2014).
[51] A. Henning, T. Hochwitz, J. Slinkman, J. Never, S. Hoffmann, P. Kaszuba, C. Daghlian, 2-Dimensional Surface Dopant Profiling In Silicon Using Scanning Kelvin Probe Microscopy, Journal of Applied Physics, 77 (1995) 1888-1896.
[52] T. Meoded, R. Shikler, N. Fried, Y. Rosenwaks, Direct measurement of minority carriers diffusion length using Kelvin probe force microscopy, Applied Physics Letters, 75 (1999) 2435-2437.
[53] R. Shikler, T. Meoded, N. Fried, Y. Rosenwaks, Potential imaging of operating light-emitting devices using Kelvin force microscopy, Applied Physics Letters, 74 (1999) 2972-2974.
[54] M. Fujihira, Kelvin probe force microscopy of molecular surfaces, Annual Review of Materials Science, 29 (1999) 353-380.
[55] C. Loppacher, U. Zerweck, S. Teich, E. Beyreuther, T. Otto, S. Grafstrom, L. Eng, FM demodulated Kelvin probe force microscopy for surface photovoltage tracking, Nanotechnology, 16 (2005) S1-S6.
[56] J. Lü, E. Delamarche, L. Eng, R. Bennewitz, E. Meyer, H.J. Güntherodt, Kelvin probe force microscopy on surfaces: investigation of the surface potential of self-assembled monolayers on gold, Langmuir, 15 (1999) 8184-8188.

[57] K. Hayashi, N. Saito, H. Sugimura, O. Takai, N. Nakagiri, Surface potential contrasts between silicon surfaces covered and uncovered with an organosilane self-assembled monolayer, Ultramicroscopy, 91 (2002) 151-156.
[58] R. Shikler, T. Meoded, N. Fried, B. Mishori, Y. Rosenwaks, Two-dimensional surface band structure of operating light emitting devices, Journal of Applied Physics, 86 (1999) 107-113.
[59] L. Burgi, H. Sirringhaus, R. Friend, Noncontact potentiometry of polymer field-effect transistors, Applied Physics Letters, 80 (2002) 2913-2915.
[60] L. Burgi, T. Richards, R. Friend, H. Sirringhaus, Close look at charge carrier injection in polymer field-effect transistors, Journal of Applied Physics, 94 (2003) 6129-6137.
[61] J. Nichols, D. Gundlach, T. Jackson, Potential imaging of pentacene organic thin-film transistors, Applied Physics Letters, 83 (2003) 2366-2368.
[62] L. Burgi, T. Richards, M. Chiesa, R. Friend, H. Sirringhaus, A microscopic view of charge transport in polymer transistors, Synthetic Metals, 146 (2004) 297-309.
[63] K. Maturova, M. Kemerink, M. Wienk, D. Charrier, R. Janssen, Scanning Kelvin Probe Microscopy on Bulk Heterojunction Polymer Blends, Advanced Functional Materials, 19 (2009) 1379-1386.
[64] A. De Sio, T. Modena, R. Huber, J. Parisi, S. Neyshtadt, F. Deschler, E. Da Como, S. Esposito, E. von Hauff, Solvent additives for tuning the photovoltaic properties of polymer-fullerene solar cells, Solar Energy Materials and Solar Cells, 95 (2011) 3536-3542.
[65] Q. Wang, Y. Zhou, H. Zheng, J. Shi, C. Li, C. Su, L. Wang, C. Luo, D. Hu, J. Pei, J. Wang, J. Peng, Y. Cao, Modifying organic/metal interface via solvent treatment to improve electron injection in organic light emitting diodes, Organic Electronics, 12 (2011) 1858-1863.
[66] T. Glatzel, H. Hoppe, N.S. Sariciftci, M.C. Lux-Steiner, M. Komiyama, Kelvin probe force microscopy study of conjugated polymer/fullerene organic solar cells, Japanese Journal of Applied Physics, Part 1: Regular Papers and Short Notes and Review Papers, 44 (2005) 5370-5373.
[67] H. Hoppe, T. Glatzel, M. Niggemann, W. Schwinger, F. Schaeffler, A. Hinsch, M. Lux-Steiner, N. Sariciftci, Efficiency limiting morphological factors of MDMO-PPV : PCBM plastic solar cells, Thin Solid Films, 511 (2006) 587-592.
[68] R. Nuzzo, D. Allara, Adsorption Of Bifunctional Organic Disulfides On Gold Surfaces, Journal of the American Chemical Society, 105 (1983) 4481-4483.
[69] J. Sagiv, Organized Monolayers By Adsorption .1. Formation And Structure Of Oleophobic Mixed Monolayers On Solid-Surfaces, Journal of the American Chemical Society, 102 (1980) 92-98.
[70] M. Stratmann, Chemically modified metal surfaces—a new class of composite materials, Advanced Materials, 2 (1990) 191-195.
[71] G. Jennings, P. Laibinis, Self-assembled monolayers of alkanethiols on copper provide corrosion resistance in aqueous environments, Colloids and Surfaces a-Physicochemical and Engineering Aspects, 116 (1996) 105-114.
[72] R. Carpick, M. Salmeron, Scratching the surface: Fundamental investigations of tribology with atomic force microscopy, Chemical Reviews, 97 (1997) 1163-1194.
[73] X. Xiao, J. Hu, D. Charych, M. Salmeron, Chain length dependence of the frictional properties of alkylsilane molecules self-assembled on Mica studied by atomic force microscopy, Langmuir, 12 (1996) 235-237.
[74] G. Choi, S. Kim, A. Ulman, Adhesion hysteresis studies of extracted poly(dimethylsiloxane) using contact mechanics, Langmuir, 13 (1997) 6333-6338.
[75] S. Kim, G. Choi, A. Ulman, C. Fleischer, Effect of chemical functionality on adhesion hysteresis, Langmuir, 13 (1997) 6850-6856.
[76] K. Prime, G. Whitesides, Self-Assembled Organic Monolayers - Model Systems For Studying Adsorption Of Proteins At Surfaces, Science, 252 (1991) 1164-1167.

[77] J. Lahiri, L. Isaacs, B. Grzybowski, J. Carbeck, G. Whitesides, Biospecific binding of carbonic anhydrase to mixed SAMs presenting benzenesulfonamide ligands: A model system for studying lateral steric effects, Langmuir, 15 (1999) 7186-7198.
[78] G. Sigal, C. Bamdad, A. Barberis, J. Strominger, G. Whitesides, A self-assembled monolayer for the binding and study of histidine tagged proteins by surface plasmon resonance, Analytical Chemistry, 68 (1996) 490-497.
[79] G. Heimel, L. Romaner, E. Zojer, J. Bredas, The interface energetics of self-assembled monolayers on metals, Accounts of Chemical Research, 41 (2008) 721-729.
[80] V. De Renzi, Understanding the electronic properties of molecule/metal junctions: The case study of thiols on gold, Surface Science, 603 (2009) 1518-1525.
[81] B. de Boer, A. Hadipour, M. Mandoc, T. van Woudenbergh, P. Blom, Tuning of metal work functions with self-assembled monolayers, Advanced Materials, 17 (2005) 621-+.
[82] F. Schreiber, Structure and growth of self-assembling monolayers, Progress in Surface Science, 65 (2000) 151-256.
[83] A. Ulman, Formation and structure of self-assembled monolayers, Chemical Reviews, 96 (1996) 1533-1554.
[84] D. Schwartz, Mechanisms and kinetics of self-assembled monolayer formation, Annual Review of Physical Chemistry, 52 (2001) 107-137.
[85] K. Szelągowska-Kunstman, P. Cyganik, B. Schüpbach, A. Terfort, Relative stability of thiol and selenol based SAMs on Au(111) - Exchange experiments, Physical Chemistry Chemical Physics, 12 (2010) 4400-4406.
[86] A. Ulman, J. Eilers, N. Tillman, Packing And Molecular-Orientation Of Alkanethiol Monolayers On Gold Surfaces, Langmuir, 5 (1989) 1147-1152.
[87] R. Pilolli, N. Ditaranto, N. Cioffi, L. Sabbatini, Non-destructive depth profile reconstruction of bio-engineered surfaces by parallel-angle-resolved X-ray photoelectron spectroscopy, Analytical and Bioanalytical Chemistry, 405 (2013) 713-724.
[88] C. Haensch, S. Hoeppener, U. Schubert, Chemical modification of self-assembled silane based monolayers by surface reactions, Chemical Society Reviews, 39 (2010) 2323-2334.
[89] N. Herzer, C. Haensch, S. Hoeppener, U. Schubert, Orthogonal Functionalization of Silicon Substrates Using Self-Assembled Monolayers, Langmuir, 26 (2010) 8358-8365.
[90] A. Sandy, S. Mochrie, D. Zehner, K. Huang, D. Gibbs, Structure And Phases Of The Au(111) Surface - X-Ray-Scattering Measurements, Physical Review B, 43 (1991) 4667-4687.
[91] A. Cossaro, R. Mazzarello, R. Rousseau, L. Casalis, A. Verdini, A. Kohlmeyer, L. Floreano, S. Scandolo, A. Morgante, M. Klein, G. Scoles, X-ray diffraction and computation yield the structure of alkanethiols on gold(111), Science, 321 (2008) 943-946.
[92] R. Mazzarello, A. Cossaro, A. Verdini, R. Rousseau, L. Casalis, M. Danisman, L. Floreano, S. Scandolo, A. Morgante, G. Scoles, Structure of a CH3S monolayer on Au(111) solved by the interplay between molecular dynamics calculations and diffraction measurements, Physical Review Letters, 98 (2007).
[93] H. Himmel, K. Weiss, B. Jager, O. Dannenberger, M. Grunze, C. Woll, Ultrahigh vacuum study on the reactivity of organic surfaces terminated by OH and COOH groups prepared by self-assembly of functionalized alkanethiols on Au substrates, Langmuir, 13 (1997) 4943-4947.
[94] O. Dannenberger, K. Weiss, H. Himmel, B. Jager, M. Buck, C. Woll, An orientation analysis of differently endgroup-functionalised alkanethiols adsorbed on Au substrates, Thin Solid Films, 307 (1997) 183-191.
[95] J. Li, K. Liang, G. Scoles, A. Ulman, Counterion Overlayers At The Interface Between An Electrolyte And An Omega-Functionalized Monolayer Self-Assembled On Gold - An X-Ray Reflectivity Study, Langmuir, 11 (1995) 4418-4427.
[96] S. Onclin, B. Ravoo, D. Reinhoudt, Engineering silicon oxide surfaces using self-assembled monolayers, Angewandte Chemie-International Edition, 44 (2005) 6282-6304.

[97] M. Stevens, Thoughts on the Structure of alkylsilane monolayers, Langmuir, 15 (1999) 2773-2778.
[98] M. Fujii, S. Sugisawa, K. Fukada, T. Kato, T. Seimiya, Hexagonally Close-Packed Alkyl Chains Silylized On Oxidized Silicon Surface, Langmuir, 11 (1995) 405-407.
[99] S. Barton, A. Goudot, F. Rondelez, X-Ray Structural Study Of Polymerized Octyldecyltrichlorosilane On Water, Langmuir, 7 (1991) 1029-1030.
[100] K. Kojio, S. Ge, A. Takahara, T. Kajiyama, Molecular aggregation state of n-octadecyltrichlorosilane monolayer prepared at an air/water interface, Langmuir, 14 (1998) 971-974.
[101] X. Zhao, R. Kopelman, Mechanism of organosilane self-assembled monolayer formation on silica studied by second-harmonic generation, Journal of Physical Chemistry, 100 (1996) 11014-11018.
[102] P. Silberzan, L. Leger, D. Ausserre, J. Benattar, Silanation Of Silica Surfaces - A New Method Of Constructing Pure Or Mixed Monolayers, Langmuir, 7 (1991) 1647-1651.
[103] L. Dubois, R. Nuzzo, Synthesis, Structure, And Properties Of Model Organic-Surfaces, Annual Review of Physical Chemistry, 43 (1992) 437-463.
[104] J.A. Venables, Introduction to Surface and Thin Film Processes, Cambridge University Press, 2000.
[105] M. Sung, C. Carraro, O. Yauw, Y. Kim, R. Maboudian, Reversible liquid-liquid transitions in the early stages of monolayer self-assembly, Journal of Physical Chemistry B, 104 (2000) 1556-1559.
[106] Y. Wang, M. Lieberman, Growth of ultrasmooth octadecyltrichlorosilane self-assembled monolayers on SiO2, Langmuir, 19 (2003) 1159-1167.
[107] J. Brzoska, N. Shahidzadeh, F. Rondelez, Evidence Of A Transition-Temperature For The Optimum Deposition Of Grafted Monolayer Coatings, Nature, 360 (1992) 719-721.
[108] A. Parikh, D. Allara, I. Azouz, F. Rondelez, An Intrinsic Relationship Between Molecular-Structure In Self-Assembled N-Alkylsiloxane Monolayers And Deposition Temperature, Journal of Physical Chemistry, 98 (1994) 7577-7590.
[109] R. Rye, Transition temperatures for n-alkyltrichlorosilane monolayers, Langmuir, 13 (1997) 2588-2590.
[110] R. Bautista, N. Hartmann, E. Hasselbrink, Two-dimensional aggregation of species with weak and strong bonding interactions: Modeling the growth of self-assembled alkylsiloxane monolayers, Langmuir, 19 (2003) 6590-6593.
[111] I. Doudevski, W. Hayes, D. Schwartz, Submonolayer island nucleation and growth kinetics during self-assembled monolayer formation, Physical Review Letters, 81 (1998) 4927-4930.
[112] I. Doudevski, D. Schwartz, Dynamic scaling of the submonolayer island size distribution during self-assembled monolayer growth, Physical Review B, 60 (1999) 14-17.
[113] D. Egger, F. Rissner, G. Rangger, O. Hofmann, L. Wittwer, G. Heimel, E. Zojer, Self-assembled monolayers of polar molecules on Au(111) surfaces: distributing the dipoles, Physical Chemistry Chemical Physics, 12 (2010) 4291-4294.
[114] L. Wang, G. Rangger, L. Romaner, G. Heimel, T. Bucko, Z. Ma, Q. Li, Z. Shuai, E. Zojer, Electronic Structure of Self-Assembled Monolayers on Au(111) Surfaces: The Impact of Backbone Polarizability, Advanced Functional Materials, 19 (2009) 3766-3775.
[115] G. Heimel, L. Romaner, J. Bredas, E. Zojer, Odd-even effects in self-assembled monolayers of omega-(biphenyl-4-yl)alkanethiols: A first-principles study, Langmuir, 24 (2008) 474-482.
[116] G. Heimel, F. Rissner, E. Zojer, Modeling the Electronic Properties of pi-Conjugated Self-Assembled Monolayers, Advanced Materials, 22 (2010) 2494-2513.
[117] C. Risko, C. Zangmeister, Y. Yao, T. Marks, J. Tour, M. Ratner, R. van Zee, Experimental and theoretical identification of valence energy levels and interface dipole trends for a

family of (oligo)phenylene-ethynylenethiols adsorbed on gold, Journal of Physical Chemistry C, 112 (2008) 13215-13225.
[118] T. Blythe, D. Bloor, Electrical Properties of Polymers, Cambridge University Press, New York, 2005.
[119] H. Klauk, Organic Electronics II. More materials and applications., Wiley-VCH Verlag & Co., Weinheim, germany, 2012.
[120] W. Barford, Electronic and Optical Properties of Conjugated Polymers, Oxford University Press Inc., New York, 2005.
[121] L.H. Sperling, Introduction to physical polymer science, John Wiley & Son, Inc., New Jersey, 2006.
[122] T.A. Skotheim, J.R. Reynolds, Conjugated polymers: theory, synthesis, properties, and characterization, in, CRC Press. Taylor & Francis Group, LLC, Boca Raton, 2007.
[123] M. Leclerc, J.-F. Morin, Design and Synthesis of Conjugated Polymers, in, Wiley-VCH Verlag GmbH & Co., Weinheim, 2010.
[124] J. Brandrup, E.H. Immergut, E.A. Grulke, Polymer Handbook, in, Wiley VCH, 2003.
[125] J.H. Hildebrand, R.L. Scott, The Solubility of Non-electrolytes", Reinhold, New York, 1959.
[126] C.M. Hansen, Hansen Solubility Parameters: a user's handbook, CRC Press. Taylor & Francis Group, LLC, New York, 2007.
[127] D. Prime, S. Paul, Electrical and morphological properties of polystyrene thin films for organic electronic applications, Vacuum, 84 (2010) 1240-1243.
[128] Composition comprising polymeric binders, in: M.P. GmbH (Ed.) European Patent Office, Germany, 2009.
[129] M. Efremov, E. Olson, M. Zhang, L. Allen, Glass transition of thin films of poly(2-vinyl pyridine) and poly(methyl methacrylate): nanocalorimetry measurements, Thermochimica Acta, 403 (2003) 37-41.
[130] J. Durkee, Cleaning with solvents: Science and technology, Elsevier Inc., Waltham, USA, 2014.
[131] Z. Wang, Y. Wang, D. Xu, E. Kong, Y. Zhang, Facile synthesis of dispersible spherical polythiophene nanoparticles by copper(II) catalyzed oxidative polymerization in aqueous medium, Synthetic Metals, 160 (2010) 921-926.
[132] I.F. Perepichka, D.F. Perepichka, Handbook of thiophene-based materials, John Wiley & Sons Ltd., West Sussex, UK, 2009.
[133] W. Huang, B. Humphrey, A. Macdiarmid, Polyaniline, A Novel Conducting Polymer - Morphology And Chemistry Of Its Oxidation And Reduction In Aqueous-Electrolytes, Journal of the Chemical Society-Faraday Transactions I, 82 (1986) 2385-&.
[134] M. Marzec, K. Awsiuk, A. Bernasik, J. Rysz, J. Haberko, W. Luzny, A. Budkowski, Buried polymer/metal interfaces examined with Kelvin Probe Force Microscopy, Thin Solid Films, 531 (2013) 271-276.
[135] M.L. Sushko, A.L. Shluger, Rough and fine tuning of metal work function via chemisorbed self-assembled monolayers, Advanced Materials, 21 (2009) 1111-1114.
[136] W. Kern, K.A. Reinhardt, 1 - Overview and Evolution of Silicon Wafer Cleaning Technology, in: Handbook of Silicon Wafer Cleaning Technology (Second Edition), William Andrew Publishing, Norwich, NY, 2008, pp. 3-92.
[137] B. Moazzez, S. O'Brien, S. Merschrod, Improved Adhesion of Gold Thin Films Evaporated on Polymer Resin: Applications for Sensing Surfaces and MEMS, Sensors, 13 (2013) 7021-7032.
[138] R. Audino, G. Destefanis, F. Gorgellino, E. Pollino, S. Tamagno, Interface Behavior Evaluation In Au-Cr, Au-Ti And Au-Pd-Ti Thin-Films By Means Of Resistivity And Stylus Measurements, Thin Solid Films, 36 (1976) 343-347.
[139] Y. Xia, G. Whitesides, Soft lithography, Angewandte Chemie-International Edition, 37 (1998) 551-575.

[140] W. Beh, I. Kim, D. Qin, Y. Xia, G. Whitesides, Formation of patterned microstructures of conducting polymers by soft lithography, and applications in microelectronic device fabrication, Advanced Materials, 11 (1999) 1038-1041.
[141] Z. Nie, E. Kumacheva, Patterning surfaces with functional polymers, Nature Materials, 7 (2008) 277-290.
[142] X. Zhao, Y. Xia, G. Whitesides, Soft lithographic methods for nano-fabrication, Journal of Materials Chemistry, 7 (1997) 1069-1074.
[143] Y. Xia, N. Venkateswaran, D. Qin, J. Tien, G. Whitesides, Use of electroless silver as the substrate in microcontact printing of alkanethiols and its application in microfabrication, Langmuir, 14 (1998) 363-371.
[144] J. Kunzler, Silicone hydrogels for contact lens application, Trends in Polymer Science, 4 (1996) 52-59.
[145] J. Wilbur, R. Jackman, G. Whitesides, E. Cheung, L. Lee, M. Prentiss, Elastomeric optics, Chemistry of Materials, 8 (1996) 1380-1385.
[146] J. Lee, C. Park, G. Whitesides, Solvent compatibility of poly(dimethylsiloxane)-based microfluidic devices, Analytical Chemistry, 75 (2003) 6544-6554.
[147] A. Kumar, G. Whitesides, Features Of Gold Having Micrometer To Centimeter Dimensions Can Be Formed Through A Combination Of Stamping With An Elastomeric Stamp And An Alkanethiol Ink Followed By Chemical Etching, Applied Physics Letters, 63 (1993) 2002-2004.
[148] P. Cyganik, A. Bernasik, A. Budkowski, B. Bergues, K. Kowalski, J. Rysz, J. Lekki, M. Lekka, Z. Postawa, Phase decomposition in polymer blend films cast on substrates patterned with self-assembled monolayers, Vacuum, 63 (2001) 307-313.
[149] P. Cyganik, A. Budkowski, J. Raczkowska, Z. Postawa, AFM/LFM surface studies of a ternary polymer blend cast on substrates covered by a self-assembled monolayer, Surface Science, 507-510 (2002) 700-706.
[150] J. Raczkowska, P. Cyganik, A. Budkowski, A. Bernasik, J. Rysz, I. Raptis, P. Czuba, K. Kowalski, Composition effects in polymer blends spin-cast on patterned substrates, Macromolecules, 38 (2005) 8486-8493.
[151] J. Raczkowska, A. Bernasik, A. Budkowski, P. Cyganik, J. Rysz, I. Raptis, P. Czuba, Pattern guided structure formation in polymer films of asymmetric blends, Surface Science, 600 (2006) 1004-1011.
[152] H. Biebuyck, C. Bian, G. Whitesides, Comparison Of Organic Monolayers On Polycrystalline Gold Spontaneously Assembled From Solutions Containing Dialkyl Disulfides Or Alkenethiols, Langmuir, 10 (1994) 1825-1831.
[153] N. Larsen, H. Biebuyck, E. Delamarche, B. Michel, Order in microcontact printed self-assembled monolayers, Journal of the American Chemical Society, 119 (1997) 3017-3026.
[154] A. Perl, D. Reinhoudt, J. Huskens, Microcontact Printing: Limitations and Achievements, Advanced Materials, 21 (2009) 2257-2268.
[155] R. Sharpe, D. Burdinski, C. van der Marel, J. Jansen, J. Huskens, H. Zandvliet, D. Reinhoudt, B. Poelsema, Ink dependence of poly(dimethylsiloxane) contamination in microcontact printing, Langmuir, 22 (2006) 5945-5951.
[156] E. Kim, Y. Xia, G. Whitesides, Polymer Microstructures Formed By Molding In Capillaries, Nature, 376 (1995) 581-584.
[157] K. Norrman, A. Ghanbari-Siahkali, N.B. Larsen, 6 Studies of spin-coated polymer films, Annual Reports Section "C" (Physical Chemistry), 101 (2005) 174-201.
[158] H. Sirringhaus, N. Tessler, R.H. Friend, Integrated optoelectronic devices based on conjugated polymers, Science, 280 (1998) 1741-1744.
[159] H. Sirringhaus, P.J. Brown, R.H. Friend, M.M. Nielsen, K. Bechgaard, B.M.W. Langeveld-Voss, A.J.H. Spiering, R.A.J. Janssen, E.W. Meijer, P. Herwig, D.M. De Leeuw, Two-dimensional charge transport in self-organized, high-mobility conjugated polymers, Nature, 401 (1999) 685-688.

[160] H. Sirringhaus, P.J. Brown, R.H. Friend, M.M. Nielsen, K. Bechgaard, B.M.W. Langeveld-Voss, A.J.H. Spiering, R.A.J. Janssen, E.W. Meijer, Microstructure-mobility correlation in self-organised, conjugated polymer field-effect transistors, Synthetic Metals, 111 (2000) 129-132.
[161] K. Eaton, A novel colorimetric oxygen sensor: Dye redox chemistry in a thin polymer film, Sensors and Actuators, B: Chemical, 85 (2002) 42-51.
[162] F. Mirkhalaf, D.J. Schiffrin, Metal-ion sensing by surface plasmon resonance on film electrodes, Journal of Electroanalytical Chemistry, 484 (2000) 182-188.
[163] D. Chang, D. Yoon, M. Ro, I. Hwang, I. Park, D. Shin, Synthesis and characteristics of protective coating on thin cover layer for high density-digital versatile disc, Japanese Journal of Applied Physics, Part 1: Regular Papers and Short Notes and Review Papers, 42 (2003) 754-758.
[164] S. Walheim, E. Schäffer, J. Mlynek, U. Steiner, Nanophase-separated polymer films as high-performance antireflection coatings, Science, 283 (1999) 520-522.
[165] P.H. Walker, J.G. Thompson, Proc. Am. Soc. Test. Mater., 22 (1922).
[166] A.G. Emslie, F.T. Bonner, L.G. Peck, Flow of a viscous liquid on a rotating disk, Journal of Applied Physics, 29 (1958) 858-862.
[167] B.D. Washo, Rheology And Modeling Of The Spin Coating Process, IBM Journal of Research and Development, 21 (1977) 190-198.
[168] S.A. Jenekhe, Rheology And Spin Coating Of Polyimide Solutions, Polymer Engineering and Science, 23 (1983) 830-834.
[169] B.G. Higgins, Film flow on a rotating disk, Phys. fluids, 29 (1986) 3522-3529.
[170] C.J. Lawrence, The mechanics of spin coating of polymer films, Phys. Fluids, 31 (1988) 2786-2795.
[171] J.H. Lai, Investigation Of Spin Coating Of Electron Resists, Polymer Engineering and Science, 19 (1979) 1117-1121.
[172] F.L. Givens, W.J. Daughton, On The Uniformity Of Thin Films: A New Technique Applied To Polyimides, J Electrochem Soc, 126 (1979) 269-272.
[173] B.T. Chen, Investigation Of The Solvent-Evaporation Effect On Spin Coating Of Thin Films, Polymer Engineering and Science, 23 (1983) 399-403.
[174] D.B. Hall, P. Underhill, J.M. Torkelson, Spin coating of thin and ultrathin polymer films, Polymer Engineering and Science, 38 (1998) 2039-2045.
[175] M. Marzec, A. Bernasik, J. Rysz, W. Luzny, A. Budkowski, Examination of polymer/metal interface modified by self-assembled monolayer by Kelvin probe force microscopy and secondary ion mass spectrometry, Electrochimica Acta, 104 (2013) 462-467.
[176] J. Rysz, M. Josiek, M. Marzec, E. Moons, Pattern replication in blends of semiconducting and insulating polymers casted by horizontal dipping, Journal of Polymer Science Part B-Polymer Physics, 51 (2013) 1419-+.
[177] B. Park, M.Y. Han, Photovoltaic characteristics of polymer solar cells fabricated by pre-metered coating process, Optics Express, 17 (2009) 13830-13840.
[178] F. Nickel, C. Sprau, M.F.G. Klein, P. Kapetana, N. Christ, X. Liu, S. Klinkhammer, U. Lemmer, A. Colsmann, Spatial mapping of photocurrents in organic solar cells comprising wedge-shaped absorber layers for an efficient material screening, Solar Energy Materials and Solar Cells, 104 (2012) 18-22.
[179] L. Landau, B. Levich, Dragging of a liquid by a moving plate, Acta Physicochim. URSS, 17 (1942) 42-54.
[180] M. Le Berre, Y. Chen, D. Baigl, From convective assembly to landau - Levich deposition of multilayered phospholipid films of controlled thickness, Langmuir, 25 (2009) 2554-2557.
[181] J. Park, S. Lee, H.H. Lee, High-mobility polymer thin-film transistors fabricated by solvent-assisted drop-casting, Organic Electronics, 7 (2006) 256-260.
[182] G. Binning, H. Rohrer, C. Gerber, E. Weibel, Surface Studies By Scanning Tunneling Microscopy, Physical Review Letters, 49 (1982) 57-61.

[183] G. Binnig, C.F. Quate, C. Gerber, Atomic Force Microscope, Physical Review Letters, 56 (1986) 930-933.
[184] Y. Martin, C. Williams, H. Wickramasinghe, Atomic Force Microscope Force Mapping And Profiling On A Sub 100-A Scale, Journal of Applied Physics, 61 (1987) 4723-4729.
[185] R. García, Amplitude Modulation Atomic Force Microscopy, 2010.
[186] S. Sadewasser, T. Glatzel, Kelvin probe force microscopy. Measuring and compensating electrostatic forces., 2012.
[187] S.N. Magonov, M.-H. Whangbo, Practical Aspects of STM and AFM Measurements, in: Surface Analysis with STM and AFM, Wiley-VCH Verlag GmbH, 1995, pp. 47-63.
[188] S.N. Magonov, Atomic Force Microscopy in Analysis of Polymers, in: Encyclopedia of Analytical Chemistry, John Wiley & Sons Ltd, Chichester, 2000, pp. 7432-7491.
[189] S. Magonov, J. Alexander, Single-pass Kelvin force microscopy and dC/dZ measurements in the intermittent contact: Applications to polymer materials, Beilstein Journal of Nanotechnology, 2 (2011) 15-27.
[190] M. Nonnenmacher, M.P. O'Boyle, H.K. Wickramasinghe, Kelvin probe force microscopy, Applied Physics Letters, 58 (1991) 2921-2923.
[191] W. Melitz, J. Shen, A.C. Kummel, S. Lee, Kelvin probe force microscopy and its application, Surface Science Reports, 66 (2011) 1-27.
[192] U. Zerweck, C. Loppacher, T. Otto, S. Grafstrom, L. Eng, Accuracy and resolution limits of Kelvin probe force microscopy, Physical Review B, 71 (2005).
[193] S. Hudlet, M. Saintjean, B. Roulet, J. Berger, C. Guthmann, Electrostatic Forces Between Metallic Tip And Semiconductor Surfaces, Journal of Applied Physics, 77 (1995) 3308-3314.
[194] S. Hudlet, M. Saint Jean, C. Guthmann, J. Berger, Evaluation of the capacitive force between an atomic force microscopy tip and a metallic surface, European Physical Journal B, 2 (1998) 5-10.
[195] Y. Martin, D.W. Abraham, H.K. Wickramasinghe, High-resolution capacitance measurement and potentiometry by force microscopy, Applied Physics Letters, 52 (1988) 1103-1105.
[196] T. Hochwitz, A.K. Henning, C. Levey, C. Daghlian, J. Slinkman, J. Never, P. Kaszuba, R. Gluck, R. Wells, J. Pekarik, R. Finch, Imaging integrated circuit dopant profiles with the force-based scanning Kelvin probe microscope, Journal of Vacuum Science and Technology B: Microelectronics and Nanometer Structures, 14 (1996) 440-446.
[197] S.J.J. Thomson, LXXXIII. Rays of positive electricity, http://dx.doi.org/10.1080/-14786441008636962, (2009).
[198] D.J. O'Connor, B. Sexton, R.C. Smart, R.J. MacDonald, B.V. King, SIMS — Secondary Ion Mass Spectrometry, in: Surface Analysis Methods in Materials Science, Springer Berlin Heidelberg, 2003, pp. 127-154.
[199] C. Mahoney, Cluster Secondary Ion Mass Spectrometry Of Polymers And Related Materials, Mass Spectrometry Reviews, 29 (2010) 247-293.
[200] J.C. Vickerman, Molecular Surface Mass Spectrometry by SIMS, in: Surface Analysis – The Principal Techniques, John Wiley & Sons, Ltd, 2009, pp. 113-205.
[201] C.M. Mahoney, G. Gillen, An Introduction to Cluster Secondary Ion Mass Spectrometry (Cluster SIMS), in: Cluster Secondary Ion Mass Spectrometry, John Wiley & Sons, Inc., 2013, pp. 1-11.
[202] Benninghoven .A, Analysis Of Monomolecular Layers Of Solids By Secondary Ion Emission, Zeitschrift Fur Physik, 230 (1970) 403.
[203] R.M.A. Heeren, Getting the picture: The coming of age of imaging MS.
[204] C.M. Mahoney, A. Wucher, Molecular Depth Profiling with Cluster Ion Beams, in: Cluster Secondary Ion Mass Spectrometry, John Wiley & Sons, Inc., 2013, pp. 117-205.
[205] D. McPhail, M. Dowsett, Dynamic SIMS, in: Surface Analysis – The Principal Techniques, John Wiley & Sons, Ltd, 2009, pp. 207-268.

[206] S. Hofmann, Depth Resolution In Sputter Profiling, Applied Physics, 13 (1977) 205-207.
[207] S. Hofmann, Approaching The Limits Of High-Resolution Depth Profiling, Applied Surface Science, 70-1 (1993) 9-19.
[208] S. Hofmann, Sputter depth profile analysis of interfaces, Reports on Progress in Physics, 61 (1998) 827-888.
[209] A. Czanderna, T. Madey, C. Powell, L.S. Dake, D.E. King, J.R. Pitts, A.W. Czanderna, Ion Beam Bombardment Effects on Solid Surfaces at Energies Used for Sputter Depth Profiling, in: Beam Effects, Surface Topography, and Depth Profiling in Surface Analysis, Springer US, 2002, pp. 97-274.
[210] R. Steinhardt, E. Serfass, X-Ray Photoelectron Spectrometer For Chemical Analysis, Analytical Chemistry, 23 (1951) 1585-1590.
[211] S. Hagstrom, C. Nordling, K. Siegbahn, Electron Spectroscopy For Chemical Analysis, Physics Letters, 9 (1964) 235-236.
[212] C. Fadley, X-ray photoelectron spectroscopy: Progress and perspectives, Journal of Electron Spectroscopy and Related Phenomena, 178 (2010) 2-32.
[213] J.F. Watts, J. Wolstenholme, Electron Spectroscopy: Some Basic Concepts, in: An Introduction to Surface Analysis by XPS and AES, John Wiley & Sons, Ltd, 2003, pp. 1-15.
[214] D. Briggs, Surface Analysis of Polymers by XPS and Static SIMS, Cambridge University Press, New York, 2005.
[215] M.P. Seah, W.A. Dench, Quantitative electron spectroscopy of surfaces: A standard data base for electron inelastic mean free paths in solids, Surface and Interface Analysis, 1 (1979) 2-11.
[216] M. Seah, G. Smith, Quantitative AES and XPS - Calibration Of Electron Spectrometers For True Spectral Measurements - Vamas Round-Robins And Parameters For Reference Spectral Data Banks, Vacuum, 41 (1990) 1601-1604.
[217] K. Awsiuk, J. Rysz, P. Petrou, A. Budkowski, A. Bernasik, S. Kakabakos, M. Marzec, I. Raptis, Immobilization of oligonucleotide probes on silicon surfaces using biotin-streptavidin system examined with microscopic and spectroscopic techniques, Applied Surface Science, 290 (2014) 199-206.
[218] J.F. Watts, J. Wolstenholme, Compositional Depth Profiling, in: An Introduction to Surface Analysis by XPS and AES, John Wiley & Sons, Ltd, 2003, pp. 79-111.
[219] J. Vickerman, N. Winograd, Cluster TOF-SIMS Imaging and the Characterization of Biological Materials, in: Cluster Secondary Ion Mass Spectrometry, John Wiley & Sons, Inc., 2013, pp. 269-312.
[220] O. Baschenko, V. Nefedov, Depth Profiling Of Elements In Surface-Layers Of Solids Based On Angular Resolved X-Ray Photoelectron-Spectroscopy, Journal of Electron Spectroscopy and Related Phenomena, 53 (1990) 1-18.
[221] T. Bussing, P. Holloway, Deconvolution Of Concentration Depth Profiles From Angle Resolved X-Ray Photoelectron-Spectroscopy Data, Journal of Vacuum Science & Technology a-Vacuum Surfaces and Films, 3 (1985) 1973-1981.
[222] H. Iwasaki, R. Nishitani, S. Nakamura, Determination Of Depth Profiles By Angular Dependent X-Ray Photoelectron-Spectra, Japanese Journal of Applied Physics, 17 (1978) 1519-1523.
[223] R. Yih, B. Ratner, A Comparison Of 2 Angular Dependent Esca Algorithms Useful For Constructing Depth Profiles Of SurfaceS, Journal of Electron Spectroscopy and Related Phenomena, 43 (1987) 61-82.
[224] P. Cumpson, Angle-Resolved Xps And Aes - Depth-Resolution Limits And A General Comparison Of Properties Of Depth-Profile Reconstruction Methods, Journal of Electron Spectroscopy and Related Phenomena, 73 (1995) 25-52.
[225] Y.K. Kyoung, J.G. Chung, H.I. Lee, D.-J. Yun, J.C. Lee, Y.S. Kim, S.K. Oh, H.J. Kang, Electronic structures of SiO2 thin films via Ar gas cluster ion beam sputtering, Surface and Interface Analysis, (2014) n/a-n/a.

[226] P. Cumpson, J. Portoles, A. Barlow, N. Sano, M. Birch, Depth profiling organic/inorganic interfaces by argon gas cluster ion beams: sputter yield data for biomaterials, in-vitro diagnostic and implant applications, Surface and Interface Analysis, 45 (2013) 1859-1868.
[227] T. Miyayama, N. Sanada, M. Suzuki, J. Hammond, S. Si, A. Takahara, X-ray photoelectron spectroscopy study of polyimide thin films with Ar cluster ion depth profiling, Journal of Vacuum Science & Technology a, 28 (2010) L1-L4.
[228] D. Yun, H. Ra, J. Kim, I. Hwang, J. Lee, S. Rhee, J. Chung, Characterizing Annealing Effect of Poly (3,4-ethylenedioxythiophene) Polymerized with Poly (4-styrenesulfonate) Conjugated Film on the Molecular Arrangement and Work Function by Core-Level and Valence-Level Band Spectra, Ecs Journal of Solid State Science and Technology, 1 (2012) M10-M14.
[229] P. Cumpson, J. Portoles, N. Sano, Material dependence of argon cluster ion sputter yield in polymers: Method and measurements of relative sputter yields for 19 polymers, Journal of Vacuum Science & Technology a, 31 (2013).
[230] D. Shirley, High-Resolution X-Ray Photoemission Spectrum Of Valence Bands Of Gold, Physical Review B, 5 (1972) 4709.
[231] M. Seah, J. Qiu, P. Cumpson, J. Castle, Simple Method Of Depth Profiling (Stratifying) Contamination Layers, Illustrated By Studies On Stainless-Steel, Surface and Interface Analysis, 21 (1994) 336-341.
[232] D.J. O'Connor, B. Sexton, R.C. Smart, R. Leckey, Ultraviolet Photoelectron Spectroscopy of Solids, in: Surface Analysis Methods in Materials Science, Springer Berlin Heidelberg, 2003, pp. 337-345.
[233] D.W. Turner, M.I.A. Jobory, Determination of Ionization Potentials by Photoelectron Energy Measurement, The Journal of Chemical Physics, 37 (1962) 3007.
[234] A. Potts, H. Lempka, D. Streets, W. Price, Photoelectron Spectra Of Halides Of Elements In Group-Iii, Group-Iv, Group-V And Group-Vi, Philosophical Transactions of the Royal Society of London Series a-Mathematical and Physical Sciences, 268 (1970) 59-&.
[235] S. Hüfner, F. Reinert, S. Hüfner, Photoemission Spectroscopy with Very High Energy Resolution: Studying the Influence of Electronic Correlations on the Millielectronvolt Scale, in: Very High Resolution Photoelectron Spectroscopy, Springer Berlin Heidelberg, 2007, pp. 13-53.
[236] N. Franz Himpsel and Per-Olof, Focus On Photoemission And Electronic Structure, New Journal of Physics, 7 (2005).
[237] T. Willey, A. Vance, T. van Buuren, C. Bostedt, L. Terminello, C. Fadley, Rapid degradation of alkanethiol-based self-assembled monolayers on gold in ambient laboratory conditions, Surface Science, 576 (2005) 188-196.
[238] D. Castner, K. Hinds, D. Grainger, X-ray photoelectron spectroscopy sulfur 2p study of organic thiol and disulfide binding interactions with gold surfaces, Langmuir, 12 (1996) 5083-5086.
[239] T. Ishida, N. Choi, W. Mizutani, H. Tokumoto, I. Kojima, H. Azehara, H. Hokari, U. Akiba, M. Fujihira, High-resolution X-ray photoelectron spectra of organosulfur monolayers on Au(111): S(2p) spectral dependence on molecular species, Langmuir, 15 (1999) 6799-6806.
[240] M. Engelhard, B. Tarasevich, D. Baer, Beam damage of HS(CH2)15 COOH Terminated Self Assembled Monolayer (SAM) as Observed by X-ray Photoelectron Spectroscopy, Surface Science Spectra, 18 (2011) 68.
[241] W. Zhang, A. Nefedov, M. Naboka, L. Cao, C. Woll, Molecular orientation of terephthalic acid assembly on epitaxial graphene: NEXAFS and XPS study, Physical Chemistry Chemical Physics, 14 (2012) 10125-10131.
[242] M. Canas-Ventura, F. Klappenberger, S. Clair, S. Pons, K. Kern, H. Brune, T. Strunskus, C. Woll, R. Fasel, J. Barth, Coexistence of one- and two-dimensional supramolecular

assemblies of terephthalic acid on Pd(111) due to self-limiting deprotonation, Journal of Chemical Physics, 125 (2006).
[243] M.J. Tarlov, J.G. Newman, Static Secondary Ion Mass Spectrometry of self-assembled alkanethiol monolayers on gold, Langmuir, 8 (1992) 1398-1405.
[244] S. Trigwell, N. Grable, C.U. Yurteri, R. Sharma, M.K. Mazumder, Effects of surface properties on the tribocharging characteristics of polymer powder as applied to industrial processes, Industry Applications, IEEE Transactions on, 39 (2003) 79-86.
[245] H. Mantz, K. Jacobs, K. Mecke, Utilizing Minkowski functionals for image analysis: a marching square algorithm, Journal of Statistical Mechanics-Theory and Experiment, (2008).
[246] L. Leiserowitz, Molecular Packing Modes - Carboxylic-Acids, Acta Crystallographica Section B-Structural Science, 32 (1976) 775-802.
[247] A. Carre, D. Gamet, J. Schultz, H. Schreiber, Nonuniformity In Thin Polymer-Films, Journal of Macromolecular Science-Chemistry, A23 (1986) 1-18.
[248] H. Schreiber, M. Croucher, Surface Characteristics Of Solvent-Cast Polymers, Journal of Applied Polymer Science, 25 (1980) 1961-1968.
[249] O. Tretinnikov, Selective accumulation of functional groups at the film surfaces of stereoregular poly(methyl methacrylate)s, Langmuir, 13 (1997) 2988-2992.
[250] T. Ishida, H. Kobayashi, Y. Nakato, Structures and properties of electron-beam-evaporated indium tin oxide films as studied by x-ray photoelectron spectroscopy and work-function measurements, Journal of Applied Physics, 73 (1993) 4344.
[251] M.M. Coleman, P.C. Painter, Hydrogen bonded polymer blends, Progress in Polymer Science (Oxford), 20 (1995) 1-59.
[252] M.L. Sushko, A.L. Shluger, Intramolecular dipole coupling and depolarization in self-assembled monolayers, Advanced Functional Materials, 18 (2008) 2228-2236.
[253] W. Unger, W. Possart, An Xps Investigation Of The Interface Between Thin Polymethylmethacrylate (Pmma) Films And Natively Oxidized A1, Physica Status Solidi a-Applied Research, 114 (1989) K175-K177.
[254] F. Fowkes, Quantitative Characterization Of The Acid-Base Properties Of Solvents, Polymers, And Inorganic Surfaces, Journal of Adhesion Science and Technology, 4 (1990) 669-691.
[255] J. Keddie, R. Jones, R. Cory, Size-Dependent Depression Of The Glass-Transition Temperature In Polymer-Films, Europhysics Letters, 27 (1994) 59-64.
[256] G. Reiter, Dewetting As A Probe Of Polymer Mobility In Thin-Films, Macromolecules, 27 (1994) 3046-3052.
[257] J. Forrest, K. DalnokiVeress, J. Stevens, J. Dutcher, Effect of free surfaces on the glass transition temperature of thin polymer films (vol 77, pg 2002, 1996), Physical Review Letters, 77 (1996) 4108-4108.
[258] J. Keddie, R. Jones, R. Cory, Interface And Surface Effects On The Glass-Transition Temperature In Thin Polymer-Films, Faraday Discussions, 98 (1994) 219-230.
[259] O. Prucker, S. Christian, H. Bock, J. Ruhe, C. Frank, W. Knoll, Glass transition in ultrathin polymer films, Organic Thin Films, 695 (1998) 233-249.
[260] O. Prucker, S. Christian, H. Bock, J. Ruhe, C. Frank, W. Knoll, On the glass transition in ultrathin polymer films of different molecular architecture, Macromolecular Chemistry and Physics, 199 (1998) 1435-1444.
[261] A. Horinouchi, K. Tanaka, An effect of stereoregularity on the structure of poly(methyl methacrylate) at air and water interfaces, Rsc Advances, 3 (2013) 9446-9452.
[262] Y. Grohens, M. Brogly, C. Labbe, M. David, J. Schultz, Glass transition of stereoregular poly(methyl methacrylate) at interfaces, Langmuir, 14 (1998) 2929-2932.
[263] R. Long, M. Guo, A. Ziletti, Charge separation across P3HT/carbon nanotube interface: First-principles calculations of electronic structures, Chemical Physics Letters, 597 (2014) 45-50.

[264] M. Schneider, A. Wagenpfahl, C. Deibel, V. Dyakonov, A. Scholl, F. Reinert, Band bending at the P3HT/ITO interface studied by photoelectron spectroscopy, Organic Electronics, 15 (2014) 1552-1556.
[265] R. Mikalo, D. Schmeisser, Electric contacts on conductive polymers: sodium on poly(3-hexylthiophene-2,5-diyl), Synthetic Metals, 127 (2002) 273-277.
[266] D. Schmeisser, Valence states of poly(3-hexyl-thiophene) as probed by photoelectron spectra at resonant excitation, Synthetic Metals, 138 (2003) 135-140.
[267] M. Al-Ibrahim, H. Roth, U. Zhokhavets, G. Gobsch, S. Sensfuss, Flexible large area polymer solar cells based on poly(3-hexylthiophene)/fullerene, Solar Energy Materials and Solar Cells, 85 (2005) 13-20.
[268] J. Haberko, A. Bernasik, W. Łuny, J. Raczkowska, J. Rysz, A. Budkowski, Dendrites and pillars in spin cast blends of polyaniline or its oligomeric analogue, Synthetic Metals, 160 (2010) 2459-2466.
[269] A. Bernasik, J. Haberko, J. Włodarczyk-Miśkiewicz, J. Raczkowska, W. Łuzny, A. Budkowski, K. Kowalski, J. Rysz, Influence of humid atmosphere on phase separation in polyaniline- polystyrene thin films, Synthetic Metals, 155 (2005) 516-522.
[270] A. Bernasik, J. Włodarczyk-Miśkiewicz, W. Łuzny, K. Kowalski, J. Raczkowska, J. Rysz, A. Budkowski, Lamellar structures formed in spin-cast blends of insulating and conducting polymers, Synthetic Metals, 144 (2004) 253-257.
[271] F. Chen, Y. Lin, C. Ko, Submicron-scale manipulation of phase separation in organic solar cells, Applied Physics Letters, 92 (2008).
[272] M. Josiek, PhD thesis in preparation, in, M. Smoluchowski Institute of Physics, Jagiellonian University.

Relevant papers and conference contributions of the author

Papers:

P1. K. Awsiuk, A. Budkowski, **M. M. Marzec**, P. Petrou, J. Rysz, A. Bernasik, Effects of Polythiophene Surface Structure on Adsorption and Conformation of Bovine Serum Albumin: A Multivariate and Multitechnique Study, Langmuir, 30 (2014) 13925-13933.

P2. K. Awsiuk, J. Rysz, P. Petrou, A. Budkowski, A. Bernasik, S. Kakabakos, **M. M. Marzec**, I. Raptis, Immobilization of oligonucleotide probes on silicon surfaces using biotin-streptavidin system examined with microscopic and spectroscopic techniques, Applied Surface Science, 290 (2014) 199-206.

P3. K. Awsiuk, A. Budkowski, P. Petrou, A. Bernasik, **M. M. Marzec**, S. Kakabakos, J. Rysz, I. Raptis, Model immunoassay on silicon surfaces: Vertical and lateral nanostructure vs. protein coverage, Colloids and Surfaces B-Biointerfaces, 103 (2013) 253-260.

P4. **M. M. Marzec**, K. Awsiuk, A. Bernasik, J. Rysz, J. Haberko, W. Luzny, A. Budkowski, Buried polymer/metal interfaces examined with Kelvin Probe Force Microscopy, Thin Solid Films, 531 (2013) 271-276.

P5. **M. M. Marzec**, A. Bernasik, J. Rysz, W. Luzny, A. Budkowski, Examination of polymer/metal interface modified by self-assembled monolayer by Kelvin probe force microscopy and secondary ion mass spectrometry, Electrochimica Acta, 104 (2013) 462-467.

P6. J. Rysz, M. Josiek, **M. M. Marzec**, E. Moons, Pattern replication in blends of semiconducting and insulating polymers casted by horizontal dipping, Journal of Polymer Science Part B-Polymer Physics, 51 (2013) 1419

P7. J.Y. Lek, Y.M. Lam, J. Niziol, **M. M. Marzec**, Understanding polycarbazole-based polymer:CdSe hybrid solar cells, Nanotechnology, 23 (2012).

Conferences:

C1. Sputter depth profiling with large Ar_n^+ cluster ion beam for characterization of interfaces in multilayer organic structures / Mateusz Marek MARZEC, Jakub Rysz, Andrzej BERNASIK, Wojciech ŁUŻNY, Andrzej Budkowski // W: SIMS Europe 2014 European workshop on Secondary Ion Mass Spectrometry : Münster, Germany, September 7–9, 2014 : final program and book of abstracts / Westfälische Wilhelms-Universität Münster, Germany

C2. Dipole-dipole interactions at buried polymer/metal interfaces examined with Kelvin Probe Force Microscopy and Secondary Ion Mass Spectrometry / M. M. MARZEC, A. BERNASIK, J. Rysz, W. ŁUŻNY, A. Budkowski // W: SIMS-19 : the 19th international conference on Secondary Ion Mass Spectrometry : September 29–October 4, 2013, ICC Jeju, Jeju, South Korea.

C3. Characterization of silicon biosensor surfaces with Time of Flight Secondary Ion Mass Spectroscopy / J. Rysz, K. Awsiuk, K. Fornal, P. Petrou, A. Budkowski, A. BERNASIK, S. Kakabakos, M. M. MARZEC, I. Raptis // W: SIMS-19 : the 19th international conference on Secondary Ion Mass Spectrometry : September 29–October 4, 2013, ICC Jeju, Jeju, South Korea.

C4. Argon gas cluster ion beam in XPS analysis of poly(3-alkylthiophene)s / A. BERNASIK, M. M. MARZEC, J. Rysz, W. ŁUŻNY, A. Budkowski // W: ECASIA'13 : 15th European conference on Applications of surface and interface analysis : 13th – 18th October 2013 Cagliari, Sardinia (Italy).

C5. Self-assembled monolayers influence on polymer/metal interfaces examined by means of Kelvin Probe Force Microscopy and secondary ion mass spectrometry / Mateusz M. MARZEC, Andrzej BERNASIK, Jakub Rysz, Wojciech ŁUŻNY, Andrzej Budkowski // W: WOREN 2013 : 3rd Polish-French workshop on Organic electronics and nanophotonics: Muszyna-Złockie, 17–21 February 2013.

C6. Organic thin films depth profiling with large Arn+ cluster ion beam by X-ray photoelectron spectroscopy / Mateusz M. MARZEC, Andrzej BERNASIK, Jakub Rysz, Wojciech ŁUŻNY, Andrzej Budkowski // W: WOREN 2013 : 3rd Polish-French workshop on Organic electronics and nanophotonics : Muszyna–Złockie, 17–21 February 2013.

C7. Charakterystyka złacza polimer-metal metoda kelvinowskiej mikroskopii sił — [Characterization of polymer-metal interface by Kelvin Probe Force Microscopy] / MARZEC M. M., BERNASIK A., Awsiuk K., Rysz J., Budkowski A., ŁUZNY W. // W:

Kryształy molekularne : materiały XVIII ogólnopolskiej konferencji : Gdansk – Sobieszewo, 10–14 września 2012.

C8. Influence of self-assembled monolayers on polymer/metal interfaces examined with Kelvin probe force microscopy and secondary ion mass spectrometry / Mateusz Marek MARZEC, Kamil Awsiuk, Andrzej BERNASIK, Jakub Rysz, Wojciech ŁUZNY, Andrzej Budkowski // W: SIMS Europe 2012 : 8th European workshop on Secondary Ion Mass Spectrometry : September 9–11, 2012, Munster, Germany.

C9. Depth profiling of multilayers for spintronics and plastic electronics / Jakub Rysz, Andrzej BERNASIK, Mateusz MARZEC, Andrzej Budkowski, Jerzy WRONA, Jarosław KANAK, Tomasz STOBIECKI // W: SIMS Europe 2012 : 8th European workshop on Secondary Ion Mass Spectrometry : September 9–11, 2012, Munster, Germany.

C10. Examination of self-assembled monolayers influence on polymer/metal interfaces by Kelvin Probe Force Microscopy and secondary ion mass spectrometry / M. M. MARZEC, K. Awsiuk, A. BERNASIK, J. Rysz, W. ŁUZNY, A. Budkowski // W: ISSIS 2012 : 3rd International Symposium on Surface Imaging/Spectroscopy at the solid/liquid interface: May 27th–June 1st, 2012, Kraków, Poland.

C11. Cancerous cells investigation by means of Secondary Ion Mass Spectrometry / Justyna Gostek, Malgorzata Lekka, Joanna Wiltowska-Zuber, Jakub Rysz, Kamil Awsiuk, Mateusz MARZEC // W: XIV. Linz Winterworkshop : Linz, Austria, February, 2012.

C12. ToF-SIMS and surface studies of oligonucleotide probe immobilization for biosensor applications / M. M. MARZEC, P. Petrou, K. Awsiuk, J. Rysz, S. Kakabakos, A. BERNASIK, A. Budkowski, I. Raptis // W: SIMS XVIII : 18th international conference on Secondary Ion Mass Spectrometry : Riva del Garda, Italy, September 18–23, 2011.

C13. Principles of Kelvin Probe Force Microscopy in determination of interfacial electronic structures at organic/metal interfaces / M. M. MARZEC, K. Awsiuk, J. Rysz, A. BERNASIK, W. ŁUŻNY, A. Budkowski // W: Scientific Workshop of the Interdisciplinary PhD Studies: Zakopane, Poland, 13 – 19 September, 2011.

C14. Morphology of PANI(CSA)-PS thin films studied by means of scanning probe microscopy / Andrzej BERNASIK, Jakub HABERKO, Jakub Rysz, Mateusz MARZEC, Andrzej Budkowski, Wojciech ŁUZNY // W: Abstracts book of the VIII International conference on X-ray investigations of polymers structure : Wrocław, Poland, 8–10 December, 2010.